UNIVERSIDADE ESTADUAL DE CAMPINAS
Faculdade de Engenharia Mecânica e Instituto de Geociências

ROBERTO FERNANDO LEUCHTENBERGER

Experimental and theoretical study of W/O emulsion flow within centrifugal pumps

Estudo teórico e experimental do fluxo de emulsões A/O dentro de bombas centrífugas

Campinas

2025

ROBERTO FERNANDO LEUCHTENBERGER

Experimental and theoretical study of W/O emulsion flow within centrifugal pumps

Estudo teórico e experimental do fluxo de emulsões A/O dentro de bombas centrífugas

Thesis presented to the School of Mechanical Engineering and the Geosciences Institute of the University of Campinas in partial fulfillment of the requirements for the degree of Doctor of Science in Petroleum Engineering, with an emphasis on Exploration.

Tese apresentada à Faculdade de Engenharia Mecânica e Instituto de Geociências da Universidade Estadual de Campinas como parte dos requisitos exigidos para a obtenção do título de Doutor em Ciências e Engenharia de Petróleo, na Área de Explotação.

Orientador: Prof. Dr. Antonio Carlos Bannwart

Coorientador: Dr. Jorge Luiz Biazussi

ESTE TRABALHO CORRESPONDE À VERSÃO FINAL DA TESE DEFENDIDA PELO ALUNO ROBERTO FERNANDO LEUCHTENBERGER E ORIENTADA PELO PROF. DR. ANTONIO CARLOS BANNWART.

Campinas

2025

Ficha catalográfica
Universidade Estadual de Campinas (UNICAMP)
Biblioteca da Área de Engenharia e Arquitetura
Rose Meire da Silva - CRB 8/5974

L571e

Leuchtenberger, Roberto Fernando, 1994-
Experimental and theoretical study of W/O emulsion flow within centrifugal pumps / Roberto Fernando Leuchtenberger. – Campinas, SP : [s.n.], 2025.

Orientador: Antonio Carlos Bannwart.
Coorientador: Jorge Luiz Biazussi.
Tese (doutorado) – Universidade Estadual de Campinas (UNICAMP), Faculdade de Engenharia Mecânica.
Em regime multiunidades com: Instituto de Geociências.

1. Bombas centrífugas submersas (BCS). 2. Escoamento multifásico. 3. Viscosidade. 4. Emulsões. 5. Distribuição de tamanhos. I. Bannwart, Antonio Carlos, 1955-. II. Biazussi, Jorge Luiz, 1984-. III. Universidade Estadual de Campinas (UNICAMP). Faculdade de Engenharia Mecânica. IV. Título.

Informações complementares

Título em outro idioma: Estudo teórico e experimental do fluxo de emulsões A/O dentro de bombas centrífugas
Palavras-chave em inglês:
Electrical submersible pumps (ESP)
Multiphase flow
Viscosity
Emulsions
Size distribution
Área de concentração: Explotação
Titulação: Doutor em Ciências e Engenharia de Petróleo
Banca examinadora:
Antonio Carlos Bannwart [Orientador]
Valdir Estevam
William Monte Verde
Oscar Mauricio Hernandez Rodriguez
Francisco José Soares Alhanati
Data de defesa: 14-02-2025
Programa de Pós-Graduação: Ciências e Engenharia de Petróleo

Objetivos de Desenvolvimento Sustentável (ODS)
ODS: 9. Inovação e infraestrutura
ODS: 12. Consumo e produção responsáveis

Identificação e informações acadêmicas do(a) aluno(a)
- ORCID do autor: https://orcid.org/0000-0001-8997-9160
- Currículo Lattes do autor: http://lattes.cnpq.br/4053071647290529

Prof. Dr. Antonio Carlos Bannwart, Presidente
Faculdade de Engenharia Mecânica - UNICAMP

Prof. Dr. Valdir Estevam
Centro de Estudos de Energia e Petróleo - UNICAMP

Dr. William Monte Verde
Centro de Estudos de Energia e Petróleo - UNICAMP

Prof. Dr. Oscar Mauricio Hernandez Rodriguez
Departamento de Engenharia Mecânica - EESC-USP

Dr. Francisco José Soares Alhanati
C-FER Technologies

A Ata de Defesa com as respectivas assinaturas dos membros encontra-se no SIGA/Sistema de Fluxo de Dissertação/Tese e na Secretaria do Programa da Unidade.

DEDICATÓRIA

Dedico este trabalho a minha amada noiva Mariana, aos meus pais Eloir e Eliamar e ao meu irmão Julio.

ACKNOWLEDGEMENTS

Este trabalho representa a concretização de uma grande realização pessoal, uma conquista que só foi possível graças ao apoio e contribuição de muitas pessoas. Gostaria de expressar minha gratidão a todos que, de maneira direta ou indireta, contribuíram para este resultado, com agradecimentos especiais a:

Ao Dr. Jorge Luiz Biazussi, meu co-orientador desde o mestrado, cuja dedicação incondicional foi fundamental ao longo de toda a minha pós-graduação. Agradeço pela oportunidade de seguir meus estudos no doutorado, pela orientação precisa, pelas discussões enriquecedoras e pelos conhecimentos compartilhados. Sua persistência nos momentos desafiadores, confiança em meu trabalho e amizade sólida foram indispensáveis.

Ao Prof. Dr. Antonio Carlos Bannwart, por oferecer a oportunidade de ingressar no doutorado e contribuir com ideias valiosas para o desenvolvimento deste trabalho. Sua orientação, confiança e as discussões esclarecedoras desempenharam um papel essencial na construção das análises.

Aos professores, Prof. Dr. Valdir Estevam, Dr. William Monte Verde e Prof. Dr. Marcelo de Souza Castro, por seu apoio contínuo, ensinamentos nas diversas disciplinas durante a pós-graduação e pelas experiências, sugestões e correções que enriqueceram este trabalho.

Aos membros externos da banca examinadora, Prof. Dr. Oscar Mauricio Hernandez Rodriguez e Dr. Francisco Alhanati, pela leitura atenta, correções e sugestões que agregaram significativamente à qualidade desta pesquisa.

Aos pesquisadores Dr. Natan Augusto Vieira e Dr. Carlos Eduardo Perles, pelo suporte e orientação ao longo de todos os anos de mestrado e doutorado. Ao parceiro de laboratório Andrey Casas por auxiliar na continuidade dos testes experimentais.

Aos funcionários do DEP, CEPETRO e LABPETRO, pelo suporte técnico e pela disposição em ajudar em momentos de necessidade.

À minha noiva, Mariana Ferreira Alves, por seu amor incondicional, paciência, palavras de conforto, confiança e apoio em todas as fases deste processo.

À minha família, meus pais e meu irmão que formaram meu alicerce principal para conquistar esse objetivo. Sou grato pelo incentivo constante, carinho e compreensão em todos os momentos desta trajetória. A presença de vocês foi fundamental neste processo para a realização desse sonho.

Aos grandes amigos Thiago Mafra, João Vargas, Henrique Foletto e Marino Bonoto, pela amizade, apoio e que, mesmo à distância, me acompanharam durante todos esses anos.

Aos amigos Guilherme Costa, Marcelo Nunes, Filipe Torres, Ellen Kindermann, Julio Orsatto e à todos da República Vira-Latas, pelos momentos de descontração, festas, churrascos e amizade que foram um respiro essencial durante essa trajetória.

Finalmente, este trabalho foi realizado com o apoio da Fundação de Amparo à Pesquisa do Estado de São Paulo (FAPESP), processo 2017/15736-3, 2019/17879-1 e 19/20767-0 e da Equinor pelo apoio financeiro e técnico que possibilitaram a construção do aparato experimental utilizado neste estudo. A todos, o meu mais sincero agradecimento.

RESUMO

Este estudo investiga o desempenho de Bombas Centrífugas Submersas (BCS) operando com emulsões de água e óleo sob diferentes condições, com foco em métricas de desempenho como altura manométrica, eficiência, consumo de potência, distribuição do tamanho de gotas (DTG) e viscosidade da emulsão. A campanha experimental avaliou a influência da velocidade de rotação, vazão, temperatura e fração de fase dispersa no comportamento das BCS, complementada pelo desenvolvimento de modelos preditivos para melhorar a eficiência operacional.

A introdução destaca o papel crítico das BCS na indústria de óleo e gás e os desafios associados ao manuseio de escoamentos multifásicos. O estudo busca abordar a degradação de desempenho causada por fluxos emulsificados e propõe estratégias de otimização. A análise teórica foca em métricas adimensionais de desempenho, incluindo coeficiente de altura manométrica, coeficiente de potência e eficiência. Coeficientes de correção baseados no número de Reynolds rotacional são aplicados para considerar os efeitos viscosos.

O estudo desenvolve modelos para quantificar a degradação do desempenho sob condições de alta viscosidade, fornecendo uma base para prever o comportamento das BCS em regimes de escoamento complexos. Os resultados revelam impactos significativos da fração de fase dispersa, da viscosidade e da velocidade de rotação no desempenho da bomba. Testes com escoamento monofásico e bifásico demonstram degradação de desempenho em condições de alta viscosidade, com curvas adimensionais evidenciando variações na altura manométrica, potência e eficiência. Um novo modelo para a viscosidade relativa da emulsão é apresentado, considerando diâmetros críticos de gotas e condições de escoamento, alcançando maior precisão em comparação com modelos existentes. Os modelos propostos aprimoram as capacidades preditivas para sistemas BCS, permitindo otimizar o desempenho na produção de petróleo.

Palavras-chave: Bombas Centrífugas Submersas (BCS), Distribuição do Tamanho de Gotas (DTG), Emulsões Água-Óleo, Desempenho de Bombas, Comportamento Shear-Thinning

ABSTRACT

This study investigates the performance of Electrical Submersible Pumps (ESP) operating with water-oil emulsions under varying conditions, focusing on performance metrics such as head, efficiency, power consumption, droplet size distribution (DSD), and emulsion viscosity. The experimental campaign evaluated the influence of rotational speed, flow rate, temperature, and dispersed phase fraction on ESP behavior, complemented by the development of predictive models to improve operational efficiency. The introduction highlights the critical role of ESPs in the oil and gas industry and the challenges of handling multiphase flows. The study aims to address performance degradation caused by emulsified flows and proposes strategies for optimization. Theoretical analysis focuses on dimensionless performance metrics, including head coefficient, power coefficient, and efficiency. Correction coefficients based on the rotational Reynolds number are applied to account for viscous effects. The study develops models to quantify performance degradation under high viscosity conditions, providing a foundation for predicting ESP behavior in complex flow regimes. Results reveal significant impacts of dispersed phase fractions, viscosity, and rotational speed on pump performance. Single-phase and two-phase flow tests demonstrate performance degradation under high-viscosity conditions, with dimensionless curves highlighting variations in head, power, and efficiency. A novel model for emulsion relative viscosity is introduced, accounting for critical droplet diameters and flow conditions, achieving improved accuracy compared to existing models. The proposed models enhance predictive capabilities for ESP systems, enabling optimized performance in oil production applications.

Keywords: Electrical Submersible Pumps (ESP), Droplet Size Distribution (DSD), Water-Oil Emulsions, Pump Performance, Shear-Thinning Behavior

LIST OF FIGURES

LIST OF TABLES

LIST OF ABBREVIATIONS AND ACRONYMS

AOF	Absolute Open Flow
API	American Petroleum Institute
BEP	Best Efficiency Point
CFD	Computational Fluid Dynamics
CLD	Chord Length Distribution
DIN	Deutsches Institut für Normung
DSD	Droplet Size Distribution
ESP	Electrical Submersible Pump
FBRM	Focused Beam Reflectance Measurement
GOF	Goodness of Fit
HI	Hydraulic Institute
HLB	Hydrophilic-Lipophilic Balance
HLD	Hydrophilic-Lipophilic Difference
KF	Karl-Fischer Titration
KSB	KSB Standard
KS	Kolmogorov-Smirnov Test
o/w	Oil-in-Water
PBM	Population Balance Models
PF	Performance Factor
PSD	Particle Size Distribution
RMSE	Root Mean Square Error

SSE	Sum of Squared Errors
VSD	Variable Speed Driver
w/o	Water-in-Oil

LIST OF SYMBOLS

A_p, A_o, A_w	Cross-sectional area of pipe, oil and water
b_2	Blade width
β_2	Blade exit angle
C_H^{BEP}	Head correction coefficient at the Best Efficiency Point
C_Q^{BEP}	Flow rate correction coefficient at the Best Efficiency Point
C_η^{BEP}	Efficiency correction coefficient at the Best Efficiency Point
ΔP	Pressure differential
D	Impeller diameter
D_p	Pipe diameter
d	Droplet size
d_{32}	Sauter Mean Droplet Diameter
d_{95}	Maximum Stable Droplet Diameter
d_{crit}	Critical Droplet Diameter
f	Friction factor
f_d, f_o, f_w	Dispersed, oil and water phase fraction
g	Gravitational acceleration
H	Head
a, b, c	Empirical coefficients
$k_1, k_2, k_3, k_4, k_5, k_6$	Empirical coefficients
n	Number of diameter size class
N_s	Specific speed

P	Pressure
q_n	Number density frequency
KS	Kolmogorov-Smirnov Test
χ^2	Chi-squared Test
R^2	Correlation coefficient
q_v	Volume density frequency
Q	Volumetric flow rate
Re	Reynolds number
L	Length
r	impeller radius
Re_ω	Rotational Reynolds number
T	Temperature
E_b	Empirical constant
Oh	Ohnesorge Number
$\bar{U}$	Average velocity
U	Real velocity
U_s	Superficial velocity
U_{slip}	Slip velocity
$\dot{W}_{\text{shaft}}$	Shaft power
$\dot{W}_{\text{hyd}}$	Hydraulic power
η	Efficiency
μ_{rel}	Relative viscosity
μ	Viscosity

μ_c	Continuous phase viscosity
μ_d	Dispersed phase viscosity
μ_e	Effective viscosity
$\bar{\epsilon}$	Average Energy Dissipation
$\bar{\epsilon}_k$	Average Kinetic Energy Dissipation
$\bar{\epsilon}_{hyd}$	Average Hydraulic Energy Dissipation
ρ	Density
ϕ	Dimensionless flow rate
ψ	Dimensionless head
Π	Dimensionless power
z	Elevation
ϵ	Surface roughness
σ	Interfacial tension
τ	Torque
$\dot{\gamma}$	Shear rate
K_M, K_{PR}	Empirical constants
ω	Rotational speed
$\dot{m}$	Mass flow rate
$w/o, o/w$	Water-in-Oil, Oil-in-Water

CONTENTS

1 INTRODUCTION

Electrical Submersible Pumps (ESPs) are widely used in the oil and gas industry for artificial lift, playing a crucial role in enhancing production efficiency, especially in challenging reservoir conditions. However, when operating in multiphase flow environments—such as emulsions consisting of water, oil, and gas—ESP performance can be significantly degraded due to complex fluid dynamics and rheological behavior. The presence of a dispersed phase—particularly at higher volume fractions—introduces challenges that affect the hydraulic performance of the pump, including head (H), efficiency (η), and shaft power consumption ($\dot{W}_{shaft}$). These challenges are further compounded by the wide range of operational conditions encountered in the field, such as varying temperatures, flow rates, and fluid viscosities.

Despite the critical role ESPs play in oil extraction, there remain gaps in the understanding of how these systems behave when handling viscous emulsions. Current literature offers limited experimental data on the influence of key parameters—such as the dispersed phase fraction (f_d), temperature, and flow geometry—on both the droplet size distribution (DSD) and overall pump performance. Furthermore, existing models often fail to account for the interplay between droplet dynamics and hydraulic performance, particularly in high-viscosity, multiphase flow scenarios. Addressing these gaps is essential for improving the design, optimization, and operation of ESPs in complex fluid environments.

This research aims to provide a detailed experimental investigation into the behavior of emulsions in ESPs, focusing on two primary aspects: droplet dynamics and pump performance. By analyzing the DSD and studying how operational parameters such as flow rate, temperature, and pump geometry affect droplet breakup and size, this work seeks to offer new insights into the mechanisms governing emulsion flow inside ESPs. Additionally, the study evaluates the performance of two distinct pump geometries—mixed and radial flow designs—under various conditions, enabling a comparative analysis of how different configurations respond to emulsions with varying rheological and droplet characteristics.

Thus, the main objective of this work is to experimentally and theoretically study the influence of droplet size on effective viscosity in water-oil emulsions and its impact on the performance of ESPs. The following specific objectives were proposed to address these aims:

- To experimentally investigate the viscous degradation caused by emulsions in ESPs.

- To analyze droplet sizes at the ESP outlet and relate emulsion microstructure to pump performance.
- To examine the correlation between effective viscosity and droplet size in ESPs.
- To develop models for estimating average and maximum droplet sizes in ESPs.

To achieve these objectives, a comprehensive experimental matrix was designed, covering a wide range of operational conditions. In parallel with the performance results acquired, a Focused Beam Reflectance Measurement (FBRM) probe was employed to capture DSD data, providing valuable information on droplet breakup and size as f_d increases.

The findings of this research are expected to contribute to a more accurate understanding of the factors that influence ESP performance in multiphase flow environments and significantly improve the prediction and management of such systems, providing important insights for both academia and industry.

2 BASIC CONCEPTS AND LITERATURE REVIEW

This chapter is organized into two main sections. The first section introduces fundamental concepts, definitions, and general theoretical aspects related to centrifugal pumps, liquid-liquid flows, and droplet size measurement techniques. The second section provides a comprehensive review of literature focusing on centrifugal pump performance under viscous single-phase and liquid-liquid two-phase flows, emulsion characterization methodologies, and the primary phenomena governing these processes.

2.1 Centrifugal Pumps

Pumps are fluid-handling machines extensively utilized for fluid transport in various industrial and engineering applications. When mechanical work is imparted to a pump, energy is consequently transferred to the fluid. For centrifugal pumps, the amount of energy transferred can be quantified using an energy balance over a specified control volume. Under the assumptions of an adiabatic, isothermal, incompressible fluid flow at steady-state conditions, the head imparted to the fluid (H) can be expressed as:

$$H = \left(\frac{P}{\rho g} + \frac{\bar{U}^2}{2g} + z\right)_{\text{outlet}} - \left(\frac{P}{\rho g} + \frac{\bar{U}^2}{2g} + z\right)_{\text{inlet}} \tag{2.1}$$

where H is the pump head (m), $\bar{U}$ is the mean fluid velocity (m/s), ρ is the fluid density (kg/m^3), g is the acceleration due to gravity (m/s^2), z is the elevation head (m), and P is the fluid pressure (Pa).

2.1.1 Head Performance

The head (H) is a fundamental parameter in centrifugal pump performance analysis, representing the energy imparted to the fluid to elevate it to a certain height. Physically, it indicates the maximum height to which the pump can lift a fluid against gravitational forces. Mathematically, the pump head correlates directly with the pressure difference, as well as with the fluid velocity and elevation differences between the pump's inlet and outlet sections. Consequently, head serves as a critical measure of the pump's capability to overcome system resistance, thereby reflecting operational efficiency.

The generalized expression for the hydraulic head derives directly from the energy balance presented previously in Equation (2.1). However, under conditions where kinetic and potential energy changes between the inlet and outlet of the pump are negligible, the hydraulic head simplifies to a relationship involving exclusively the pressure differential across the pump stage:

$$H = \frac{\Delta P}{\rho g} \tag{2.2}$$

This simplified equation holds under the assumption that variations in fluid velocity and elevation between inlet and outlet are minimal and can be reasonably neglected—a scenario frequently encountered in practical centrifugal pump applications.

The variables in Equation (2.2) are defined as follows:

- H – Hydraulic head per pump stage (m);
- ΔP – Pressure differential across the pump stage (Pa);
- ρ – Fluid density (kg/m³);
- g – Gravitational acceleration (m/s²).

2.1.2 Shaft Power Performance

Shaft power ($\dot{W}_{shaft}$) represents the mechanical energy transmitted to the pump shaft, subsequently transferred to the fluid to generate flow and overcome system resistance. The shaft power is typically determined from measurements of torque (τ) applied to the shaft and the rotational speed (N) of the pump. It is an essential parameter for evaluating the energy consumption and operational efficiency of centrifugal pumps.

The shaft power per pump stage is calculated by:

$$\dot{W}_{shaft} = \frac{2\pi N \tau}{60} \tag{2.3}$$

Where:

- $\dot{W}_{shaft}$ – Shaft power per stage (W),
- N – Rotational speed (rpm),
- τ – Torque applied to the shaft (N·m).

2.1.3 Efficiency Performance

Pump efficiency (η) is a crucial performance parameter defined as the ratio between the useful hydraulic power transferred to the fluid and the mechanical shaft power supplied to the pump. Efficiency quantifies how effectively a pump converts mechanical input power into useful hydraulic output power.

Hydraulic power ($\dot{W}_{hyd}$) delivered to the fluid is calculated based on the volumetric flow rate (Q) and the pump head (H), using:

$$\dot{W}_{hyd} = \rho g Q H \tag{2.4}$$

Where:

- $\dot{W}_{hyd}$ – Hydraulic power per stage (W),
- ρ – Fluid density (kg/m³),
- g – Gravitational acceleration (m/s²),
- Q – Volumetric flow rate (m³/s),
- H – Hydraulic head per stage (m).

Pump efficiency (η) is thus expressed as:

$$\eta = \frac{\dot{W}_{hyd}}{\dot{W}_{shaft}} \tag{2.5}$$

Additionally, the total hydraulic head (H) and shaft power ($\dot{W}_{shaft}$) depend on operational conditions such as volumetric flow rate (Q) and rotational speed (ω) in rad/s, pump geometry including impeller diameter (D) and surface roughness (ϵ), and fluid properties such as density (ρ) and dynamic viscosity (μ). Applying Buckingham's Π theorem to these variables yields dimensionless relationships:

$$\frac{gH}{\omega^2 D^2} = g_1\left(\frac{Q}{\omega D^3}, \frac{\rho\omega D^2}{\mu}, \frac{\epsilon}{D}\right) \tag{2.6}$$

$$\frac{\dot{W}_{shaft}}{\rho\omega^3 D^5} = g_2\left(\frac{Q}{\omega D^3}, \frac{\rho\omega D^2}{\mu}, \frac{\epsilon}{D}\right) \tag{2.7}$$

Important dimensionless groups emerge from these relations, including dimensionless flow rate (ϕ), dimensionless head (ψ), dimensionless power (Π), and rotational Reynolds number (Re_ω):

$$Re_\omega = \frac{\rho \omega D^2}{\mu} \tag{2.8}$$

$$\phi = \frac{Q}{\omega D^3} \tag{2.9}$$

$$\psi = \frac{gH}{\omega^2 D^2} \tag{2.10}$$

$$\Pi = \frac{\dot{W}_{shaft}}{\rho \omega^3 D^5} \tag{2.11}$$

Thus, equations (2.6) and (2.7) can be simplified to:

$$\psi = g_1 \left(\phi, Re_\omega, \frac{\epsilon}{D} \right) \tag{2.12}$$

$$\Pi = g_2 \left(\phi, Re_\omega, \frac{\epsilon}{D} \right) \tag{2.13}$$

For high Reynolds number conditions (low viscosity and high rotational speeds), White (2011) experimentally demonstrated that Re_ω and ϵ/D have negligible effects on ψ and Π, thereby simplifying these dimensionless parameters to functions of ϕ alone. Consequently, pump efficiency (2.5) can also be represented dimensionlessly as:

$$\eta = \frac{\psi \phi}{\Pi} \tag{2.14}$$

Finally, the specific speed (N_s) is an important parameter for selecting and characterizing pump performance. It can be derived by eliminating the diameter (D) from ϕ and ψ. The physical meaning of N_s is the rotational speed of a centrifugal pump operating with water, required to produce a unit head at unit volumetric flow rate at the best efficiency point (BEP) (Fox *et al.*, 2011):

$$N_s = \frac{\phi^{1/2}}{\psi^{3/4}} = \frac{\omega Q_{\text{BEP,w}}^{1/2}}{(g H_{\text{BEP,w}})^{3/4}} \tag{2.15}$$

2.1.4 Physical Phenomena in Centrifugal Pumps Handling Viscous Flow

Understanding the physical phenomena occurring within centrifugal pumps is crucial for analyzing their performance with viscous fluids. The principal mechanisms influencing pump performance and viscous fluid behavior are shear and turbulence. These effects are interrelated, varying according to pump geometry and operational conditions, ultimately impacting the effective viscosity and stability of any emulsions formed.

2.1.5 Primary Physical Phenomena

- Shear: Shear results from velocity gradients within the pump and significantly impacts droplet breakup. Higher shear rates typically produce smaller droplets, increasing interfacial area and influencing the effective viscosity of emulsions. Within pump flows, two primary shear sources are identified:

  - Disk Friction: Occurs due to shear stresses between rotating impeller surfaces and fluid layers near stationary pump components, such as diffusers. This phenomenon generates additional energy losses, notably at high rotational speeds, affecting pump efficiency. Disk friction sensitivity is heightened by variations in temperature and the fraction of stagnant fluid, thus affecting its viscosity (Takacs, 2017).

  - Internal Friction: Arises from interactions between fluid layers, droplets of the dispersed phase, and internal pump surfaces. Droplet distribution within the continuous phase modifies flow resistance. Rigid droplets typically increase resistance, whereas deformable droplets can reduce friction, acting as lubricants within the flow (Takacs, 2017).

- Shock Losses: Result from abrupt changes in flow velocity or direction as the fluid enters the impeller or diffuser under non-ideal angles. These losses induce localized energy dissipation, particularly evident under off-design conditions, reducing hydraulic efficiency and increasing turbulence, which further influences droplet breakup and emulsion stability (Gülich, 1999).

- Recirculation Losses: Emerge due to flow reversal near pump inlet (suction recirculation) or outlet regions (discharge recirculation), predominantly at low-flow conditions. Suction recirculation risks cavitation and pump performance reduction, whereas discharge recirculation enhances turbulence and shear stress. Both phenomena significantly impact emulsion properties by affecting droplet coalescence and breakup rates (Gülich, 1999).

2.1.6 Turbulence in Pumps

Turbulence within centrifugal pumps involves chaotic, irregular flow fluctuations. Such fluctuations promote kinetic energy transfer from larger flow structures to smaller scales through an energy cascade process, eventually dissipating as thermal energy due to viscous action at the smallest scales. Flow path characteristics—such as bends, expansions, contractions, and surface roughness—can induce disturbances leading to turbulence. Additionally, impeller rotation itself can trigger turbulent fluctuations, especially when operating outside the pump's best efficiency point (BEP), such as at extremely low or high flow rates (Takacs, 2017). Increased turbulence influences effective viscosity and emulsion stability.

2.1.7 Liquid-Liquid Two-Phase Flow

Herein, the basic concepts of liquid-liquid two-phase flow in pipes will be introduced to aid on the study of emulsion flow within centrifugal pumps. The main parameters presented are in dimension and dimensionless terms and will be used throughout this work. The subscripts m, o and w represent the mixture, oil and water phases, respectively.

The mass flow rate of the liquid-liquid mixture is defined by the sum of mass flow rate of each one of the liquid phases.

$$\dot{m}_m = \dot{m}_o + \dot{m}_w \tag{2.16}$$

where $\dot{m}_o$ is the mass flow rate of oil and $\dot{m}_w$ is the mass flow rate of water. The mixture volumetric flow rate is defined in the same way.

$$Q_m = Q_o + Q_w \tag{2.17}$$

$$Q_o = \frac{\dot{m}_o}{\rho_o} \quad ; \quad Q_w = \frac{\dot{m}_w}{\rho_w} \tag{2.18}$$

where ρ_i and Q_i (for $i = o, w$) are the phase density and the volumetric flow rate of each one of the phases.

The superficial velocities of oil (U_{so}) and water (U_{sw}) represents the average velocity of each phase assuming they are flowing independently and are defined by the ratio of volumetric flow rate and pipe cross-sectional area. The mixture velocity (U_m) is the sum of the superficial velocities of each one the phases.

$$U_{so} = \frac{q_o}{A_p} \quad ; \quad U_{sw} = \frac{q_w}{A_p} \tag{2.19}$$

$$U_m = U_{so} + U_{sw} \tag{2.20}$$

where A_p is the pipe cross-sectional area.

Assuming that hypothesis that one phase flows independently of the other phase, the holdup is an statistical property of the flow which represents the probability of existence of certain phase in the flow field (Verde, 2016). The phase holdup or fraction is defined by the ratio of cross-sectional area of the phase and the cross-sectional area of the pipe. The sum of each one of the phase fraction is equal unit.

$$f_o = \frac{A_o}{A_p} \quad ; \quad f_w = \frac{A_w}{A_p} \tag{2.21}$$

$$f_o + f_w = 1 \tag{2.22}$$

The average real velocity of each phase is defined by the ratio of volumetric flow rate and cross-sectional area of the phase or they can be expressed in terms of superficial velocities and phase fraction, as it follows.

$$U_o = \frac{Q_o}{A_o} \quad ; \quad U_w = \frac{Q_w}{A_w} \tag{2.23}$$

$$U_o = \frac{U_{so}}{f_o} \quad ; \quad U_w = \frac{U_{sw}}{f_w} \tag{2.24}$$

Due to density and viscosity difference, the phases tend to move at different velocities and this difference between the local velocities results in a slippage of one phase in relation to the other (Aziz; Govier, 1972). The slip velocity (U_{slip}) is defined as:

$$U_{slip} = U_o - U_w \tag{2.25}$$

There are some flow patterns where there is no macroscopic differentiation between the phases and thus can be considered as a homogeneous mixture, i.e. do not show slippage between the phases. The liquid-liquid dispersed flow is the basic flow pattern found in upward vertical and off-vertical inclined flows. They will be always formed by two immiscible liquids under sufficiently intense mixing or can also be achieved in a low velocity scenario by the aid of a device which introduces the two fluids in the flow pipe (Brauner, 2003).

In liquid-liquid systems, a flow pattern often observed is the dispersion of two immiscible liquids, where one of them forms a continuous phase while the other becomes the dispersed phase into it. Generally, the dispersions can be of water-in-oil (w/o) and oil-in-water (o/w). In petroleum industry, oftentimes we have the ideal scenario of turbulence and mixing to produce a dispersed flow. The presence of natural surfactants that are produced with the crude oil stabilizes these dispersions by inhibiting coalescence of the dispersed droplets, forming emulsions.

In such intense mixing scenarios with stable emulsions and small droplets formed, as abovementioned, the simplest approach is the homogeneous model which neglects the slippage between the two liquid phases. The slippage between the phases was also found to be negligible in w/o dispersions in high viscosity oils and fine dispersions, however in o/w dispersions with low mixture velocities, large oil droplets are formed and slippage can not be neglected anymore (Brauner, 2003).

In the homogeneous model, the emulsion mixture is treated as pseudofluid with averaged properties, and the usual equations of single-phase flow are used. The phase density can be calculated by the following equation.

$$\rho_e = \rho_o f_o + \rho_w f_w \tag{2.26}$$

The viscosity of an emulsion (μ_e) cannot be defined usually like newtonian fluids, i.e., by the ratio between shear stress and rate. Since emulsions can behave differently and viscosity can show anomalous behavior in liquid-liquid flow (Angeli; Hewitt, 1999). One way is to calculate a relative viscosity (μ_r) with the viscosity of continuous phase (μ_c).

$$\mu_r = \frac{\mu_e}{\mu_c} \tag{2.27}$$

In addition to dispersed phase fraction (f_d), many other factors seem to contribute to the emulsion effective viscosity such as droplet size (d), temperature (T) and the emulsion rheology, which exhibits Newtonian behavior at low to moderate dispersed phase fraction (Brauner, 2003). In the following section, a literature review over emulsion formation, rheological behavior under certain conditions and existing models for effective viscosity prediction is presented.

2.1.8 Droplet size measurement

During analysis of liquid-liquid multiphase flows, the experimental measurement of droplet size can be expressed by statistical distributions. To enhance and aid data processing, usually these distributions are approximated by some known mathematical functions (Schmitt *et al.*, 2021). Given this, the number density frequency $q_n(d_i)$ and volume density frequency $q_v(d_i)$ can be determined using (2.28) and (2.29), respectively.

$$q_n(d_i) = \frac{n_i}{\sum_{j=1}^{k} n_i} \tag{2.28}$$

$$q_v(d_i) = \frac{n_i d_i^3}{\sum_{j=1}^{k} n_j d_j^3} \tag{2.29}$$

Where d_i and n_i are the class diameter and number of droplets in respective class i and k is the number of size classes of distribution.

2.1.9 Sauter Mean Diameter (d_{32})

The Sauter mean diameter (d_{32}) is of a particular interest in liquid-liquid dispersions as it represents a volume to surface mean diameter of overall distribution and is defined as it follows (2.30).

$$d_{32} = \frac{\sum_{i=1}^{k} n_i d_i^3}{\sum_{i=1}^{k} n_i d_i^2} \tag{2.30}$$

Also, several authors have shown that d_{32} can be correlated with d_{95} in terms of a linear relationship and for a more detailed review, refer to these works (Calabrese *et al.*, 1986; Lemenand *et al.*, 2003; Boxall *et al.*, 2012; Morales *et al.*, 2013; Bulgarelli *et al.*, 2022a).

2.1.10 Maximum stable droplet diameter (d_{95})

Another way to characterize liquid-liquid dispersions is by means of maximum stable droplet diameter d_{95}. This diameter is defined as the droplet size which belongs to 95% of cumulative volume frequency curve (Schmitt *et al.*, 2021). Several authors have performed experimental studies to predict d_{95} under shear and turbulence. Kolmogorov (1941) suggested that

d_{95} is related to the size of turbulent eddy sizes and thus, dependent on average kinetic energy dissipation rate $\bar{\epsilon}_k$. Hinze (1955) proposed that droplet break-up relies on the ratio between inertial stress of continuous phase and interfacial stress of dispersed phase. Additionally, based on Kolmogorov's theory, Hinze suggested that the critical Weber number could be determinant to droplet break-up occurrence and, so he proposed the following expression for maximum stable droplet diameter (2.31).

$$d_{95} = \left(\frac{\sigma \, \mathrm{We}_{\mathrm{crit}}}{2\rho_c} \right)^{\frac{3}{5}} \bar{\epsilon}_k^{-2/5} \tag{2.31}$$

where σ is the interface tension and ρ_c is the continuous phase density. However, these models do not consider the influence of viscous force and it is only valid in case the viscosity of continuous phase is equal or greater than dispersed phase. To address that, Davies (1985) proposed a modification on Hinze's model by adding a viscous force term for dispersed phase, as it follows:

$$d_{95} = \left(\frac{\mathrm{We}_{\mathrm{crit}}}{\rho_c} \right)^{3/5} \left(\frac{\sigma + \left(\mu_D \left(\bar{\epsilon}_k d_{95} \right)^{1/3} \right)}{4} \right)^{3/5} \bar{\epsilon}_k^{-2/5} \tag{2.32}$$

Furthermore, Pereyra (2011) performed several experiments regarding droplet break-up within static mixers, pipes, and jets. A further model improvement was presented based on the definition of the critical Weber number as the ratio between disruptive shear stress in the continuous phase and cohesive stress in the dispersed phase, as shown in Equation (2.33).

The classical Kolmogorov-Hinze theory assumes that droplet breakup occurs when the inertial stresses imposed by the turbulent eddies exceed the cohesive forces acting within the droplet, which are primarily governed by surface tension. However, this assumption is strictly valid only for low-viscosity droplets, where internal viscous dissipation can be neglected. To account for cases where the dispersed phase exhibits significant viscosity, an additional cohesive stress term related to the viscous resistance of the droplet was included.

$$d_{95} = \frac{\mathrm{We}_{\mathrm{crit}} \left(\sigma + 2^{-3/2} \mu_D \left(\bar{\epsilon}_k d_{95} \right)^{1/3} \right)^{3/5}}{\rho_d^{1/5} \rho_c^{2/5}} \bar{\epsilon}_k^{-2/5} \tag{2.33}$$

Herein, the cohesive stress acting against droplet deformation is composed of two main contributions: the interfacial stress due to surface tension (σ) and the viscous stress within the droplet (μ_D). The latter term arises from the resistance to deformation caused by internal shear within the droplet, which depends on the droplet size and the turbulent energy dissipation rate ($\bar{\epsilon}_k$).

By incorporating both interfacial and viscous effects into the force balance, this model achieves a more accurate prediction of the maximum stable droplet size (d_{95}), particularly in systems where high dispersed-phase viscosity plays a crucial role in inhibiting droplet breakup. The final expression maintains a dependency on the critical Weber number ($\mathrm{We}_{\mathrm{crit}}$), ensuring that the model remains consistent with classical turbulence-based breakup theories while extending its applicability to more complex multiphase flow conditions.

Dabirian *et al.* (2018) compared their experimental results with the models above and proved that the latter predicted the most accurate results for maximum stable droplet diameter.

2.2 Literature Review

2.2.1 Centrifugal Pumps Operating with Viscous Single-Phase Flow

The literature on the performance of centrifugal pumps operating with viscous fluids demonstrates that viscosity has a direct impact on the efficiency and flow rate of these pumps. One of the pioneering studies was conducted by Stepanoff (1949), who investigated the impact of viscosity on centrifugal pumps of different sizes and with viscosities up to 1900 mPa.s. His experiments showed that, at a constant rotation speed, increased viscosity reduces both the pump flow rate and head, while maintaining the specific speed constant at the best efficiency point. Stepanoff (1949) proposed correction factors based on dimensionless parameters, such as the Reynolds number and specific speed, offering a theoretical foundation that remains relevant today.

The The Hydraulic Institute (1955) expanded on this work by proposing charts to correct the effects of viscous fluids in conventional centrifugal pumps, taking into account parameters like efficiency and head. This methodology provides a practical approach for calculating pump performance with viscous fluids, serving as a reference in the industry. Additionally, the work by Gülich (1999) presented a semi-empirical model for viscosity correction in pump performance, based on energy dissipation within the pump. This model emphasizes the impact of disk friction and viscous dissipation within the impeller channels, which are primary causes of performance degradation when handling viscous fluids.

Amaral (2007) developed a theoretical-experimental study to examine the influence of viscosity on centrifugal pump performance. Using experimental data with different fluid viscosities and pump configurations, Amaral proposed a predictive model to estimate pump performance under viscous conditions, achieving validation through experimental testing. Solano (2009) also explored the effects of viscosity on pump performance and employed dimensionless groups to represent pump behavior, highlighting the importance of maintaining consistent relationships between flow and head coefficients across different viscosities and rotational speeds.

Biazussi (2014) developed a detailed single-phase loss model to characterize the hydraulic performance of electrical submersible pumps (ESPs) operating with viscous oil. The model is based on the classical Euler head formulation, corrected by subtracting the energy losses associated with real fluid flow. These losses are categorized into frictional losses due to wall shear, turbulent losses arising from flow phenomena such as recirculation, secondary flows, and incidence effects, and localized losses occurring at the pump inlet and outlet. Each component is described using dimensionless correlations that incorporate geometric parameters of the impeller and operational variables such as flow rate and rotational speed. The model includes both laminar and turbulent contributions to wall friction and captures flow-dependent phenomena through empirical terms calibrated from experimental data. The model equation is expressed as follows:

$$\psi = \frac{1}{4} - k_4 + (-k_1 - \frac{k_2}{Re_\omega} + 2k_4k_5)\phi + \left[- \left(\frac{1}{\phi Re_\omega} \right)^n k_3 - k_4k_5^2 - k_6 \right] \phi^2 \tag{2.34}$$

Where:

- ψ is the dimensionless head,
- ϕ is the dimensionless flow rate,
- k_1 is a parameter related with the geometry of the pump and is defined below,
- k_4, k_5, k_6 are empirical coefficients adjusted based on water performance curves,
- k_2, k_3 and n are empirical coefficients adjusted based on oil performance curves,
- Re_ω is the rotational Reynolds number, accounting for the effects of rotational speed (ω) on the flow's viscous characteristics.

The term k_1 is defined by:

$$k_1 = \frac{D \cot(\beta_2)}{2\pi b_2} \tag{2.35}$$

Where:

- D is the impeller diameter,
- β_2 is the blade exit angle,
- b_2 is the impeller blade width.

And, the rotational Reynolds number (Re_ω) is defined by:

$$Re_\omega = \frac{\rho_m \omega D^2}{\mu_m} \tag{2.36}$$

Where ρ_m and μ_m are the mixture density and viscosity.

This comprehensive formulation enables the prediction of pressure head over a wide range of operating conditions and serves as a physically grounded baseline for analyzing pump behavior. In later stages of the study, this single-phase model was extended to estimate pump performance under gas-liquid flow conditions by introducing modifications to account for phase slip and flow regime transitions.

In recent years, advancements in computational fluid dynamics (CFD) have enabled detailed numerical studies of pump performance under viscous flow conditions. Studies by Ofuchi *et al.* (2015) and Vieira *et al.* (2015) have applied CFD models to simulate viscous fluid behavior within centrifugal pumps, providing a deeper understanding of internal flow dynamics and identifying sources of energy dissipation.Vieira *et al.* (2015), in particular, categorized losses into internal and external types within the impeller, applying models for friction, shock, and recirculation losses based on the Euler equation for theoretical head.

Estrada (2019) conducted an experimental study to investigate the single-phase performance of a 10-stage Electrical Submersible Pump (ESP) with mixed geometry, commonly used in the petroleum industry, when operating with ultra-viscous crude oil. The experiments were carried out in a custom-built test circuit using crude oils with viscosities ranging from 8 cP to 1000 cP and rotation speeds between 1200 and 3500 rpm, with flow rates up to 210 m^3/h.

In this single-phase study, performance curves were plotted to illustrate the pressure gain and shaft power for various liquid flow rates, providing insight into the pump's operational behavior under different viscosities. Additionally, a comparative analysis of the experimental results against major correction methods available in the literature to evaluate their applicability to high viscosity fluids was performed. A one dimensional model was also developed to calculate performance parameters based on loss analysis and to predict fluid heating throughout the pump stages, contributing valuable data for understanding ESP performance with viscous fluids.

Ofuchi *et al.* (2020) investigated the degradation in performance of Electric Submersible Pumps (ESPs) when operating with highly viscous fluids, such as oil, as opposed to water. In scenarios where centrifugal pumps are used with viscous liquids, their performance tends to deteriorate, and conventional correction methods in the literature often fail to accurately predict this degradation. Many existing methods are pump specific or require hard-to-obtain geometric parameters, making them challenging to apply broadly.

To overcome these limitations, Ofuchi *et al.* (2020) developed a new model to estimate the degradation in head and flow rate for centrifugal pumps operating across a wide range of Reynolds numbers. The model considers both high liquid viscosities and low rotational speeds. It was formulated based on experimental data obtained from tests conducted on two mixed-flow ESPs and one radial type pump, operating at rotational speeds of up to 3500 rpm and viscosities as high as 822 cP. One notable advantage of this model is that it does not depend on geometric parameters. Instead, it utilizes the water baseline curve and standard design data, which are typically included in pump datasheets.

The proposed model demonstrated superior accuracy compared to other correction methods in the literature, such as the HI and KSB standards. Maximum deviations from experimental data were 53.3% for the proposed model, while Hydraulic Institute and KSB methods described by Gülich (2008) showed deviations of 176.5% and 136.2%, respectively, confirming the effectiveness of Ofuchi *et al.* (2020) model for performance prediction of ESPs with viscous fluids.

One notable study was conducted by Kindermann (2022), providing valuable insights into the performance of centrifugal pumps operating with viscous fluids. The author conducted experiments on six pump models using glycerin and glycerin-water solutions at different rotational speeds, with viscosities ranging from 24 to 1273 cP. The study demonstrated significant performance degradation due to viscosity, showing reductions in head, efficiency, and flow rate as viscosity increased. Additionally, Kindermann evaluated the accuracy of existing empirical models for predicting pump performance under viscous conditions, highlighting their limitations and proposing modifications to improve their predictive capabilities. A new empirical model was also developed specifically for submersible centrifugal pumps, validated across different configurations, and designed for integration into pump selection tools and production system simulations. The findings reinforce the need for refined models that better capture the complexities of ESP operation with viscous fluids, as current methods often fail to provide accurate performance predictions.

2.2.2 Centrifugal Pumps Operating with Liquid-Liquid Two-Phase Flow

Despite extensive research on centrifugal pumps and Electrical Submersible Pumps (ESPs) in single-phase flow, recent work has focused increasingly on complex two-phase liquid-liquid flows, specifically oil-water emulsions. This shift is driven by the growing relevance of mature and heavy crude oil wells. While few studies address centrifugal pumps operating under dispersed oil-water and emulsion conditions, early foundational work explored the behavior of such dispersions.Ibrahim e Maloka (2006) experimentally examined oil-water dispersions in centrifugal pumps, characterizing droplet size at the inlet using advanced laser techniques. This initial work paved the way for Khalil *et al.* (2008), who conducted one of the first studies on pump performance with oil-water emulsions, demonstrating that temperature and emulsion stability significantly impact performance. Specifically, stable emulsions led to greater performance derating.

Building on these early studies, Morales *et al.* (2013) analyzed droplet formation in oil-water flows through a centrifugal pump, examining droplet size distribution at the outlet as a function of pump speed, flow rate, and water cut. Morales et al. determined that pump speed strongly influenced droplet size, which decreased with higher speed, while flow rate and water cut had minimal effects. They identified turbulent breakup as the primary droplet formation mechanism and provided a predictive model with good agreement to experimental data.

Furthering this research, Bulgarelli *et al.* (2020) explored ESP performance under emulsion flow, investigating phase inversion with varying oil types, viscosities, ESP speeds, and flow rates. They identified phase inversion points using logistic functions based on dimensionless head and proposed an indirect method to estimate the effective emulsion viscosity within the ESP from performance curves. Their findings showed that emulsion effective viscosity within an ESP can differ markedly from pipeline flow, likely due to intense centrifugal forces unique to ESPs.

In an important development, Croce e Pereyra (2020) examined the formation and inversion of oil-water emulsions in a multistage ESP. They observed that increasing water cuts up to the inversion point (water-in-oil, w/o) led to greater head deration. Beyond the inversion point (oil-in-water, o/w), higher water cuts resulted in enhanced pump performance due to reduced emulsion viscosity. This work emphasized the performance impact of phase inversion, contributing valuable insights into handling emulsion flows in ESPs.

Subsequent studies have offered deeper insights into emulsion rheology and droplet dynamics in ESPs. For instance, Banjar e Zhang (2019) investigated emulsion viscosity within ESPs across different water fractions, rotational speeds, and temperatures, employing dimensional analysis to model effective viscosity. Their study indicated that low viscosity oils led to larger deviations in viscosity measurements due to emulsion instability, with recommendations for refining the model by including factors like salinity.

Lastly, Perissinotto *et al.* (2019) focused on oil droplet kinematics within an ESP impeller, examining oil-in-water flows at different rotational speeds. Their experimental design enabled direct visualization of droplet motion, revealing that higher speeds and flow rates intensified turbulence, resulting in smaller droplets. Droplet velocities varied by impeller position, with higher velocities near the suction blade, attributed to pressure gradients and drag forces. This study highlighted the effects of high rotational Reynolds numbers, where turbulence strongly influences droplet size and behavior.

Together, these studies highlight the need for advanced models and adaptive ESP designs to optimize performance under challenging multiphase oil-water flow conditions. They underscore the critical role of factors such as droplet breakup, emulsion stability, and rheological characteristics under high shear and centrifugal fields in improving ESP performance with emulsions.

2.2.3 Emulsion Characterization and Stability

Emulsions differ slightly from general dispersions, primarily due to their reliance on surface-active agents known as surfactants. These molecules, which are typically soluble in one phase and adsorbed at the interface, enable interaction between both phases simultaneously, thereby stabilizing droplets at specific sizes (Maffi *et al.*, 2021).

The formation of a reasonably stable emulsion generally requires three key conditions: the presence of two immiscible liquids, an interfacially active agent (i.e., a surfactant), and sufficient mechanical agitation to promote the mixing of the liquids and the distribution of the surfactant at the interface.

Surfactants are amphiphilic compounds containing both polar (hydrophilic) and nonpolar (lipophilic) functional groups. Natural surfactants are often present in crude oils, particularly in the form of resins and asphaltenes, and play a central role in the spontaneous formation of emulsions in oil reservoirs (Guo *et al.*, 2016).

Emulsion type (e.g., water-in-oil or w/o, and oil-in-water or o/w), its properties, and phase inversion phenomena can be characterized based on three main categories:

1. Field Variables: Related to the thermodynamic equilibrium of the system, including the chemical nature of components, pressure, and temperature.
2. Compositional Variables: Representing the relative proportions of water, oil, and surfactant within the ternary system.
3. Process Variables: Describing how the emulsion is formed or modified, including the time and spatial evolution of the variables in (a) and (b).

According to Salager (2006), heavier fractions such as asphaltenes, resins, waxes, and oxidation byproducts may act as effective emulsifying agents when dissolved or dispersed in oil. Consequently, emulsions derived from heavier crude oils are generally more stable and more resistant to separation.

Emulsion stability is defined as the ability of the dispersed phase to remain uniformly distributed within the continuous phase. It is typically assessed by the resistance of droplets to gravitational forces, which promote sedimentation or creaming and lead to droplet coalescence and eventual phase separation (Salager, 2006). Despite potential kinetic stability, emulsions are generally thermodynamically unstable due to the high interfacial area, which increases the system's Gibbs free energy. Emulsion stability depends on interfacial tension, entropy, droplet size, volume fraction of the dispersed phase, temperature, and preparation method. In special cases, such as microemulsions, entropy gains can offset interfacial energy, enabling thermodynamic stability (Zhu *et al.*, 2019).

Bellary *et al.* (2017) studied the effects of dispersed phase fraction (f_d) and mixing duration on w/o emulsions in electrical submersible pumps (ESPs). Their results demonstrated that increasing f_d led to greater droplet crowding, increased coalescence, and reduced stability (Ushikubo; Cunha, 2014). Furthermore, elevated pump speeds induced higher shear rates, which promoted both droplet collision and breakup, with competing effects on emulsion stability (Morales *et al.*, 2013). The addition of chemical emulsifiers increases effective viscosity, which, in turn, negatively impacts pump performance by increasing hydraulic resistance (Khalil *et al.*, 2006).

2.2.4 Droplet Breakup and Coalescence in Liquid-Liquid Dispersions

The phenomena of droplet breakup and coalescence in liquid-liquid dispersions are critical to understanding emulsion behavior and stability. In recent years, several studies have employed numerical techniques such as Population Balance Models (PBM) coupled with Computational Fluid Dynamics (CFD) to simulate these processes with high accuracy, albeit at significant computational cost (Oshinowo; Vilagines, 2020).

Droplet coalescence generally follows three sequential steps:

1. Approach and collision between two droplets,
2. Drainage of the thin continuous-phase film that separates them,
3. Rupture of the interfacial film and subsequent merging into a larger droplet.

Early coalescence models, such as that proposed by Smoluchowski (1917), did not consider detailed particle interactions but identified a "rapid coalescence" regime in which most droplet collisions result in merging. Later, Shinnar (1961) suggested that above a critical droplet size, coalescence could be suppressed due to energy and adhesion barriers between colliding droplets.

A widely accepted theory posits that coalescence depends on the time required for film drainage between approaching droplets. During this period, hydrodynamic forces and interfacial properties may either facilitate or hinder film rupture. According to Groothuis e Zuiderweg (1960), an increased coalescence rate may be attributed to surfactant-induced interfacial tension gradients, a phenomenon known as the Marangoni effect. Surfactant accumulation near the interface lowers local interfacial tension, promoting fluid movement out of the interfacial film region and accelerating film drainage. This mechanism explains why not all collisions lead to coalescence. Additional influencing factors include interface mobility, density differences between phases, and the presence of electrolytes in the continuous phase (Liu *et al.*, 2019; Besagni; Inzoli, 2017).

Using a microfluidic approach, Dudek *et al.* (2020) developed an experimental method to investigate coalescence under controlled conditions. Their results demonstrated that the presence of heavy crude oil fractions, such as resins and asphaltenes, significantly suppressed coalescence frequency, suggesting enhanced interfacial stabilization.

In contrast, droplet breakup occurs when external stresses overcome interfacial cohesion. Mechanisms responsible for breakup include turbulent eddies, pressure fluctuations, and viscous shear. As described by Herø *et al.* (2020), droplets exposed to dynamic pressure and velocity gradients may deform, elongate, and eventually split into daughter droplets. The breakup process depends on a balance between disruptive hydrodynamic forces and restorative surface tension. In many cases, daughter droplets may undergo secondary breakup, especially under high shear or turbulent conditions.

The interplay between droplet coalescence and breakup is essential to determining the steady-state droplet size distribution in emulsions, directly impacting their rheological properties and stability in dynamic flow systems.

2.2.5 Emulsion effective viscosity

At low concentrations of the dispersed phase, emulsions typically exhibit Newtonian behavior. However, as the concentration of the dispersed phase increases, emulsions tend to display non-Newtonian characteristics, strongly influenced by the flow hydrodynamics and local shear rate distribution. Beyond the dispersed phase fraction, emulsion rheology is affected by several parameters, including the continuous phase viscosity (μ_c), temperature (T), shear rate ($\dot{\gamma}$), droplet size distribution (d), dispersed phase viscosity (μ_d), and the presence and concentration of emulsifying agents (Rønningsen, 1995).

Numerous empirical and semi-empirical models have been developed to describe the effective viscosity of oil-water emulsions, many of which originated from studies on solid-liquid suspensions. While only a few models are specifically tailored for liquid-liquid systems, solid dispersion models are frequently adapted for emulsion systems due to their relative simplicity and predictive capacity (Vielma, 2006).

One of the earliest models was proposed by Einstein (1906), who derived an expression for the relative viscosity of highly dilute suspensions ($f_d < 0.02$), assuming non-interacting rigid spherical particles:

$$\mu_r = 1 + 2.5 f_d \tag{2.37}$$

For emulsions, Taylor (1932) extended Einstein's model to include internal circulation within deformable droplets, leading to the following relationship:

$$\mu_r = 1 + 2.5\left(\frac{\mu_d + 0.4\mu_c}{\mu_d + \mu_c}\right) f_d \tag{2.38}$$

Subsequent models by Mooney (1951) and Brinkman (1952) accounted for droplet interactions and higher phase concentrations. For example, Mooney proposed a model suitable for moderate concentrations ($f_d < 0.5$) assuming monodisperse spherical particles:

$$\mu_r = \exp\left(\frac{2.5 f_d}{1 - K_M f_d}\right) \tag{2.39}$$

where K_M is an empirical constant that depends on droplet arrangement and deformation.

Similarly, Brinkman proposed:

$$\mu_r = (1 - f_d)^{-2.5} \tag{2.40}$$

Pal e Rhodes (1989) further refined these models to consider shear-dependent viscosity, droplet deformation, and higher dispersed phase fractions (up to $f_d < 0.74$), incorporating a fitting constant K_{PR}:

$$\mu_r = \left(1 + \frac{f_d}{K_{PR}(1.1884 - f_d)}\right)^{2.5} \tag{2.41}$$

While most of these models are applicable to Newtonian emulsions, some have been adapted to predict non-Newtonian flow behavior in pipeline systems. Nonetheless, no general model currently exists that accurately predicts emulsion viscosity under all operational conditions, especially within dynamic environments such as pumps.

Bulgarelli (2018) investigated effective emulsion viscosity within electrical submersible pumps by indirectly estimating viscosity through ESP head performance curves. Their results showed discrepancies between pump and pipeline viscosity behavior, attributed to centrifugal effects inducing phase separation and droplet slippage within the pump stages.

Building on this, Zhu *et al.* (2019) introduced a mechanistic model for ESP performance under emulsion flow, integrating a novel viscosity correlation and a phase inversion model based on the Brinkman approach. The model demonstrated predictive accuracy within ±10% for emulsions and ±15% for single-phase viscous fluids.

In general, emulsion stability and viscosity are closely linked. Stable emulsions, particularly those formed with surfactants or natural emulsifiers, tend to exhibit higher effective viscosities. Phase separation, on the other hand, typically reduces viscosity due to reduced interfacial area and droplet interactions.

Studies such as Raya *et al.* (2020) and Zolfaghari *et al.* (2016) highlight that emulsion viscosity and phase separation time are often used in tandem as stability indicators. Furthermore, the emulsion microstructure (e.g., droplet size distribution and concentration) has a direct influence on bulk rheological behavior (Tadros, 2013).

Bulgarelli *et al.* (2021b) also proposed a model based on Taylor (1932), as it follows. This formulation incorporates Reynolds, Weber, and Ohnesorge numbers to characterize the interplay between inertial, viscous, and interfacial forces within the pump.

$$\mu_r = 1 + 2.5 \left(\frac{E_b\, Oh}{\phi + \mathrm{Re}_\omega^{-k}} \right) \left(\frac{\mu_d + 0.4\mu_c}{\mu_d + \mu_c} \right) f_d \tag{2.42}$$

Additionally, parameters E_b and k were introduced to capture interfacial elasticity and the influence of shear rate due to ESP rotational speed. These modifications enhance the model's capability to represent the complex rheological behavior of emulsions in high-shear environments, improving predictions of viscosity-related performance losses. A more detailed discussion of this model is presented in Chapter 4.

In unstable w/o emulsions, Bulgarelli (2018) observed that effective viscosity decreases as the water cut increases toward the phase inversion point. This phenomenon resembles drag reduction seen in pipeline flows, where frictional resistance diminishes as the continuous phase becomes dominant.

In centrifugal systems, this drag reduction is exacerbated by phase slippage due to radial acceleration. The terminal velocity of dispersed droplets, influenced by droplet size, interfacial tension, surfactants, and density difference, governs the extent of phase separation. Morales *et al.* (2013) reported that smaller droplets—resulting from higher pump speeds—were more likely to remain entrained in the flow, increasing apparent viscosity and emulsion stability within centrifugal pumps.

2.2.6 Phase Inversion

Phase inversion refers to the abrupt transition between emulsion types, typically from water-in-oil (w/o) to oil-in-water (o/w), or vice versa. This phenomenon occurs when the volume fraction of the dispersed phase surpasses a critical threshold, resulting in a structural reorganization of the emulsion. Inversion is influenced not only by phase fraction but also by operational variables such as temperature, salinity, shear rate, and surfactant characteristics (Salager, 2006; Croce; Pereyra, 2020).

Phase inversion can be detected by monitoring sudden changes in key emulsion properties, such as electrical conductivity, viscosity, or droplet morphology. Viscosity is particularly indicative, as it typically increases near the inversion point due to droplet crowding and intensified interactions, followed by a sharp drop once the inversion occurs (Genovese, 2012).

Two principal theoretical frameworks are used to explain phase inversion: the kinetic approach focuses on the dynamic balance between coalescence and droplet breakup. At critical dispersed phase fractions, coalescence events become dominant, leading to the formation of a continuous network that ultimately triggers inversion (Maffi *et al.*, 2021). The thermodynamic approach proposed by Luhning (1971) considers phase inversion as the result of system energy minimization. In this context, inversion corresponds to a state where the total Gibbs free energy is reduced. However, this model does not always fully explain observed behaviors, particularly those involving partial inversion or hysteresis. Yeo *et al.* (2002) expanded this concept, suggesting that interfacial energy plays a more significant role than kinetic energy in governing inversion behavior.

Most research on phase inversion has been conducted in pipeline or stirred-tank systems. Only a limited number of studies have addressed phase inversion in centrifugal pumps. Achour *et al.* (2024) compiled a comprehensive review of pump-based inversion studies, highlighting the influence of emulsion type, fluid properties, pump speed, and dispersed phase fraction on inversion behavior. In many of these studies, simultaneous injection of both oil and water at the pump inlet was used to analyze inversion onset and effects on pump performance.

Findings suggest that unstable emulsions undergo phase inversion at lower dispersed phase fractions than stable emulsions (Croce; Pereyra, 2020; Banjar; Zhang, 2019; Valdés *et al.*, 2020; Bulgarelli *et al.*, 2020). Moreover, o/w emulsions typically invert at lower dispersed phase concentrations than w/o emulsions, likely due to the greater wettability of water with pump components, which favors continuous phase dominance (Zhang *et al.*, 2019; Bulgarelli *et al.*, 2021a).

The choice of surfactant is a critical factor influencing phase inversion. The Hydrophilic-Lipophilic Balance (HLB) value of the surfactant determines its tendency to stabilize either w/o or o/w emulsions. High HLB values favor o/w emulsions, while low HLB values promote w/o structures. The Hydrophilic-Lipophilic Deviation (HLD) model further refines this understanding, predicting inversion near a critical HLD value: negative for w/o emulsions and positive for o/w emulsions (Salager, 2006).

Experimental studies by Bellary *et al.* (2017), Barrios *et al.* (2017), and Bulgarelli *et al.* (2022a) show that the presence of surfactants delays phase inversion, requiring higher dispersed phase fractions for stable emulsions. Conversely, the introduction of demulsifiers lowers the inversion threshold, facilitating destabilization.

In highly viscous systems, the emulsion viscosity can increase dramatically near the inversion point. As shown in Rondon-Gonzalez *et al.* (2007), this behavior is characterized by three regimes: (i) a pre-inversion zone of exponential viscosity increase, (ii) a narrow transition zone, and (iii) a post-inversion regime with reduced and stabilized viscosity.

In conclusion, phase inversion within centrifugal pumps is a complex, multi-variable phenomenon influenced by dispersed phase fraction, emulsion stability, surfactant properties, and pump operating conditions. A deeper understanding of phase inversion is essential for the optimization of multiphase flow systems, particularly those involving emulsions in high-shear environments.

2.2.7 Conclusion of Literature Review

The literature review presented in this chapter has highlighted the main concepts and advancements in the study of centrifugal pumps, with a particular focus on Electrical Submersible Pumps (ESPs) operating with viscous fluids and liquid-liquid flows, especially water-oil emulsions. The existing literature provides a solid foundation for understanding performance parameters such as head, shaft power, and efficiency, as well as the physical phenomena influencing the behavior of viscous fluids and emulsions, including shear, turbulence, droplet breakup and coalescence, and phase inversion.

However, significant gaps remain that justify the need for further research. First, most studies focus on empirical corrections for single-phase viscous fluids, while the behavior of ESPs operating with liquid-liquid emulsions remains underexplored, particularly under high viscosity and turbulent conditions. Additionally, existing models for predicting emulsion effective viscosity and droplet size distribution (DSD) often fail to account for the specific operating conditions of centrifugal pumps, such as high shear rates and centrifugal forces. The influence of parameters such as dispersed phase fraction, rotational speed, and temperature on ESP performance also lacks a comprehensive and systematic approach.

In this context, the present work aims to address these gaps by investigating the performance of ESPs operating with water-oil emulsions under various operational conditions. The study proposes a detailed analysis of performance metrics, including head, efficiency, and power consumption, as well as the characterization of droplet size distribution and emulsion viscosity. The experimental and theoretical approach adopted seeks to develop more accurate predictive models that consider the combined effects of dispersed phase fraction, viscosity, rotational speed, and flow conditions.

By integrating established concepts from the literature with novel approaches, this work aims to advance the understanding of ESP behavior in complex multiphase flows, providing insights for optimizing pump design and operation in the oil and gas industry. The identification and quantification of physical phenomena, such as droplet breakup and phase inversion, will enable the development of more effective strategies to mitigate performance degradation under emulsion conditions.

3 EXPERIMENTAL METHODOLOGY

A brief explanation of the experimental methodology used in the testing of electrical submersible centrifugal pump will be provided in this chapter. Section 3.1 will present the experimental facility, section 3.2 will cover the fluid characterization, section 3.3 will describe the pumps tested, section 3.4 will cover the details of droplet size measurement technique and section 3.5 will outline the proposed experimental test matrix and the experimental procedure.

3.1 Experimental Facility

An experimental setup was developed (Figure 3.1) to evaluate the performance of the ESP under stable water-oil emulsion flow conditions. The facility employed in this study was previously presented in the works of Bulgarelli *et al.* (2021a) and Castellanos *et al.* (2023), with minor modifications to accommodate the testing of stable emulsions.

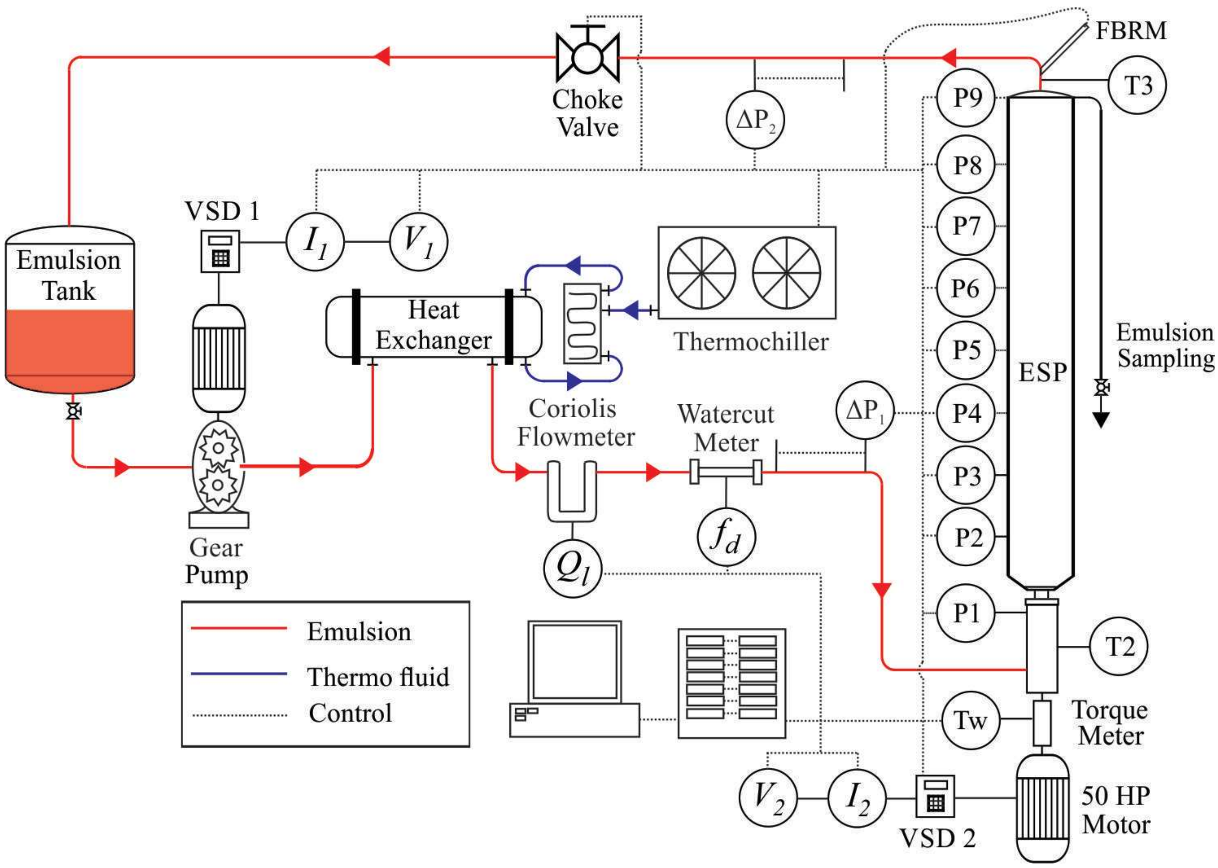

Figure 3.1 – Experimental layout.

The entire setup was instrumented to measure all relevant variables required for pump performance calculations using the aforementioned dimensionless groups. The emulsion was initially prepared in a dedicated tank, incorporating a surfactant additive (1 wt.%) to ensure stability, and was homogenized using mixing blades. The prepared emulsion is circulated from the tank using a two-screw booster pump (Figure 3.2) and the tested ESP within a closed-loop system. Due to the heating up scenario, a temperature control system is essential in the experimental setup. It also allows to carry out tests with different properties (viscosity and density) by using the same fluids. The system is composed by a shell and tube heat exchanger, a thermochiller and temperature is measured by resistance temperature detectors positioned along the experimental bench (PT100, four wires, 1/100 DIN), as shown in (Figure 3.1).

Figure 3.2 – Booster used to pump the emulsion mixture through the system flow loop.

The water fraction in the mixture is measured using a water cut meter, model Nemko 05 ATEX 112 (Roxar®), while the mixture's density and flow rate are determined with a Coriolis flow meter, series F300 (Micro Motion®). Differential pressure gauges are installed along a horizontal 3-inch pipeline, positioned upstream and downstream of the ESP, to calculate the emulsion's effective viscosity. Two ESPs, described in greater detail in Section 4.3, were tested. These pumps are powered by a 50 hp electric motor and equipped with nine pressure transmitters, series 2088 (Emerson Rosemount®), distributed across their stages.

The rotational speed of the ESPs and the booster pump is regulated by a variable speed drive (VSD) and tracked with an optical tachometer (Minipa®, MDT-2238A). The torque of the ESP is recorded using a torque meter (HBM, T21WN).

Figure 3.3 – Experimental setup of motor, P100L pump with all pressure transmitters and FBRM probe installed in the outlet.

A probe for measuring chord length distribution (ParticleTrack™ G600 Ex/Mettler-Toledo Lasentec®) was positioned at the ESP outlet (Figure 3.4) to capture measurements of droplet size and distribution. The FBRM data was collected and analyzed using the iC FBRM™ Software. Data acquisition and system control were managed through National Instruments hardware integrated with a custom LabView® program.

Figure 3.4 – FBRM probe installed in the outlet of ESP, in detail.

3.2 Fluid characterization

The experiments were carried out using a Newtonian mineral oil at four different temperatures to encompass a wide range of viscosities. Therefore, it is crucial to characterize the fluid properties as a function of temperature. The oil density was measured using a tube densimeter (Anton Paar, DM5000), while its viscosity was determined with a rotational rheometer (HAAKE MARS III). Measurements were performed across a temperature range from 30 °C (882 kg/m^3 and 177 cP) to 45 °C (870 kg/m^3 and 77 cP). The temperature-dependent curves for density and viscosity are presented in Figure 3.5. The emulsion was prepared using tap water, a chosen mineral oil and an emulsifier additive (SPAN 80, Aldrich®). The choice of additive was guided by Simonsen *et al.* (2014), who developed synthetic oil emulsions to replicate the flow characteristics of crude oil. Interfacial tension was measured using the spinning drop technique (PAT 1 M, Sinterface®), yielding a average value of 2 mN/m in the temperature range of data acquired.

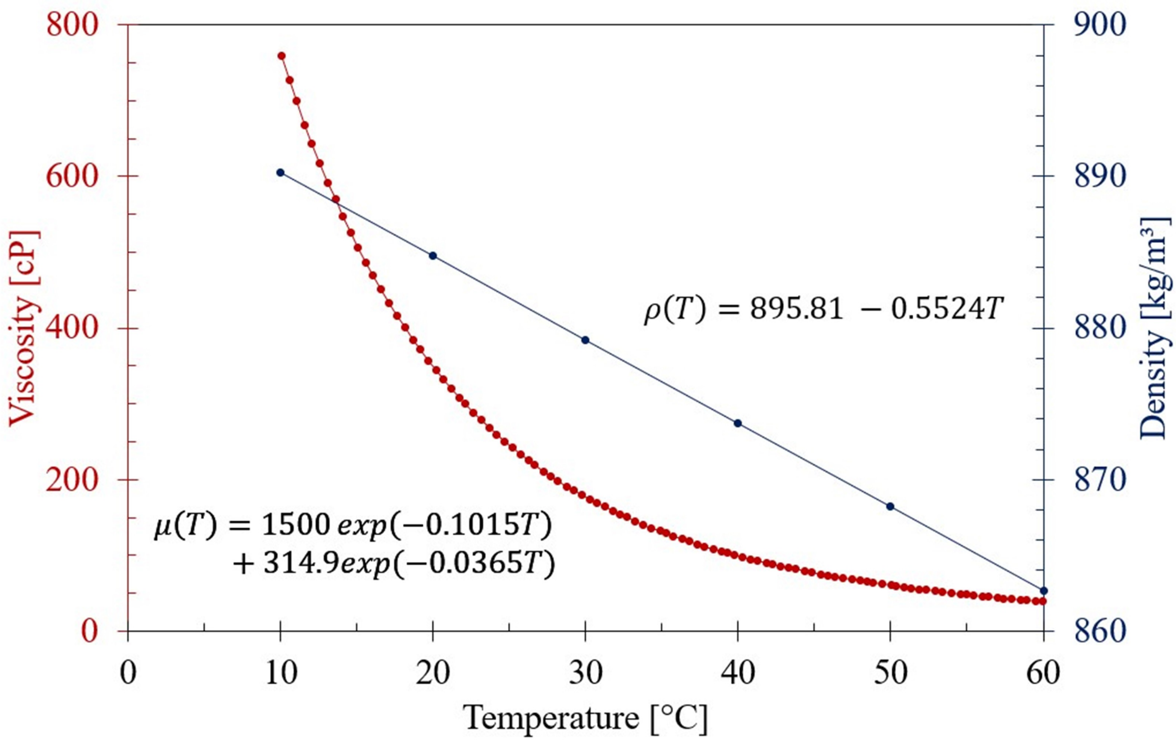

Figure 3.5 – Viscosity and density temperature curves acquired from 10 °C to 60 °C.

3.3 Pumps Tested

To evaluate the performance of ESPs operating with water-oil emulsions, the P47 and P100L pumps (538 series) from the manufacturer Baker Hughes - Centrilift were used. The P47 has 9 stages and features a mixed internal geometry, while the P100L has 8 stages with a mixed geometry. The geometric characteristics of the rotors are referenced in the work of Biazussi (2014).

a) **b)**

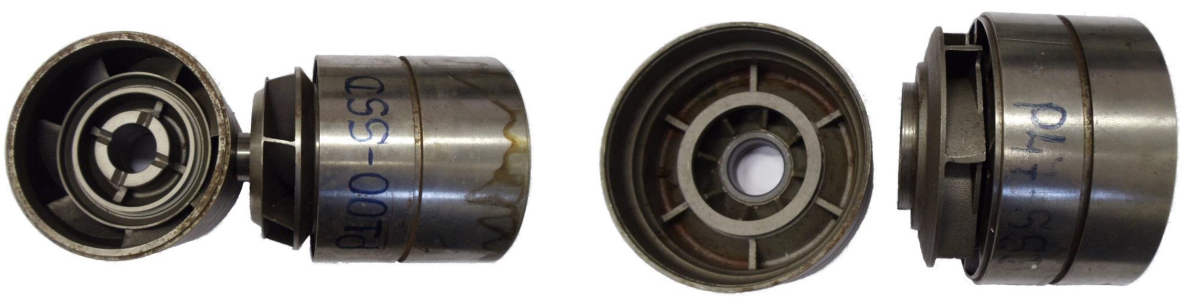

Figure 3.6 – Impeller and diffuser of the a) P100L pump, featuring mixed flow geometry and b) P47 pump, featuring mixed flow geometry as presented in Biazussi's work.

It is worth to mention that besides both pumps has the same impeller outer diameter and number of blades, they have different characteristics in terms of internal design and thus, the following table summarizes these key geometric and performance characteristics of the P100L and P47, which were tested under water flow to assess their operational efficiency.

Characteristics	**P100L**	**P47**
Number of Blades	7	7
Blade Height at Inlet	24 mm	9 mm
Blade Height at Outlet	13 mm	9 mm
Outer Diameter	108 mm	108 mm
Blade Thickness	2 mm	2 mm
Disk Thickness	3 mm	3 mm
Inner Diameter	60.5 mm	54 mm
Shaft Diameter	28.5 mm	28.5 mm
Outlet Angle	31.23°	36.45°
Number of Stages	8	9
Flow Rate (BEP)	66.6 m^3/h	31.9 m^3/h
Head (BEP)	12.8 m per stage	15.7 m per stage
Efficiency (BEP)	73%	65%

Table 3.1 – Geometric and Performance Data for P100L and P47 Rotors

3.4 Droplet size measurement

Droplet size measurements were performed using a focused beam reflectance measurement (FBRM) probe, which provides real-time monitoring of particle size distribution. The FBRM device used in this study was the ParticleTrack™ G600 Ex (Mettler-Toledo Lasentec®) particle size analyzer.

The FBRM operates by directing a highly focused laser beam through a rotating optical lens positioned at the probe tip, scanning the sample at high speed across a sapphire window (Figure 3.7a). As the laser beam interacts with a particle (Figure 3.7b), backscattered light is detected by the probe, and the reflectance signal is processed to determine the particle's chord length. The chord length is calculated as the product of the scan speed and the duration of the reflected signal, representing the linear distance across the particle intercepted by the laser beam.

The acquired reflectance signals undergo real-time processing through an embedded algorithm that filters noise, distinguishes valid particle interactions, and classifies the detected chord lengths into a histogram known as the chord length distribution (CLD). The CLD provides a statistical representation of particle sizes within the sample, updating continuously as new measurements are recorded.

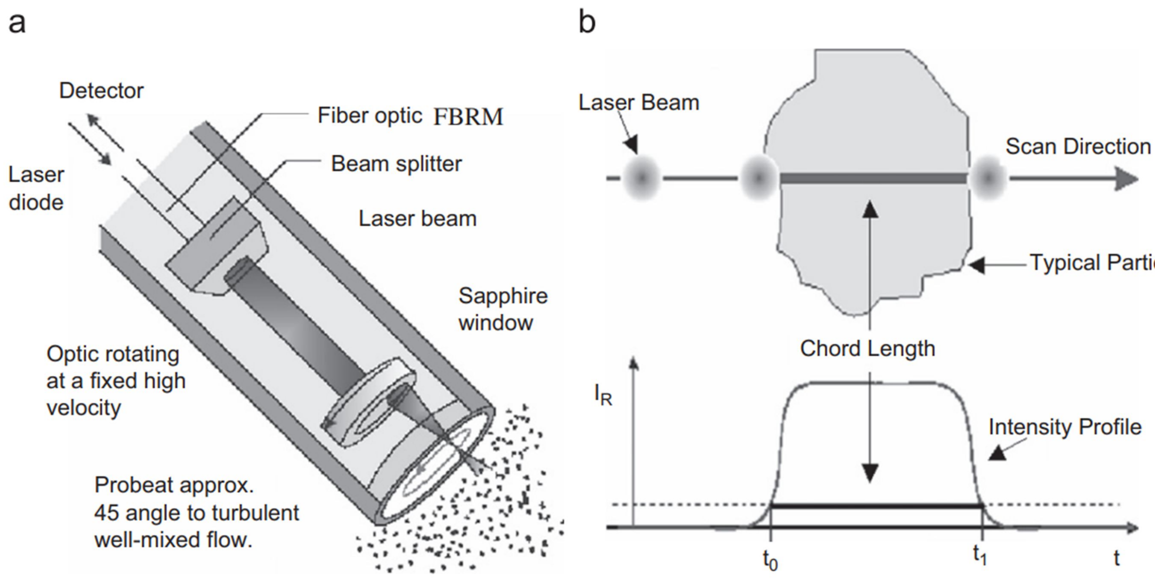

Figure 3.7 – (a) Detailed view of the FBRM probe. (b) Illustration of the particle measurement technique using FBRM. (Image courtesy of Mettler-Toledo, Autochem, Inc.)

The FBRM probe captures thousands of individual chord length measurements per second, ensuring high temporal resolution. The results are displayed as a dynamic distribution curve, showing the frequency of detected chord lengths within predefined size bins. This data can be further analyzed to extract key statistical parameters, such as the mean, median, and percentiles of the size distribution.

It is important to note that the FBRM method measures chord lengths rather than actual particle diameters. In non-spherical or polydisperse systems, chord length distributions must be interpreted carefully, as multiple reflections and irregular particle shapes can influence the results. To enhance accuracy, correction factors may be applied based on calibration data or comparative techniques such as optical microscopy or laser diffraction (Greaves *et al.*, 2008; Bulgarelli *et al.*, 2020; Muhaimin *et al.*, 2021).

To ensure accurate measurements, the probe was cleaned and calibrated using a 70% aqueous ethanol solution before each experiment, ensuring zero particle counts. All FBRM measurements were conducted at two-second intervals, with recorded particle counts spanning a size range from 1 to 1000 μm.

3.5 Experimental matrix

The experimental matrix was developed to evaluate the effects of dispersed phase fraction (f_d), temperature (related to oil phase viscosity), flow rate, and rotational speed on emulsion flow behavior and effective viscosity. To this end, Experiments were conducted at four temperatures (30 °C, 35 °C, 40 °C, and 45 °C), corresponding to continuous phase viscosities of approximately 177 cP, 131 cP, 99 cP, and 77 cP, respectively. Three ESP rotational speeds (2400, 3000, and 3500 rpm) were tested to evaluate shear effects. Additionally, two pumps with different flow geometries were analyzed to assess potential geometric influences on emulsion flow behavior. The pump performance curves were mapped over a flow rate range from 10 m³/h to the absolute open flow (AOF), and tests were conducted across a range of f_d up to continuous phase inversion, as summarized in Table 3.2.

Parameter	**P100L**	**P47**
Temperature [°C]	30 - 45 [in 5°C steps]	30 - 45 [in 5°C steps]
ESP speed [rpm]	2400, 3000, 3500	2400, 3000, 3500
f_d **[%]**	12, 16, 20, 24, 28, 32, 36	8, 12, 16, 21, 27, 31, 34, 38
Flow Rate [m³/h]	10 to AOF [in steps of 2 m³/h]	10 to AOF [in steps of 2 m³/h]

Table 3.2 – Experimental matrix developed.

3.6 Experimental Procedure

The experimental procedure involved testing the ESP using a controlled flow loop system, with the preparation and testing of the emulsion as follows:

The emulsion was prepared directly in the emulsion tank, eliminating the need for intermediate storage. Initially, the surfactant additive was dissolved in the oil within the tank, ensuring proper dispersion. The required volume of water was then added to achieve the desired phase ratio, and the mixture was circulated for a set period to promote homogenization. Given that the experiments were conducted sequentially over a few weeks, the risk of emulsion degradation due to prolonged storage was minimized. However, if left stagnant for extended periods, the emulsion could degrade, potentially altering its properties.

A sample was collected before each test following the addition of water to the system and analyzed using optical microscopy to assess droplet size distribution and verify the water cut using Karl-Fischer titration (Figure 3.8), confirming accuracy with the water cut meter.

Figure 3.8 – Karl-Fischer Volumetric Moisture Titrator (Mettler-Toledo, Autochem, Inc.)

The system was first conditioned to reach a setpoint temperature of 30°C using a control and data acquisition system developed in LabView. Once the target temperature was reached, the ESP speed was set to an initial value of 2400 rpm, maintaining it constant throughout the tests. To ensure sufficient suction pressure and prevent cavitation at the ESP inlet, the booster pump was activated at an initial speed of approximately 200 rpm. This configuration enabled an initial flow rate of 10 m^3/h by adjusting the downstream choke valve.

From this initial condition, a LabView control script was used to apply incremental steps to the booster pump speed and choke valve position to reach the next flow rate setpoint of 12 m^3/h, while ensuring the suction pressure remained above 1 bar, preventing cavitation. At each step, the algorithm allowed the system to stabilize before recording an average of pressure, temperature, flow rate, density, and other sensor readings over a 15-second interval. Once the measurements stabilized, the next flow step was initiated, increasing in increments of 2 m^3/h until the absolute open flow (AOF) condition of the pump was reached, defined as a pressure differential (ΔP) close to zero.

Simultaneously, the Focused Beam Reflectance Measurement (FBRM) probe was calibrated using 70% alcohol to establish a baseline of zero particles. During testing, the FBRM probe acquired droplet size data at 2-second intervals. When a stable point was reached and confirmed by the LabView system, the corresponding flow rate was noted alongside the droplet size distribution data. This ensured precise alignment between the flow conditions and the droplet size measurements for later data processing.

After completing the pump curve at 30°C, the system was adjusted to the next temperature setpoint, continuing the same procedure for 35°C, 40°C, and up to the maximum tested temperature of 45°C. Upon completing the temperature series at 2400 rpm, the pump speed was increased to the next rotational setting, repeating the temperature tests in the same manner for each speed.

4 ESP PERFORMANCE RESULTS

This chapter provides a comprehensive analysis of the experimental performance of two Electrical Submersible Pumps (ESPs) operating under different experimental conditions. The primary objective is to evaluate the influence of operational characteristics and fluid properties on pump efficiency, head, and shaft power, using both dimensional and dimensionless parameters.

Initially, the performance of the pumps operating with water is presented, analyzing their behavior at three different rotational speeds. The main parameters are expressed using dimensionless relationships, allowing for scale-independent comparisons of pump performance. Subsequently, the performance is analyzed for single-phase oil flow, considering viscosity variations with temperature. The pump behavior is evaluated at four different viscosities while maintaining the same rotational speeds as in the water tests. This analysis quantifies performance degradation due to increased viscosity, examining variations in head, efficiency, and shaft power under different viscosity conditions.

Beyond single-phase flow, this chapter investigates pump performance when operating with water-oil emulsions, a common occurrence in petroleum production. The influence of the dispersed phase fraction on the emulsion's effective viscosity and its impact on pump performance is discussed in detail. Variations in operational conditions, including rotational speed and temperature, as well as the emulsion's rheological behavior inside the pump and in the outlet piping, are analyzed. To describe these interactions, an optimized relative viscosity model is developed and validated, providing a robust tool for predicting ESP performance in industrial applications.

Additionally, the chapter addresses the primary hydraulic losses affecting ESP performance, including internal friction, recirculation losses, and disk friction. Correction coefficients used to predict pump performance degradation when handling viscous fluids are also discussed. Finally, the analysis is complemented by an evaluation of the effective viscosity of emulsions inside the pump and in the outlet piping, highlighting differences between flow regimes in the pump and the discharge line.

4.1 Dimensionless Analysis of ESP Performance with Water

To provide a scale-independent analysis of the ESP performance, results are presented in non-dimensional form. The use of dimensionless parameters allows for a general comparison across different operating conditions and pump sizes, which is especially useful for characterizing the pump's behavior in a universal context. Three key dimensionless parameters were used: the dimensionless head (ψ), dimensionless power (Π), and efficiency (η), all plotted as functions of the dimensionless flow rate (ϕ).

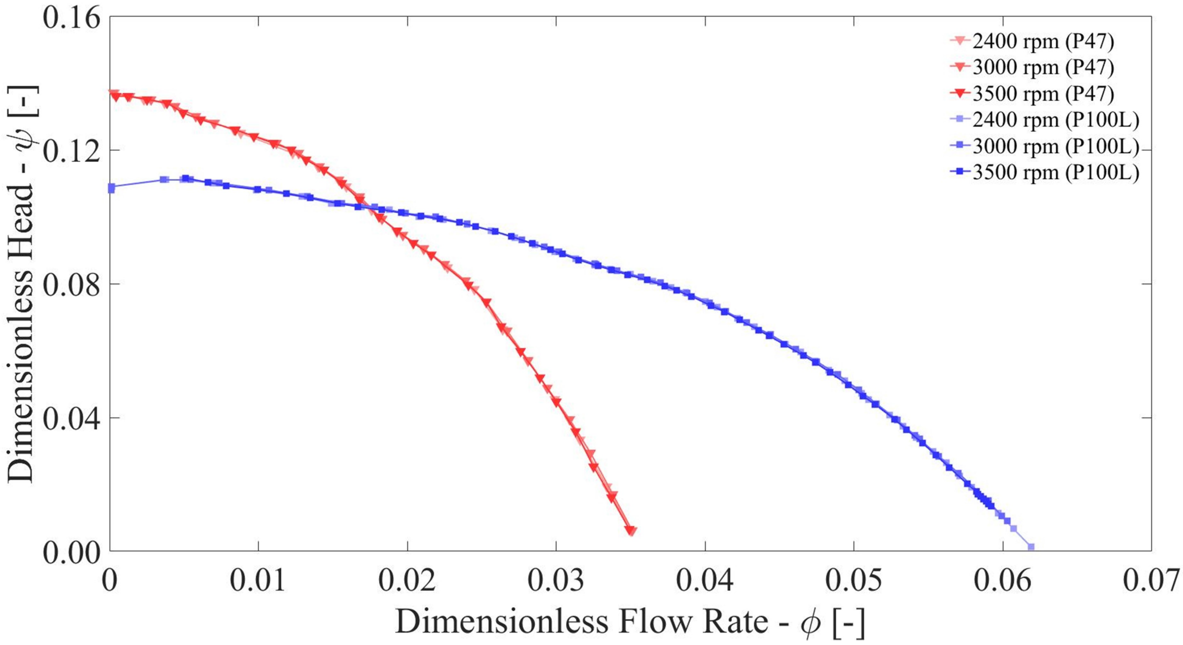

Figure 4.1 – Dimensionless Head (ψ) versus liquid flow rate for both pumps operating with water at each rotational speed.

The dimensionless head curves (Figure 4.1) show that both pumps maintain a consistent head across the range of flow rates at each speed. The P47, being more radial in design, is capable of delivering a higher head compared to the P100L, which, due to its mixed-flow design, is able to deliver a higher flow rate.

The dimensionless power curves (Figure 4.2) illustrate the energy required to sustain each flow rate, showing a gradual increase as flow rate rises. However, the power consumption behavior varies according to pump geometry.

According to fluid machinery theory, radial-flow pumps exhibit a continuous increase in power consumption as flow rate increases. Axial-flow pumps, on the other hand, tend to have higher power consumption at lower flow rates, which then decreases as flow increases. Mixed-flow pumps combine characteristics of both types, typically showing an initial rise in

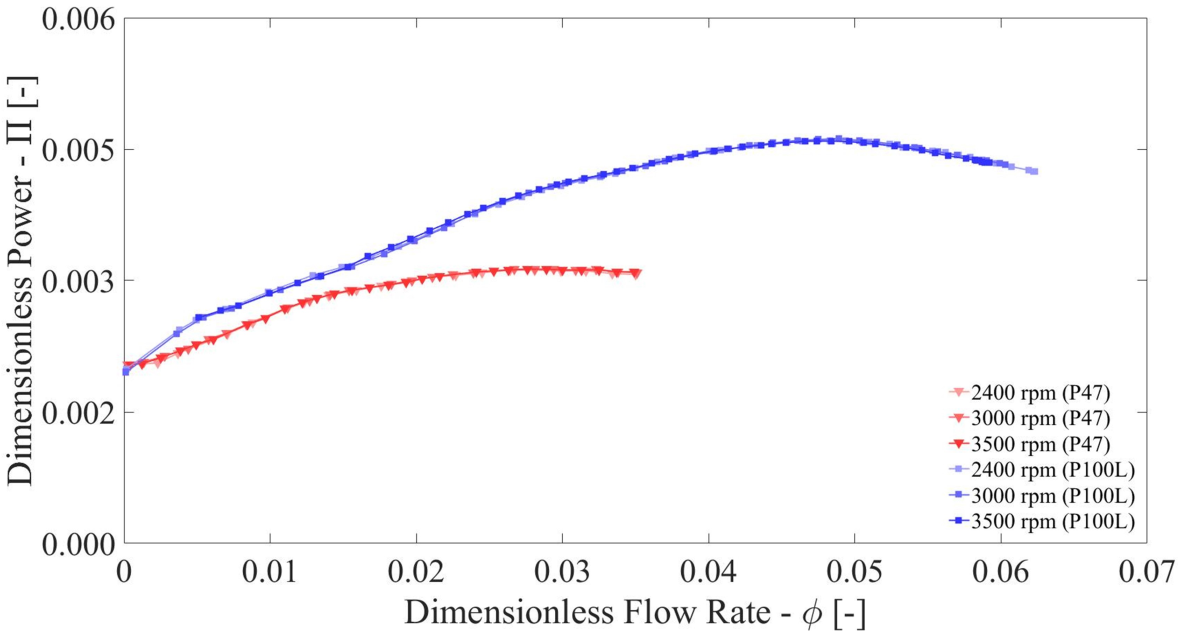

Figure 4.2 – Dimensionless Power (Π) versus liquid flow rate for both pumps operating with water at each rotational speed.

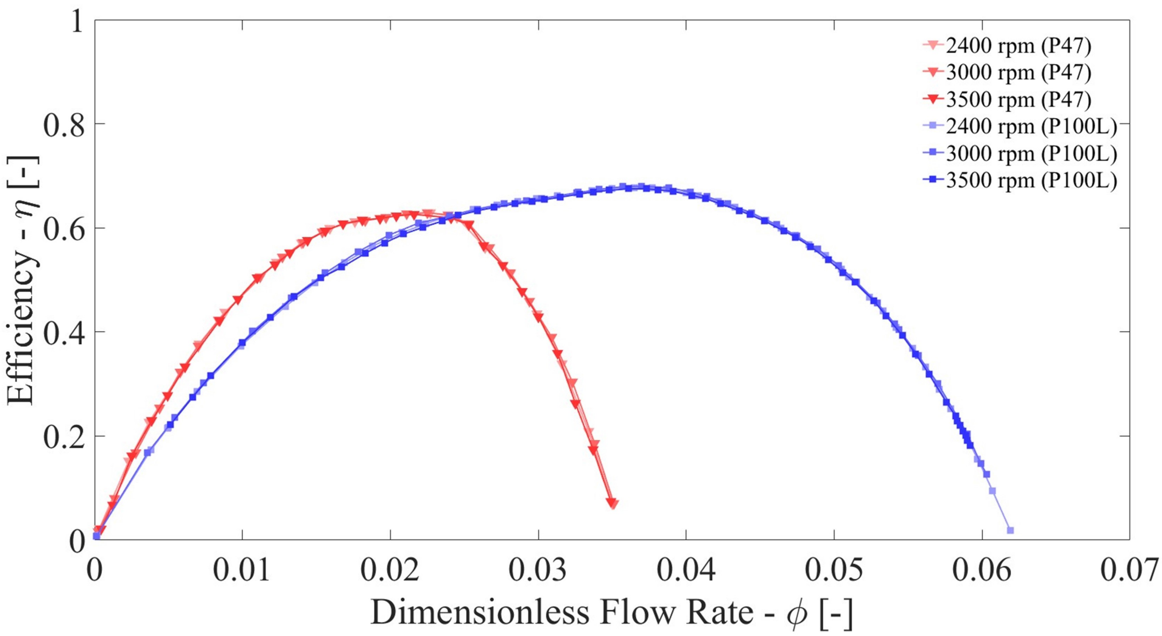

Figure 4.3 – Efficiency (η) versus liquid flow rate for both pumps operating with water at each rotational speed.

power consumption up to a plateau, followed by a slight decline at higher flow rates. This behavior is a result of the transition in flow characteristics within the pump, affecting stage efficiency (Franke, 2002).

The dimensionless head curves (Figure 4.1) illustrate that both pumps maintain a consistent head across a range of flow rates at each speed, with slight variations due to changes in flow patterns as the speed increases. The dimensionless power curves (Figure 4.2) indicate the energy required to maintain each flow rate, showing a gradual increase as flow rate rises, which is consistent with expected power demands in multistage ESPs. Efficiency curves (Figure 4.3) highlight that both pumps achieve peak efficiency near their best efficiency point (BEP), with performance decreasing as flow rates move further from this optimal point.

Table 4.1 provides a comparison of dimensionless parameters (ψ, Π, and η) for the two pumps (P47 and P100L) at 80%, 100%, and 120% of the BEP flow rate. This comparative approach showcases the pumps' performance across different operational points, revealing that P100L generally achieves higher efficiency (η) near the BEP, while both pumps exhibit efficiency drops as flow rate increases beyond optimal levels. This pattern is typical for centrifugal pumps and reinforces the critical role of dimensionless analysis in evaluating and optimizing pump performance under varying flow conditions.

	P47			P100L		
	80% Q_{BEP}	100% Q_{BEP}	120% Q_{BEP}	80% Q_{BEP}	100% Q_{BEP}	120% Q_{BEP}
ψ	0.1024	0.0848	0.0569	0.0670	0.0807	0.0916
Π	0.0029	0.0031	0.0031	0.0045	0.0043	0.0040
η	0.61	0.63	0.56	0.66	0.68	0.64

Table 4.1 – Comparison of dimensionless parameters (ψ, Π, and η) for P47 and P100L at different flow rates around the BEP (80%, 100%, 120% of Q_{BEP}).

4.2 Oil Single-Phase Flow ESP Performance

This section presents the performance of the pumps when operating with pure oil. Three rotational speeds (2400, 3000 and 3500 rpm) and four different viscosities (approximately 177 cP, 131 cP, 99 cP, and 77 cP) were tested.

Herein, only the results for the 3500 rpm rotational speed will be presented and the other conditions can be found on Annex A. The focus is to vary the temperature, and consequently the oil viscosity, in order to highlight the performance degradation of the pump due to viscous effects. By analyzing the performance at a constant speed while varying the viscosity, the impact of increased viscous forces on the pump's head, efficiency, and shaft power becomes more evident. The higher viscosity at lower temperatures leads to greater internal friction within the pump, resulting in a noticeable decrease in head and efficiency, while the shaft power increases to compensate for the additional energy required to maintain the same flow rate.

While the law of similarity works well for low-viscosity fluids like water, this law does not apply when dealing with high-viscosity fluids, such as oils. As the viscosity increases, the Reynolds number decreases, leading to a more laminar flow regime. This results in higher friction losses and energy dissipation. However, at higher rotational speeds, the flow can transition into a more turbulent regime, reducing friction losses and improving efficiency. This change in behavior is not easily captured by the law of similarity and requires a more detailed analysis of viscous effects and flow regime transitions. Thus, the impact of rotation on pump performance becomes more complex, with the efficiency improving as the flow becomes more turbulent.

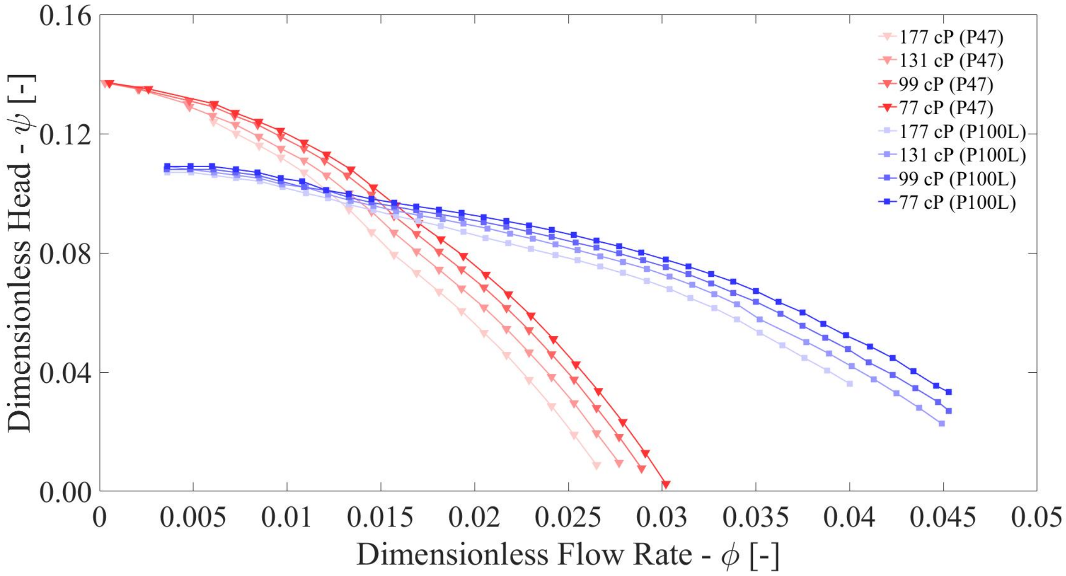

Figure 4.4 – Dimensionless head performance curve for both pumps operating with oil at 3500 rpm in each viscosity.

As mentioned, the presence of oil in the pump significantly increases the viscosity of the working fluid, leading to a noticeable degradation in pump performance. The increase in viscous forces act against the flow, causing more friction within the pump's internal passages. This increased resistance results in a reduction of the pump's head (Figure 4.4), as the energy imparted to the fluid is partially dissipated in overcoming viscous friction rather than contributing to fluid elevation.

Simultaneously, the dimensionless power (Π) increases (Figure 4.5), indicating that higher energy input is required to sustain the same flow rate under increased viscosity conditions. This behavior results from a combination of hydraulic, mechanical, and leakage losses, which are exacerbated in viscous flows. The suppression of flow acceleration inside the impeller

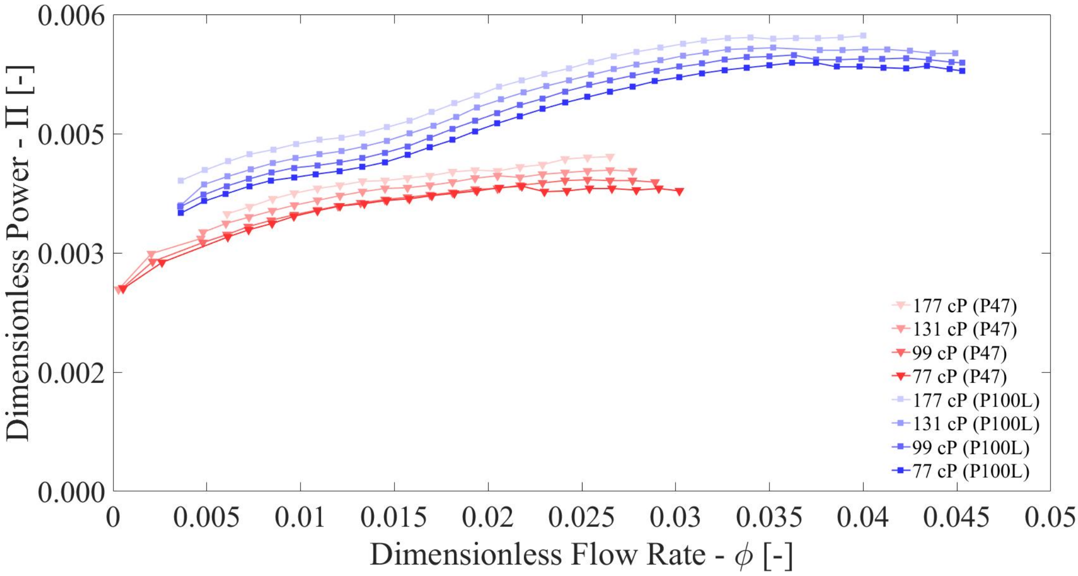

Figure 4.5 – Dimensionless power performance curve for both pumps operating with oil oil at 3500 rpm in each viscosity.

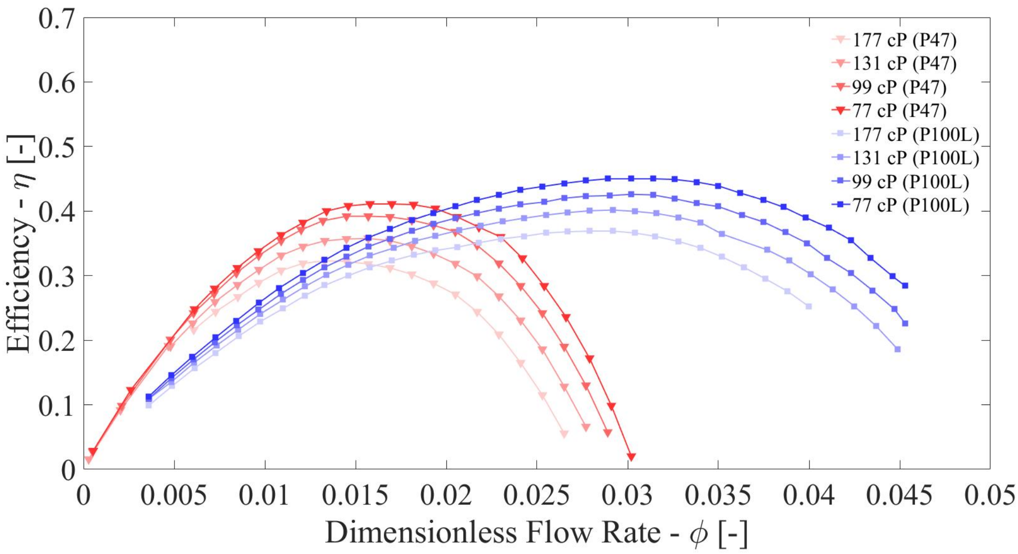

Figure 4.6 – Dimensionless efficiency curve for both pumps operating with oil at 3500 rpm in each temperature.

due to increased shear stresses reduces the effective energy transfer to the fluid, leading to a deterioration in pump head. Additionally, secondary flow structures, such as recirculation zones and boundary layer thickening, intensify as viscosity increases, contributing to head losses in both the impeller and diffuser passages.

Another critical factor is the increase in disk friction losses. As viscosity rises, the fluid shear stress acting on the pump's rotating surfaces—such as impeller shrouds and casing walls—significantly increases. This results in higher torque requirements to maintain the same rotational speed, leading to additional power dissipation in the form of heat. Leakage losses are also affected, as higher viscosity increases resistance in clearance gaps (e.g., wear rings, balancing holes), altering pressure distributions and promoting recirculation effects that further degrade efficiency.

The cumulative effect of these loss mechanisms negatively impacts the pump's efficiency (Figure 4.6). A higher proportion of the mechanical energy supplied to the pump shaft is dissipated internally rather than being converted into useful hydraulic work, reducing the overall efficiency (η) of the system. In summary, the dominance of viscous effects in the flow regime leads to a reduction in head and efficiency while increasing the mechanical power demand of the pump. The efficiency values at 80%, 100%, and 120% of the BEP flow rate are presented in Table 4.2.

		$\eta - P47$				$\eta - P100L$			
N (rpm)	Flow Rate	177 cP	131 cP	99 cP	77 cP	177 cP	131 cP	99 cP	77 cP
2400	80% Q_{BEP}	0.232	0.275	0.298	0.335	0.278	0.312	0.331	0.362
	100% Q_{BEP}	0.251	0.290	0.321	0.354	0.287	0.320	0.348	0.379
	120% Q_{BEP}	0.247	0.281	0.319	0.339	0.263	0.288	0.328	0.349
3000	80% Q_{BEP}	0.285	0.312	0.348	0.371	0.325	0.355	0.388	0.413
	100% Q_{BEP}	0.300	0.335	0.366	0.398	0.337	0.367	0.400	0.424
	120% Q_{BEP}	0.288	0.321	0.353	0.389	0.313	0.339	0.366	0.384
3500	80% Q_{BEP}	0.299	0.350	0.378	0.390	0.361	0.393	0.418	0.444
	100% Q_{BEP}	0.322	0.363	0.400	0.420	0.369	0.401	0.426	0.451
	120% Q_{BEP}	0.318	0.342	0.387	0.405	0.341	0.367	0.389	0.411

Table 4.2 – Efficiency (η) values at flow rates near BEP for pumps P47 and P100L when operating with pure oil at different viscosities and rotational speeds.

4.3 Water-Oil Two-Phase Flow ESP Performance

This section presents the results of the pump operating in a two-phase water-in-oil emulsion flow condition. Again, the performance of the pump was evaluated at three different rotational speeds (2400, 3000, and 3500 rpm) and four temperatures (30, 35, 40, and 45 °C), which mainly affects the viscosity of the oil phase (177 cP, 131 cP, 99 cP, and 77 cP, respectively). The results are presented similarly to the single-phase tests, focusing on dimensionless parameters. The figures below will be provided for both the P100L and P47 pumps at 3500 rpm and 99 cP.

4.3.1 P100L Performance Results

As mentioned earlier, emulsions exhibit a notable increase in effective viscosity as the dispersed phase fraction (f_d) increases. This effect of viscous degradation can be observed across all performance parameters as the dispersed phase fraction rises.

The interaction between the phases introduces complex flow dynamics, which progressively degrade the pump performance. This is evidenced by the reduction in head and efficiency and the increased power consumption compared to single-phase flow conditions. The viscosity losses become more pronounced as the dispersed phase fraction increases, posing significant challenges for handling emulsions in electrical submersible pumps (ESP).

In Figure 4.7, the efficiency (η) of the P100L pump is presented for various dispersed phase fractions at 3500 rpm and 45°C (77 cP). The blue dashed line represents the water single-phase flow (100% f_d), while the black dashed line represents the oil single-phase flow (0% f_d). The two-phase flow tests begin at 12% f_d, and as the dispersed phase fraction increases, efficiency decreases progressively from 37% to below 30% at the best efficiency point (BEP) for higher fractions.

With the increase of f_d the system approaches the inversion point, where the dispersed water content becomes significant enough to alter the flow characteristics. The interaction between water droplets disrupts the oil's continuous phase and thus the pump's hydraulic performance, causing increased internal energy dissipation and results in a sharper decline in efficiency.

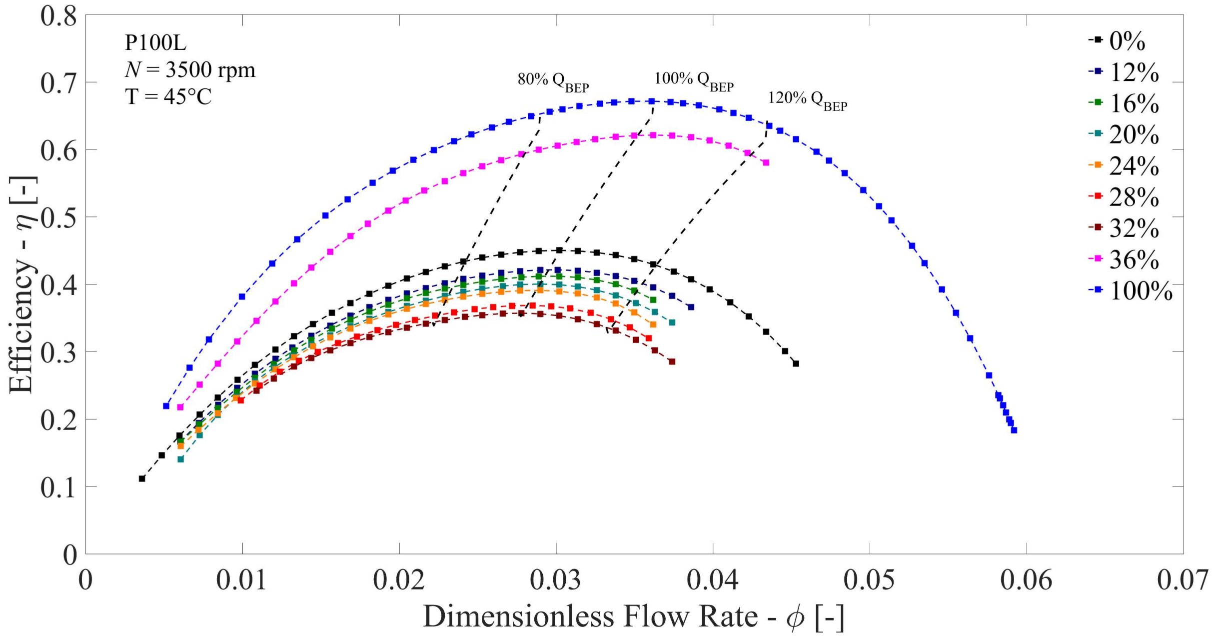

Figure 4.7 – Efficiency curves of P100L operating with different W/O emulsion f_d at 3500 rpm and 45 °C (77 cP).

The emulsion exhibited a clear continuous phase inversion between the tests conducted at 34% and 38% f_d, specifically during the controlled addition of water. To ensure a smooth transition in water content, the water was added in two stages: first, half of the required volume was introduced, followed by the remaining half. This approach minimized abrupt changes in the emulsion properties. The identification of the phase inversion was based on the pump's performance response during system startup. When the system was started with 36% f_d to homogenize the emulsion, an immediate increase in pump head was observed at low flow rates, indicating a shift from an oil-dominated to a water-dominated continuous phase. This transition marked a pivotal point in the efficiency, head, and power recovery trends observed in the performance curves.

Similar trends are observed in the head and power performance, as shown in Figure 4.8 and Figure 4.9. The performance degradation in terms of efficiency, head, and power across increasing dispersed phase fractions is evident in all curves. The continuous phase inversion reduces viscous losses, as water begins to wet the walls of the blades, altering the frictional interactions within the pump. More importantly, the transition to a water-dominated regime significantly mitigates disk friction losses, which are a major contributor to power consumption in high-viscosity flows. As a result, the pump experiences a partial recovery in performance and operates with lower power demand, highlighting the intricate relationship between phase interactions and ESP performance under two-phase flow conditions, where both dispersed phase fraction and emulsion effective viscosity play a critical role in performance degradation.

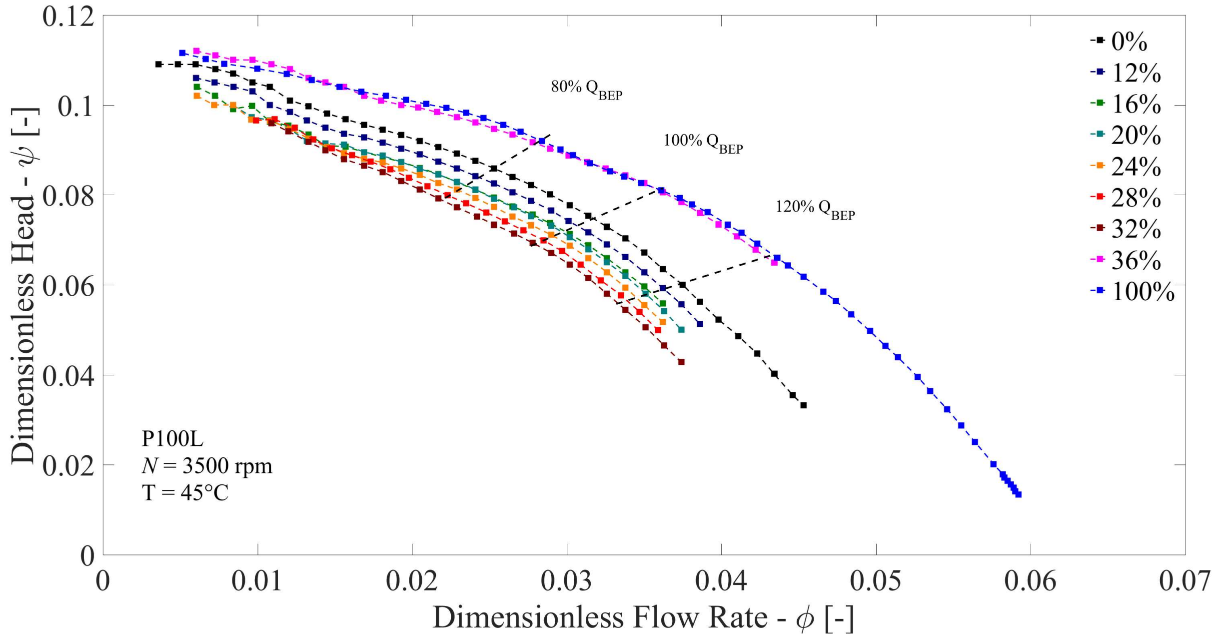

Figure 4.8 – Dimensionless head curves of P100L operating with different W/O emulsion f_d at 3500 rpm and 45 °C (77 cP).

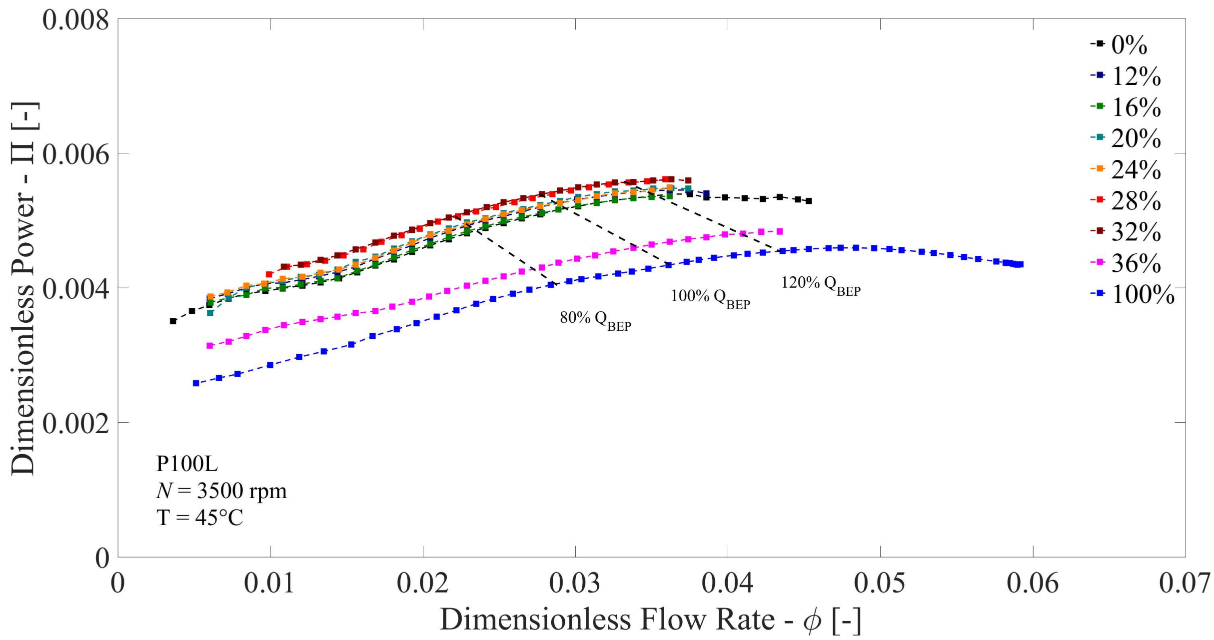

Figure 4.9 – Dimensionless power curves of P100L operating with different W/O emulsion f_d at 3500 rpm and 45 °C (77 cP).

In Figure 4.10 we can observe for the same ESP speed and flow rate how the dimensionless head (ψ) behaves with the increase of f_d. In the highlighted area between 32 % and 36% we have the phase inversion transition between water-in-oil emulsion and oil-in-water emulsion. Unfortunately, we could not capture differences in phase inversion across the variables covered in this experimental matrix for the P100L due to the fact that the phase inversion occurred during the water addition in the emulsion tank between the tests.

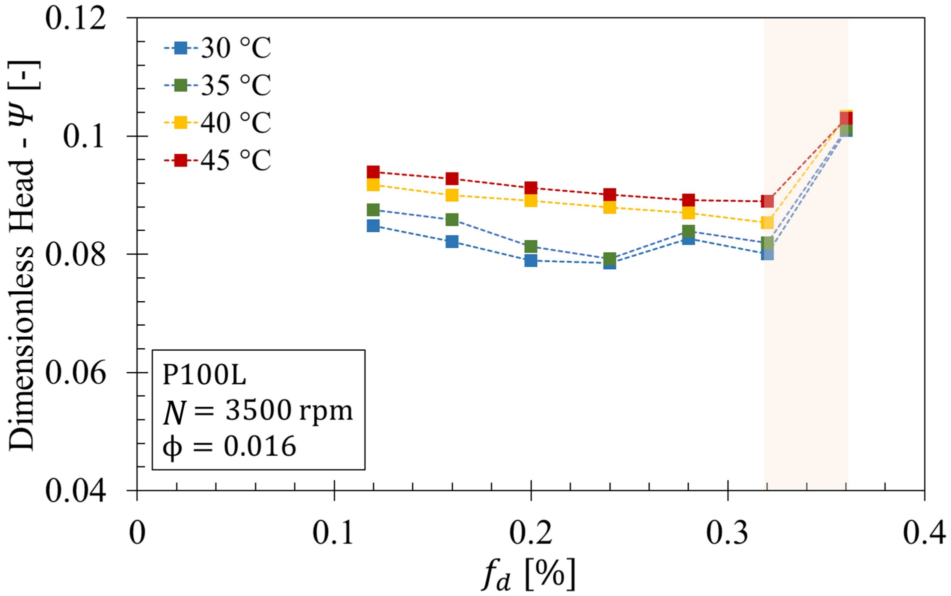

Figure 4.10 – Dimensionless Head versus f_d showing the phase inversion for P100L at 36%.

4.3.2 P47 Performance Results

As observed in the results for the P100L pump, the presence of a dispersed phase significantly affects the performance of the pump, particularly in terms of efficiency, head, and power consumption. The same patterns of performance degradation due to increased viscosity and phase interaction are evident in these results.

In the same way, the efficiency (η) of the P47 pump is presented in Figure 4.11 for various dispersed phase fractions at 3500 rpm and 45°C (77 cP). The blue dashed line represents the water single-phase flow condition (100% f_d) and the black dashed line represents the oil single-phase flow condition (0% f_d). Here, the two-phase flow tests begins at 8% f_d, and as the dispersed phase fraction increases, the efficiency gradually declines. At higher dispersed phase fractions the increased emulsion viscosity leads to higher internal friction, increased hydraulic losses, and a more complex flow regime within the pump.

Again, similar trends are observed in the head and power performance, as shown in Figure 4.12 and Figure 4.13. As the dispersed phase fraction increases, the higher emulsion viscosity intensifies shear stresses within the pump, leading to greater hydraulic losses due to increased resistance in the impeller channels and diffuser passages. Additionally, disk friction losses escalate as the more viscous fluid imposes higher drag on the rotating components, further increasing the power required to sustain operation. The combination of these effects results in a reduction of head, as the pump struggles to impart energy efficiently to the fluid, while also elevating power consumption due to the greater mechanical effort needed to overcome internal resistance. These trends underscore the significant impact of dispersed phase concentration on pump performance, with higher fractions exacerbating energy dissipation mechanisms and reducing overall efficiency.

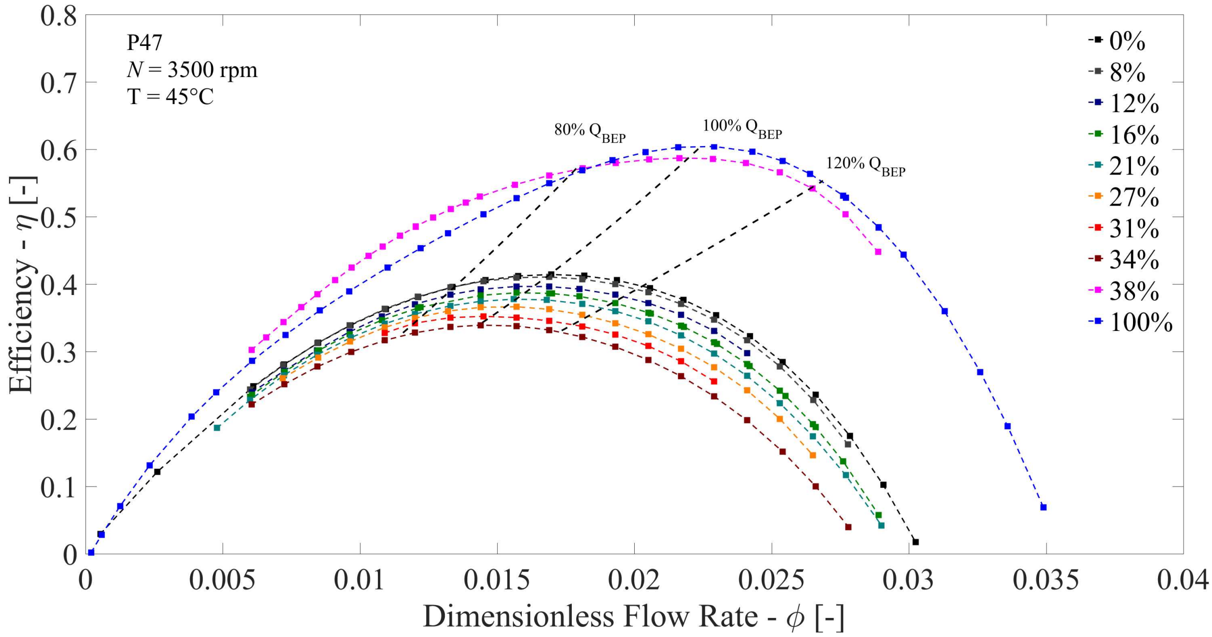

Figure 4.11 – Efficiency curves of P47 operating with different W/O emulsion f_d at 3500 rpm and 45 °C (77 cP).

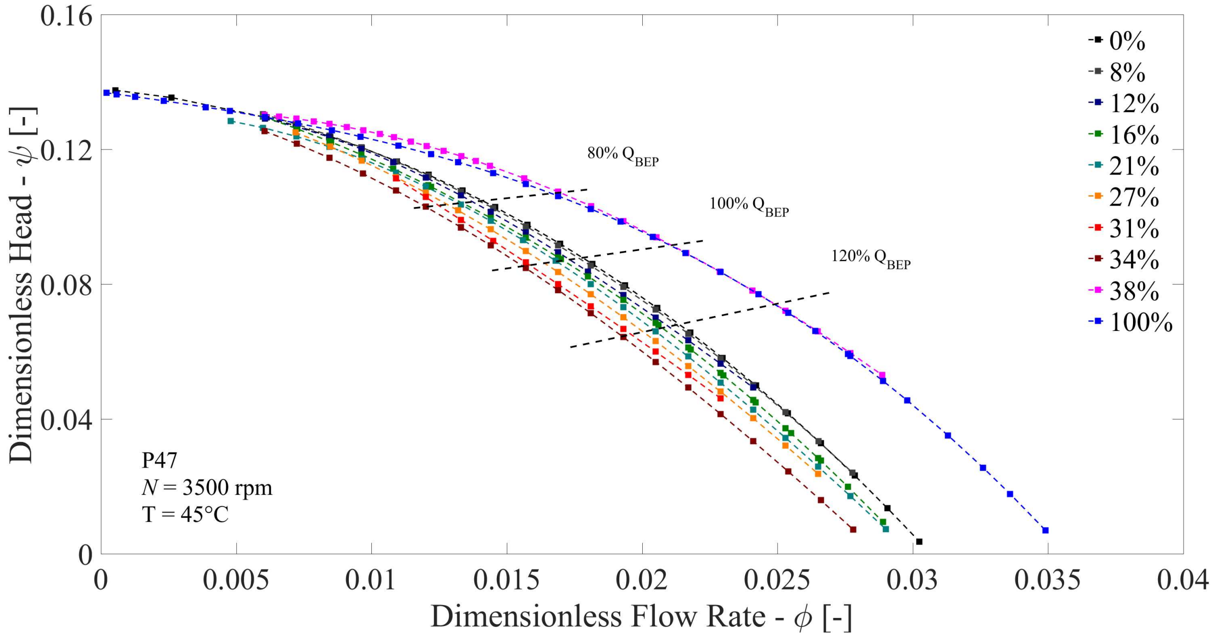

Figure 4.12 – Dimensionless head curves of P47 operating with different W/O emulsion f_d at 3500 rpm and 45 °C (77 cP).

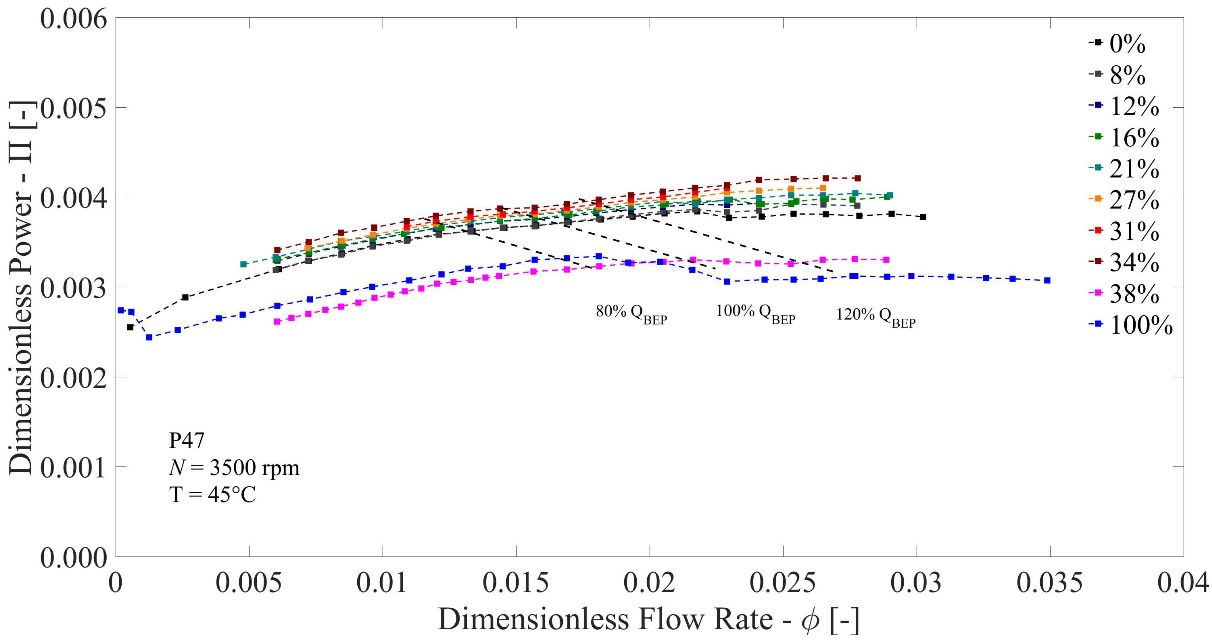

Figure 4.13 – Dimensionless power curves of P47 operating with different W/O emulsion f_d at 3500 rpm and 45 °C (77 cP).

As observed previously for the P100L, the emulsion underwent a continuous phase inversion at 36% dispersed phase fraction for all curves, indicating a catastrophic phase inversion between the 34% and 38% water fractions during emulsion preparation. Surprisingly, for the same condition, the P47 pump did not experience the phase inversion phenomenon and continued to exhibit degraded performance as the dispersed phase fraction increased.

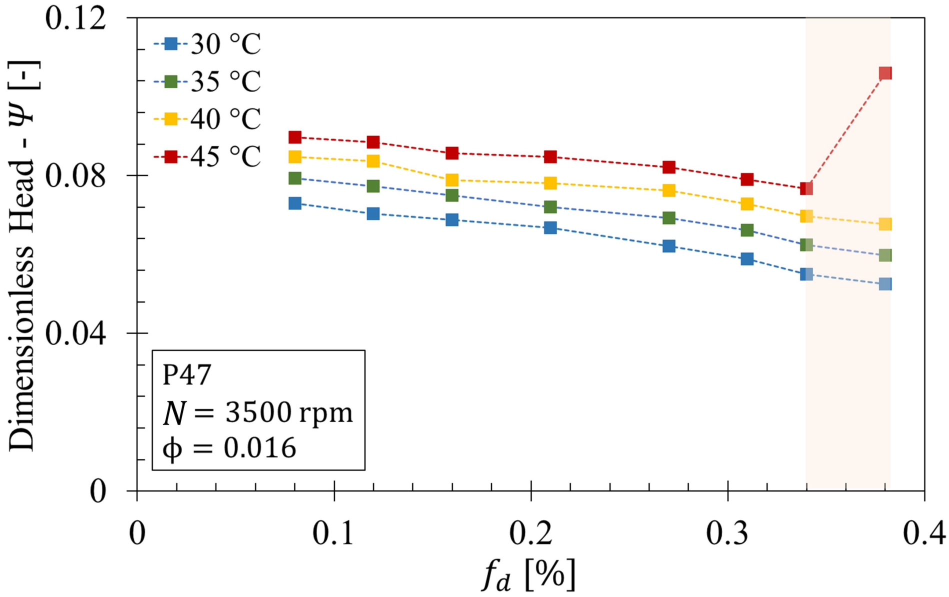

Figure 4.14 – Dimensionless Head versus f_d showing the phase inversion for P47 at 36%.

However, phase inversion was observed at a dispersed phase fraction of 38% at the same rotational speed but only at a higher temperature of 45°C (77 cP), as illustrated in Figure 4.14. This finding indicates that phase inversion in the P47 pump is influenced not only by the dispersed phase fraction but also by fluid temperature, which directly affects mixture viscosity. At 45°C, the reduction in viscosity likely facilitated the formation of a continuous aqueous phase, leading to phase inversion and improved hydraulic performance of the pump.

Although lower viscosity generally enhances turbulence, which promotes droplet fragmentation and reduces their average size, the observed phase inversion suggests that coalescence ultimately prevailed over fragmentation. In lower-viscosity fluids, the increased turbulence enhances droplet collisions, and the reduced viscosity decreases the hydrodynamic resistance to coalescence by accelerating the drainage of the thin liquid film between colliding droplets. Consequently, despite an initial increase in droplet breakup, the net coalescence rate may rise, allowing for the formation of a continuous phase.

This observation underscores the intricate interplay between viscosity, turbulence, and phase transition in two-phase flow within electrical submersible pumps. It highlights that phase inversion is not governed by viscosity alone but rather by the dynamic competition between fragmentation and coalescence, which is strongly influenced by flow conditions. A more comprehensive analysis of phase inversion under different temperature and pump speed conditions is presented in Annex A of this thesis.

4.4 Emulsion Effective Viscosity inside the ESP

The effective viscosity of emulsions inside an Electrical Submersible Pump (ESP) plays a crucial role in determining the hydraulic performance, particularly under two-phase flow conditions. Emulsions, consisting of a dispersed phase (oil or water) and a continuous phase, exhibit complex rheological behaviors, where the effective viscosity can vary significantly from that of the individual phases, depending on the volume fraction, temperature, and shear rate. Understanding and quantifying the effective viscosity of emulsions is essential for accurate performance predictions and efficient operation of ESPs in oil production systems.

4.4.1 Definition of Emulsion Effective Viscosity

Effective viscosity refers to the apparent viscosity of a multiphase fluid system, such as an emulsion, as it flows through a mechanical system like an ESP. Unlike the viscosity of a single-phase fluid, the effective viscosity in an emulsion takes into account the interaction between the dispersed and continuous phases, which alters the flow dynamics. This is particularly important in the context of ESPs, as the pump's hydraulic efficiency, head, and power consumption are directly influenced by the fluid's rheological properties.

In emulsions, as the dispersed phase fraction (f_d) increases, the effective viscosity of the mixture generally rises due to increased internal friction between the two phases. This rise in viscosity can lead to higher hydraulic losses and reduced pump efficiency, particularly when the emulsion transitions from an oil-dominated to a water-dominated flow regime or vice versa.

4.4.2 Methodology for Calculating Effective Viscosity in the ESP

To quantify the viscous degradation within the ESP, the relative effective viscosity of the emulsion is estimated with respect to that of pure oil under comparable flow conditions. One approach involves the use of the single-phase viscous model (Equation 2.34) proposed by Biazussi (2014), which accounts for the viscosity difference between single-phase water and oil flows. In this context, the governing equation for the ESP head performance (ψ) is modified to incorporate the effective viscosity of the emulsion. This modification enables the pump to function as an indirect viscosity measurement device, whereby its hydraulic performance is used to infer the rheological behavior of the emulsion. In essence, the model allows the ESP to be calibrated as a viscometer under operating conditions.

4.4.3 Adjusting the Model for Emulsion Flow

The parameters k_4, k_5, k_6 are adjusted based on the single-phase water performance curve, while k_2, k_3, and n are adjusted using the single-phase oil curve. These adjustments allow the model to capture the behavior of the fluid as it moves from single-phase to two-phase flow, accommodating the increased viscosity and the shift in the dominant phase. The adjusted parameters for each pump are presented in Table 4.3

Parameter	**P100L**	**P47**
k_1	1.49	2.58
k_2	1.59×10^4	1.09×10^4
k_3	8.39	3.33×10^4
k_4	1.43×10^{-1}	1.13×10^{-1}
k_5	7.29	1.62×10^1
k_6	2.85×10^1	1.27×10^2
n	5.7×10^{-4}	9.78×10^{-1}

Table 4.3 – Adjusted Parameters for P100L and P47 Pumps

To evaluate the effective viscosity in two-phase flow conditions, the following key variables are considered: the volumetric flow rate (Q_L), measured by the Coriolis flow meter; the mixture density (ρ_m) which changes with temperature and depends on the proportion of oil and water, measured also by the Coriolis flow meter; temperature (T) which affects the viscosity of both phases and, consequently, the effective viscosity of the emulsion, measured in the inlet and outlet of the ESP and an average value is used, and finally, the differential pressure (ΔP), which is obtained by the difference between inlet and outlet pressure of the ESP and divided by the number of stages to have an average pressure increment per stage.

As the rotational Reynolds number depends on the effective viscosity, a convergence method is applied between the head calculated by the model and the head measured experimentally to estimate the effective viscosity of the emulsion. By iterating this process, the effective viscosity μ_e is determined. Once the effective viscosity is known, a ratio between the effective viscosity and the pure oil viscosity can be used to compute the relative viscosity (Equation 2.27), quantifying how many times more viscous the emulsion is compared to its continuous phase.

4.4.4 Relative Viscosity of the Emulsion in the P100L pump

The effective viscosity of an emulsion in an ESP directly influences the pump hydraulic performance. Understanding how the effective viscosity changes as a function of flow rate and phase fraction is critical for evaluating the energy losses and performance degradation in two-phase flow conditions. One way to quantify this is through the relative viscosity (μ_r), which represents the ratio between the effective viscosity of the emulsion and the viscosity of the continuous phase (in this case, oil).

In Figure 4.15, the relative viscosity (μ_r) of the P100L pump is presented as a function of the dimensionless flow rate (ϕ) for various dispersed phase fractions (f_d) at a constant rotational speed of 3500 rpm and a temperature of 40 °C. Each curve corresponds to a different dispersed phase fraction, ranging from 12% to 32%, allowing for a comprehensive view of how the presence of a dispersed water phase affects the emulsion's rheology inside the pump.

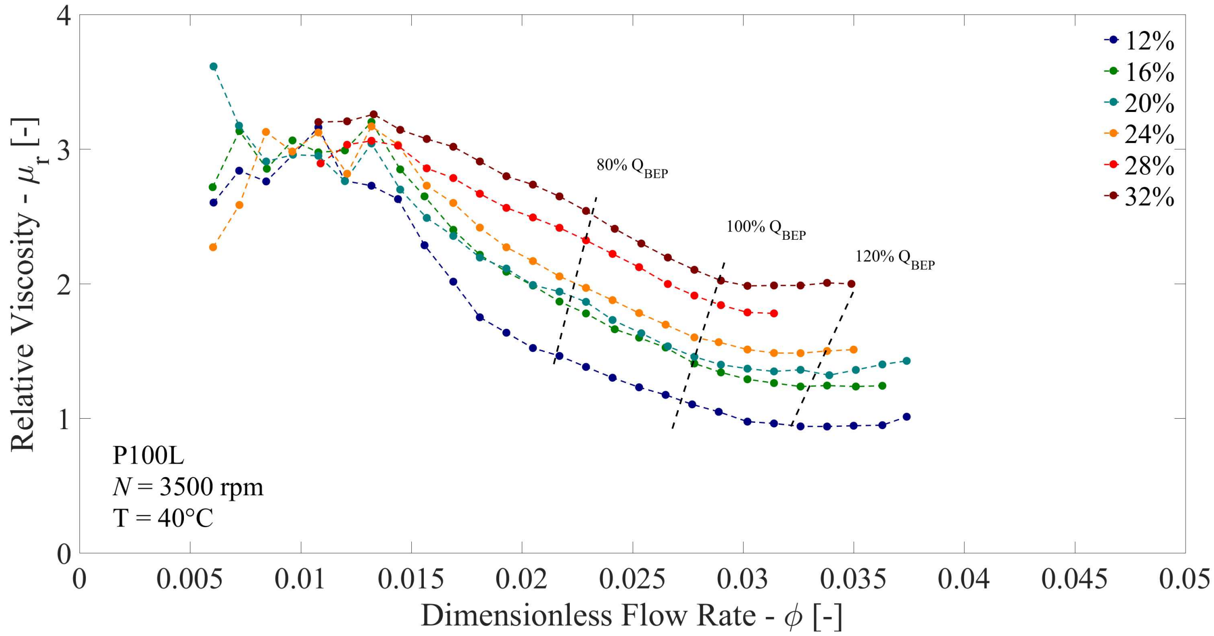

Figure 4.15 – Relative viscosity versus dimensionless flow rate for P100L operating with different W/O emulsion dispersed phase fractions at 3500 rpm and 40°C.

At low values of ϕ, the relative viscosity remains fairly stable, with values hovering around 3, which indicates that the emulsion is approximately three times more viscous than pure oil. This suggests that at low flow rates, the shear within the pump is not yet sufficient to significantly disrupt the droplet structure of the emulsion, maintaining a relatively high viscosity. As the flow rate increases, we can observe a decreasing trend of μ_r until the BEP, which is explained by the shear-thinning effect. This phenomena is a non-newtonian behavior of emulsions where the shear imposed is able to disrupt the particles dispersed in the continuous media and thus, reduces its viscosity.

With the dispersed phase fraction increase, the curves shift upwards, indicating higher relative viscosities. At 32% f_d, the relative viscosity almost doubles at the BEP when comparing to 12% f_d, representing a substantial increase in internal friction due to the higher concentration of water droplets within the oil. This higher viscosity is primarily due to the increased interaction between droplets, which generates greater resistance to flow and results in higher energy losses.

Close to the BEP, the relative viscosity exhibits a smoother trend, showing a progressive reduction as the flow rate increases. This is likely due to the higher shear rates experienced at larger flow rates, which tend to break up the droplets more effectively and also disrupt their agglomeration, reducing the internal friction and thus lowering the emulsion effective viscosity. The micro-scale turbulence in this region also helps stabilize the droplet sizes, leading to a more uniform distribution of particles and a decrease in relative viscosity.

Another key observation is that, for higher dispersed phase fractions (greater than 28%), the relative viscosity before the BEP region starts to decrease at lower flow rates. This may be related to coalescence effects, where droplets start to aggregate into larger clusters, overcoming the droplet breakup processes typically driven by shear. The reduced shear rate at lower flow rates allows for this coalescence, which effectively lowers the viscosity since larger droplets generate less internal resistance compared to a finely dispersed system.

4.4.5 Relative Viscosity of the Emulsion in the P47 pump

As observed with the P100L pump, the effective viscosity of an emulsion within an ESP is a key factor in determining the pump hydraulic performance. Figure 4.16 presents the relative viscosity (μ_r) of the P47 pump as a function of the dimensionless flow rate (ϕ) for various dispersed phase fractions at a rotational speed of 3500 rpm and a temperature of 40°C. The dispersed phase fractions (f_d) range from 8% to 38%, allowing for a detailed analysis of how the increase in water content influences the emulsion's viscosity and, consequently, the pump behavior.

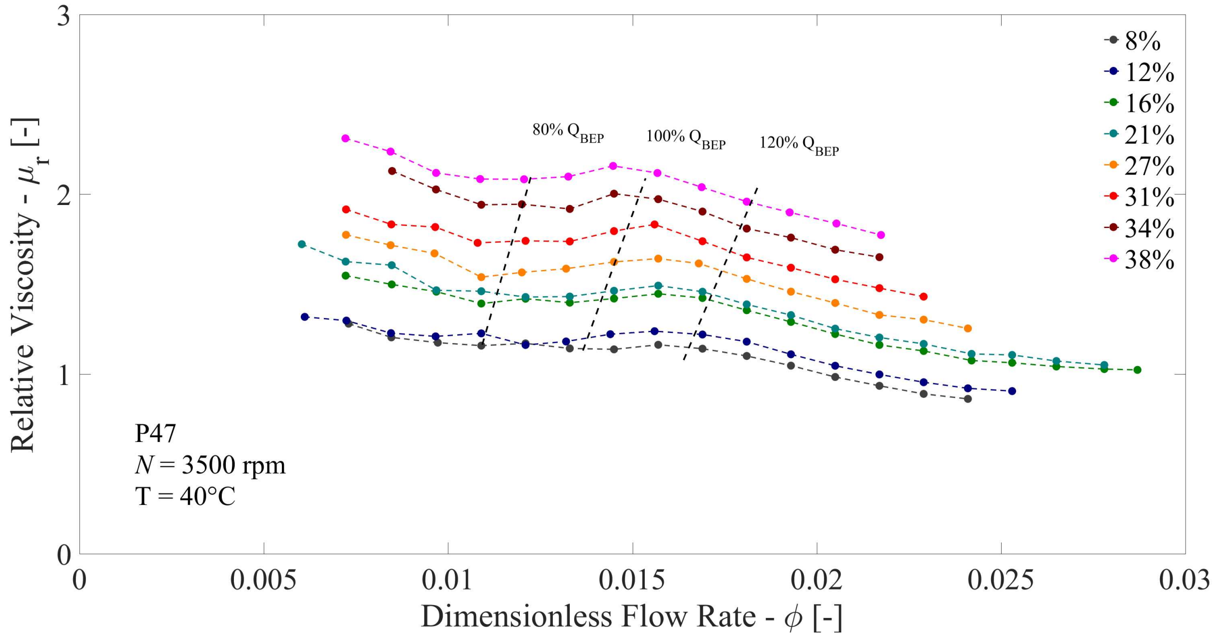

Figure 4.16 – Relative viscosity versus dimensionless flow rate for P47 operating with different W/O emulsion dispersed phase fractions at 3500 rpm and 40°C.

In contrast to the P100L, the relative viscosity of the P47 generally exhibits lower values across all flow rates and dispersed phase fractions. For example, at 8% f_d, the relative viscosity hovers around unity, indicating that the emulsion effective viscosity is only slightly higher than that of pure oil. This is a notable difference compared to the P100L, where even at lower dispersed phase fractions, the relative viscosity was significantly higher for low flow rates, suggesting that the P47 impeller geometry promotes higher shear due to a more aggressive blade angle.

As the dispersed phase fraction increases, the relative viscosity rises progressively, but still maintains slightly lower values compared to the P100L. For instance, at 27% f_d, the relative viscosity remains below 2, which is a bit lower than the equivalent value for the P100L at similar conditions. In terms of flow rate behavior, the P47 shows a relatively consistent trend across all dispersed phase fractions, maintaining a more stable viscosity compared to the mixed flow configuration of the P100L.

At lower flow rates, near 80% Q_{BEP}, the relative viscosity tends to be higher, reflecting the increased internal friction and reduced shear rates in this operating regime. However, as the flow rate increases beyond the BEP, the relative viscosity decreases smoothly. This behavior suggests that the predominant effect is the shear-thinning characteristic of the emulsion, where higher shear rates imposed by the pump lead to a reduction in viscosity. Although the increase in flow rate may also contribute to smaller droplet sizes, which could increase the viscosity due to enhanced droplet interactions, the dominant effect appears to be shear-thinning, leading to an overall reduction in viscosity.

4.4.6 Comparison of Relative Viscosity Results

Comparing the results of the P100L (Figure 4.15) and P47 (Figure 4.16) pumps reveals key differences in how each pump handles emulsions in terms of relative viscosity. The most notable difference is the magnitude of the relative viscosities. The P100L, with its mixed-flow design, generally exhibits higher relative viscosity values across all dispersed phase fractions, particularly at lower flow rates. This suggests that the mixed-flow configuration of the P100L imposes less shear on the emulsion, leading to a weaker shear-thinning effect and, consequently, higher effective viscosity.

Conversely, the P47, with its radial-flow design, maintains lower relative viscosities even at higher dispersed phase fractions. This can be attributed to the greater shear imposed by its internal geometry. The radial impeller design promotes higher energy dissipation through shear, enhancing the droplet breakup process and reducing the emulsion's effective viscosity more efficiently than the mixed-flow impeller. Additionally, the viscosity trend in the P47 shows a smoother decrease with increasing flow rate, which suggests that the shear-thinning effect is more pronounced, even at lower flow rates.

The results for both the P100L and P47 pumps highlight the significant impact of pump geometry on the handling of emulsions in ESPs. The P100L, with its mixed-flow configuration, exhibits higher relative viscosities, particularly at lower flow rates, indicating that it is more susceptible to viscosity-related performance degradation when handling high dispersed phase fractions. The P47, with its radial-flow design, performs better in this regard, maintaining lower relative viscosities and exhibiting a more stable flow regime. However, radial pumps tend to suffer more from viscous degradation due to their increased dependence on shear to maintain efficiency. In high-viscosity conditions, this can lead to higher energy dissipation and reduced overall performance.

From a design perspective, these findings suggest that optimizing the blade geometry can help mitigate performance degradation in emulsified flow conditions. For instance, radial pumps designed for high-viscosity applications may benefit from slightly lower blade angles to reduce excessive shear and mitigate efficiency losses. Conversely, mixed-flow pumps could be improved by minimizing internal recirculation zones, which could stabilize flow patterns and reduce viscosity fluctuations.

In conclusion, the choice of pump geometry plays a critical role in determining the effectiveness of an ESP in handling emulsions. While the P47 seems to be better suited for handling emulsions with higher dispersed phase fractions due to its enhanced shear-thinning effects, the P100L offers superior performance in conditions where minimizing shear-induced viscosity reduction is desirable. This is particularly relevant when evaluating energy losses, as relative viscosity alone does not fully capture the complexities of energy dissipation within the pump.

4.4.7 Correction Coefficients Analysis

As discussed previously, the correction coefficients utilized by Stepanoff (1949) help quantifying the performance degradation of pumps handling viscous fluids at the best efficiency point (BEP). These correction coefficients, defined for head (C_H^{BEP}), flow rate (C_Q^{BEP}), and efficiency (C_η^{BEP}), represent the ratio between the performance parameters when pumping a viscous fluid compared to the same parameters when handling water. Given this, for low viscosity cases, the value of these coefficients will be close to unity and as viscosity increases the values became degraded towards lower values. Porcel *et al.* (2022) proposed correlations for the correction coefficients based on the rotational Reynolds number (Re_ω) adjusted with empirical parameters on a exponential curve. The proposed correlations for each coefficient are shown in equations below with empirical coefficients a, b and c.

$$C_H^{BEP} = e^{a_H\left(\frac{b_H}{Re_\omega}+c_H\right)} \tag{4.1}$$

$$C_Q^{BEP} = e^{a_Q\left(\frac{b_Q}{Re_\omega}+c_Q\right)} \tag{4.2}$$

$$C_\eta^{BEP} = e^{a_\eta\left(\frac{b_\eta}{Re_\omega}+c_\eta\right)} \tag{4.3}$$

The same methodology was used and the parameters were adjusted to fit our data points. The main difference here is that we have an emulsion flow and therefore, the emulsion effective viscosity (μ_r) calculated previously was used instead of oil viscosity.

Figure 4.17 presents the correction coefficients for the P100L pump on y-axis versus Re_ω on the x-axis. The continuous lines represent fitted curves for correction coefficients, which show how the experimental data aligns with an exponential decay model as viscosity increases. Below 10^5, we can observe a possibly flow regime dominate by viscous forces which is dependent on Re_ω. The respective parameters a, b and c for each correction coefficient and pump are shown in Table 4.4 below.

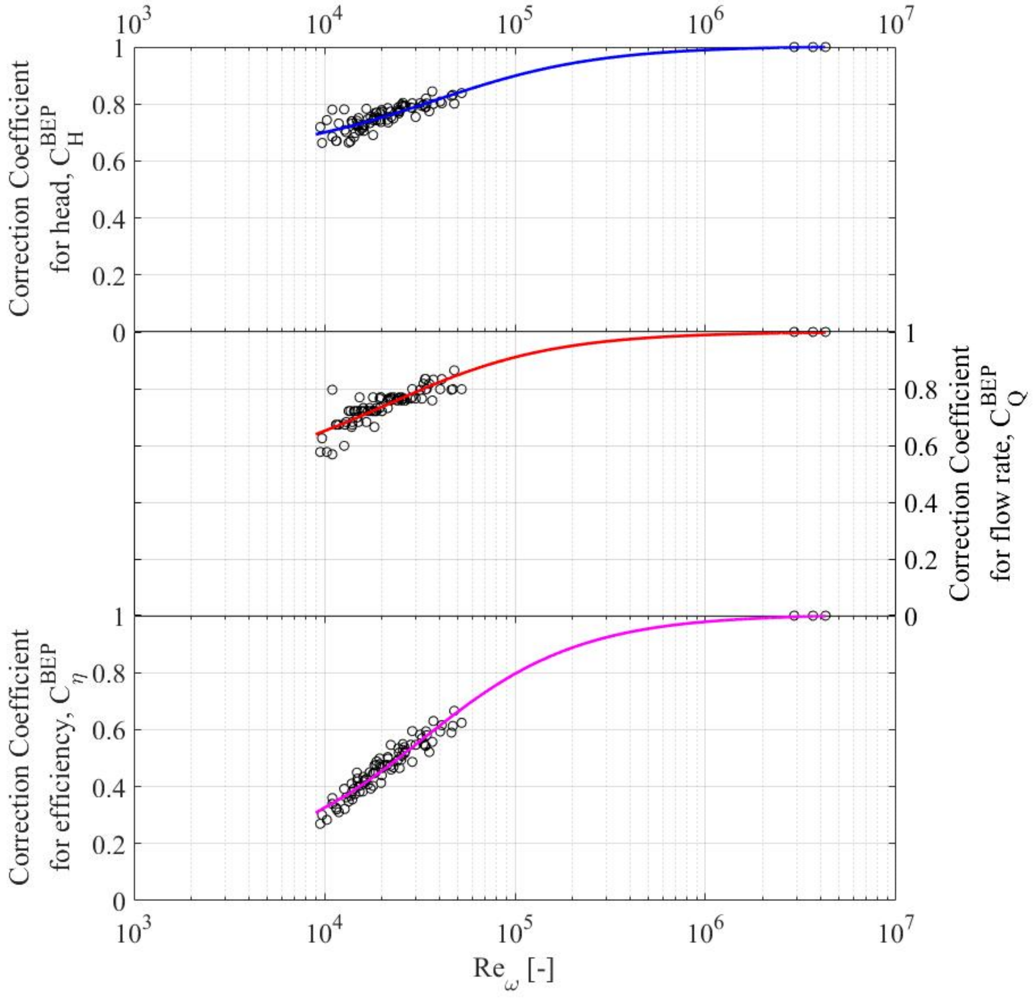

Figure 4.17 – Correction coefficients for head, flow rate, and efficiency at BEP for the P100L pump as a function of rotational Reynolds number Re_ω.

Table 4.4 – Coefficients used in the correction equations for P47 and P100L

Pump	**Parameter**	a	b	c
P47	Head (C_H^{BEP})	0.0073	-4874	5309
	Flow Rate (C_Q^{BEP})	0.0039	-9788	8036
	Efficiency (C_η^{BEP})	0.0067	-24631	7291
P100L	Head (C_H^{BEP})	0.0034	-14264	29594
	Flow Rate (C_Q^{BEP})	0.0002	-10727	14940
	Efficiency (C_η^{BEP})	0.0045	-26384	13330

The points merge into a exponential trend curve, no matter the viscosity or rotational speed related and it follows the same trend observed in the literature for other pump systems. The higher the fluid viscosity (lower Re_ω), the greater the degradation in pump performance. For fluids with low viscosities (i.e., high Reynolds number), the correction coefficients remain relatively close to unity, indicating minimal performance degradation. However, as the viscosity increases (i.e., lower Re_ω), a continuous drop in the coefficients is observed.

This behavior is consistent with the findings of Patil *et al.* (2018) and Porcel *et al.* (2022), who also observed that the drop in correction coefficients is possibly linked to a change in the flow regime within the pump.

Figure 4.18 presents the correction coefficients for the P47 pump. The correction coefficients for both the P100L and P47 pumps follow a similar pattern, where higher viscosities result in significant degradation of pump performance. However, several differences can be noted when comparing the two pumps. The P47 pump exhibits slightly better performance in terms of head (C_H^{BEP}) compared to the P100L pump at lower Reynolds numbers. This suggests that the P47 is more resilient to viscous effects in terms of head generation, maintaining higher values of C_H^{BEP} at lower values of Re_ω. Despite the general evidence found on the work of Kindermann (2022) that radial pumps tend to present a greater performance reduction with viscosity increase than mixed-flow geometries, for viscosities below 450 cP, the P100 pump presents a greater decline of (C_H^{BEP}) when compared with P47.

Both pumps show a significant reduction in flow rate correction coefficient (C_Q^{BEP}) as viscosity increases. However, the P47 pump experiences a sharper decline in C_Q^{BEP}, indicating a greater sensitivity to viscosity in terms of flow rate compared to the P100L. Efficiency degradation is substantial in both pumps, but the P100L seems to retain higher efficiency values

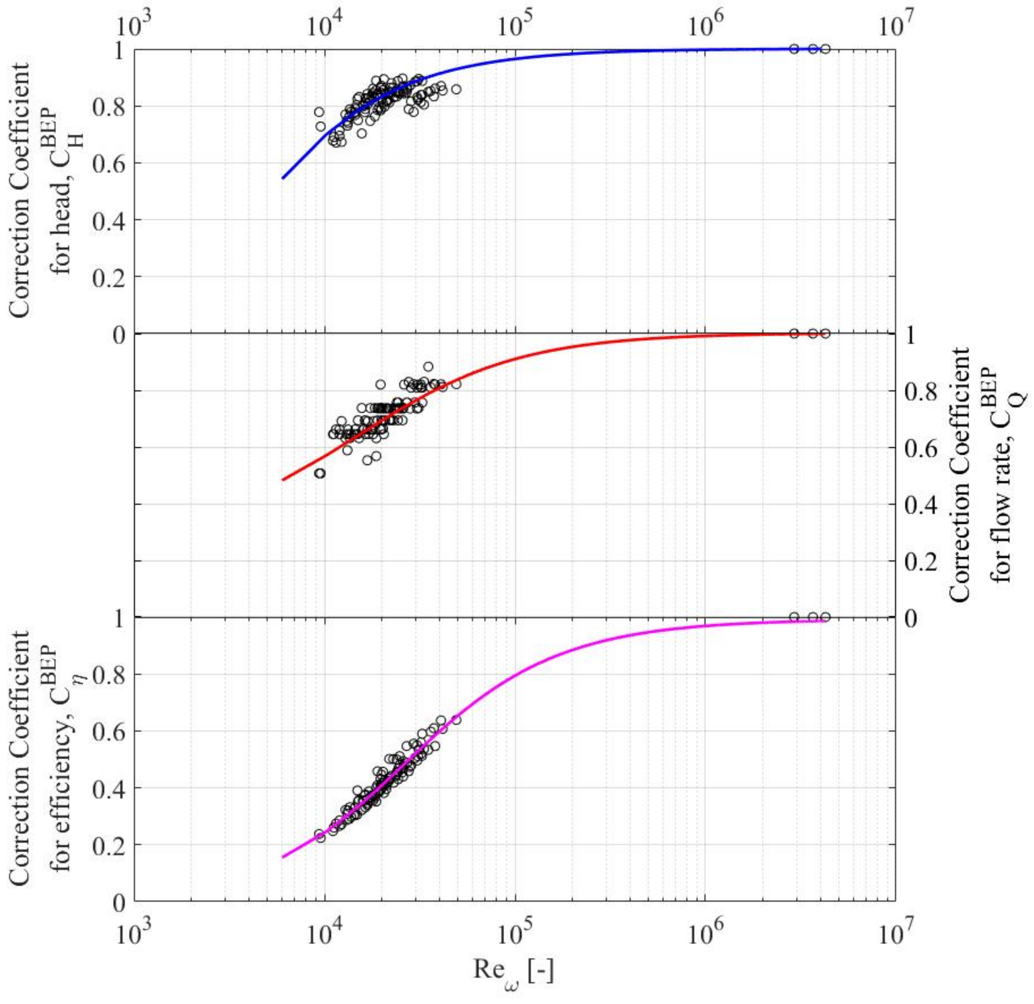

Figure 4.18 – Correction coefficients for head, flow rate, and efficiency at BEP for the P47 pump as a function of rotational Reynolds number Re_ω.

(C_η^{BEP}) at higher viscosities than the P47.

In summary, while both the P100L and P47 pumps exhibit similar trends in performance degradation with increasing viscosity, distinct differences emerge in their behavior. The P47 pump demonstrates greater resilience in maintaining head performance (C_H^{BEP}) at lower Reynolds numbers, suggesting a better capability to handle viscous effects in terms of head generation. However, the P100L pump retains a higher overall efficiency (C_η^{BEP}) at elevated viscosities, making it more suitable for applications involving highly viscous emulsions. In contrast, the P47 pump is more sensitive to viscosity-related losses, particularly in terms of flow rate, as evidenced by its sharper decline in the flow rate correction coefficient (C_Q^{BEP}).

Analyzing the P100L results, we observe that the correction coefficient for head (C_H^{BEP}) and flow rate (C_Q^{BEP}) exhibits a reduction of 30% on average. The efficiency correction coefficient (C_{η}^{BEP}) shows the most significant degradation, with up to 75% loss in efficiency at high viscosities, reinforcing the substantial impact that viscous fluids have on the overall performance of ESP systems.

This continuous degradation of pump performance with increasing viscosity underscores the importance of considering viscosity effects when designing and optimizing ESP systems for use in viscous fluid environments. By understanding how these correction coefficients behave, operators can better predict performance losses and adjust operational parameters accordingly.

4.5 Development and Optimization of the Relative Viscosity Model for Emulsion Flow in ESP

Previous research indicates that various parameters influence the complex rheological behavior of water-oil emulsions, especially within Electrical Submersible Pumps (ESPs). Factors such as continuous phase viscosity (μ_c), temperature (T), continuous phase density (ρ_c), shear rate ($\dot{\gamma}$), interfacial tension (σ), dispersed phase viscosity (μ_d), droplet size (d), dispersed phase density (ρ_d), and the concentration of emulsifying agents directly impact the effective viscosity of emulsions in flow (Barnes, 1994; Rønningsen, 1995; Derkach, 2009; Tadros, 2013; Bulgarelli *et al.*, 2021b).

In the context of ESPs, the emulsion is subjected to an intense shear field due to the pump's rotational speed and geometric characteristics. This results in a complex flow influenced not only by fluid properties but also by operational and design parameters, such as rotational speed (ω), flow rate (Q), impeller geometry, and the level of generated turbulence.

The initial model adopted in this study is based on Taylor (1932), modified by Bulgarelli *et al.* (2021b) to account for flow dynamics within the ESP (Equation 2.42).

A comparison between the relative viscosity model proposed by Bulgarelli *et al.* (2021b) with optimized parameters and the calculated relative viscosity using the methodology by Biazussi (2014) is illustrated in Figure 4.19. The figure displays the optimized model plotted against our experimental data for each pump (P47 and P100L).

As shown in Figure 4.19, the optimized model by Bulgarelli et al. (2022) does not accurately capture the behavior of the relative viscosity. This discrepancy may be attributed to several factors. One possible explanation is the correct modeling of flow rate influence and average particle size to better account the fluid dynamics in the model. This could result in

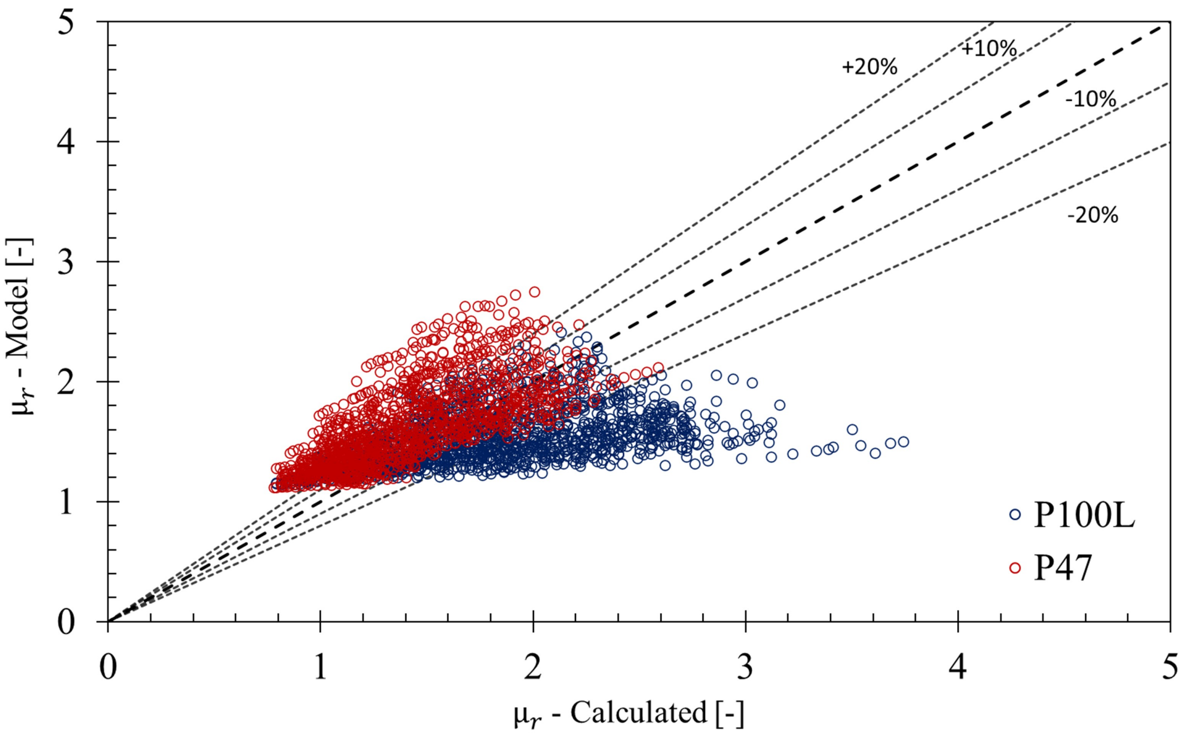

Figure 4.19 – Comparison between calculated and predicted μ_r using Bulgarelli et al. (2022) model with optimized parameters. E_b = 2.498 and k = 0.358

greater data dispersion and a systematic underestimation of effective viscosity for this pump.

Another potential reason for the discrepancy is the limited dataset utilized in the prior work by Bulgarelli *et al.* (2022a). The smaller dataset may have constrained the model's generalizability, leading to underperformance when applied to a broader range of conditions, such as those tested in our experiments. The additional data points from our experiments likely capture a more diverse set of flow behaviors and emulsion characteristics, further challenging the model's predictive capability.

To address these issues, modifications to the model that incorporate these factors were proposed, ultimately enhancing prediction accuracy for ESP applications under various emulsion flow conditions.

To refine the model and account for the stability conditions of droplets in an emulsion, we introduce the concept of the critical droplet diameter (d_{crit}), which defines the maximum droplet size that maintains spherical stability. This critical diameter is determined by the balance of forces acting on a static droplet, where the gravitational force balances the interface tension on the droplet. The first tends to deform the droplet as its volume increases while the second acts to maintain its spherical shape. When the droplet reaches a critical size, the gravitational force becomes large enough to overcome the interface tension, causing the droplet to deform.

The gravitational force can be expressed by $F_{\text{grav}} = \Delta\rho V g$, where $\Delta\rho = \rho_c - \rho_d$ is the density difference between continuous fluid and the droplet, V is the volume of the droplet, and g is the acceleration due to gravity. The interface tension force F_σ is expressed as $F_\sigma = \sigma A$, where A is the surface area of the spherical droplet, $A = \pi d_{\text{crit}}$.

At the point of critical stability, the gravitational force equals the interface tension force:

$$(\rho_c - \rho_d) \cdot \frac{\pi d_{\text{crit}}^3}{6} \cdot g = \sigma \cdot \pi d_{\text{crit}}$$

By canceling π from both sides of the equation and simplifying, we obtain:

$$(\rho_c - \rho_d) \cdot \frac{d_{\text{crit}}^3}{6} \cdot g = \sigma \cdot d_{\text{crit}}$$

Next, we isolate d_{crit} to find:

$$d_{\text{crit}} = \sqrt{\frac{6\sigma}{(\rho_c - \rho_d)g}}$$

To adapt this model for flow transition effects, Barnea *et al.* (1982) introduced an empirical adjustment, yielding:

$$d_{\text{crit}} = 2\sqrt{\frac{0.4\sigma}{(\rho_c - \rho_d)g}}$$

This model provides an estimate of the maximum size of a droplet that remains stable in an emulsion, considering the balance between surface tension and gravity. However, in the case of ESPs, where centrifugal forces dominate over gravitational acceleration, g is replaced with the centrifugal acceleration generated within the impeller:

$$g = \omega^2 r_m = \omega^2 \frac{(r_1 + r_2)}{2} = \omega^2 \frac{D}{4}\left(1 + \frac{r_1}{r_2}\right), \tag{4.4}$$

where r_m is the mean radius, r_1 and r_2 are the inner and outer radii, respectively, and D is the impeller diameter.

Based on these adaptations, a new expression for the relative viscosity (μ_r) is proposed:

$$\mu_r = 0.5 + 2.5E_b \left(\frac{1}{a\phi^b + \mathrm{Re}_\omega^{-\left(cN_s/\frac{d_{\text{crit}}}{d_{32}}\right)}} \right) \left(\frac{\mu_d + 0.4\mu_c}{\mu_d + \mu_c} \right) f_d, \tag{4.5}$$

where:

- E_b is an adjustable parameter related to the interfacial properties of the emulsion, influenced by the presence of surfactants.
- a, b, c, and N_s are empirically determined constants.
- ϕ is the dimensionless flow rate.
- Re_ω is the rotational Reynolds number.
- d_{crit} is the critical droplet diameter.
- d_{32} is the Sauter mean diameter, characterizing the droplet size distribution.

This revised model accounts for the combined effects of various parameters influencing the relative viscosity of emulsions within an ESP. The inclusion of interfacial parameters and the use of dimensionless numbers facilitate a more accurate description of emulsion behavior under high shear flow conditions.

A comparison between the proposed relative viscosity model and the calculated relative viscosity using the methodology by Biazussi (2014) is presented in Figure 4.20 for each pump (P47 and P100L).

Observing both figures, it becomes evident that the newly proposed model offers a closer fit to the experimental data, with significantly less dispersion around the parity line. This reduction in dispersion underscores the improvements made to the model's accuracy through the refinement of key parameters and the overall structure.

The enhanced accuracy of the proposed model is primarily due to three major modifications: the removal of the Ohnesorge number, the inclusion of the critical-to-Sauter diameter ratio, and a refined dimensionless flow parameter consistent with the previously discussed d_{32} model.

First, by eliminating the Ohnesorge number, the model focuses on the dominant forces impacting emulsion flow within the ESP. In high-shear environments typical of ESP operation, the effects captured by the Ohnesorge number balancing viscous, inertial, and interfacial

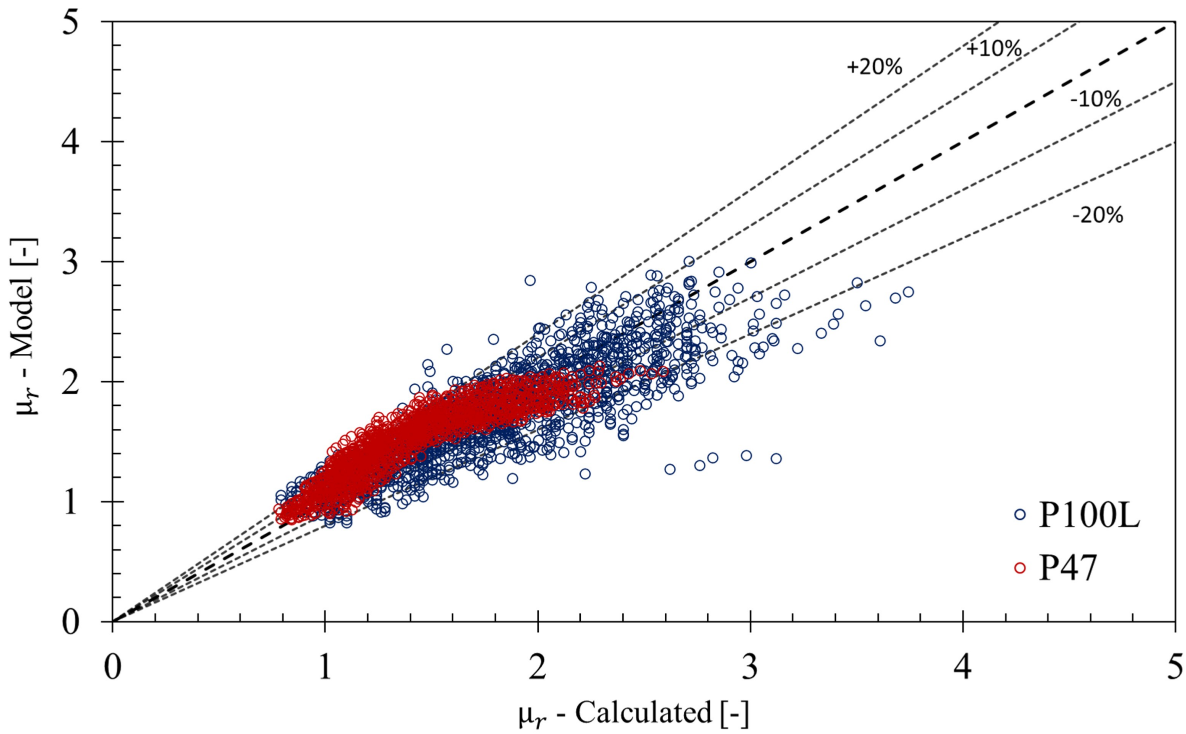

Figure 4.20 – Comparison between calculated and predicted μ_r using the proposed model with optimized parameters.

forces are overshadowed by the centrifugal forces generated within the pump. Consequently, removing the Ohnesorge parameter streamlines the model, concentrating on the primary influencing factors without compromising predictive accuracy.

Second, introducing the ratio between the critical droplet diameter (d_{crit}) and the Sauter mean diameter (d_{32}) within the rotational Reynolds number (Re_ω) allows for a more nuanced representation of droplet behavior in the flow. The critical diameter d_{crit} defines the maximum droplet size that maintains stability in the emulsion, enhancing the model's sensitivity to droplet size distribution and better capturing the shear-thinning characteristics observed in the ESP's emulsion behavior.

The proposed model provides a robust tool for predicting the relative viscosity of water-oil emulsions under ESP operational conditions. By incorporating critical parameters and utilizing dimensionless numbers, it offers an accurate representation of droplet breakup and coalescence phenomena. This refinement enhances the model's applicability for analyzing and optimizing ESP performance under varying flow conditions, potentially improving the efficiency and predictability of pumps operating with emulsions.

4.6 Emulsion Effective Viscosity in the Pipe

In addition to evaluating the emulsion's effective viscosity inside the ESP, it is also critical to understand how the emulsified mixture behaves in the piping system downstream of the pump. In this section, we present the results of the emulsion's effective viscosity measured in a segment of the outlet pipe, located after the pump. This segment is equipped with a differential pressure (ΔP) sensor that allows for a reverse calculation of the emulsion viscosity based on Reynolds number (Re), and flow characteristics.

4.6.1 Methodology for Calculating Effective Viscosity in the Pipe

The process of estimating the effective viscosity in the outlet pipe segment follows a convergence method similar to that used for the pump analysis. The initial assumption for the effective viscosity is based on the pure oil viscosity. From there, the following steps are applied to iteratively refine the viscosity estimate.

The calculation starts with the assumption that the emulsion mixture viscosity is equal to the viscosity of pure oil. Using this value, the Reynolds number (Re) in the pipe is calculated as follows:

$$Re = \frac{\rho_m U_m D_p}{\mu_e} \tag{4.6}$$

where:

- ρ_m is the density of the emulsion mixture (kg/m³),
- U_m is the mixture velocity in the pipe (m/s), calculated using the volumetric flow rate (Q_L) and the pipe's cross-sectional area,
- D_p is the diameter of the pipe (m),
- μ_e is the emulsion mixture viscosity (cP).

Considering that, for all cases we have a laminar flow ($Re < 2300$), the friction factor f is determined directly using:

$$f = \frac{64}{Re} \tag{4.7}$$

Once the friction factor is determined, the theoretical pressure drop ($\Delta P_{theoretical}$) in the pipe is calculated using the Darcy-Weisbach equation:

$$\Delta P_{theoretical} = f \frac{L}{D_p} \frac{\rho_o U_m^2}{2} \tag{4.8}$$

where:

- L is the length of the pipe segment (m),
- D_p is the diameter of the pipe (m),
- ρ_o is the density of the oil phase (kg/m³),
- U_m is the mixture velocity (m/s).

The initial $\Delta P_{theoretical}$ is compared with the measured $\Delta P_{measured}$ obtained from the differential pressure sensor. If the values do not match, the effective viscosity μ_e is adjusted iteratively until the calculated $\Delta P_{theoretical}$ matches the experimentally measured $\Delta P_{measured}$. This convergence process refines the value of μ_e, providing an accurate estimate of the emulsion's effective viscosity in the pipe.

Once the effective viscosity is determined, the relative viscosity (μ_r) is calculated in a similar manner as done for the pump (Equation **??**). This ratio provides insight into how much more viscous the emulsion is compared to its continuous phase, in this case, oil.

4.6.2 Effective Viscosity Results in the Pipe

Figures 4.21 and 4.22 show the relative viscosity of the emulsion as a function of the mixture velocity (U_m) for various dispersed phase fractions at 3500 rpm and 40°C in the outlet pipe for the P100L and P47 pumps, respectively. The behavior observed in the outlet pipe follows a pattern where relative viscosity tends to decrease as the flow rate increases, which is consistent with the expected shear-thinning behavior often exhibited by emulsions under turbulent flow conditions.

The P100L pump (Figure 4.21) exhibits, for dispersed phase fractions until 24%, an almost linear trend of relative viscosity with increasing U_m, indicating a nearly Newtonian behavior. In this regime, the internal structure of the emulsion remains relatively stable, and the viscosity does not vary significantly with changes in shear rate, which is typical of Newtonian fluids. However, at higher dispersed phase fractions, such as 28% and 32%, the emulsion

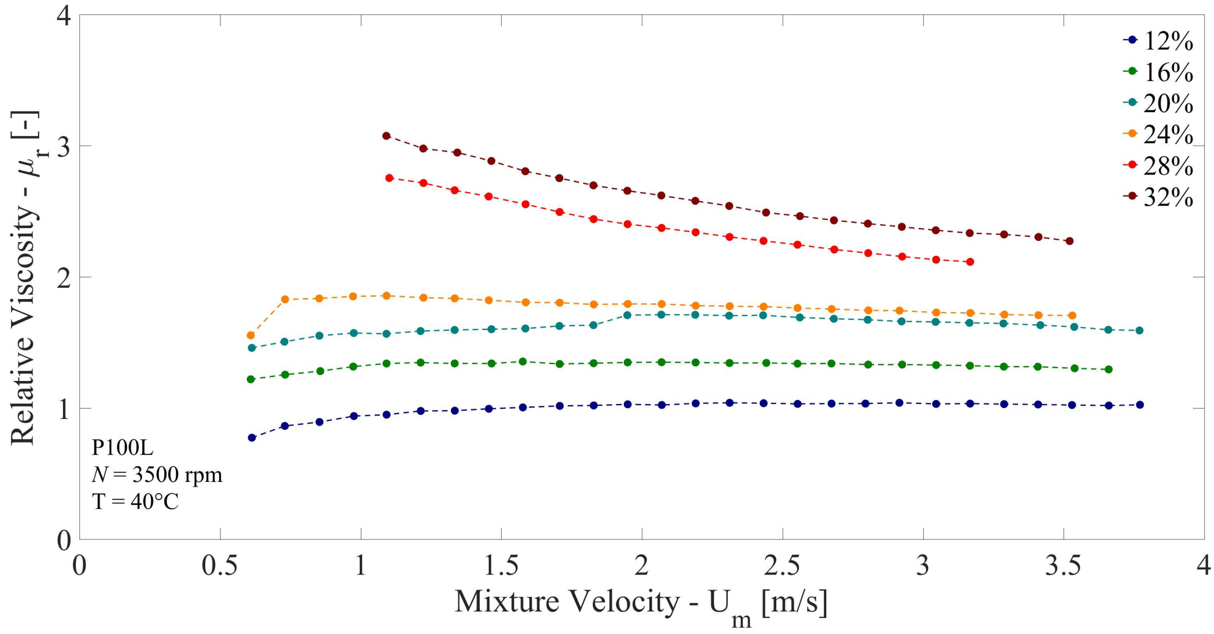

Figure 4.21 – Relative viscosity versus ϕ for the outlet pipe operating with different W/O emulsion dispersed phase fractions for P100L at 3500 rpm and 40°C.

exhibits more pronounced shear-thinning behavior. Here, the relative viscosity decreases more sharply with increasing U_m, reflecting the breakdown or rearrangement of the emulsion's internal structure as the shear rate increases.

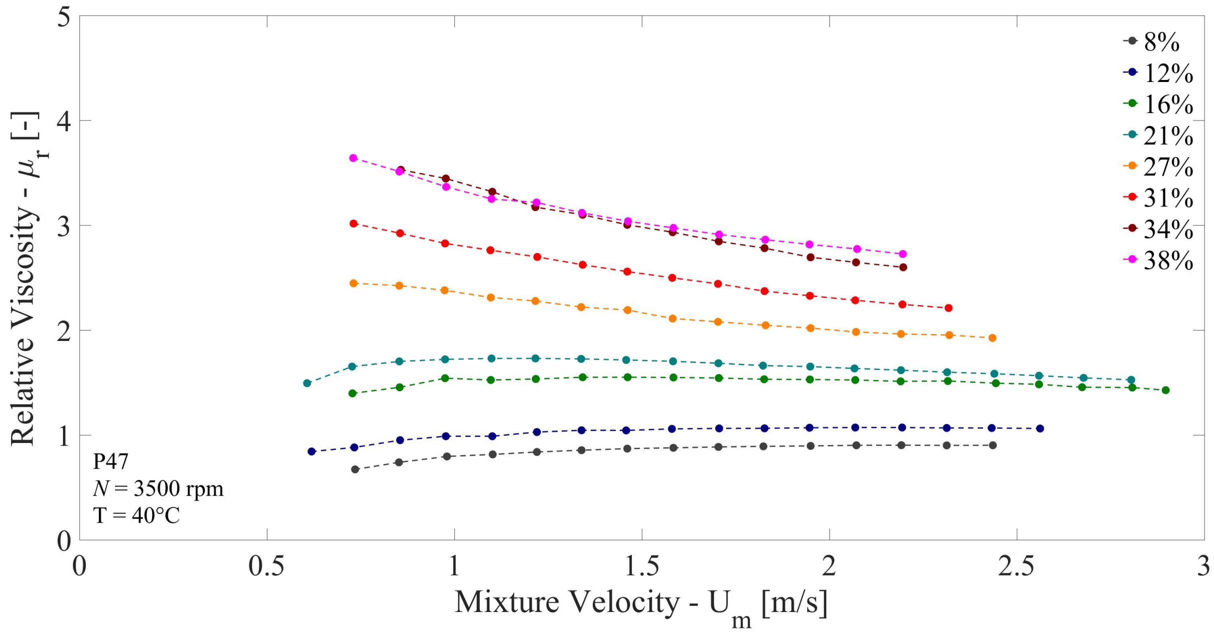

Figure 4.22 – Relative viscosity versus ϕ for the outlet pipe operating with different W/O emulsion dispersed phase fractions for P47 at 3500 rpm and 40°C.

For the P47 pump (Figure 4.22), a similar pattern is observed. At lower dispersed phase fractions, until 21%, the relative viscosity remains nearly constant as the velocity increases, suggesting that the emulsion behaves in a nearly Newtonian manner under these conditions. However, as the dispersed phase fraction increases above 27%, the emulsion exhibits a noticeable shear-thinning behavior. The relative viscosity decreases more significantly with increasing ϕ, suggesting that the increased shear rate disrupts the internal structure of the emulsion, leading to a reduction in internal resistance to flow.

4.6.3 Comparison Between Pump and Pipe Viscosity Results

One of the key observations is the difference in relative viscosity between the pump and the outlet pipe. Inside the pump, the relative viscosity is a bit lower than in the pipe, particularly at higher flow rates. Several plausible explanations exist for this phenomenon, grounded in the differences in flow dynamics and the effects of centrifugal forces within the pump.

First, the intense centrifugal field inside the pump plays a crucial role in critical droplet diameter (d_{crit}) which diminishes a lot and therefore, allows the droplets to be deformed inside the impeller. This effect allows the formation of agglomerates of water being denser than oil, which are pushed toward the outer regions of the pump, promoting a drift between the phases while the oil tends to occupy preferential flow paths nearer the core of the impeller. This may facilitate the movement of the oil layers, thereby reducing the overall effective viscosity observed inside the pump. This phenomenon becomes particularly pronounced at high flow rates, where the centrifugal forces are stronger. As a result, the oil-dominated regions experience less internal friction, which, in turn, lowers the apparent viscosity of the emulsion inside the pump.

These filaments or clusters of water droplets could aid in displacing the surrounding oil more efficiently 4.23). The coalescence of water droplets into larger structures reduces the total interfacial area, thereby lowering the system's overall interfacial energy. While the interfacial tension itself remains unchanged, the redistribution of the dispersed phase alters the flow dynamics. Larger water structures can facilitate the formation of continuous water pathways along the pump walls, reducing viscous dissipation and enhancing the overall flow efficiency. Consequently, this rearrangement of the emulsion microstructure may contribute to a reduction in the effective viscosity within the pump, lowering internal friction and improving performance.

In contrast, the flow in the outlet pipe is more uniform and consequently, the emul-

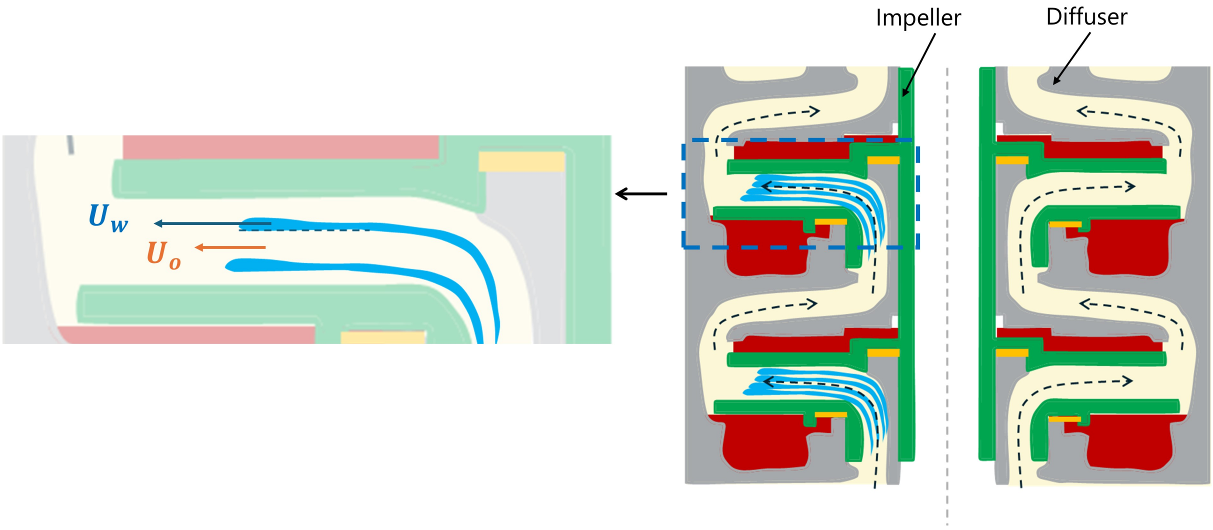

Figure 4.23 – Scheme of how the filaments of water droplets helps with oil displacement due to drag.

sion in the pipe remains more homogeneously dispersed, leading to higher relative viscosity values. The absence of a strong centrifugal field means that the water and oil phases remain stable, which increases internal friction and thus raises the effective viscosity. Additionally, the shear stress in the pipe are lower compared to the intense shear generated by the impeller blades. This further explains the higher relative viscosity observed in the pipe, as the uniform flow in the pipe prevents localized phase segregation, maintaining a higher internal resistance to flow.

These observations highlight the importance of considering both pump and pipe dynamics when analyzing the behavior of emulsions in ESP systems. Understanding these transitions is crucial for optimizing pump performance and selecting the appropriate operating conditions when handling emulsions with varying dispersed phase fractions.

5 EXPERIMENTAL DROPLET SIZE RESULTS

This chapter has been published as:

Leuchtenberger, R. F., Biazussi, J. L., Bannwart, A. C. (2024). Experimental and theoretical modeling of droplet break-up of W/O emulsion flow in ESPs. *Chemical Engineering Research and Design*, 210, 724-734.

5.1 Analysis and Modeling of Droplet Size Distribution (DSD)

The droplet size distribution (DSD) was measured at the pump outlet using an FBRM probe, which records the number of droplets (n_i) for each size class i. These measurements are represented as a logarithmically scaled vector, encompassing droplet sizes between 1 and 1000 μm. During data analysis, outliers were identified, potentially caused by droplet coalescence, leading to the formation of agglomerates. Since the primary objective of this study is to investigate droplet breakup mechanisms, the concept of maximum stable droplet diameter, as defined by (Pereyra, 2011), was employed to exclude such anomalies. Across all experimental conditions, the mean value of the maximum stable droplet diameter was approximately 100 μm. Thus, droplets exceeding this threshold were attributed to coalescence or agglomeration phenomena and excluded from further analysis.

The study of droplet size distribution in liquid-liquid multiphase flows involves both experimental measurements and the approximation of these data using DSD functions. To identify the distribution function that best represents the experimental data, a goodness-of-fit (GOF) analysis was performed.

The initial candidates for the DSD function were the log-normal, log-logistic, and Rosin-Rammler distributions. However, only the first two were retained for further analysis due to their better qualitative alignment with the experimental data. Both functions exhibit left-skewed asymmetry, and statistical parameters for these two models, like Sum of Squared Errors (SSE) and Root Mean Squared Error (RMSE) values as defined in previous chapter, were found to be very close. Despite this, these metrics alone were insufficient to determine the most suitable function. To address this limitation, additional goodness-of-fit (GOF) criteria were employed, including the Kolmogorov-Smirnov (KS) test, Chi-squared test (χ^2), and correlation coefficient (R^2).

The KS test assesses the likelihood of the dataset conforming to a given probability distribution, while the Chi-squared test evaluates the degree of agreement between observed and expected frequencies under the assumed distribution. The results of these tests, presented in Appendix A (Table A.1), indicate that the p-values for the log-logistic function were predominantly close to zero, strongly suggesting that this model does not adequately represent the data. In contrast, the log-normal distribution yielded higher p-values, particularly in the KS test, indicating a better fit for the experimental data. These findings are further supported by Figure 5.1, which illustrates the visual alignment between the experimental histogram and the log-normal model.

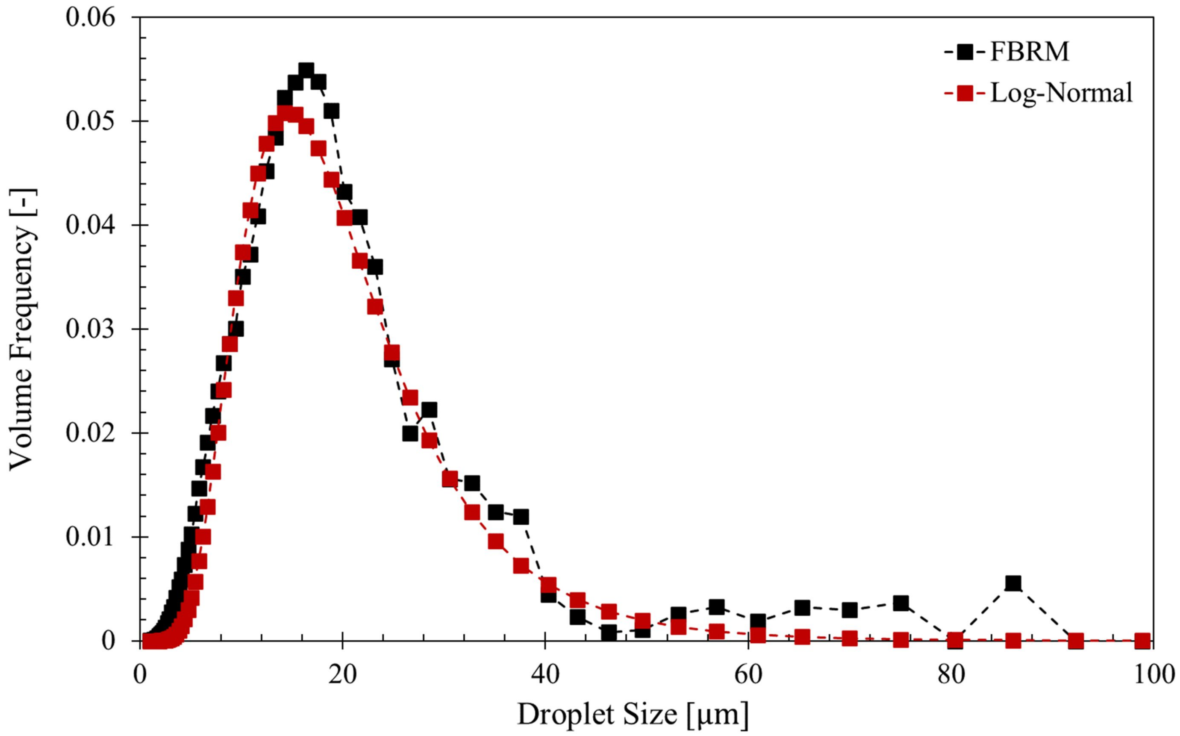

Figure 5.1 – Fit of the log-normal model to the experimental droplet size distribution measured using FBRM. Operating conditions: $N = 3500$ rpm, $f_d = 32\%$, $T = 40$°C, and $Q_l = 30$ m^3/h.

The volumetric probability density function for the log-normal distribution is expressed as:

$$q_v(\mu_v, \sigma_v) = \frac{1}{d_i \sigma_v \sqrt{2\pi}} \exp\left[-\frac{(\log(d_i) - \mu_v)^2}{2\sigma_v^2}\right], \tag{5.1}$$

where σ_v represents the standard deviation of the logarithmic values (also referred to as the scale or shape parameter), and μ_v denotes the mean of the probability density function.

These statistical parameters are relevant for predicting phase inversion points and supporting further modeling efforts based on DSD analysis.

As previously mentioned, the experimental design matrix was developed to assess the influence of temperature, ESP rotational speed, flow rate, and dispersed phase fraction (f_d) on the DSD. As shown in Figure 5.2, an increase in the dimensionless flow rate (ϕ) caused the distributions to narrow, accompanied by an increase in volume frequency for smaller droplet diameters.

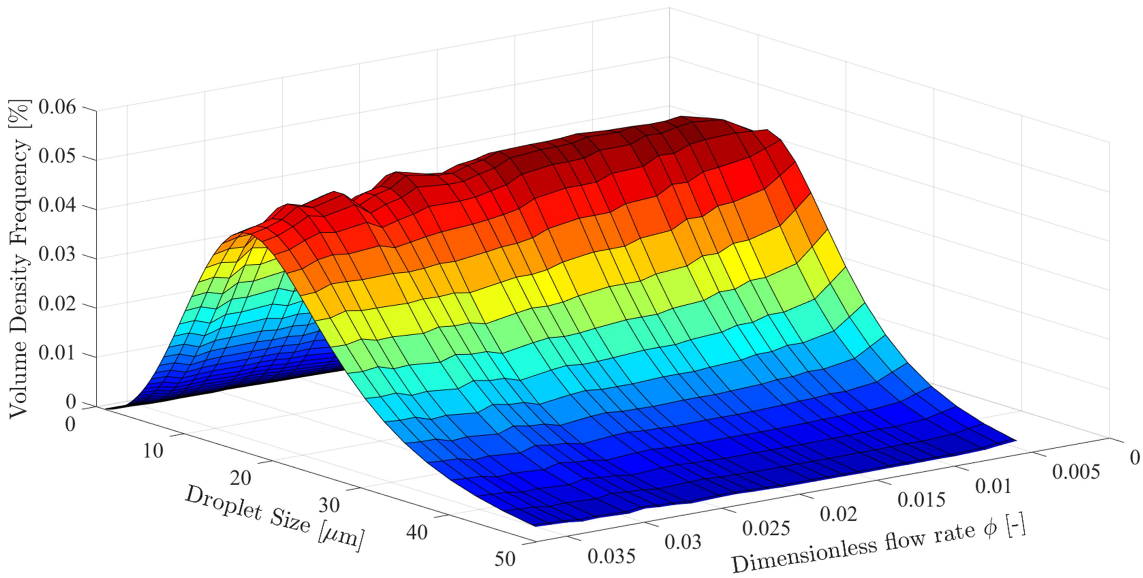

Figure 5.2 – Three-dimensional representation of the influence of the dimensionless flow rate (ϕ) on the droplet size distributions measured at the P100L outlet ($N = 3500$ rpm; $T = 45$°C).

5.2 Characterization of Sauter Mean Diameter (d_{32})

The Sauter mean diameter (d_{32}) is a parameter of significant relevance in liquid-liquid dispersion studies. By correlating droplet volume to surface area, it can serve as a metric to analyze and evaluate the influence of operational parameters on droplet size distributions.

Among the variables investigated, the dispersed phase fraction (f_d) demonstrated the most pronounced effect on both the droplet size distribution and the Sauter mean diameter. As shown in Figure 5.2, increasing f_d caused the distribution to shift towards smaller droplet sizes. This behavior suggests that a higher concentration of dispersed phase enhances droplet breakage, likely due to intensified interactions and collisions among droplets. Although coalescence is induced by the higher concentration and closer proximity of droplets, the increased turbulent dissipation ultimately dominates, preventing excessive coalescence and promoting further droplet breakup.

In Figure 5.3, it can be observed that d_{32} decreases significantly with increases in both the dispersed phase fraction (f_d) and the dimensionless flow rate (ϕ). Although the reduction in d_{32} diminishes as ϕ increases, even under lower f_d conditions, flow rate and shear stress remain significant contributors to droplet breakage.

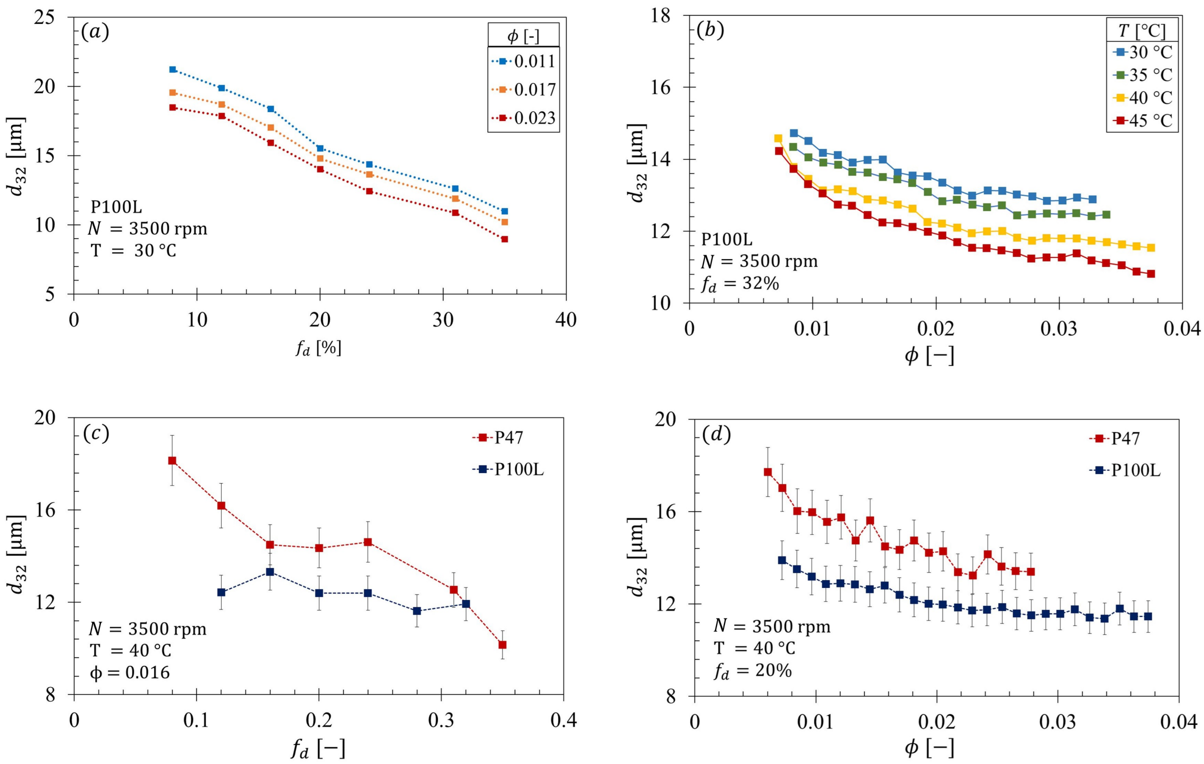

Figure 5.3 – Impact of dispersed phase fraction (f_d), dimensionless flow rate (ϕ), and temperature (T) on the Sauter mean diameter (d_{32}) based on experimental observations.

The experimental setup included a temperature control system that allowed precise adjustment of the continuous phase viscosity during the tests. As shown in Figure 5.3b, higher temperatures resulted in smaller droplet sizes. This observation aligns with findings by Husin e Hussain (2018), who reported that temperature exerts minimal influence on the shear-thinning effect in water-in-oil emulsions. However, temperature significantly impacts the viscosity of the continuous phase; lower viscosity intensifies the shear stress exerted by the ESP, promoting enhanced droplet breakage.

Variations in the impact of parameters on d_{32} between the P47 and P100L ESP geometries are illustrated in Figure 5.3. The most notable difference is the P100L's higher mixed flow, which enhances droplet breakage intensity, leading to smaller droplet sizes under equivalent conditions. Additionally, uncertainty bars were incorporated for d_{32}, as explained in the experimental uncertainty analysis presented in Appendix B. The combined uncertainty values (Table B.1) were not significant enough to invalidate the observed trends.

For the P47, the increase in f_d results in a more substantial reduction in droplet size. However, due to its more radial mixing flow, the P47 only achieved similar droplet sizes when f_d reached 30%, which is near the emulsion phase inversion threshold. Regarding ϕ, a marked decrease in droplet size was also observed. It is worth noting that the P100L exhibited intense droplet breakage even at lower ϕ and f_d values.

5.3 Characterization of Maximum Stable Droplet Diameter (d_{95})

The characterization of liquid-liquid dispersions is closely linked to the maximum stable droplet diameter (d_{95}), which defines the upper threshold for droplet stability under given flow conditions. The determination of d_{95} typically relies on the equilibrium between turbulent forces, which drive droplet breakup, and cohesive forces, which preserve droplet stability (Hinze, 1955).

In practical applications, such as stirred tanks, vessels, and centrifugal pumps, the direct measurement of d_{95} is often challenging due to the complexity of the system dynamics. As a result, the Sauter mean diameter (d_{32}) is frequently employed as an indicator. Several studies have reported a linear relationship between d_{32} and d_{95}. However, as illustrated in Figure 5.4, the results of our experimental tests do not provide strong evidence supporting such a linear correlation. This discrepancy highlights the need for a more nuanced understanding of the factors influencing d_{95} in multiphase flow systems.

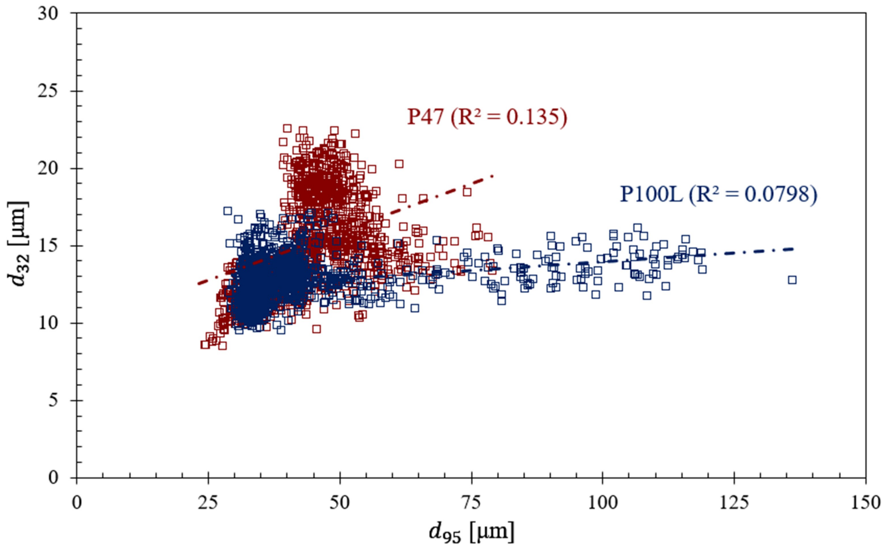

Figure 5.4 – Relationship between experimental Sauter mean diameter (d_{32}) and maximum stable droplet diameter (d_{95}) for the full set of experimental data.

5.4 Semi-Empirical Models for Droplet Diameter

5.4.1 Sauter Mean Diameter (d_{32}) Modeling

According to Schmitt *et al.* (2021), in stirred tank systems, the stability of droplets in liquid-liquid dispersions is determined by the interplay between cohesive and disruptive forces. This interplay can be described by the ratio of surface energy, which stabilizes droplets, to turbulent energy in the surrounding continuous phase, which promotes droplet destabilization.

With respect to turbulent energy, Kolmogorov (1941) proposed the concept of local isotropic turbulence, which assumes that at high Reynolds numbers, small regions exist within the flow where turbulence behaves isotropically. Under this framework, the energy spectrum is divided into the inertial subrange, where inertial forces dominate, and the viscous subrange, where energy dissipation is governed by viscous forces (Padron, 2004).

In the context of ESPs, droplet deformation is primarily influenced by inertial effects resulting from turbulent pressure fluctuations within the impeller (Gülich, 2008). Droplets smaller than the Kolmogorov length scale are located in the viscous subrange of turbulence, where viscosity plays a critical role (Padron, 2004).

Considering this viscous subrange, Padron (2004) proposed a model for predicting the droplet size in a rotor-stator mixer under viscous-dominated turbulent stress:

$$\frac{d_{32}}{D} = a_1 \left(\mathrm{We}_\omega \mathrm{Re}_\omega\right)^{-1/3}, \tag{5.2}$$

where a_1 is an empirical constant, We_ω and Re_ω represents the rotational Weber and rotational Reynolds number. Although insightful, this model does not consider the effects of water fraction or flow rate variations, limiting its applicability under broader operational conditions.

To address these limitations, Bulgarelli *et al.* (2022b) proposed a modified model that incorporates the dimensionless flow rate (ϕ), a parameter previously investigated by Perissinotto *et al.* (2020):

$$\frac{d_{32}}{D} = b_1 \left(\mathrm{We}_\omega \mathrm{Re}_\omega\right)^{-1/3} \left(1 + b_2 \phi^{-1}\right), \tag{5.3}$$

where b_1 and b_2 are empirical constants specific to the ESP design, with reported values of 0.35 and 0.025, respectively.

Given this, adjustments to Bulgarelli *et al.* (2021b) coefficients were performed for each pump tested (Figure 5.5a). While the influence of ϕ is apparent in the original model, discrepancies remain due to variations in water fraction and pump geometry. These were expected, as Bulgarelli's original model was calibrated exclusively with P100L data.

As demonstrated in Figure 5.3, the Sauter mean diameter (d_{32}) decreases with increasing dimensionless flow rate (ϕ), as well as with dispersed phase fraction (f_d). Recognizing these influences, a new semi-empirical model that accounts for the dispersed phase fraction effect and incorporates specific speed (N_s) to reflect ESP design influences was proposed below.

$$\frac{d_{32}}{D} = a_1 N_s \left(\phi^2 \mathrm{We}_\omega^3 \mathrm{Re}_\omega\right)^{-a_2} \exp\left(\frac{a_3}{N_s(1-f_d)}\right), \tag{5.4}$$

where a_1, a_2, and a_3 are empirical constants, and f_d represents the water fraction. The introduction of specific speed allowed correlation between experimental data from both pumps, yielding good agreement (Figure 5.5). It is notable that the P47 pump, characterized by greater radial flow, produced larger droplets at lower flow rates compared to the predominantly mixed-flow P100L.

When comparing models to experimental data from both pumps, our proposed model demonstrated smaller deviations than others in the literature (Figure 5.6). Notably, the exponential decrease of d_{32} with f_d was more pronounced for the P47 results. This trend is

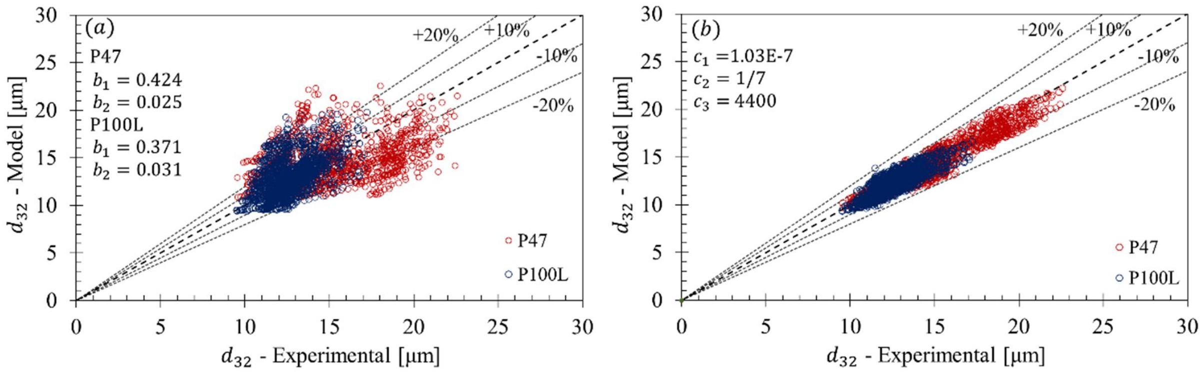

Figure 5.5 – Comparison of experimental data and predicted d_{32} values obtained using Bulgarelli's model (a) and the newly proposed model (b).

consistent with findings in Figure 5.3, where temperature, ESP speed, and ϕ were held constant while varying f_d.

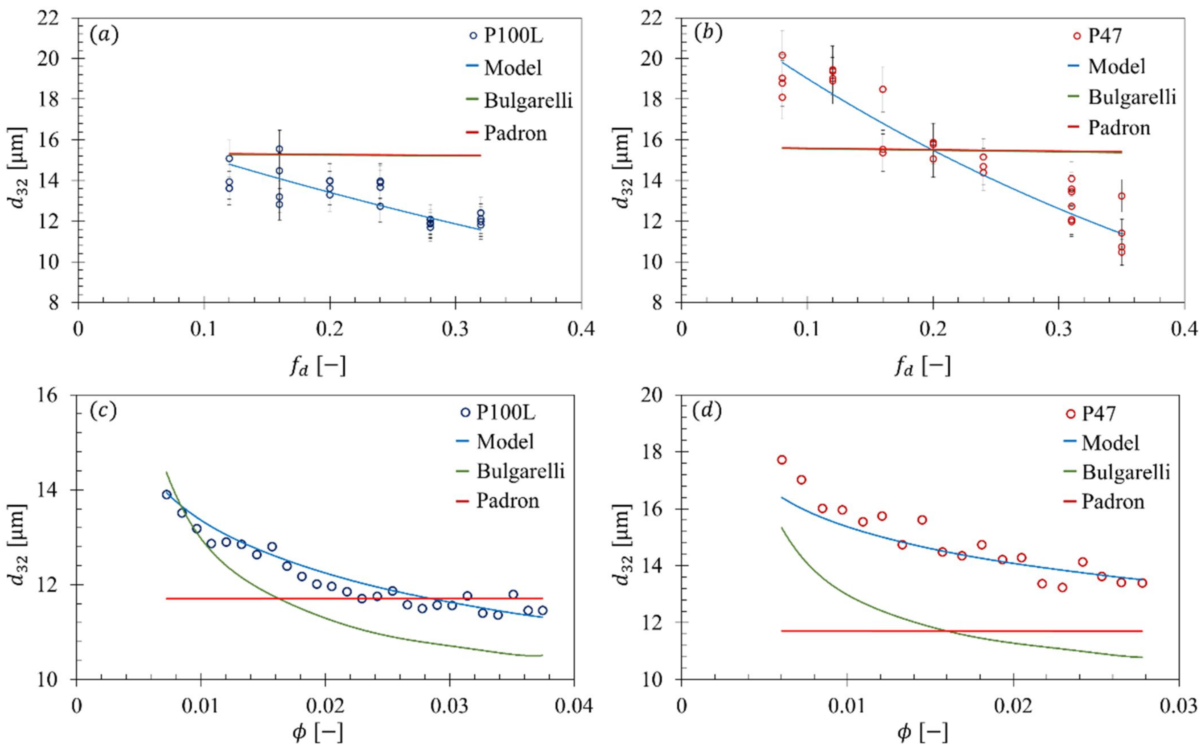

Figure 5.6 – Influence of f_d and ϕ on predicted d_{32} compared to experimental data for both pumps. ($N = 3500$ rpm; $T = 30$°C; (a,b) $\phi = 0.016$; (c,d) $f_d = 20\%$).

In Figure 5.6c and d, ϕ was varied while the temperature, ESP speed, and f_d was held constant. Incorporating an empirically derived exponent for ϕ into our model yielded predictions that aligned more closely with the experimental data compared to the model proposed by Bulgarelli *et al.* (2022b).

To evaluate the accuracy of the models statistically, we applied the weighted relative performance factor (PF) method. This statistical metric is commonly used to rank correlations and models based on their predictive accuracy (Abubakar *et al.*, 2016). The approach follows the equation provided by García *et al.* (2003):

$$PF = \frac{|E_1| - |E_1|_{min}}{|E_1|_{max} - |E_1|_{min}} + \frac{E_2 - E_{2min}}{E_{2max} - E_{2min}} + \frac{E_3 - E_{3min}}{E_{3max} - E_{3min}} + \frac{|E_4| - |E_4|_{min}}{|E_4|_{max} - |E_4|_{min}} + \frac{E_5 - E_{5min}}{E_{5max} - E_{5min}} + \frac{E_6 - E_{6min}}{E_{6max} - E_{6min}} \tag{5.5}$$

Where E_1 represents the average percent error, E_2 denotes the average absolute percent error, E_3 corresponds to the root mean square percent error, E_4 indicates the average error, E_5 stands for the average absolute error, and E_6 is the root mean square error. These metrics are defined as follows:

$$E_1 = \left[\frac{1}{n}\sum_{i=1}^{n}\frac{(y_{pred} - y_{exp})}{y_{exp}}\right] \times 100 \tag{5.6}$$

$$E_2 = \left[\frac{1}{n}\sum_{i=1}^{n}\left|\frac{(y_{pred} - y_{exp})}{y_{exp}}\right|\right] \times 100 \tag{5.7}$$

$$E_3 = \left[\sqrt{\frac{1}{n-1}\sum_{i=1}^{n}\left(\frac{(y_{pred} - y_{exp})}{y_{exp}}\right)^2}\right] \times 100 \tag{5.8}$$

$$E_4 = \frac{1}{n}\sum_{i=1}^{n}(y_{pred} - y_{exp}) \tag{5.9}$$

$$E_5 = \frac{1}{n}\sum_{i=1}^{n}|y_{pred} - y_{exp}| \tag{5.10}$$

$$E_6 = \sqrt{\frac{1}{n-1}\sum_{i=1}^{n}(y_{pred} - y_{exp})^2} \tag{5.11}$$

The average percent error (E_1) quantifies the level of agreement between the predicted and observed data, distinguishing whether the model tends to overestimate (positive values) or underestimate (negative values). On the other hand, the average absolute percent error (E_2) eliminates the cancellation of negative and positive discrepancies, serving as a critical metric for evaluating the predictive accuracy of a model or correlation (García *et al.*, 2003). Similarly, the root mean square percent error (E_3), often referred to as the standard deviation, measures how closely the predicted values align with the observed results. The remaining parameters, while not based on relative errors, offer additional insights into the absolute differences between the modeled and experimental data.

The performance factor (PF) provides a weighted metric that integrates E_1-E_6 to rank the performance of various models. This factor ranges from 0, representing the most accurate model, to 6, indicative of the least accurate. It thus offers a comprehensive means of evaluating model reliability under the tested conditions.

As detailed in Table 5.1, the statistical parameters were computed for each pump dataset. The results demonstrate that the proposed model outperformed others, exhibiting a higher overall accuracy. Notably, predictions for the P100L pump showed smaller deviations compared to the P47 pump, with errors remaining below 7% for both cases.

Table 5.1 – Evaluation of the tested models accuracy in predicting the Sauter Mean Diameter using 2,594 experimental data points.

Model	**ESP**	**PF**	**E$_1$**	**E$_2$**	**E$_3$**	**E$_4$**	**E$_5$**	**E$_6$**
Padron	P100L	4.031	5.862%	12.871%	14.322%	0.651	1.601	1.802
Padron	P47	3.532	-14.501%	19.692%	20.281%	-2.662	3.302	3.431
Bulgarelli	P100L	3.891	3.112%	10.871%	14.472%	0.362	1.361	1.802
Bulgarelli	P47	3.392	-1.181%	17.662%	20.951%	-0.601	2.712	3.201
This Model	P100L	2.831	-2.222%	5.311%	6.332%	-0.292	0.681	0.822
This Model	P47	3.102	-3.861%	5.622%	6.811%	-0.611	0.872	1.071

Finally, as depicted in Figure 5.4, noticeable differences in d_{32} were observed between the two pumps tested. It is worth highlighting that incorporating the specific speed (N_s) significantly improved the alignment of our model with the data from both ESPs. For future investigations, it is recommended to extend the analysis to a broader range of pump geometries, which could further refine and enhance the applicability of the proposed model.

5.4.2 Maximum Stable Droplet Diameter (d_{95})

Previously discussed models based on the Kolmogorov-Hinze theory express the maximum stable droplet diameter (d_{95}) in terms of various rheological properties of the emulsion and the kinetic energy dissipation rate ($\bar{\epsilon}_k$). An increase in $\bar{\epsilon}_k$ leads to the formation of smaller droplets, causing the ESP to generate more stabilized emulsions.

First, to further understand this behavior, the introduction of the time average energy dissipation per stage ($\bar{\epsilon}$) is needed. This parameter is very relevant for the flow of emulsions inside pumps since it can help to understand the behavior of d_{95} and how to model it properly. Using previous definitions from Chapter 2, it can be expressed in dimensionless form as:

$$\bar{\epsilon} = \frac{\dot{W}_{shaft} - \dot{W}_{hyd}}{\rho\omega^3 D^5} = \frac{\frac{\dot{W}_{hyd}}{\eta} - \dot{W}_{hyd}}{\rho\omega^3 D^5} = \frac{(1-\eta)}{\eta}\phi\psi \tag{5.12}$$

Second, the rate of dissipation along the path followed by the fluid can be obtained from the Guoy-Stokes theorem of dissipation, which in dimensionless form means:

$$\bar{\epsilon}_{\text{hyd}} = \frac{\Delta P_L Q}{\rho\omega^3 D^5} = \frac{Q}{\omega D^3}\frac{\Delta P_{\text{Euler}} - \Delta P}{\rho\omega^2 D^2} = (\psi_{\text{Euler}} - \psi)\phi \tag{5.13}$$

where:

$$\psi_{\text{Euler}} = \frac{1}{4} - \frac{D\cot\beta_2}{2\pi b_2}\phi \tag{5.14}$$

The difference between both definitions derives from the energy balance for the fluid inside the pump, considered to behave adiabatically. Neglecting mechanical losses, this balance can be written as:

$$\dot{W}_{\text{shaft}} = \dot{W}_{\text{hyd}} + \Delta P_L Q + \dot{W}_{\text{disk}}$$

Rearranging and using the equations above, we have:

$$\dot{W}_{\text{shaft}} - \dot{W}_{\text{hyd}} > \Delta P_L Q \quad \rightarrow \quad \underbrace{\frac{\dot{W}_{\text{shaft}} - \dot{W}_{\text{hyd}}}{\rho\omega^3 D^5}}_{\bar{\epsilon}} > \underbrace{\frac{\Delta P_L Q}{\rho\omega^3 D^5}}_{\bar{\epsilon}_{\text{hyd}}} \tag{5.15}$$

Thus, $\bar{\epsilon} > \bar{\epsilon}_{\text{hyd}}$. Using Equation 5.12, the average energy dissipation rate ($\bar{\epsilon}$) can be determined, which is influenced by the turbulent kinetic energy dissipation rate ($\bar{\epsilon}_k$).

$$\bar{\epsilon}_{\text{hyd}} = \left(\frac{1}{4} - \frac{D\cot\beta_2}{2\pi b_2}\phi - \psi\right)\phi \tag{5.16}$$

The hydraulic dissipation can be further expanded using Equation 2.34:

$$\begin{aligned}\bar{\epsilon}_{\text{hyd}} = \Bigg\{ \left(\frac{1}{4} - k_1\phi\right) - \left[\frac{1}{4} - k_4 + \left(-k_1 - \frac{k_2}{\text{Re}_\omega} + 2k_4k_5\right)\phi\right] \\ - \left[\left(\frac{1}{\phi\,\text{Re}_\omega}\right)^n k_3 + k_4k_5^2 + k_6\right]\phi^2\Bigg\}\phi\end{aligned} \tag{5.17}$$

$$= k_4\phi + \left(\frac{k_2}{\text{Re}_\omega} - 2k_4k_5\right)\phi^2 + \left[\left(\frac{1}{\phi\,\text{Re}_\omega}\right)^n k_3 + k_4k_5^2 + k_6\right]\phi^3 \tag{5.18}$$

The above expression can be rewritten as a sum of viscous (v) and inertial (i) contributions as follows:

$$\bar{\epsilon}_{\text{hyd}} = \underbrace{\frac{k_2\phi^2}{\text{Re}_\omega} + \frac{k_3\phi^{3-n}}{\text{Re}_\omega^n}}_{\bar{\epsilon}_{\text{hyd},v}} + \underbrace{k_4\phi(1-k_5\phi)^2 + k_6\phi^3}_{\bar{\epsilon}_{\text{hyd},i}} \tag{5.19}$$

For $n > 0$, the viscous contribution tends to zero as $\text{Re}_\omega \to \infty$, as expected. Notice that, due to their definitions, $\bar{\epsilon}_{\text{hyd}}$ must be lower than $\bar{\epsilon}$.

Figure 5.7 illustrates the variation of the average energy dissipation rate ($\bar{\epsilon}$) and its hydraulic components as a function of ϕ for the P47 pump operating at 3500 rpm with $f_d = 34\%$. As observed, $\bar{\epsilon}$ exhibits a non-monotonic behavior along the performance curve. At flow rates below the Best Efficiency Point (BEP), $\bar{\epsilon}$ decreases with increasing ϕ, reaching a minimum near the BEP. This reduction is associated with the attenuation of recirculation zones and shear layers that dominate at lower flow regimes. Beyond the BEP, $\bar{\epsilon}$ increases again as higher flow rates intensify turbulence and enhance viscous dissipation within the pump passages.

The hydraulic dissipation rate ($\bar{\epsilon}_{\text{hyd}}$) exhibits a increasing trend but consistently remains below $\bar{\epsilon}$, as expected from its definition. The inertial component ($\bar{\epsilon}_{\text{hyd},i}$) contributes significantly to the total hydraulic dissipation at moderate to high flow rates, reflecting the growing importance of inertial effects. In contrast, the viscous component ($\bar{\epsilon}_{\text{hyd},v}$) remains relatively small across the entire range of ϕ, gradually increasing with flow rate but diminishing in relative importance due to the high Reynolds number, which suppresses viscous effects.

This decomposition highlights the distinct physical mechanisms contributing to energy dissipation and reinforces the relevance of separating viscous and inertial contributions when analyzing pump performance and internal flow dynamics.

As a result, the characteristic diameter d_{95} reaches its maximum value at the BEP, a trend that has been experimentally observed under various operating conditions, as shown in Figure 5.8a. In Figure 5.8b we can observe the effect of increasing (f_d) on ($\bar{\epsilon}$) which increases as well due to higher emulsion effective viscosity, leading to higher viscous losses on the pump.

On the other hand, the effect of the dispersed phase fraction (f_d) on d_{95} is governed by two opposing phenomena. The shear and turbulence generated by the ESP promote intense droplet breakage. However, as f_d increases, the droplet volume also tends to increase. This results in a higher droplet density and an increase in the emulsion's effective viscosity, particularly below the phase inversion point. Consequently, the impact of increasing f_d is substantially

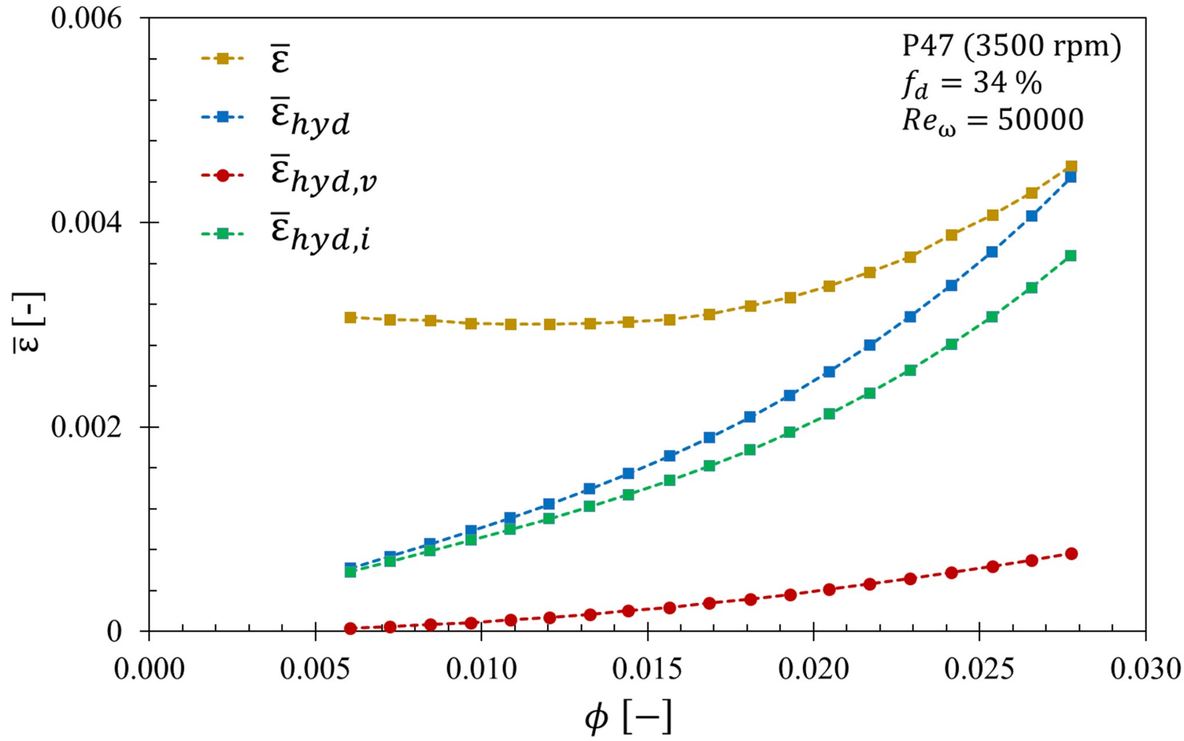

Figure 5.7 – Comparison of how $\bar{\epsilon}$, $\bar{\epsilon}_{\mathrm{hyd}}$, $\bar{\epsilon}_{\mathrm{hyd},v}$ and $\bar{\epsilon}_{\mathrm{hyd},i}$ variates with ϕ on P47 test.

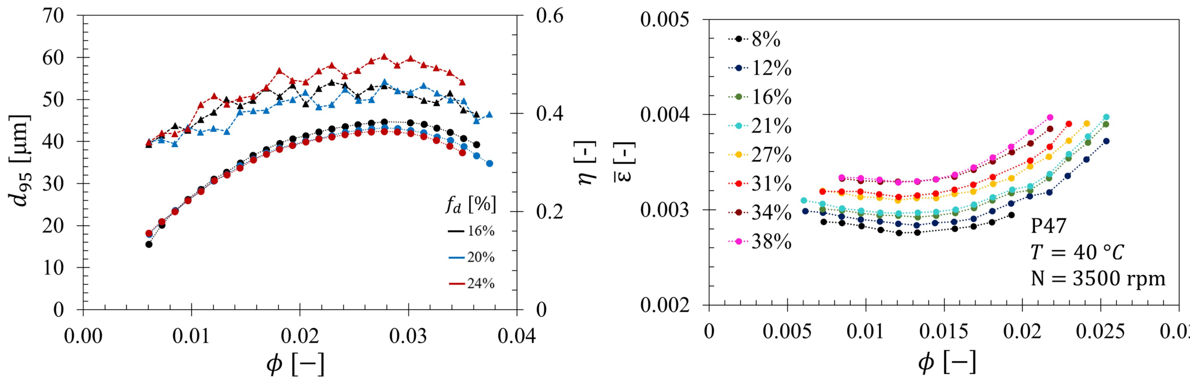

Figure 5.8 – (a) Comparison of measured maximum stable droplet diameter (d_{95}, ▲) and pump efficiency (η, •) during P100L tests ($N = 3500$ rpm; $T = 40$°C). (b) Variation of $\bar{\epsilon}$ with f_d and ϕ during P47 tests.

offset by the droplet breakage occurring within the ESP.

In light of this, we propose a model that incorporates the effects of dispersed phase fraction by maintaining the influences of energy dissipation, flow rate (Perissinotto *et al.*, 2020), and the rotational Weber number (We_ω), which balances cohesive and disruptive forces:

$$\frac{d_{95}}{D} = h_1 \left(\phi \sqrt[3]{f_d}\right)^{\frac{1}{8}} We_\omega^{-\frac{3}{5}} \bar{\epsilon}^{-\frac{2}{5}}, \tag{5.20}$$

where h_1 represents an empirical constant, and $\bar{\epsilon}$ denotes the energy dissipation rate. Although incorporating specific speed (N_s) significantly improved the proposed model for d_{32}, a similar enhancement was not observed in this context. This may be attributed to the fact that $\bar{\epsilon}$ already encompasses the influence of the ESP design. A similar rationale applies to the emulsion's effective viscosity, as it is implicitly considered within $\bar{\epsilon}$, increasing with f_d prior to phase inversion which can be explained by the viscous dissipation.

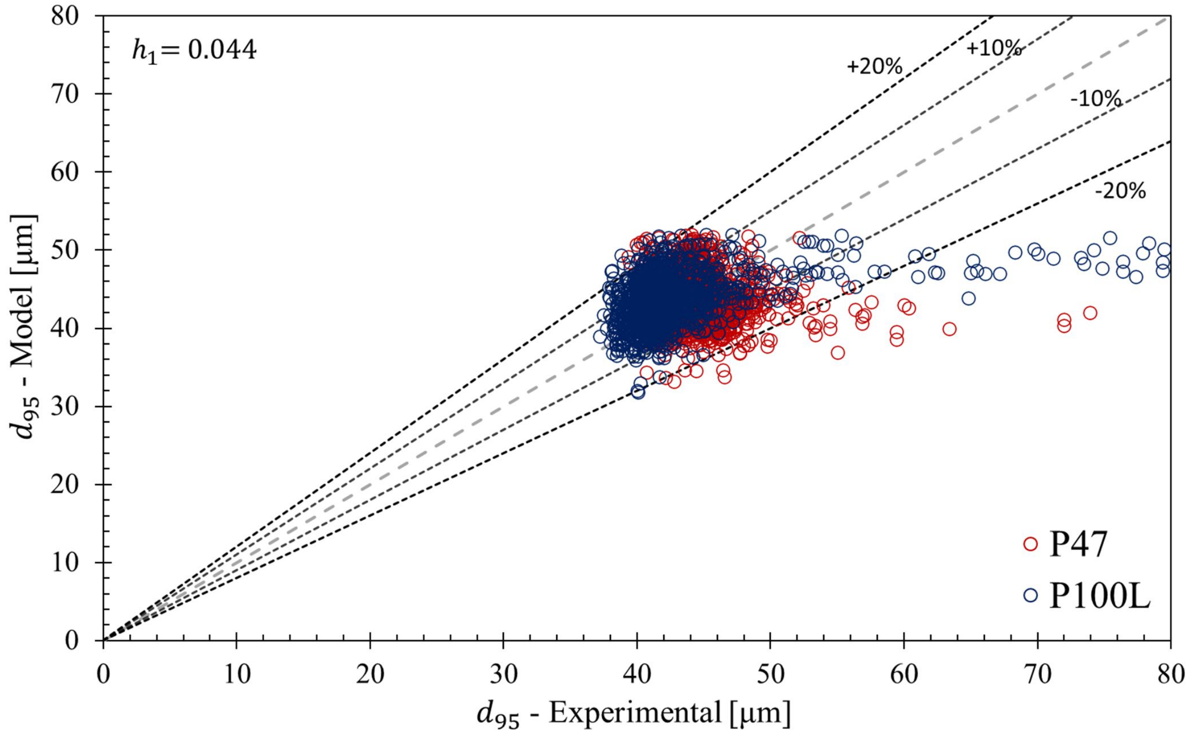

Figure 5.9 – Comparison of experimental and predicted maximum stable droplet diameter (d_{95}) based on the proposed model.

It is worth noting that the models discussed earlier in Section 2 rely on estimating the critical Weber number (We_{crit}). However, the correlations available in the literature are primarily tailored to liquid-liquid flows in tubes, which do not adequately capture the complex dynamics of emulsion flow in ESPs.

To overcome this limitation, the proposed model incorporates operational parameters specific to ESPs, enabling a more accurate representation and prediction of the intricate behavior of emulsion flow in these systems. Figure 5.9 demonstrates that the proposed model aligns closely with the experimentally observed d_{95} values.

5.5 Closing Remarks

This chapter presented a comprehensive analysis of droplet size distribution (DSD) in water-oil emulsions flowing through Electrical Submersible Pumps (ESPs), with a focus on the Sauter mean diameter (d_{32}) and the maximum stable droplet diameter (d_{95}). The experimental results and proposed models provide valuable insights into the mechanisms governing droplet breakup and coalescence under varying operational conditions, such as rotational speed, flow rate, temperature, and dispersed phase fraction (f_d). Notably, the study highlights the significant influence of energy dissipation and shear stress on droplet size, particularly near the Best Efficiency Point (BEP), where emulsion stability and phase inversion phenomena are most pronounced.

The proposed semi-empirical models for d_{32} and d_{95} incorporate key dimensionless parameters, including the rotational Weber number (We_ω), specific speed (N_s), and energy dissipation rate ($\bar{\epsilon}$). These models demonstrate improved accuracy in predicting droplet sizes compared to existing correlations, offering a robust framework for understanding and optimizing ESP performance in emulsion flow conditions. Specifically, the models account for the effects of dispersed phase fraction and pump geometry, which are critical factors in real-world applications.

One of the key findings is the relationship between energy dissipation and droplet size near the BEP. As the flow rate approaches the BEP, energy dissipation reaches a minimum, leading to larger droplet sizes. Conversely, at flow rates above or below the BEP, increased turbulence and shear stress promote droplet breakup, resulting in smaller droplets. This behavior is particularly relevant for operators seeking to optimize ESP performance in emulsion-dominated flows, as it provides a clear link between operational conditions and emulsion stability.

For oil and gas operators, the practical implications of these findings are significant. The proposed models can be integrated into ESP design and operational strategies to enhance performance and mitigate issues related to emulsion flow. The models can be validated and fine-tuned using field data from specific oil wells, ensuring their applicability to real-world conditions. This iterative process can further enhance the accuracy and reliability of the predictions, providing operators with a powerful tool for optimizing ESP performance. Also, they can be incorporated into real-time monitoring systems to predict droplet size and emulsion stability based on operational data. This enables proactive adjustments to pump settings, reducing the risk of performance degradation and extending equipment lifespan.

In conclusion, this study advances the understanding of emulsion flow in ESPs and provides practical tools for optimizing pump performance in challenging multiphase flow conditions. The proposed models for d_{32} and d_{95} offer a robust framework for predicting droplet size and emulsion stability, enabling operators to make informed decisions and improve the efficiency and reliability of ESP systems. Future work should focus on extending the models to a wider range of pump geometries and operational scenarios, as well as integrating them into real-time monitoring and control systems for field applications.

6 CONCLUSIONS

This work provided a comprehensive analysis of both droplet dynamics and the performance of Electrical Submersible Pumps (ESPs) operating under various conditions, filling important gaps in the experimental investigation of emulsion flow behavior inside ESPs. The study covered a wide range of operational parameters, including flow rate, temperature, ESP rotational speed, dispersed phase fraction, and two pump geometries (mixed and radial flow designs). By leveraging droplet size distribution (DSD) data collected with a Focused Beam Reflectance Measurement (FBRM) probe, alongside pump performance metrics such as head, efficiency, and power, this work presents a holistic understanding of how emulsions behave in ESPs.

The experimental results on droplet size distributions, particularly the Sauter mean diameter (d_{32}) and the maximum stable droplet diameter (d_{95}), revealed that the dispersed phase fraction (f_d) plays a crucial role in emulsion flow behavior. As the fraction of the dispersed phase increased, the droplet sizes were reduced, and the distributions shifted towards smaller diameters. This trend was especially evident in the pump with mixed flow geometry (P100L), which demonstrated a more intense droplet breakage compared to the radial-flow P47 pump, within the tested range. The increased droplet breakage observed in the P100L was attributed to its higher specific speed (N_S), which promotes stronger shear forces inside the ESP, resulting in smaller droplet sizes even at lower flow rates and dispersed phase fractions.

This droplet breakup phenomenon had a direct influence on the pump hydraulic performance. The reduction in droplet size increased the effective viscosity of the emulsion, especially at higher dispersed phase fractions, leading to a degradation of pump performance. As the dispersed phase fraction increased, the emulsion behaved more like a non-Newtonian fluid, exhibiting increased viscous resistance. This was evidenced by the reduction in both efficiency and head as f_d increased, with the P100L generally maintaining better performance due to its mixed geometry, which is more effective in handling viscous emulsions.

The results from the performance analysis clearly show that the presence of a dispersed phase significantly impacted all key performance metrics (head, efficiency, and power consumption). As viscosity increased, both pumps experienced a noticeable reduction in head and efficiency, accompanied by an increase in shaft power, particularly at higher temperatures and lower rotational Reynolds numbers (Re_ω). When comparing the two pumps, the P100L, with its mixed flow design, proved to be more resilient to performance degradation. Its ability to maintain higher efficiency at lower Re_ω values suggests that this design is better suited for applications involving emulsions with higher dispersed phase fractions. In contrast, the correction coefficients for head (C_H^{BEP}), flow rate (C_Q^{BEP}), and efficiency (C_η^{BEP}) helped quantify the performance degradation in both pumps when handling viscous fluids. The correction coefficients followed an exponential decay pattern as viscosity increased, reflecting the increasing dominance of viscous forces in degrading pump performance. The results showed that the P47 generally retained better head compared to the P100L, which was less impacted by high viscosities. The efficiency degradation was significant in both pumps, but the P100L showed a relatively higher retention of efficiency values (C_η^{BEP}) at higher viscosities, suggesting that its design geometry allowed for better handling of emulsions.

One of the key insights from the study is the relationship between droplet size distribution and pump performance. The reduction in droplet size, driven by increased dispersed phase fraction and flow rate, was found to exacerbate performance degradation, particularly in terms of head and efficiency. As smaller droplets were generated, the effective viscosity of the emulsion increased, leading to higher internal friction and energy losses within the pump. This effect was especially noticeable in the P100L, where the mixed flow configuration led to a greater increase in viscosity at high dispersed phase fractions. However, it is possibly due to the less shear imposed when compared to the radial flow design from P47. The increased shear-thinning effect was able to reduce more the effective viscosity even at lower flow rates. Also, P100L experienced very high viscosity values at low flow rates, indicating that the shear was not sufficient high to reduce the viscosity and the formation of recirculation and secondary flows inside the impeller disrupted the emulsion structure and this reflects into some oscillations in the relative viscosity results.

The proposed models for predicting the Sauter mean diameter (d_{32}) and maximum stable droplet diameter (d_{95}) based on the experimental data showed good agreement with the experimental results. These models successfully captured the combined influence of dispersed phase fraction, dimensionless flow rate, and ESP geometry on droplet size, providing a valuable tool for future analyses. The incorporation of specific speed (N_s) and energy dissipation rate ($\bar{\epsilon}$) into the models allowed for a more accurate prediction of droplet behavior, particularly under conditions of high viscous degradation.

It is important to note that since the system operates in a closed-loop flow, the imposed shear history could influence the emulsion properties over time. This aspect may impact the accuracy of results compared to cases where a freshly prepared emulsion is used for each test. Although the potential impact of prolonged recirculation on emulsion stability was not the primary focus of this study, future work could explore methods to quantify such effects, possibly by analyzing pressure variations in the pump or changes in droplet size distribution over time.

The findings of this study have significant implications for oil and gas operators, particularly in optimizing ESP performance under emulsion flow conditions. The proposed models for droplet size (d_{32} and d_{95}) and relative viscosity (μ_{rel}) provide a robust framework for predicting emulsion behavior and pump performance degradation. These models can be integrated into real-time monitoring systems to enable proactive adjustments to pump settings, reducing the risk of performance degradation and extending equipment lifespan. Additionally, the insights into phase inversion and its impact on pump performance can guide operators in managing emulsion stability, particularly in scenarios where water cuts are high or phase inversion is likely to occur. For field applications, adjusting flow rates, rotational speeds, and temperature to minimize viscous losses and maintain stable emulsion flow is recommended. Choosing pump geometries (e.g., mixed-flow vs. radial-flow) based on the expected emulsion properties and operational conditions can also enhance performance. Implementing systems to monitor droplet size, viscosity, and pump performance in real-time allows for dynamic adjustments to maintain optimal operation. Identifying and managing phase inversion points can help avoid sudden performance drops and ensure stable pump operation.

While this study provides valuable insights into emulsion flow behavior in ESPs, several areas warrant further investigation. Expanding the analysis to include a wider range of pump geometries and configurations can refine the applicability of the proposed models. Validating the models using field data from oil wells ensures their accuracy and reliability under real-world conditions. Investigating the long-term effects of shear history on emulsion stability and pump performance, particularly in closed-loop systems, can provide deeper insights into emulsion behavior over time. Developing advanced monitoring techniques, such as inline viscosity sensors or high-speed imaging, can capture real-time changes in emulsion properties and pump performance. Enhancing models to predict phase inversion points more accurately, incorporating additional factors such as surfactant concentration and salinity, can improve operational strategies. Exploring strategies to minimize energy losses and improve pump efficiency under high-viscosity and emulsion flow conditions can further optimize ESP performance.

In summary, this work advances the understanding of emulsion flow in ESPs and provides practical tools for optimizing pump performance in challenging multiphase flow conditions. The proposed models for droplet size and performance correction coefficients offer a robust framework for further research and practical applications, enabling better prediction and optimization of ESP performance in challenging operating conditions. By integrating these findings into operational strategies, oil and gas operators can enhance the efficiency, reliability, and longevity of ESP systems in emulsion-dominated environments.

BIBLIOGRAPHY

Abubakar, A.; Al-Wahaibi, T.; Al-Hashmi, A. R.; Al-Wahaibi, Y.; Al-Ajmi, A.; Eshrati, M. Empirical correlation for predicting pressure gradients of oil-water flow with drag-reducing polymer. **Experimental Thermal and Fluid Science**, v. 79, p. 275–282, 2016.

Achour, L.; Specklin, M.; Asuaje, M.; Kouidri, S.; Belaidi, I. A review of emulsion flows, their characterization and their modeling in pumps. **Chemical Engineering Research and Design**, 2024.

Amaral, G. D. Modelagem do escoamento monofásico em bomba centrífuga submersa operando com fluidos viscosos. **Campinas: Faculdade de Engenharia Mecânica, Universidade Estadual de Campinas**, 2007.

Angeli, P.; Hewitt, G. Pressure gradient in horizontal liquid–liquid flows. **International journal of multiphase flow**, v. 24, n. 7, p. 1183–1203, 1999.

Aziz, K.; Govier, G. W. Pressure drop in wells producing oil and gas. **Journal of Canadian Petroleum Technology**, v. 11, n. 03, 1972.

Banjar, H.; Zhang, H.-Q. Experiments and emulsion rheology modeling in an electric submersible pump. In: IPTC. **International Petroleum Technology Conference**. [S.l.], 2019. p. D011S007R005.

Barnea, D.; Shoham, O.; Taitel, Y. Flow pattern transition for downward inclined two phase flow; horizontal to vertical. **Chemical Engineering Science**, v. 37, n. 5, p. 735–740, 1982.

Barnes, H. A. Rheology of emulsions—a review. **Colloids and surfaces A: physicochemical and engineering aspects**, v. 91, p. 89–95, 1994.

Barrios, L.; Rojas, M.; Monteiro, G.; Sleight, N. Brazil field experience of esp performance with viscous emulsions and high gas using multi-vane pump mvp and high power esps. In: SPE. **SPE Gulf Coast Section Electric Submersible Pumps Symposium?** [S.l.], 2017. p. D021S002R002.

Bellary, S. A.; Siddique, M. H.; Samad, A.; Sangwai, J. S.; Chon, B. Effects of crude oil-water emulsions at various water-cut on the performance of the centrifugal pump. **International Journal of Oil, Gas and Coal Technology**, v. 16, n. 1, p. 71–88, 2017.

Besagni, G.; Inzoli, F. The effect of electrolyte concentration on counter-current gas–liquid bubble column fluid dynamics: Gas holdup, flow regime transition and bubble size distributions. **Chemical Engineering Research and Design**, v. 118, p. 170–193, 2017.

Biazussi, J. L. **Modelo de deslizamento para escoamento gás-líquido em bomba centrífuga submersa operando com líquido de baixa viscosidade**. Tese (Doutorado) — [sn], 2014.

Boxall, J. A.; Koh, C. A.; Sloan, E. D.; Sum, A. K.; Wu, D. T. Droplet size scaling of water-in-oil emulsions under turbulent flow. **Langmuir**, v. 28, n. 1, p. 104–110, 2012.

Brauner, N. Liquid-liquid two-phase flow systems. In: **Modelling and Experimentation in Two-Phase Flow**. [S.l.]: Springer, 2003. p. 221–279.

Brinkman, H. C. The viscosity of concentrated suspensions and solutions. **The Journal of Chemical Physics**, v. 20, n. 4, p. 571, 1952.

Bulgarelli, N. A. V. **Experimental Study of Electrical Submersible Pump (ESP) Operating with Water/Oil Emulsion**. 133 p. Dissertação (M.Sc. Thesis) — University of Campinas, Campinas, Brazil, 2018.

Bulgarelli, N. A. V.; Biazussi, J. L.; Monte Verde, W.; Castro, M. S. d.; Bannwart, A. C. Experimental study of phase inversion phenomena in electrical submersible pumps under oil/water flow. **Journal of Offshore Mechanics and Arctic Engineering**, v. 142, n. 4, p. 041402, 2020.

Bulgarelli, N. A. V.; Biazussi, J. L.; Verde, W. M.; Perles, C. E.; Castro, M. S. de; Bannwart, A. C. Experimental investigation on the performance of electrical submersible pump (esp) operating with unstable water/oil emulsions. **Journal of Petroleum Science and Engineering**, v. 197, p. 107900, 2021.

Bulgarelli, N. A. V.; Biazussi, J. L.; Verde, W. M.; Perles, C. E.; Castro, M. S. de; Bannwart, A. C. Relative viscosity model for oil/water stable emulsion flow within electrical submersible pumps. **Chemical Engineering Science**, v. 245, p. 116827, 2021.

Bulgarelli, N. A. V.; Biazussi, J. L.; Verde, W. M.; Perles, C. E.; Castro, M. S. de; Bannwart, A. C. Experimental investigation of the electrical submersible pump's energy consumption under unstable and stable oil/water emulsions: A catastrophic phase inversion analysis. **Journal of Petroleum Science and Engineering**, v. 216, p. 110814, 2022.

Bulgarelli, N. A. V.; Biazussi, J. L.; Verde, W. M.; Perles, C. E.; Castro, M. S. de; Bannwart, A. C. A novel criterion based on slip ratio to assess the flow behavior of w/o emulsions within centrifugal pumps. **Chemical Engineering Science**, v. 247, p. 117050, 2022.

Calabrese, R. V.; Chang, T. P. K.; Dang, P. T. Drop breakup in turbulent stirred-tank contactors. part i: Effect of dispersed-phase viscosity. **AIChE Journal**, v. 32, n. 4, p. 657–666, 1986.

Castellanos, M. B.; Carvalho, F. d. C. T.; Biazussi, J. L.; Serpa, A. L. Phase inversion identification in electrical submersible pumps using mechanical vibrations. **Flow Measurement and Instrumentation**, v. 93, p. 102419, 2023.

Croce, D.; Pereyra, E. Study of oil/water flow and emulsion formation in electrical submersible pumps. **SPE Production & Operations**, v. 35, n. 01, p. 026–036, 2020.

Dabirian, R. *et al.* Evaluation of models for droplet shear effect of centrifugal pump. In: **Fluids Engineering Division Summer Meeting**. [S.l.]: American Society of Mechanical Engineers, 2018. v. 51555.

Davies, J. T. Drop sizes of emulsions related to turbulent energy dissipation rates. **Chemical Engineering Science**, v. 40, n. 5, p. 839–842, 1985.

Derkach, S. R. Rheology of emulsions. **Advances in colloid and interface science**, v. 151, n. 1-2, p. 1–23, 2009.

Dudek, M.; Fernandes, D.; Herø, E. H.; Øye, G. Microfluidic method for determining drop-drop coalescence and contact times in flow. **Colloids and Surfaces A: Physicochemical and Engineering Aspects**, v. 586, p. 124265, 2020.

Einstein, A. Eine neue bestimmung derxolehw-diamensionen; von. **Ann. Phys**, v. 324, p. 289–306, 1906.

Estrada, C. P. **Estudo experimental do desempenho de bomba centrífuga submersa operando com óleo ultraviscoso**. Tese (Doutorado) — [sn], 2019.

Fox, R. W.; McDonald, A. T.; Pritchard, P. J. **Introdução à Mecânica dos Fluidos**. 8. ed. Rio de Janeiro, Brasil: LTC, 2011. ISBN 9788521614685.

Franke, S. L. **Fluid Machinery: Performance, Analysis, and Design**. 1st. ed. [S.l.]: John Wiley & Sons, 2002.

García, F.; García, R.; Padrino, J. C.; Mata, C.; Trallero, J. L.; Joseph, D. D. Power law and composite power law friction factor correlations for laminar and turbulent gas–liquid flow in horizontal pipelines. **International Journal of Multiphase Flow**, v. 29, n. 10, p. 1605–1624, 2003.

Genovese, D. B. Shear rheology of hard-sphere, dispersed, and aggregated suspensions, and filler-matrix composites. **Advances in colloid and interface science**, v. 171, p. 1–16, 2012.

Greaves, D.; Boxall, J.; Mulligan, J.; Montesi, A.; Creek, J.; Sloan, E. D.; Koh, C. A. Measuring the particle size of a known distribution using the focused beam reflectance measurement technique. **Chemical Engineering Science**, v. 63, n. 22, p. 5410–5419, 2008.

Groothuis, H.; Zuiderweg, F. Influence of mass transfer on coalescence of drops. **Chemical Engineering Science**, v. 12, n. 4, p. 288–289, 1960.

Gülich, J. Pumping highly viscous fluids with centrifugal pumps—part 2. **World pumps**, v. 1999, n. 396, p. 39–42, 1999.

Gülich, J. F. **Operation of centrifugal pumps**. [S.l.]: Springer, 2008.

Guo, K.; Li, H.; Yu, Z. In-situ heavy and extra-heavy oil recovery: A review. **Fuel**, v. 185, p. 886–902, 2016.

Herø, E. H.; La Forgia, N.; Solsvik, J.; Jakobsen, H. A. Single drop breakage in turbulent flow: Statistical data analysis. **Chemical Engineering Science: X**, v. 8, p. 100082, 2020.

Hinze, J. O. Fundamentals of the hydrodynamic mechanism of splitting in dispersion processes. **AIChE Journal**, v. 1, n. 3, p. 289–295, 1955.

Husin, H.; Hussain, H. H. Temperature effect on shear thinning behavior of low-viscous oilfield emulsion. In: **Science and Technology Behind Nanoemulsions**. [S.l.]: IntechOpen, 2018.

Ibrahim, S. Y.; Maloka, I. E. Emulsification of secondary oil/water dispersions using a centrifugal pump. **Petroleum Science and Technology**, v. 24, n. 5, p. 513–522, 2006.

Khalil, M.; Kassab, S.; Ismail, A.; Elazab, I. Influence of various parameters on the characteristics of stable and unstable oil-in-water emulsion. In: **8th International Conference of Fluid Dynamics and Propulsion. In Proceedings of the ASME 8th International Conference of Fluid Dynamics and Propulsion**. [S.l.: s.n.], 2006. p. 14–17.

Khalil, M.; Kassab, S.; Ismail, A.; Elazab, I. Centrifugal pump performance under stable and unstable oil-water emulsions flow. In: **Twelfth International Water Technology Conference**. [S.l.: s.n.], 2008. p. 687–702.

Kindermann, E. **Estudo Experimental e Modelagem Empírica do Desempenho de Bombas Centrífugas Submersas (BCSs) Operando com Fluidos Viscosos**. Tese (Doutorado) — [sn], 2022.

Kolmogorov, A. N. Energy dissipation in locally isotropic turbulence. **Dokl. Akad. Nauk SSSR**, v. 32, p. 19–21, 1941.

Lemenand, T.; Della Valle, D.; Zellouf, Y.; Peerhossaini, H. Droplets formation in turbulent mixing of two immiscible fluids in a new type of static mixer. **International Journal of Multiphase Flow**, v. 29, n. 5, p. 813–840, 2003.

Liu, B.; Manica, R.; Liu, Q.; Klaseboer, E.; Xu, Z.; Xie, G. Coalescence of bubbles with mobile interfaces in water. **Physical review letters**, v. 122, n. 19, p. 194501, 2019.

Luhning, R. Sawistowski, 11.," phase inversion in stirred liquid-liquid systems," solvent extraction proceedings international solvent extraction conference, edited by ja gregory, soc. **Chem. Ind., London**, p. 873, 1971.

Maffi, J. M.; Meira, G. R.; Estenoz, D. A. Mechanisms and conditions that affect phase inversion processes: A review. **The Canadian Journal of Chemical Engineering**, v. 99, n. 1, p. 178–208, 2021.

Moffat, R. J. Describing the uncertainties in experimental results. **Experimental Thermal and Fluid Science**, v. 1, n. 1, p. 3–17, 1988.

Mooney, M. The viscosity of a concentrated suspension of spherical particles. **Journal of Colloid Science**, v. 6, n. 2, p. 162–170, 1951.

Morales, R.; Pereyra, E.; Wang, S.; Shoham, O. Droplet formation through centrifugal pumps for oil-in-water dispersions. **Spe Journal**, v. 18, n. 01, p. 172–178, 2013.

Muhaimin, M.; Chaerunisaa, A. Y.; Bodmeier, R. Real-time particle size analysis using focused beam reflectance measurement as a process analytical technology tool for continuous microencapsulation process. **Scientific Reports**, v. 11, n. 1, p. 19390, 2021.

Ofuchi, E.; Cubas, J.; Stel, H.; Dunaiski, R.; Vieira, T.; Morales, R. A new model to predict the head degradation of centrifugal pumps handling highly viscous flows. **Journal of Petroleum Science and Engineering**, v. 187, p. 106737, 2020.

Ofuchi, E. M. *et al.* **Desenvolvimento de um método para correção de curvas de desempenho em bombas centrífugas submersas operando com fluidos viscosos**. Dissertação (Mestrado) — Universidade Tecnológica Federal do Paraná, 2015.

Oshinowo, L. M.; Vilagines, R. D. Modeling of oil–water separation efficiency in three-phase separators: Effect of emulsion rheology and droplet size distribution. **Chemical engineering research and design**, v. 159, p. 278–290, 2020.

Padron, G. A. **Effect of surfactants on drop size distributions in a batch, rotor-stator mixer**. Tese (Doutorado), 2004.

Pal, R.; Rhodes, E. Viscosity/concentration relationships for emulsions. **Journal of Rheology**, v. 33, n. 7, p. 1021–1045, 1989.

Patil, A.; Morrison, G.; Delgado, A.; Casillas, H. Centrifugal pump head prediction using affinity laws modified for viscosity. In: SPE. **SPE Artificial Lift Conference and Exhibition-Americas?** [S.l.], 2018. p. D021S007R001.

Pereyra, E. J. **Modeling of integrated compact multiphase separation system (CMSS®)**. Tese (Doutorado) — The University of Tulsa, 2011.

Perissinotto, R. M.; Monte Verde, W.; Biazussi, J. L.; Castro, M. S. de; Carlos Bannwart, A. Experimental analysis on the velocity of oil drops in oil–water two-phase flows in electrical submersible pump impellers. **Journal of offshore mechanics and arctic engineering**, v. 141, n. 4, p. 041301, 2019.

Perissinotto, R. M. *et al.* Experimental analysis on the behavior of water drops dispersed in oil within a centrifugal pump impeller. **Experimental Thermal and Fluid Science**, v. 112, p. 109969, 2020.

Porcel, C.; Biazussi, J. L.; Monte Verde, W.; Estevam, V.; Bannwart, A. C.; Tavares, A.; Santos, M. P. d. L.; Rocha, P. S. d. Experimental study on the performance of electrical submersible pump operating with ultraviscous oil. **SPE Journal**, v. 27, n. 04, p. 2470–2490, 2022.

Raya, S. A. *et al.* A critical review of development and demulsification mechanisms of crude oil emulsion in the petroleum industry. **Journal of Petroleum Exploration and Production Technology**, v. 10, p. 1711–1728, 2020.

Rondon-Gonzalez, M.; Madariaga, L. F.; Sadtler, V.; Choplin, L.; Marquez, L.; Salager, J.-L. Emulsion catastrophic inversion from abnormal to normal morphology. 6. effect of the phase viscosity on the inversion produced by continuous stirring. **Industrial & engineering chemistry research**, v. 46, n. 11, p. 3595–3601, 2007.

Rønningsen, H. P. Correlations for predicting viscosity of w/o-emulsions based on north sea crude oils. In: SPE. **SPE International Conference on Oilfield Chemistry?** [S.l.], 1995. p. SPE–28968.

Salager, J.-L. Emulsion phase inversion phenomena. **Surfactant science series**, v. 132, p. 185–226, 2006.

Schmitt, P. *et al.* Droplet size distributions of liquid-liquid dispersions in centrifugal pumps. **Chemie Ingenieur Technik**, v. 93, n. 1-2, p. 129–142, 2021.

Shinnar, R. On the behaviour of liquid dispersions in mixing vessels. **Journal of fluid mechanics**, v. 10, n. 2, p. 259–275, 1961.

Simonsen, G.; Pettersen, B.; Kelesoğlu, S.; Sjöblom, J. Preparation and characterization of reference fluid mimicking behavior of north sea heavy crude oil. **Fuel**, v. 135, p. 308–314, 2014.

Smoluchowski, M. Mathematical theory of colloidal coagulation kinetics. **Phys. Z.**, v. 17, 1917.

Solano, E. **Viscous Effects on the Performance of Electro Submersible Pumps (ESP's)**. Dissertação (Master's Thesis) — The University of Tulsa, Oklahoma, USA, 2009. Examines the impact of fluid viscosity on ESP performance, providing experimental and analytical insights.

Stepanoff, A. Elements of graphical solution of water-hammer problems in centrifugal-pump systems. **Transactions of the American Society of Mechanical Engineers**, v. 71, n. 5, p. 515–527, 1949.

Tadros, T. F. Emulsion formation, stability, and rheology. **Emulsion formation and stability**, p. 1–75, 2013.

Takacs, G. **Electrical submersible pumps manual: design, operations, and maintenance**. [S.l.]: Gulf professional publishing, 2017.

Taylor, G. I. The viscosity of a fluid containing small drops of another fluid. **Proceedings of the Royal Society of London. Series A, Containing Papers of a Mathematical and Physical Character**, v. 138, n. 834, p. 41–48, 1932.

The Hydraulic Institute. **Engineering Data Book**. Parsippany, NJ, USA: Hydraulic Institute, 1955. Provides foundational correction factors for centrifugal pump performance under viscous fluid conditions.

Ushikubo, F. Y.; Cunha, R. L. Stability mechanisms of liquid water-in-oil emulsions. **Food Hydrocolloids**, v. 34, p. 145–153, 2014.

Valdés, J. P.; Asuaje, M.; Ratkovich, N. Study of an esp's performance handling liquid-liquid flow and unstable ow emulsions part i: Experimental. **Chemical Engineering Science**, v. 223, p. 115726, 2020.

Monte Verde, W. Modelagem do desempenho de bombas de bcs operando com misturas gás-óleo viscoso. **Campinas: Tese (Doutorado)-Universidade Estadual de Campinas**, 2016.

Vieira, T. S.; Siqueira, J. R.; Bueno, A. D.; Morales, R. E.; Estevam, V. Analytical study of pressure losses and fluid viscosity effects on pump performance during monophase flow inside an esp stage. **Journal of Petroleum Science and Engineering**, v. 127, p. 245–258, 2015.

Vielma, J. **Rheological behavior of oil-water dispersion flow in horizontal pipes**. Tese (Ph.D. Thesis) — University of Tulsa, 2006. 98 p.

White, F. M. **Mecânica dos Fluidos**. 6. ed. Porto Alegre, Brasil: AMGH Editora, 2011. ISBN 9788580550092.

Yeo, L. Y.; Matar, O. K.; Ortiz, E. S. P. de; Hewitt, G. F. Simulation studies of phase inversion in agitated vessels using a monte carlo technique. **Journal of colloid and interface science**, v. 248, n. 2, p. 443–454, 2002.

Zhang, M.; Dabirian, R.; Mohan, R. S.; Shoham, O. Effect of shear and water cut on phase inversion and droplet size distribution in oil–water flow. **Journal of Energy Resources Technology**, v. 141, n. 3, p. 032905, 2019.

Zhu, Q.; Pan, Y.; Jia, X.; Li, J.; Zhang, M.; Yin, L. Review on the stability mechanism and application of water-in-oil emulsions encapsulating various additives. **Comprehensive reviews in food science and food safety**, v. 18, n. 6, p. 1660–1675, 2019.

Zolfaghari, R.; Fakhru'l-Razi, A.; Abdullah, L. C.; Elnashaie, S. S.; Pendashteh, A. Demulsification techniques of water-in-oil and oil-in-water emulsions in petroleum industry. **Separation and Purification Technology**, v. 170, p. 377–407, 2016.

Appendix

APPENDIX A – STATISTICAL TEST RESULTS

The average results of the statistical tests conducted for each pump and dataset of dispersed phase fraction (f_d) are presented for the log-logistic and log-normal functions.

Table A.1 – Comparison of Log-Logistic and Log-Normal distributions

		Log-Logistic			Log-Normal		
ESP	f_d [%]	KS	χ^2	R^2	KS	χ^2	R^2
P100L	12	0.028	0.000	0.929	0.551	0.000	0.923
	16	0.014	0.004	0.853	0.498	0.500	0.855
	20	0.001	0.250	0.861	0.455	0.699	0.864
	24	0.070	0.083	0.957	0.740	0.249	0.947
	28	0.127	0.000	0.970	0.680	0.002	0.958
	32	0.137	0.000	0.968	0.771	0.000	0.956
P47	8	0.000	0.250	0.808	0.524	0.779	0.814
	12	0.000	0.169	0.744	0.764	0.698	0.752
	16	0.000	0.000	0.728	0.753	0.495	0.736
	20	0.001	0.084	0.802	0.789	0.416	0.803
	24	0.007	0.000	0.875	0.733	0.416	0.869
	31	0.056	0.083	0.922	0.689	0.167	0.913
	35	0.187	0.000	0.944	0.687	0.088	0.931

APPENDIX B – EXPERIMENTAL UNCERTAINTY ANALYSIS

To guarantee the reliability of the experimental results presented in this study, an uncertainty analysis was conducted. Initially, the uncertainties associated with the instruments used for measuring the variables were evaluated. Subsequently, the combined uncertainty for derived results was calculated based on these experimental measurements. The methodology described herein follows the approach outlined by Moffat (1988).

Let $f(x, y)$ represent a function of statistically independent variables. The standard uncertainty propagated through this function is expressed as:

$$u_f^2 = \left(\frac{\partial f}{\partial x} u_x\right)^2 + \left(\frac{\partial f}{\partial y} u_y\right)^2 \tag{A.1}$$

where u_x and u_y represent the estimated standard uncertainties of their respective variables. The general expression for estimating the propagation of uncertainty in a function involving multiple independent variables is provided as follows:

$$\delta f = \left[\sum_{i=1}^{n} \left(\frac{\partial f}{\partial y_i} \delta(y_i)\right)^2\right]^{1/2} \tag{A.2}$$

Moreover, when the function representing the phenomenon involves the multiplication of independent variables:

$$f = f(y_1^a, y_2^b, y_3^c, \ldots, y_i^n) \tag{A.3}$$

The propagated uncertainty, as described in the formula above, can be calculated using:

$$\frac{\delta f}{f} = \left[\left(a\frac{\partial y_1}{y_1}\right)^2 + \left(b\frac{\partial y_2}{y_2}\right)^2 + \left(c\frac{\partial y_3}{y_3}\right)^2 + \cdots + \left(n\frac{\partial y_i}{y_i}\right)^2\right]^{1/2} \tag{A.4}$$

Assuming the following:

$$\frac{\delta f}{f} = u_f \tag{A.5}$$

$$\frac{\delta y}{y_i} = u_{y_i} \tag{A.6}$$

Therefore:

$$u_f = \left[(au_{y_1})^2 + (bu_{y_2})^2 + (cu_{y_3})^2 + \cdots + (nu_{y_i})^2\right]^{1/2} \tag{A.7}$$

As previously stated, the combination of uncertainties depends on the relative uncertainties of the instruments utilized in the experimental setup. The values specified by each equipment manufacturer used in the flow loop, along with the combined uncertainties for derived variables, are presented in Table B.1.

Table B.1 – Assessment of relative and combined uncertainties associated with the analyzed variables.

Measured Variables	**Relative Uncertainty (%)**
Emulsion mass flow rate ($\dot{m}_e$)	0.20
Pressure gauge (P)	0.075
Differential pressure gauge ($\overline{\Delta P}$)	0.04
Torque (T_{shaft})	0.20
Impeller diameter (D)	0.05
Density (ρ)	0.05
Temperature (T)	0.20
Viscosity (μ)	0.05
Rotational speed (ω)	0.05
Dispersed phase fraction (f_d)	1.00
FBRM particle count (n_i)	2.50
FBRM particle size (d_i)	2.00
Calculated Variables	**Combined Uncertainty (%)**
Emulsion volumetric flow rate (q_e)	0.20
Dimensionless flow rate (Φ)	0.60
Dimensionless head (Ψ)	0.20
Dimensionless power (Π)	0.40
ESP efficiency (η)	0.70
Brake horsepower ($\overline{\text{BHP}}$)	0.20
Rotational speed (ω)	0.05
Dispersed phase fraction (f_d)	1.00
ESP Relative Viscosity (μ_r)	5.23
Pipe Relative Viscosity (μ_r)	3.63
Sauter mean diameter (d_{32})	6.50
Maximum stable droplet diameter (d_{95})	3.20

Annex

ANNEX A – ESP PERFORMANCE GRAPHS

A.1 Pure Oil - Efficiency

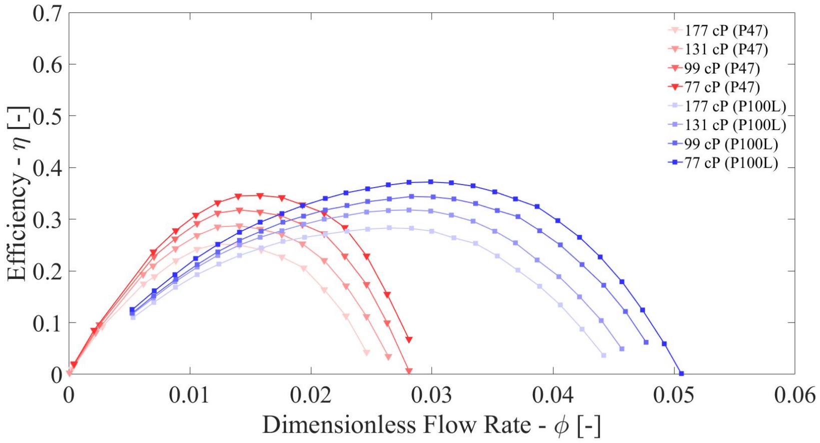

Figure A.1 – P47 Efficiency with oil single-phase flow at 2400 rpm.

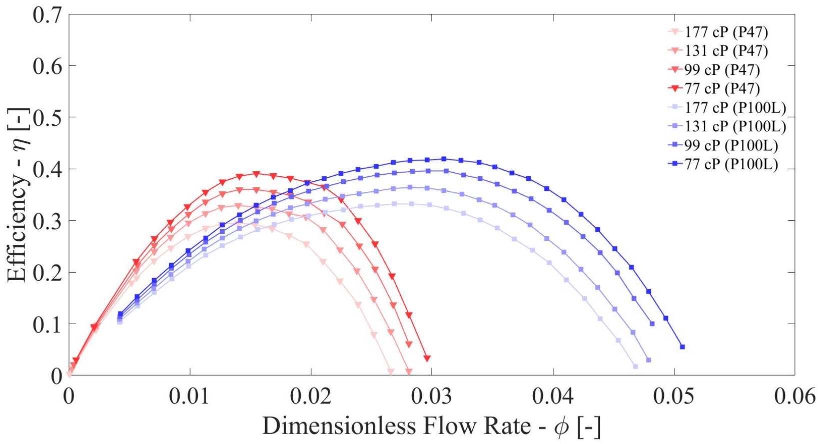

Figure A.2 – P47 Efficiency with oil single-phase flow at 3000 rpm.

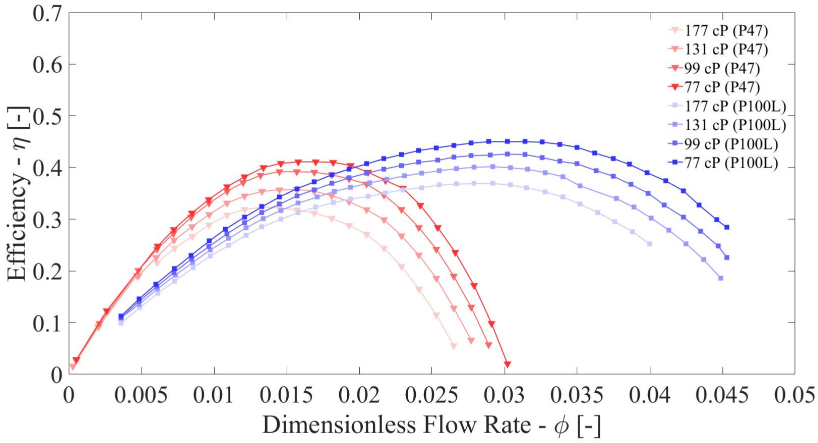

Figure A.3 – P47 Efficiency with oil single-phase flow at 3500 rpm.

A.2 Pure Oil - Head

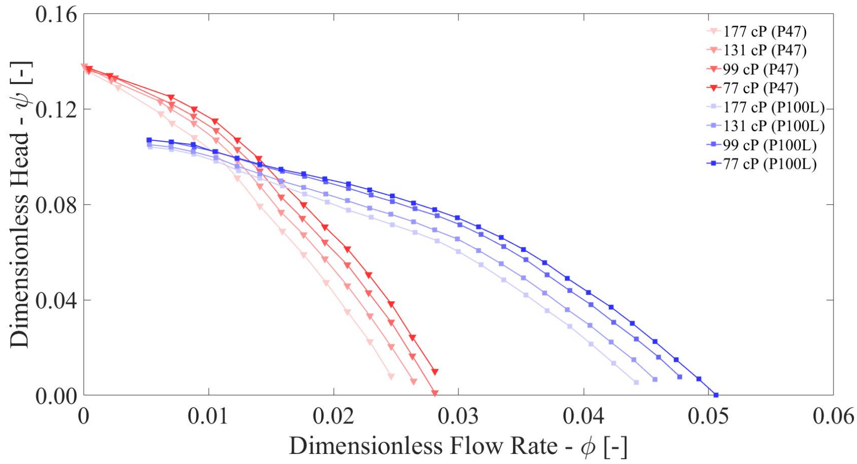

Figure A.4 – P47 Head with oil single-phase flow at 2400 rpm.

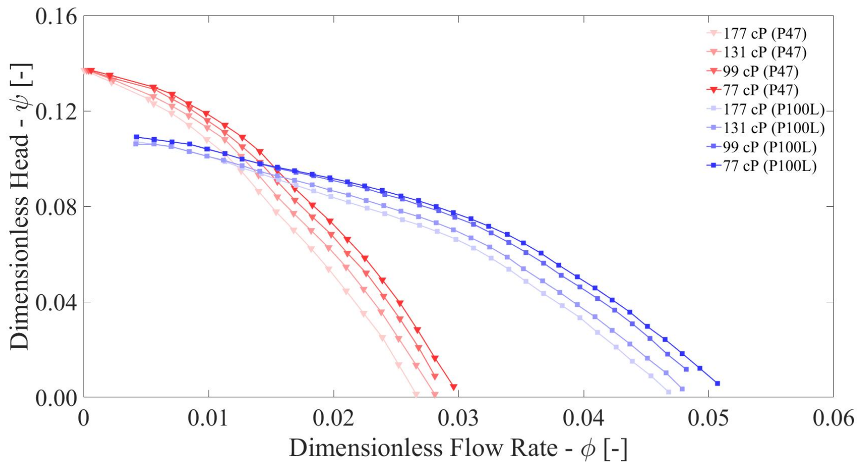

Figure A.5 – P47 Head with oil single-phase flow at 3000 rpm.

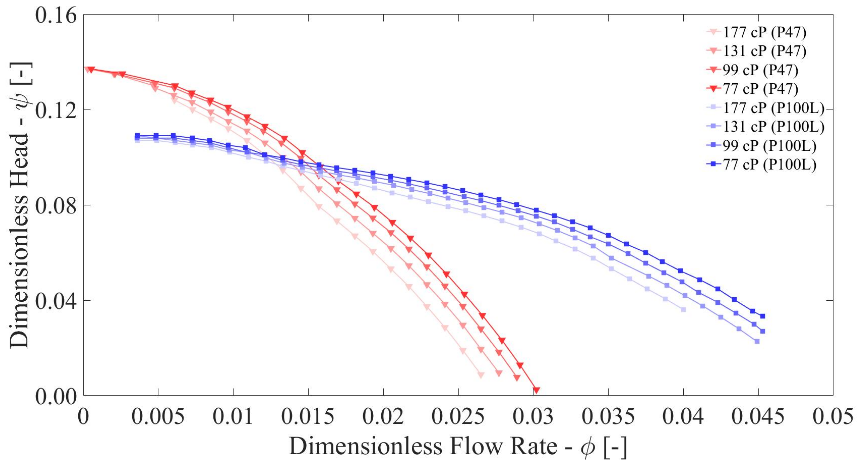

Figure A.6 – P47 Head with oil single-phase flow at 3500 rpm.

A.3 Pure Oil - Power

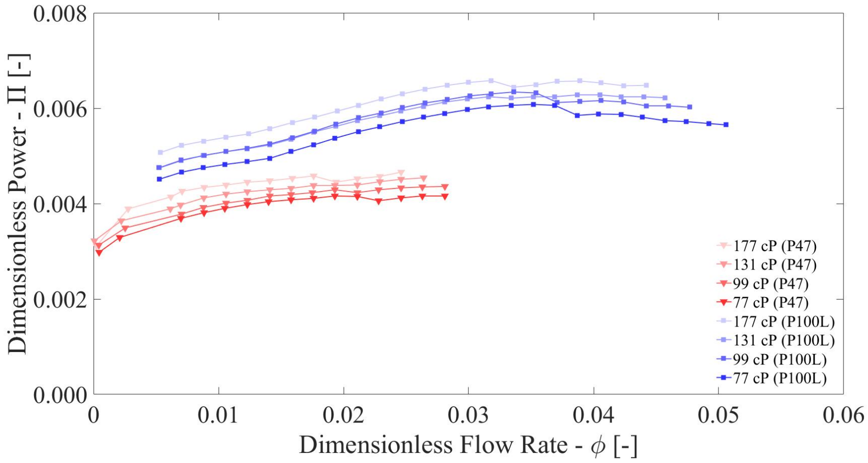

Figure A.7 – P47 Power with oil single-phase flow at 2400 rpm.

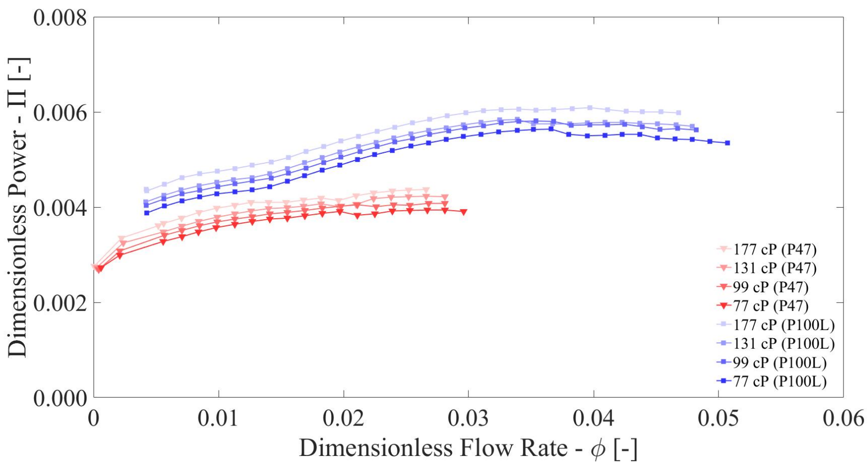

Figure A.8 – P47 Power with oil single-phase flow at 3000 rpm.

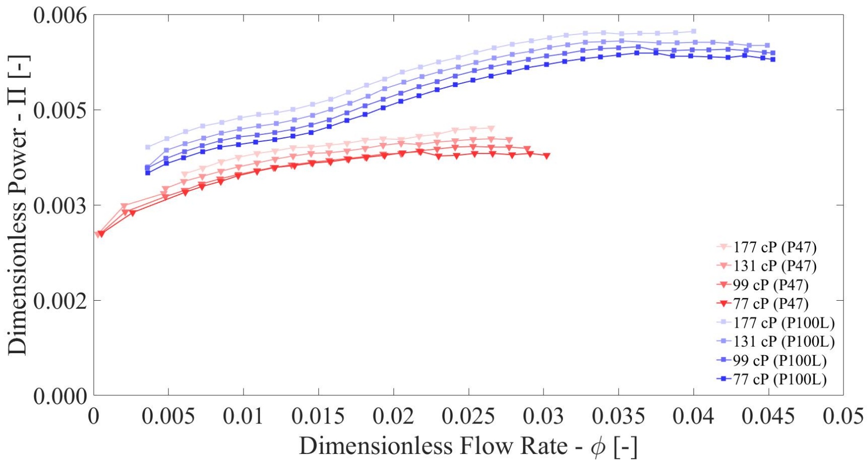

Figure A.9 – P47 Power with oil single-phase flow at 3500 rpm.

A.4 Water-Oil Emulsion - Efficiency

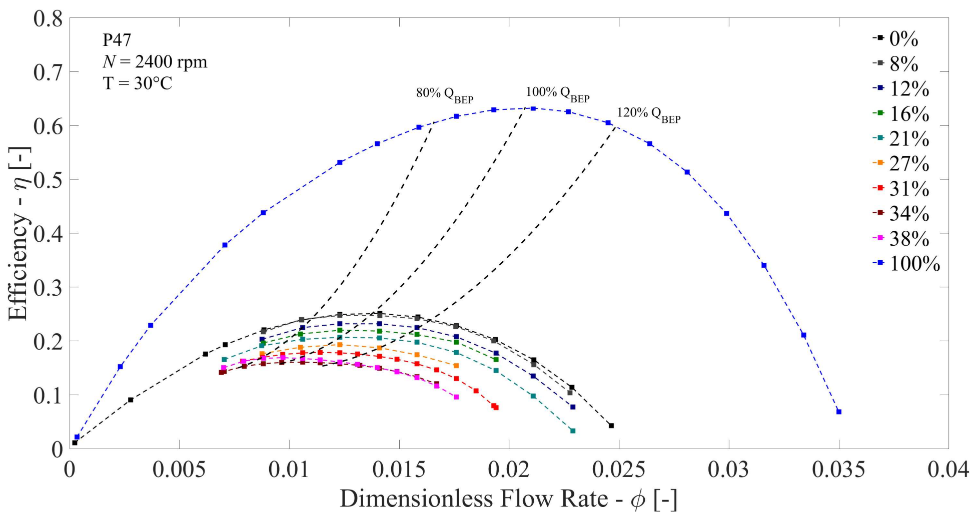

Figure A.10 – P47 Efficiency at 2400 rpm, 30°C.

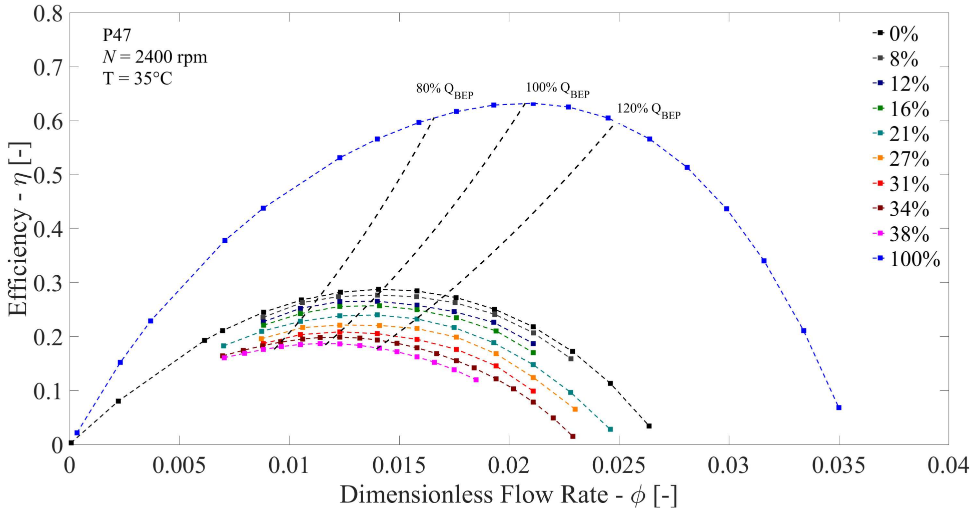

Figure A.11 – P47 Efficiency at 2400 rpm, 35°C.

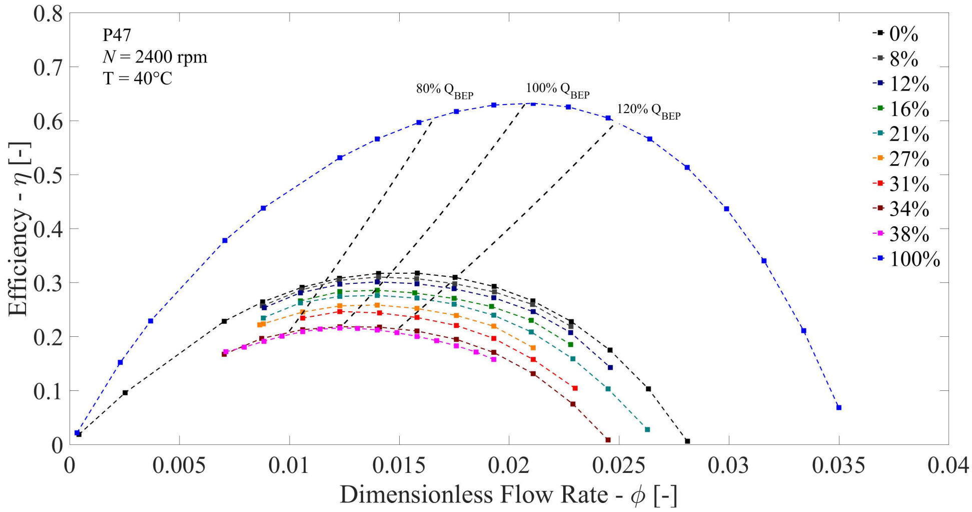

Figure A.12 – P47 Efficiency at 2400 rpm, 40°C.

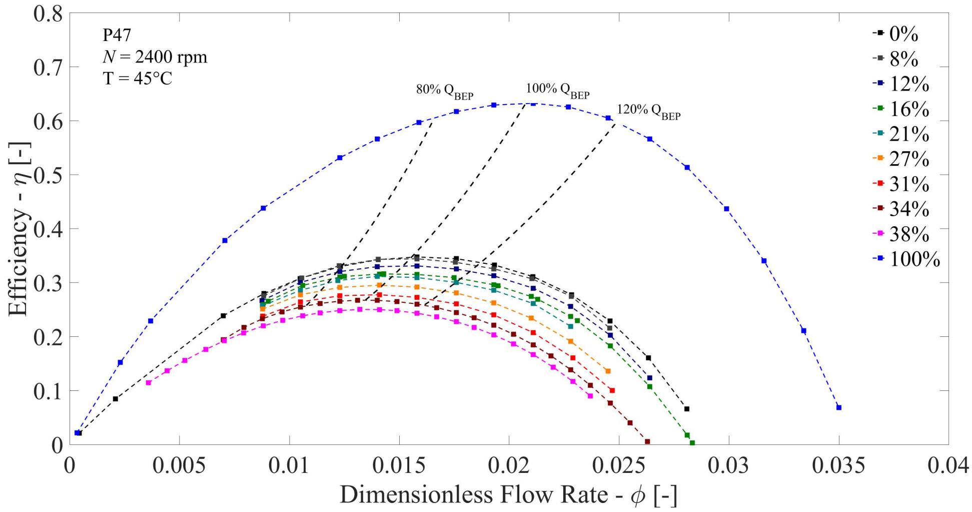

Figure A.13 – P47 Efficiency at 2400 rpm, 45°C.

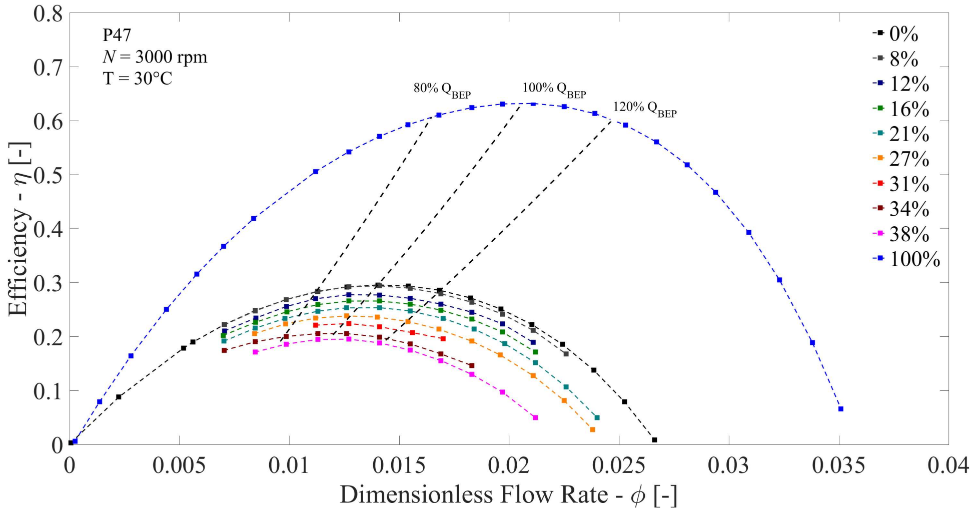

Figure A.14 – P47 Efficiency at 3000 rpm, 30°C.

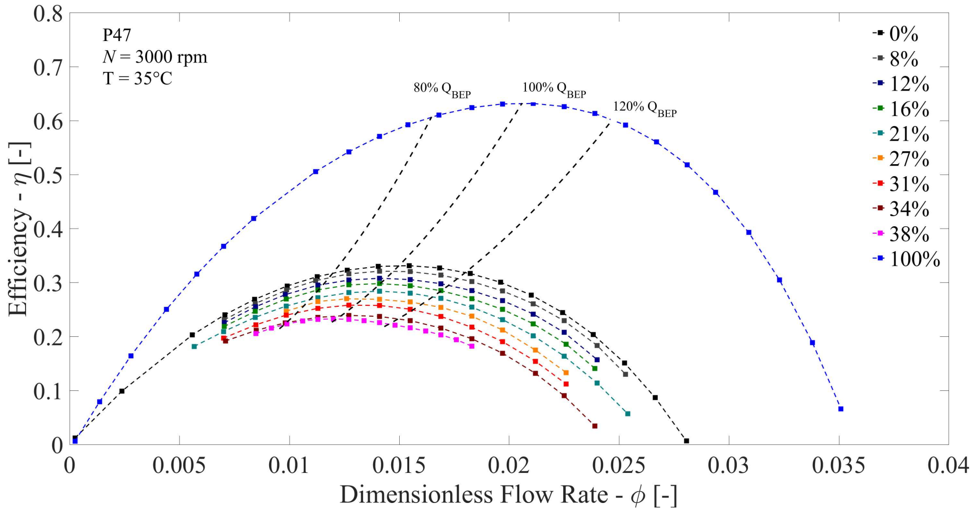

Figure A.15 – P47 Efficiency at 3000 rpm, 35°C.

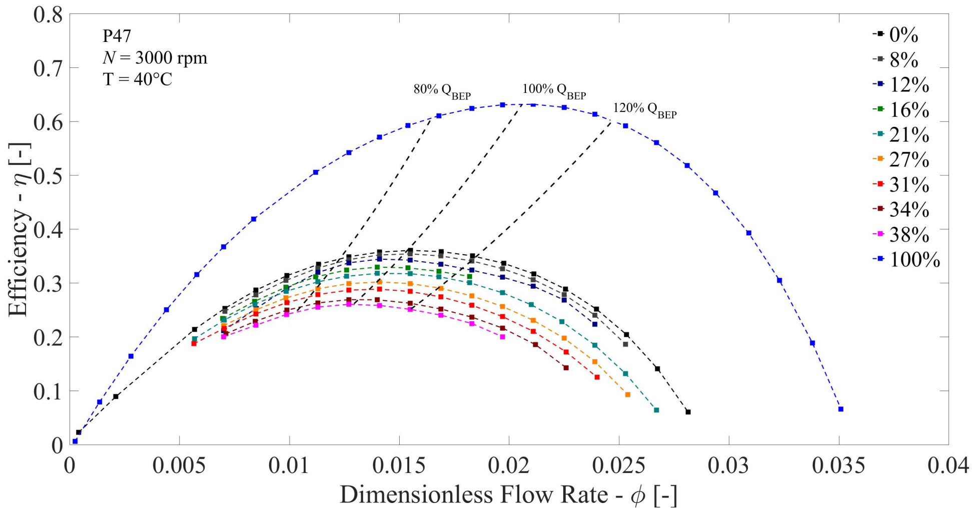

Figure A.16 – P47 Efficiency at 3000 rpm, 40°C.

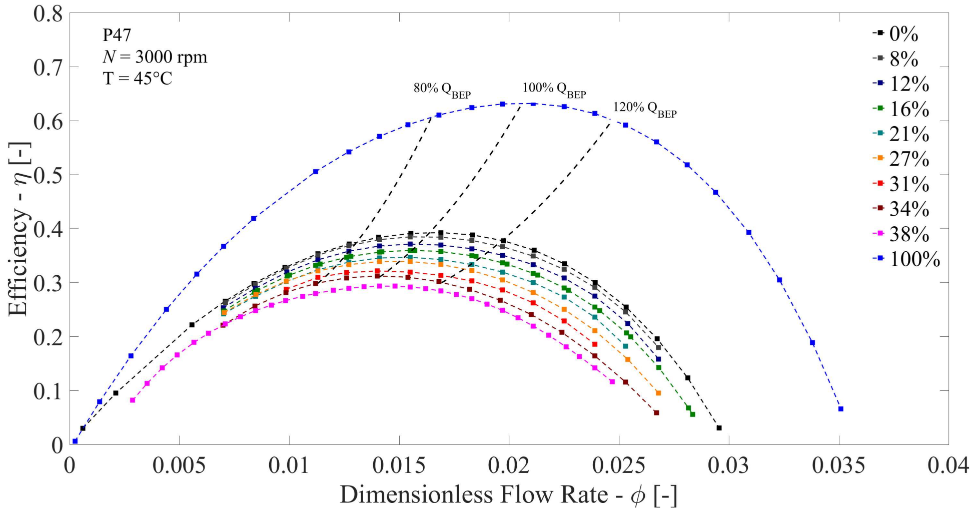

Figure A.17 – P47 Efficiency at 3000 rpm, 45°C.

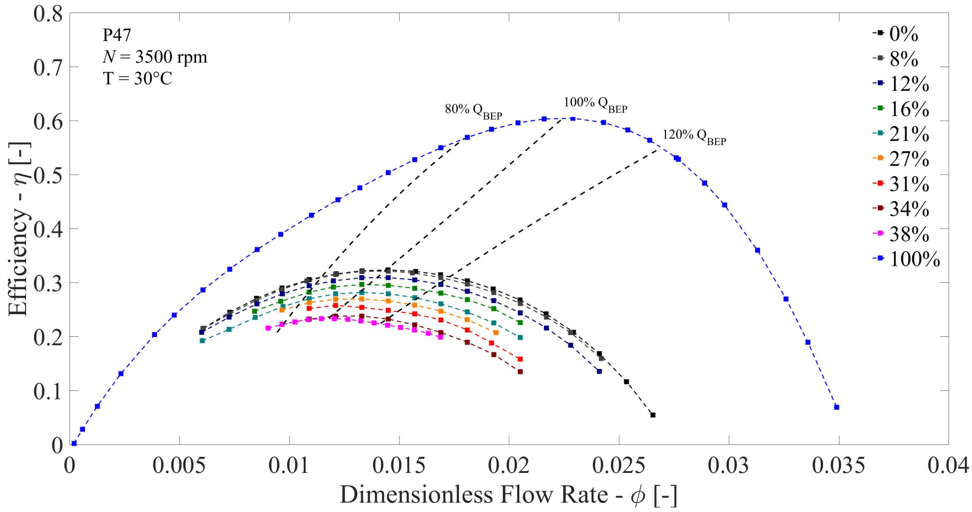

Figure A.18 – P47 Efficiency at 3500 rpm, 30°C.

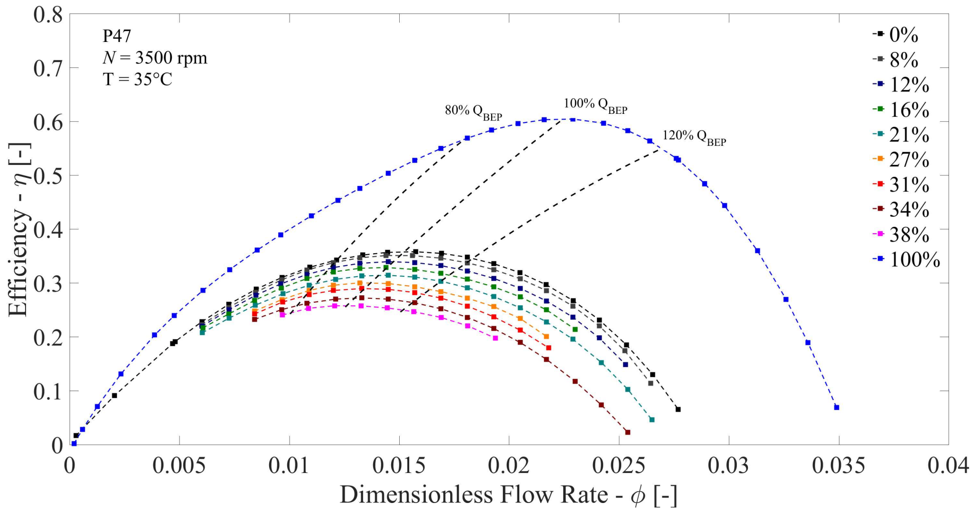

Figure A.19 – P47 Efficiency at 3500 rpm, 35°C.

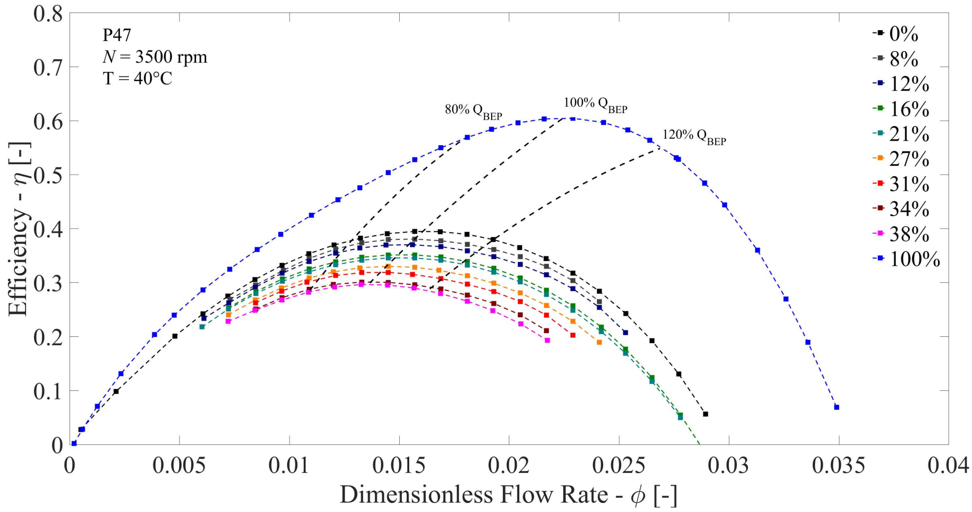

Figure A.20 – P47 Efficiency at 3500 rpm, 40°C.

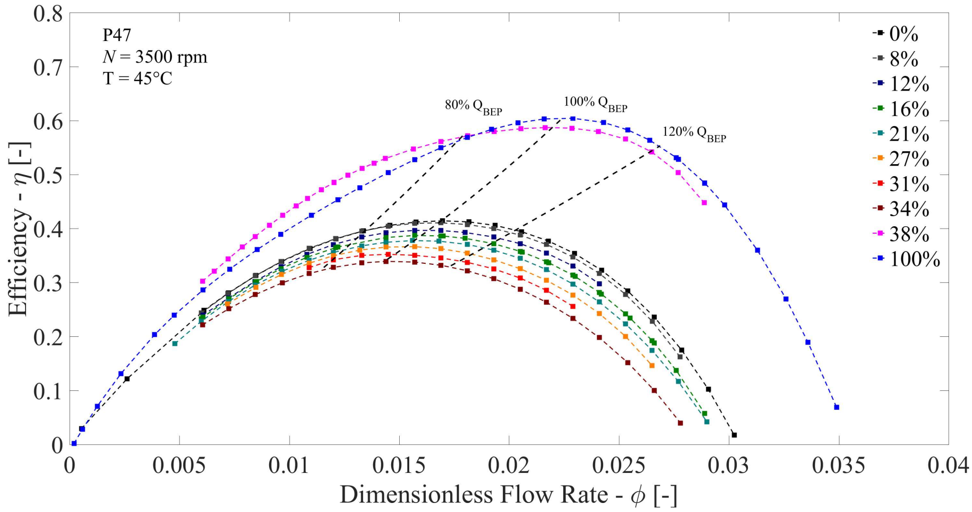

Figure A.21 – P47 Efficiency at 3500 rpm, 45°C.

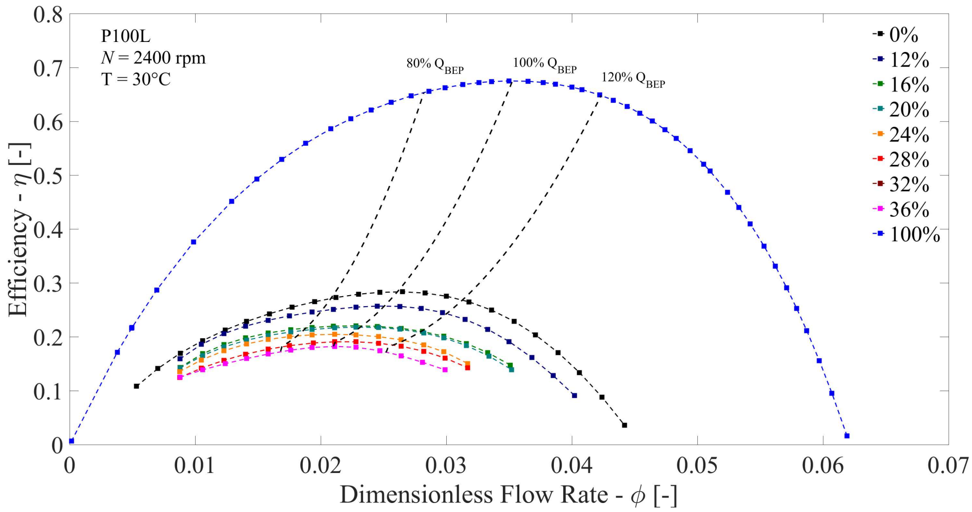

Figure A.22 – P100L Efficiency at 2400 rpm, 30°C.

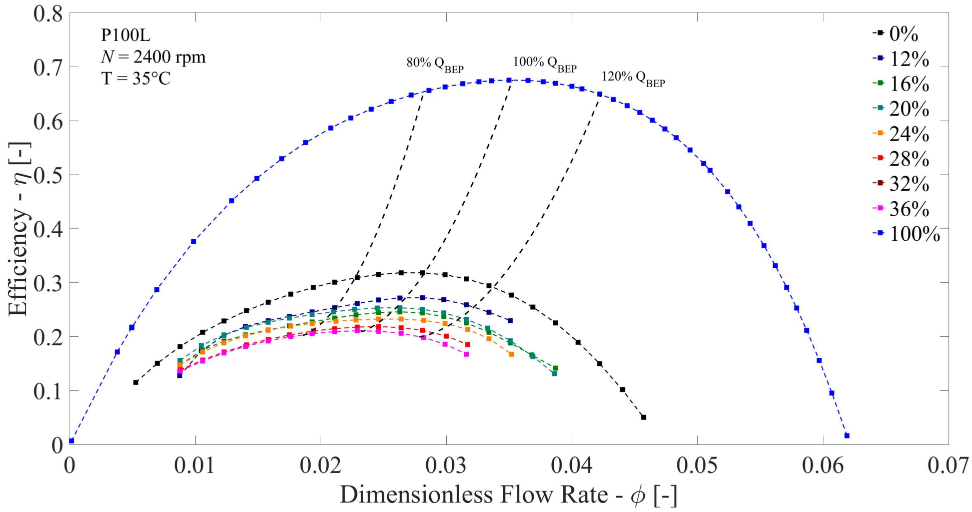

Figure A.23 – P100L Efficiency at 2400 rpm, 35°C.

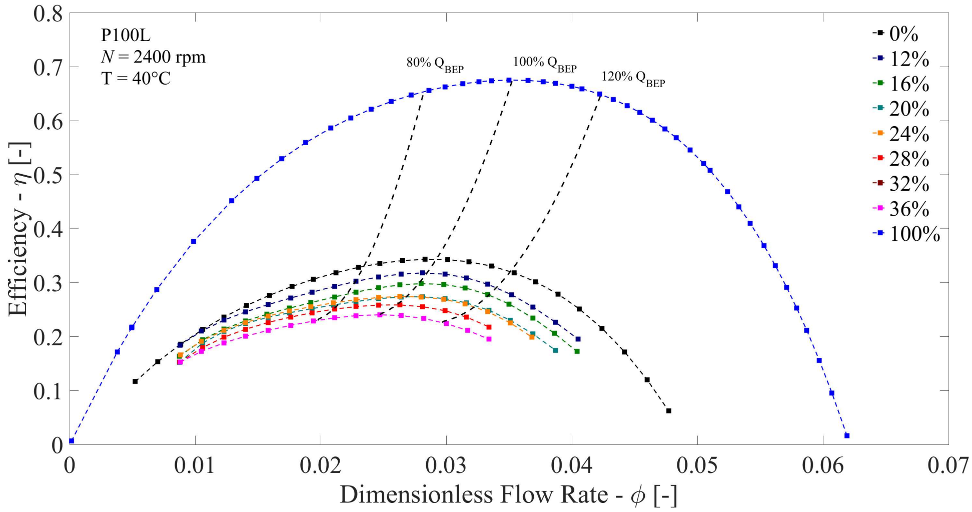

Figure A.24 – P100L Efficiency at 2400 rpm, 40°C.

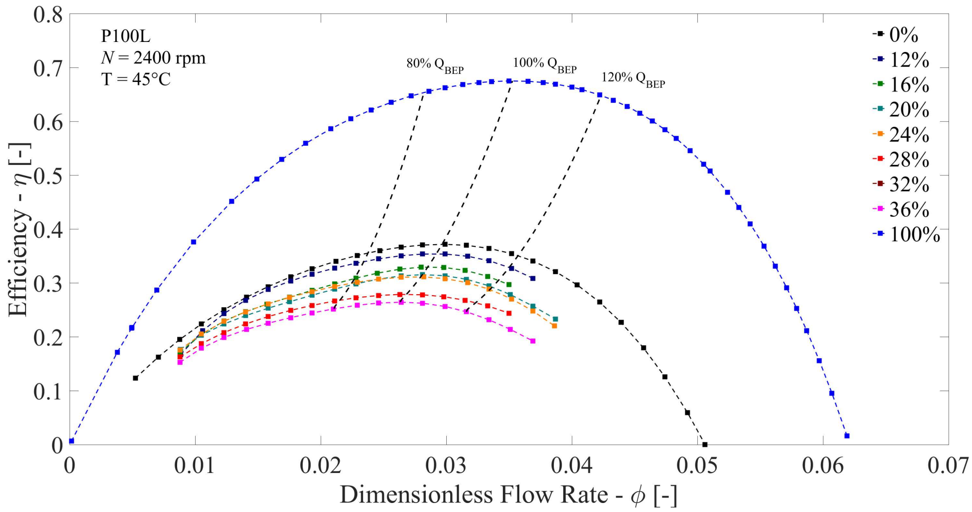

Figure A.25 – P100L Efficiency at 2400 rpm, 45°C.

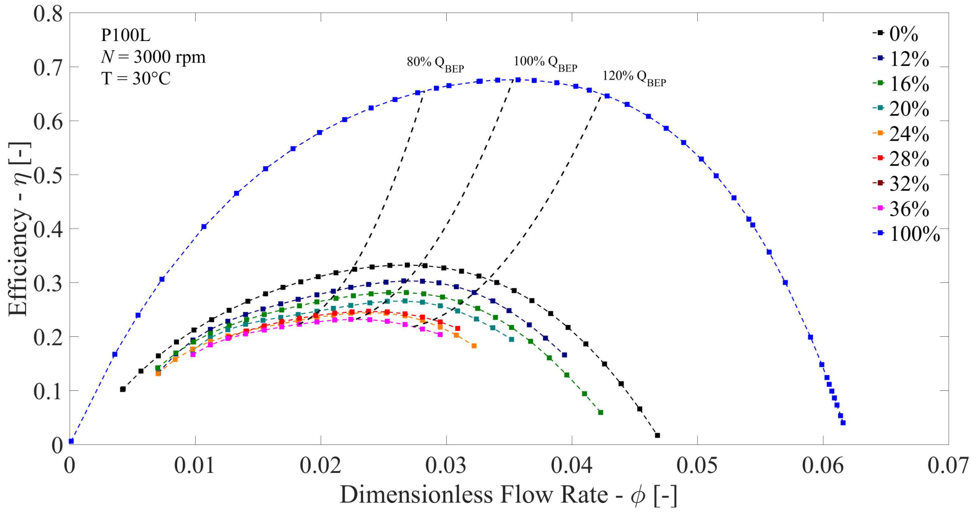

Figure A.26 – P100L Efficiency at 3000 rpm, 30°C.

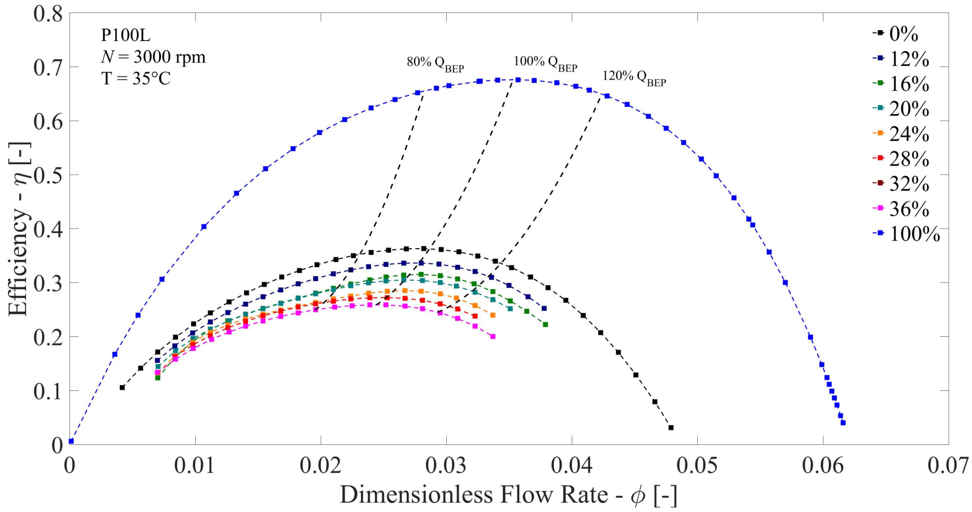

Figure A.27 – P100L Efficiency at 3000 rpm, 35°C.

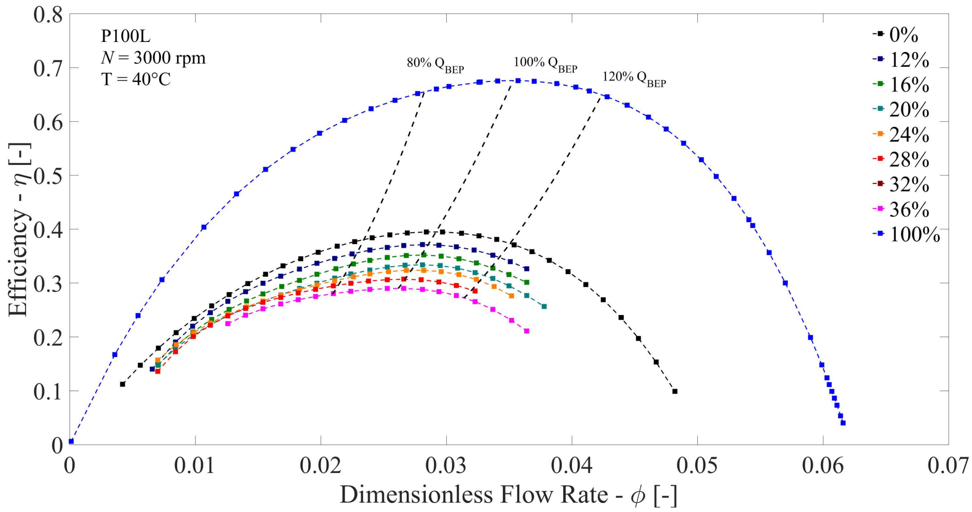

Figure A.28 – P100L Efficiency at 3000 rpm, 40°C.

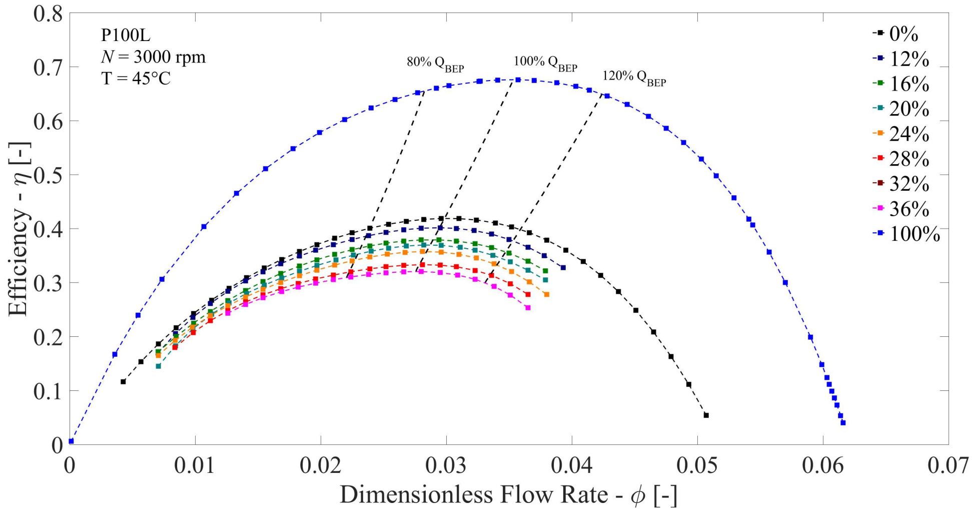

Figure A.29 – P100L Efficiency at 3000 rpm, 45°C.

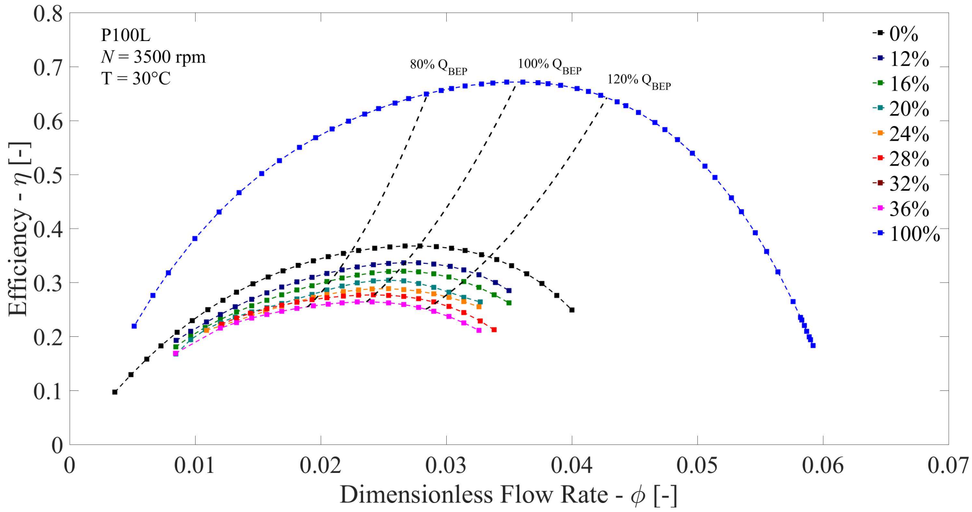

Figure A.30 – P100L Efficiency at 3500 rpm, 30°C.

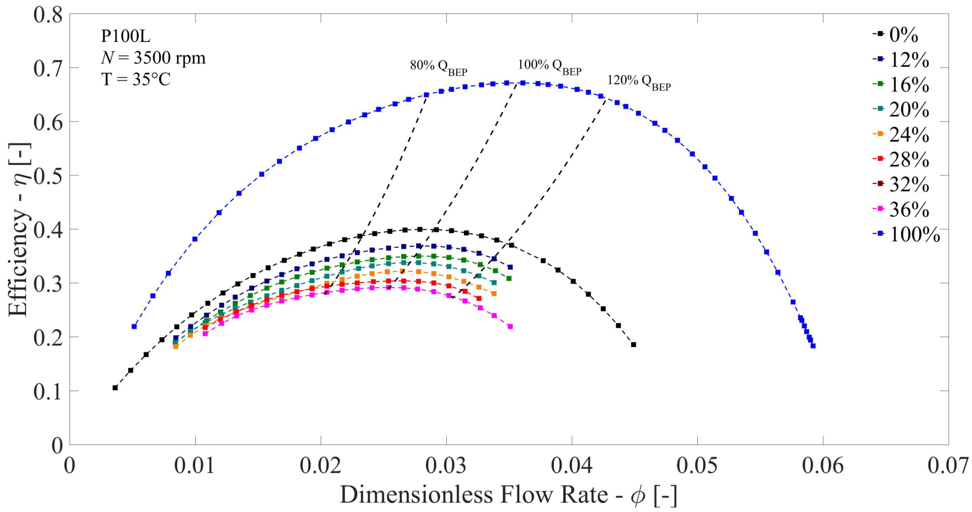

Figure A.31 – P100L Efficiency at 3500 rpm, 35°C.

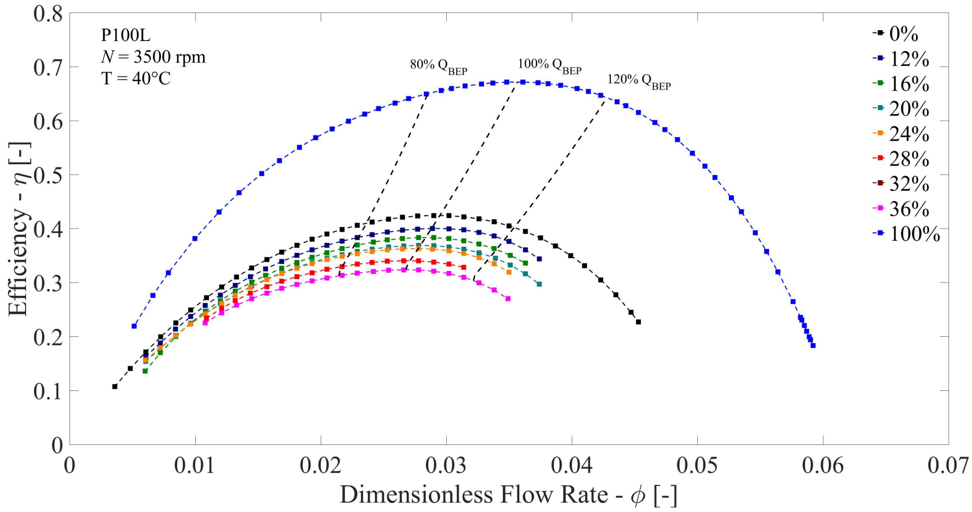

Figure A.32 – P100L Efficiency at 3500 rpm, 40°C.

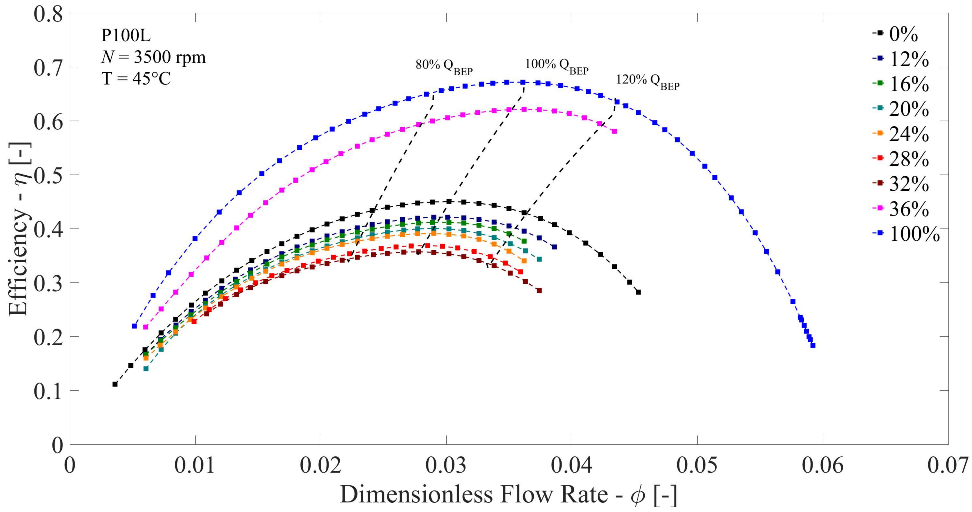

Figure A.33 – P100L Efficiency at 3500 rpm, 45°C.

A.5 Water-Oil Emulsion - Head

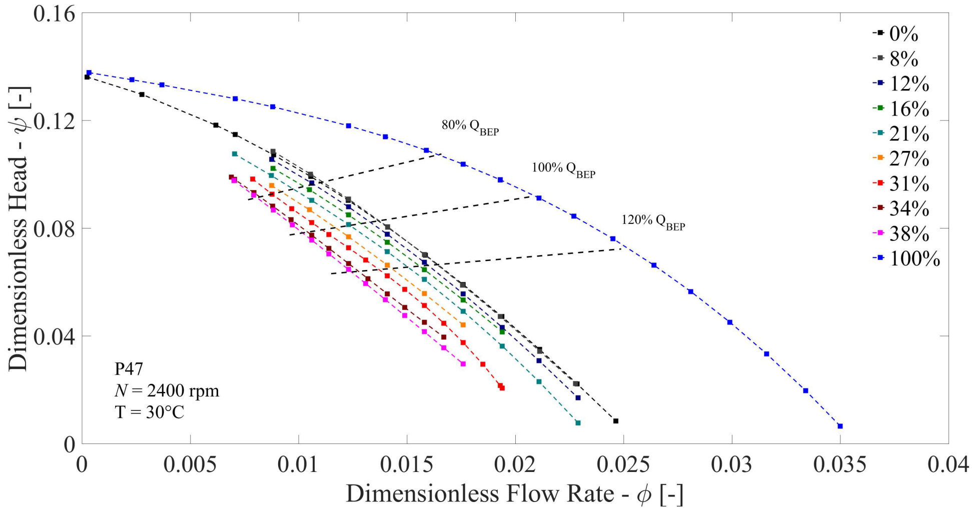

Figure A.34 – P47 Dimensionless Head at 2400 rpm, 30°C.

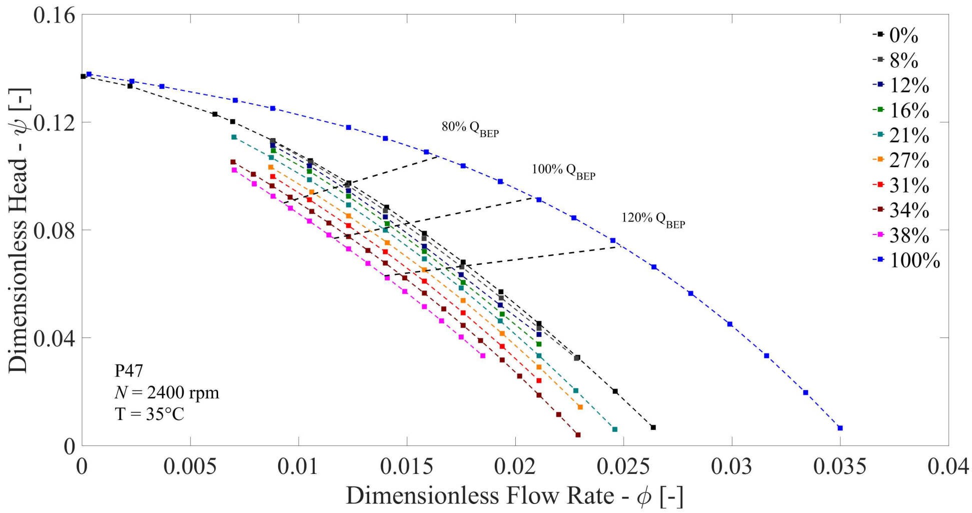

Figure A.35 – P47 Dimensionless Head at 2400 rpm, 35°C.

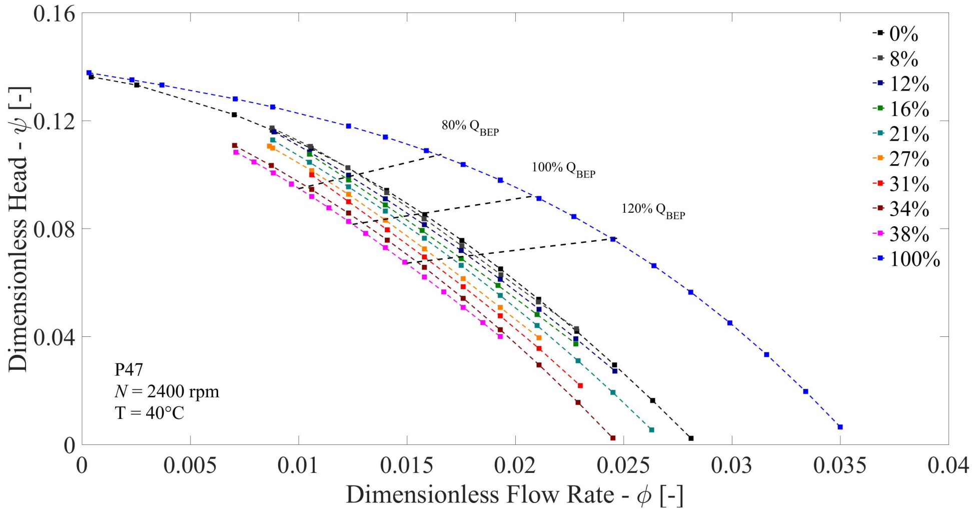

Figure A.36 – P47 Dimensionless Head at 2400 rpm, 40°C.

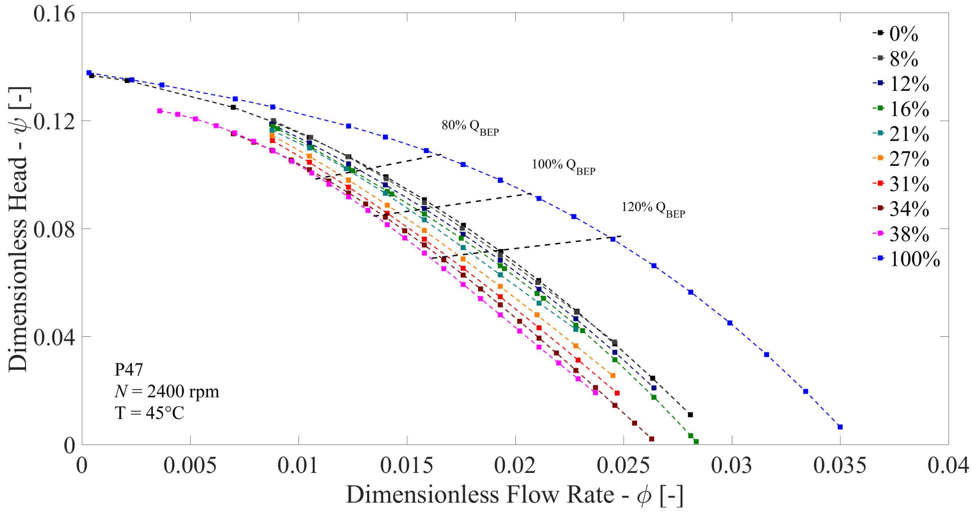

Figure A.37 – P47 Dimensionless Head at 2400 rpm, 45°C.

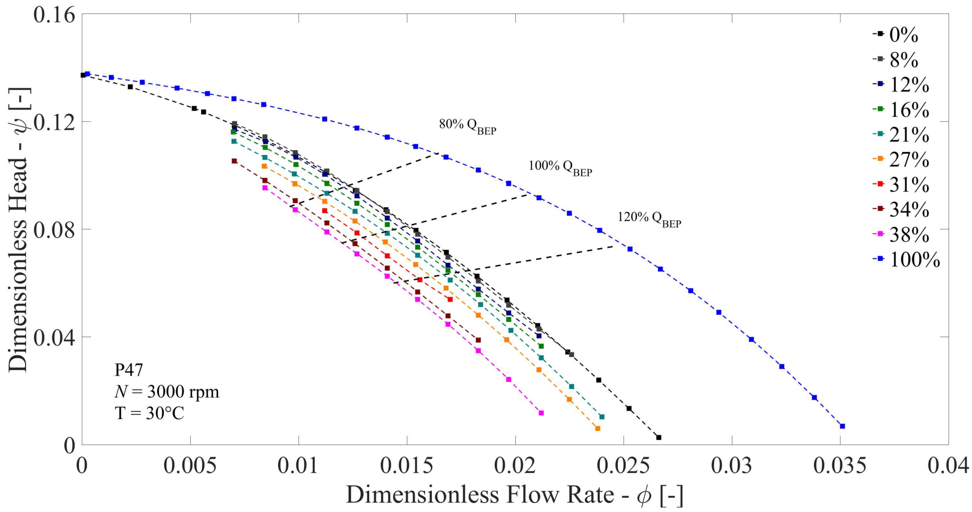

Figure A.38 – P47 Dimensionless Head at 3000 rpm, 30°C.

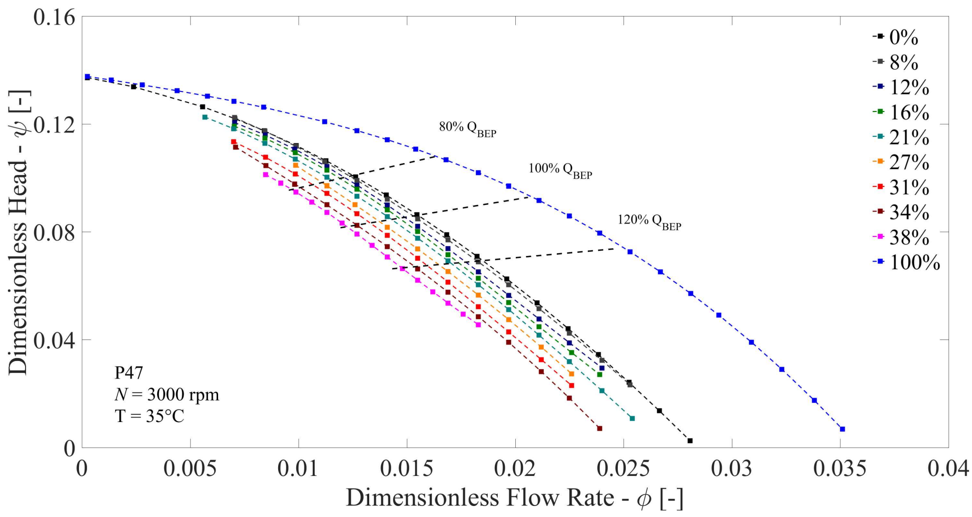

Figure A.39 – P47 Dimensionless Head at 3000 rpm, 35°C.

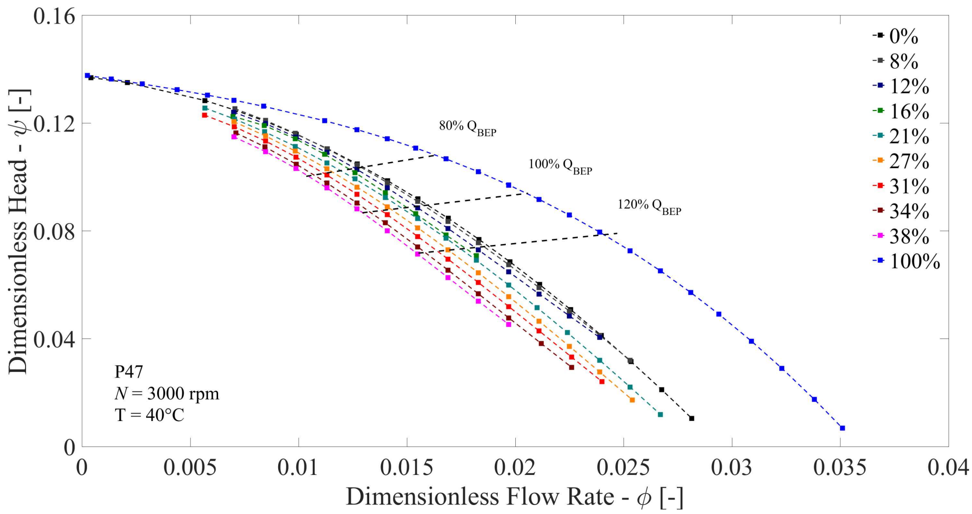

Figure A.40 – P47 Dimensionless Head at 3000 rpm, 40°C.

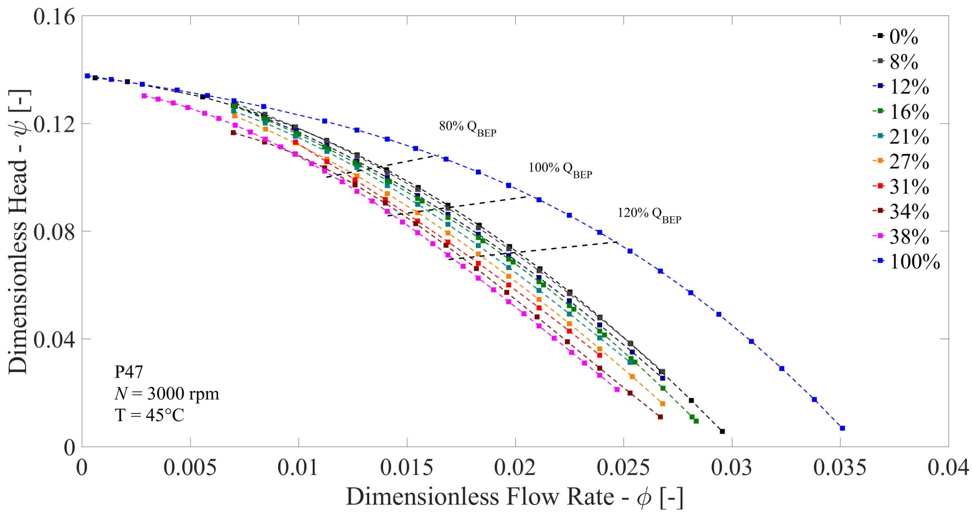

Figure A.41 – P47 Dimensionless Head at 3000 rpm, 45°C.

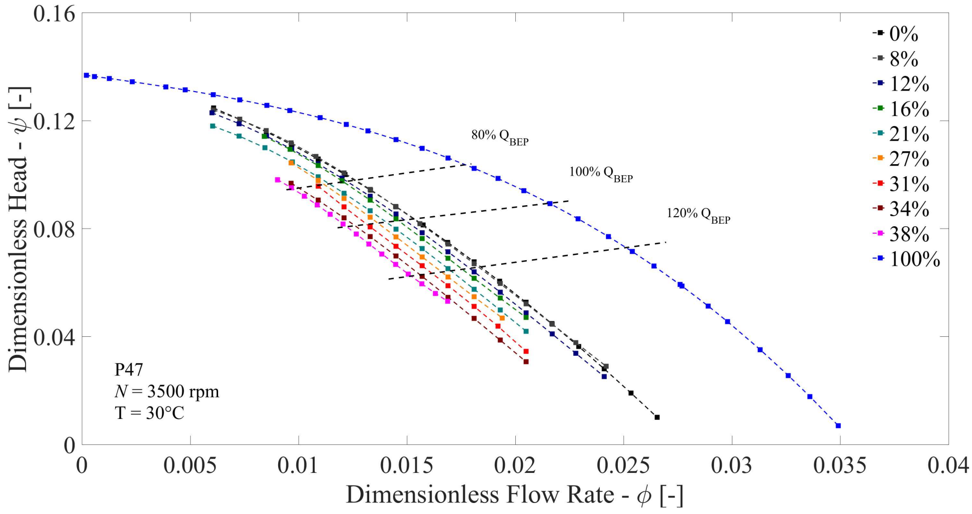

Figure A.42 – P47 Dimensionless Head at 3500 rpm, 30°C.

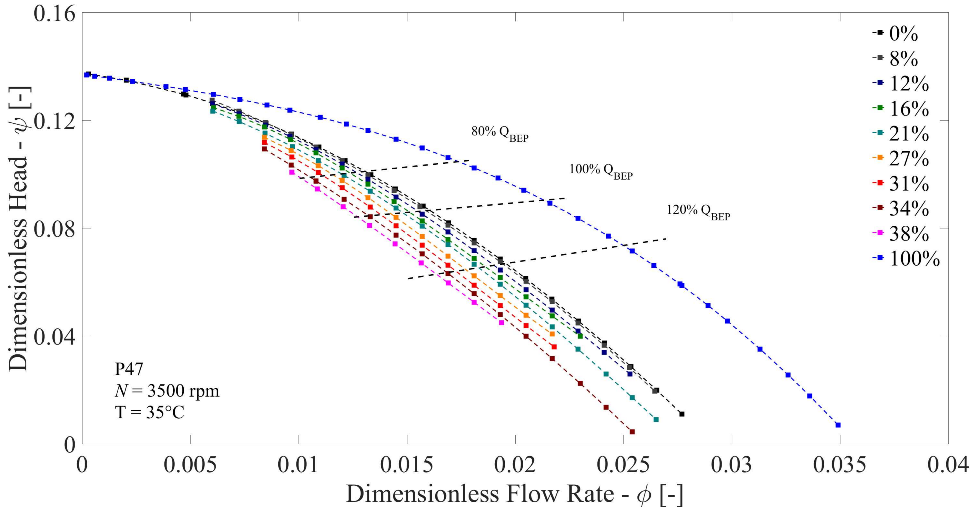

Figure A.43 – P47 Dimensionless Head at 3500 rpm, 35°C.

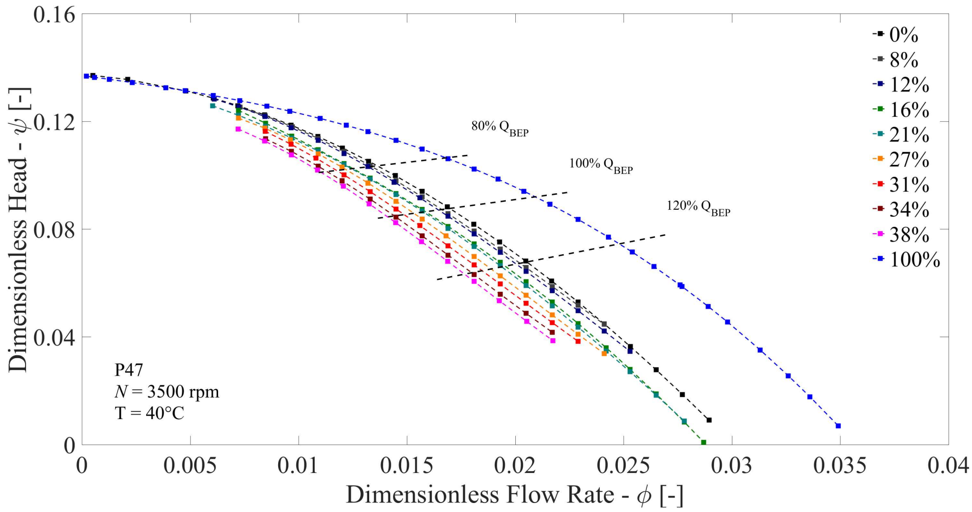

Figure A.44 – P47 Dimensionless Head at 3500 rpm, 40°C.

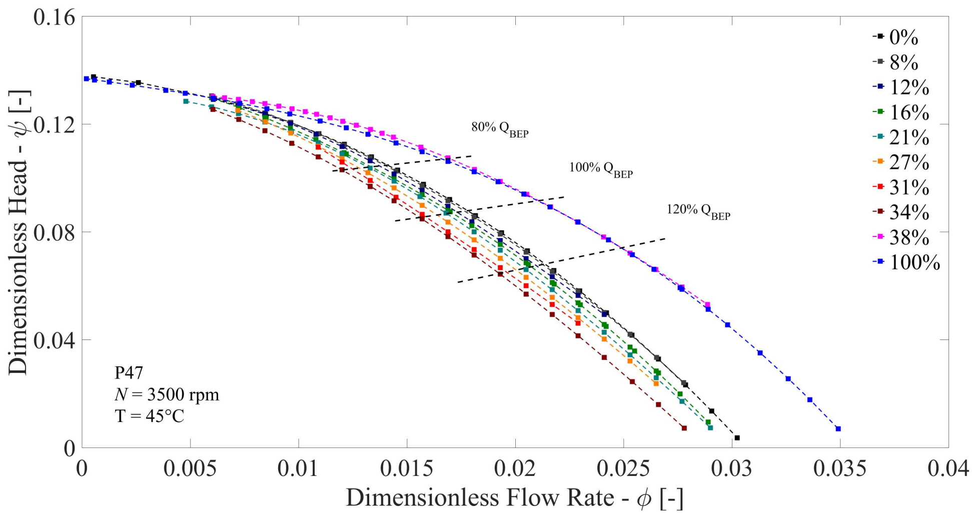

Figure A.45 – P47 Dimensionless Head at 3500 rpm, 45°C.

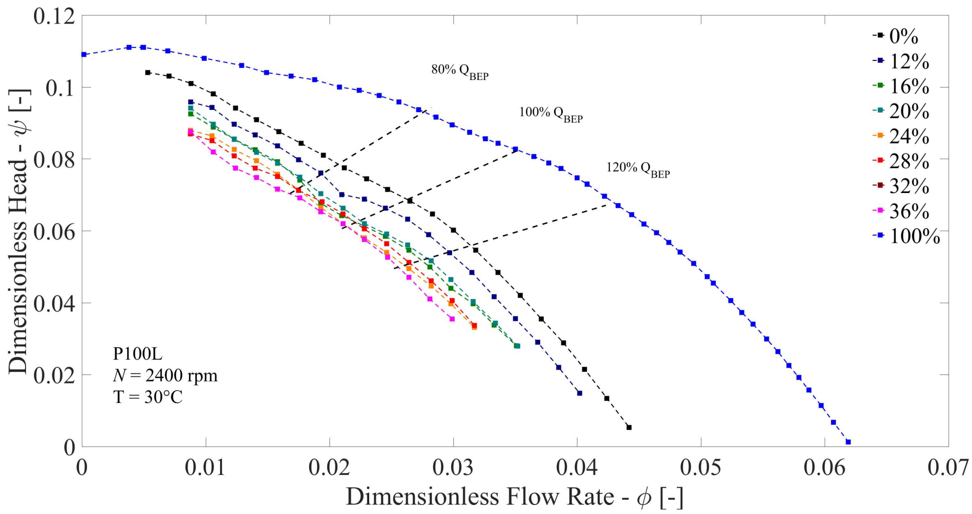

Figure A.46 – P100L Dimensionless Head at 2400 rpm, 30°C.

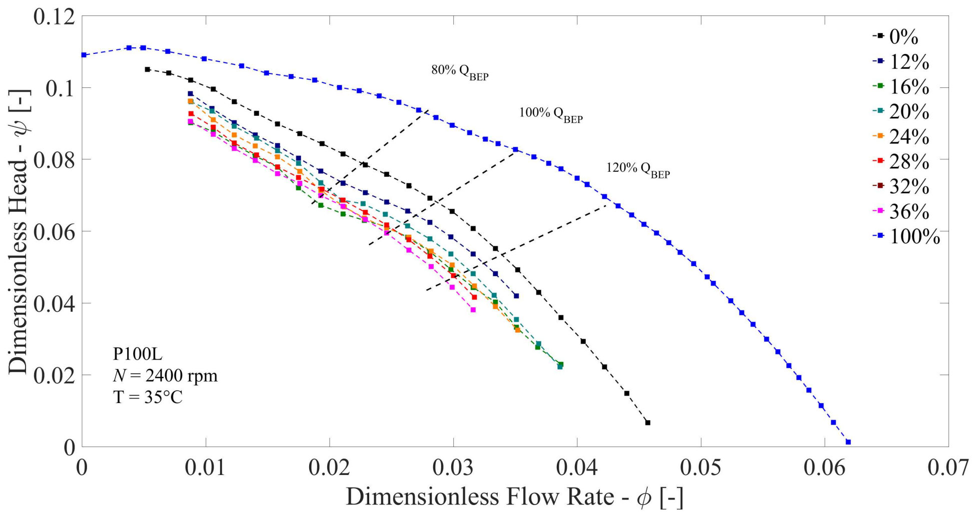

Figure A.47 – P100L Dimensionless Head at 2400 rpm, 35°C.

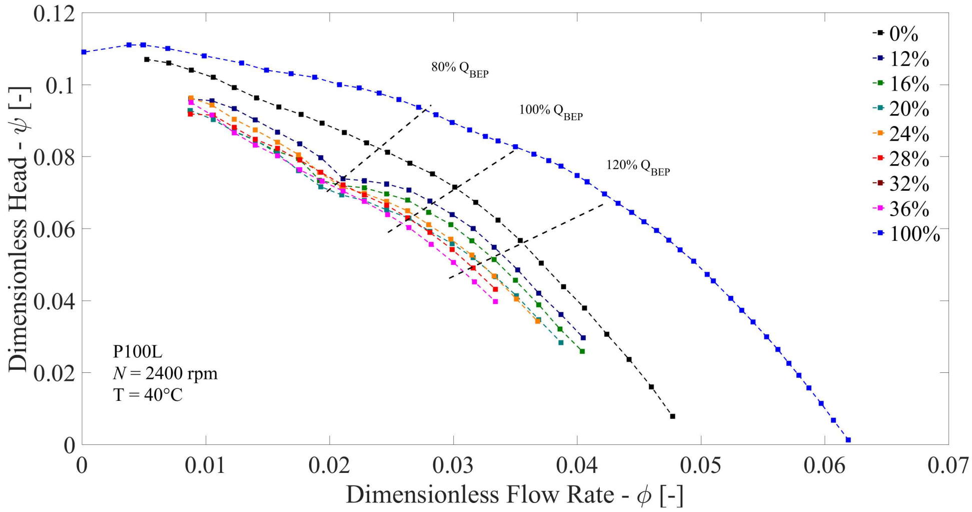

Figure A.48 – P100L Dimensionless Head at 2400 rpm, 40°C.

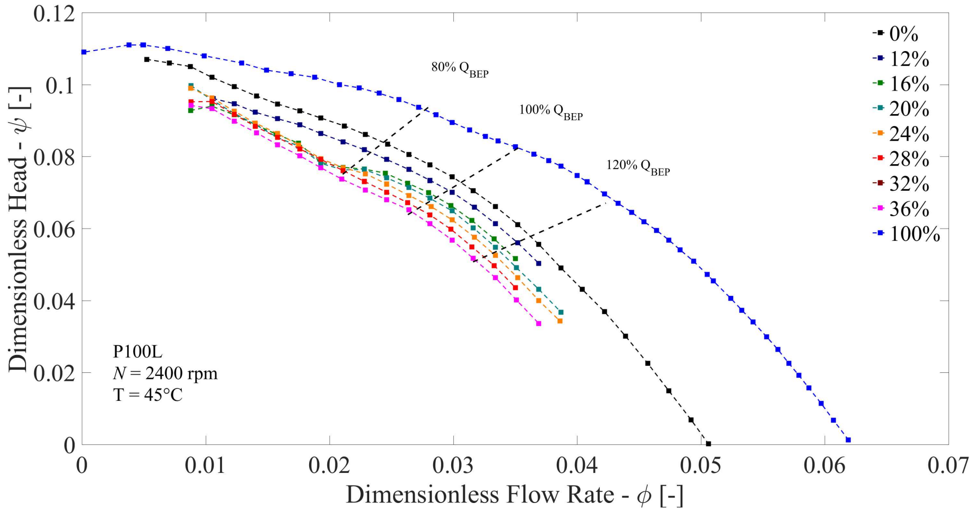

Figure A.49 – P100L Dimensionless Head at 2400 rpm, 45°C.

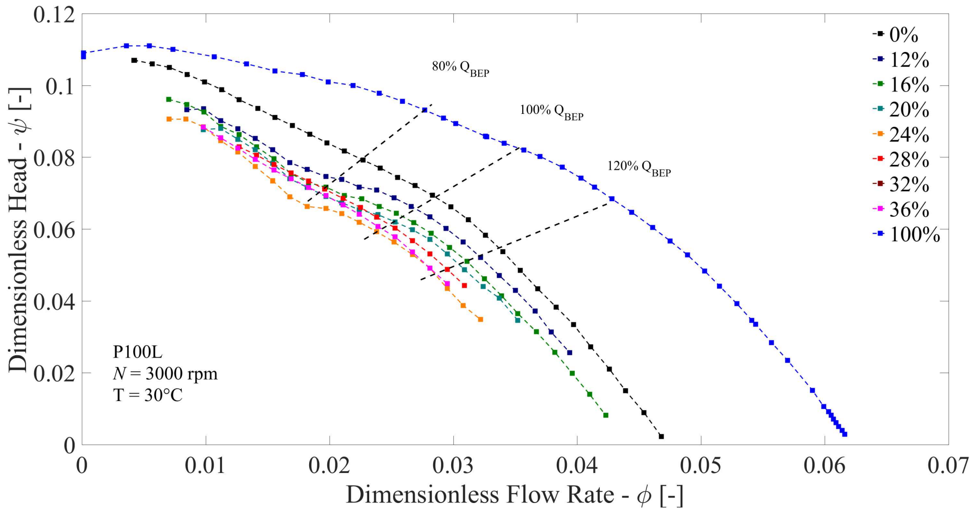

Figure A.50 – P100L Dimensionless Head at 3000 rpm, 30°C.

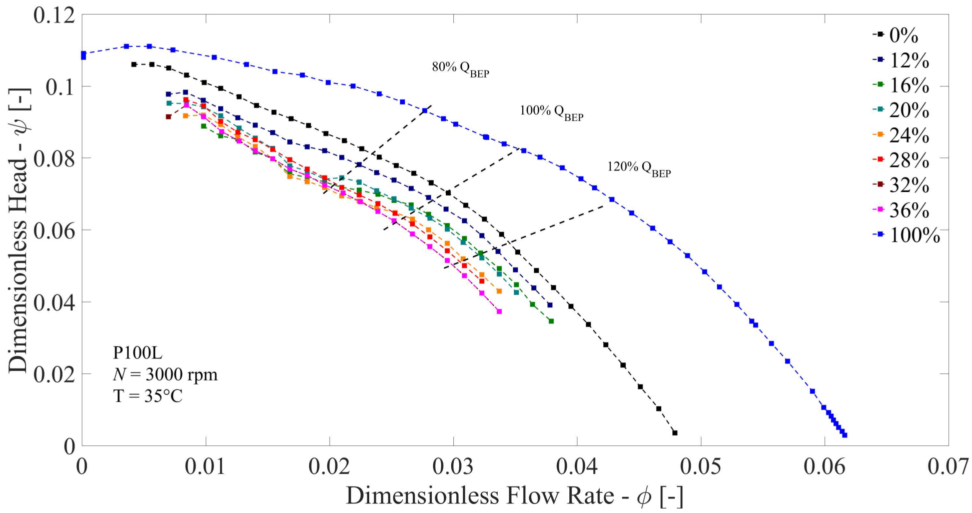

Figure A.51 – P100L Dimensionless Head at 3000 rpm, 35°C.

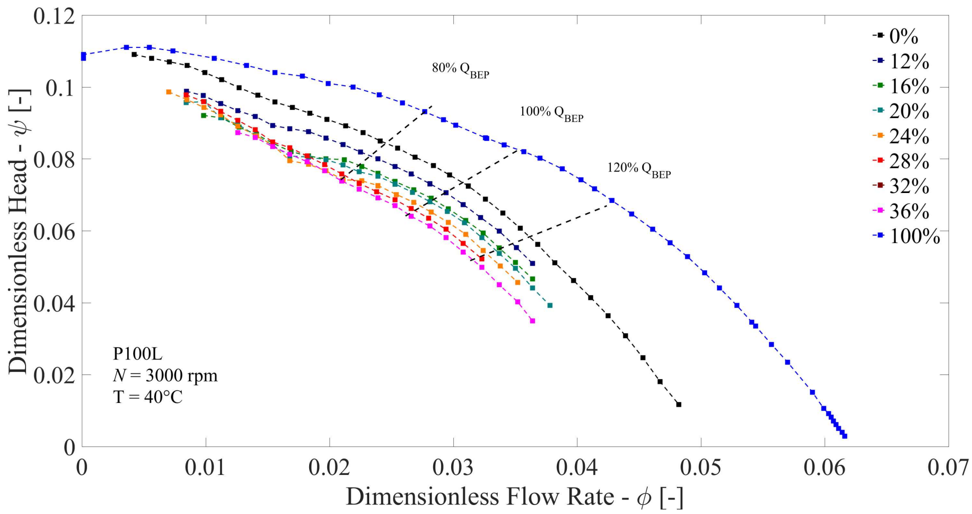

Figure A.52 – P100L Dimensionless Head at 3000 rpm, 40°C.

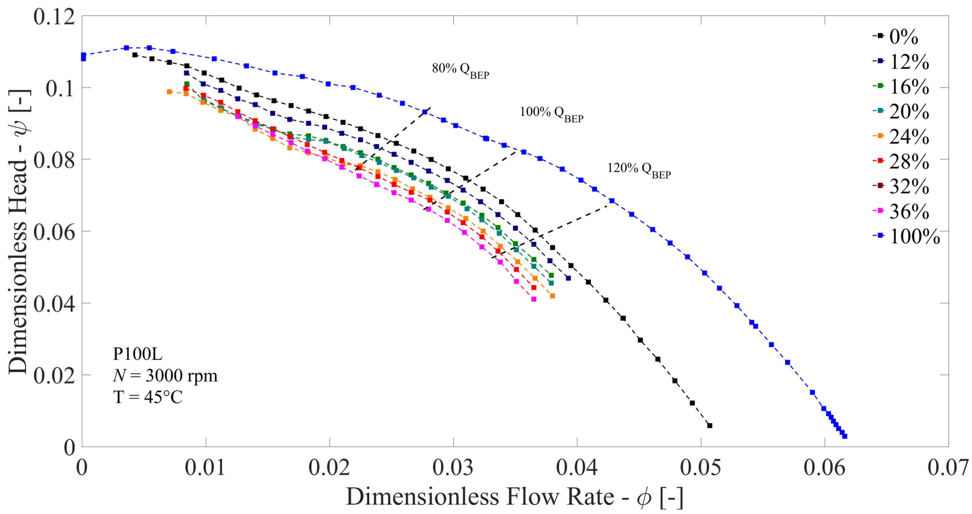

Figure A.53 – P100L Dimensionless Head at 3000 rpm, 45°C.

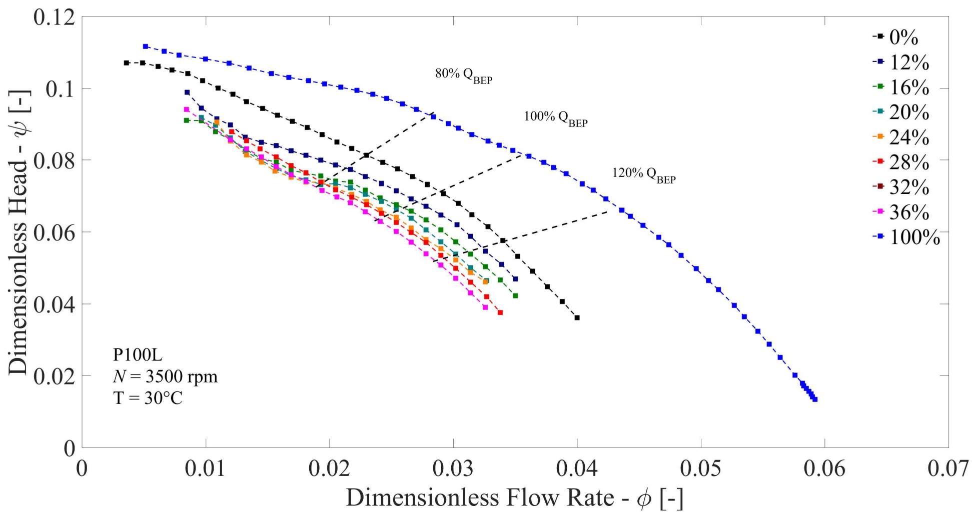

Figure A.54 – P100L Dimensionless Head at 3500 rpm, 30°C.

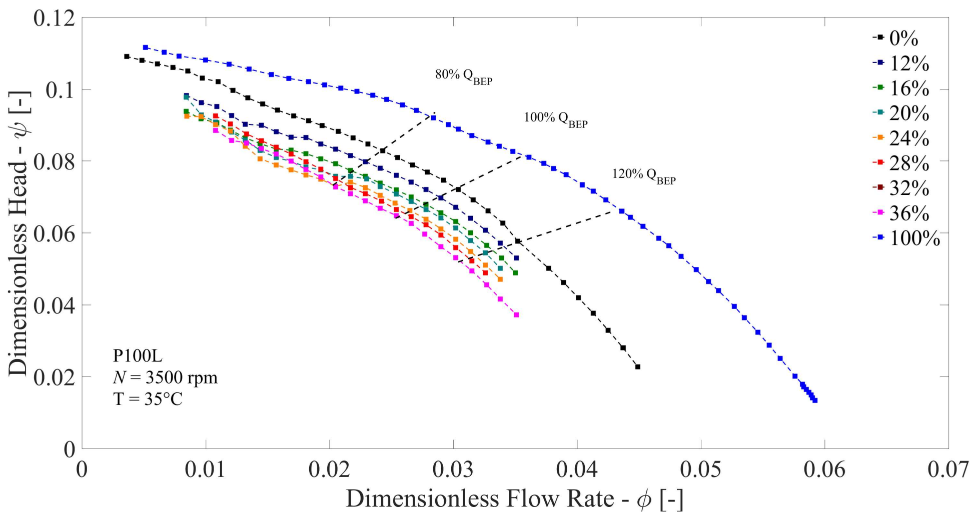

Figure A.55 – P100L Dimensionless Head at 3500 rpm, 35°C.

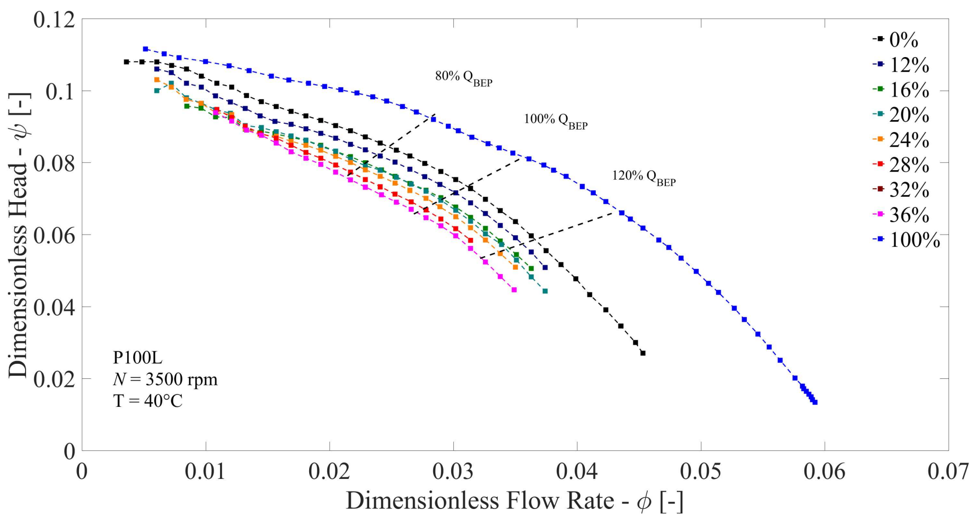

Figure A.56 – P100L Dimensionless Head at 3500 rpm, 40°C.

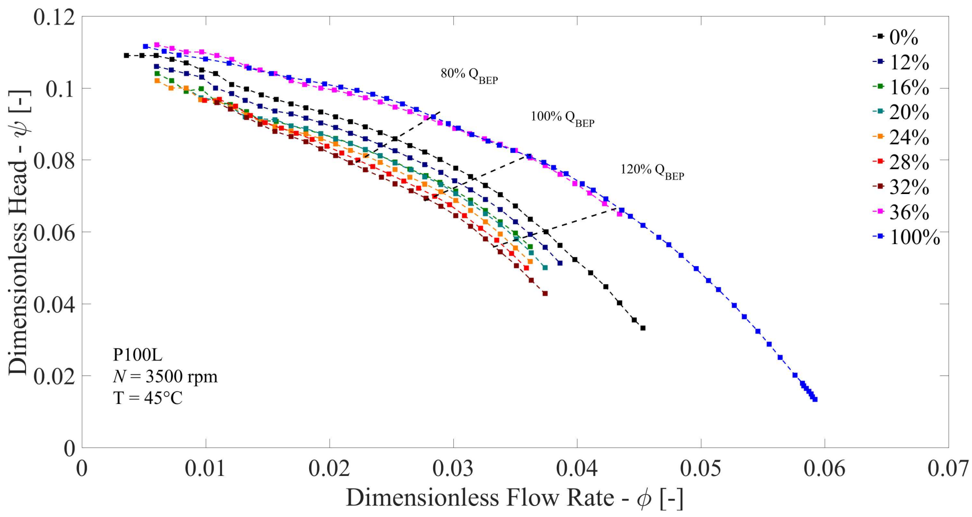

Figure A.57 – P100L Dimensionless Head at 3500 rpm, 45°C.

A.6 Water-Oil Emulsion - Power

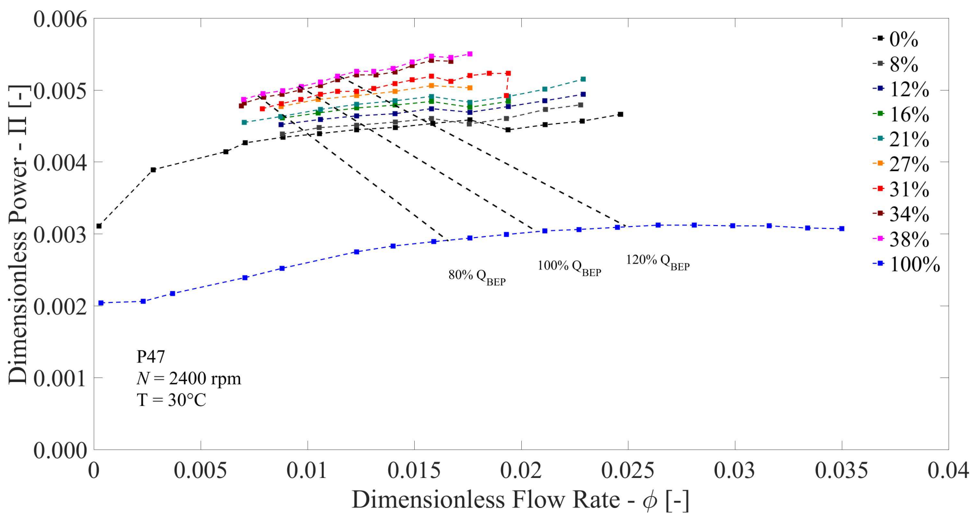

Figure A.58 – P47 Dimensionless Power at 2400 rpm, 30°C.

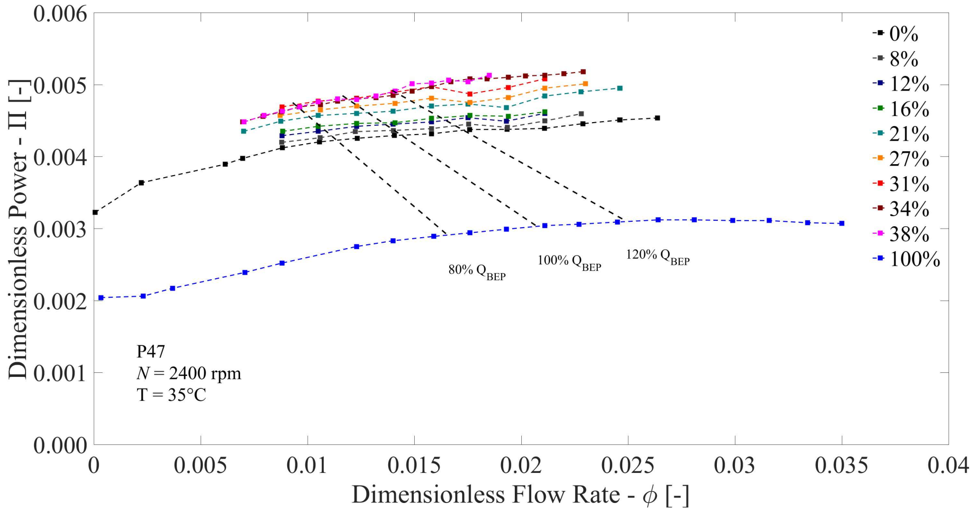

Figure A.59 – P47 Dimensionless Power at 2400 rpm, 35°C.

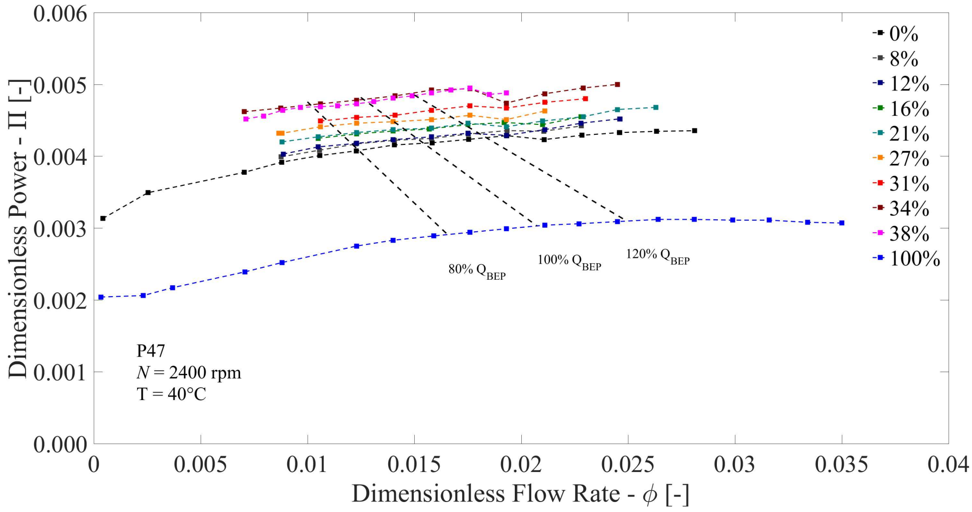

Figure A.60 – P47 Dimensionless Power at 2400 rpm, 40°C.

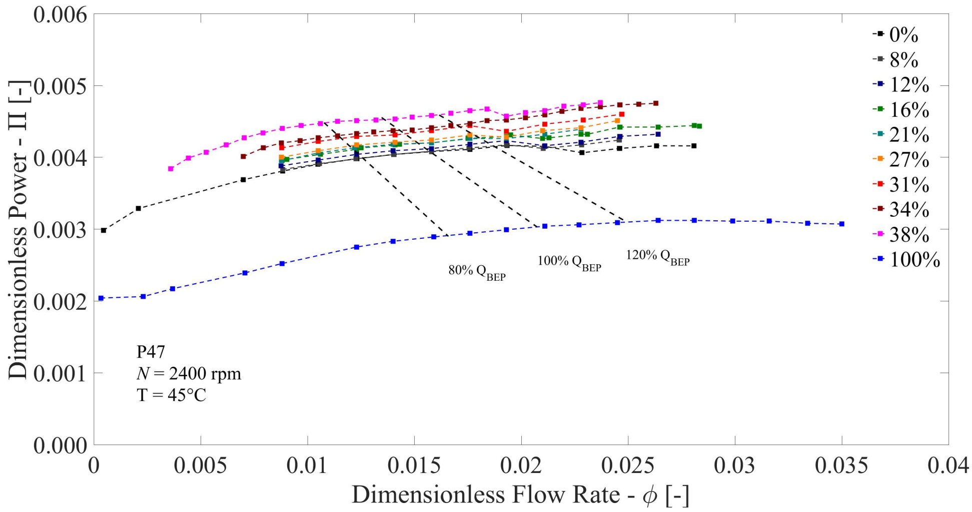

Figure A.61 – P47 Dimensionless Power at 2400 rpm, 45°C.

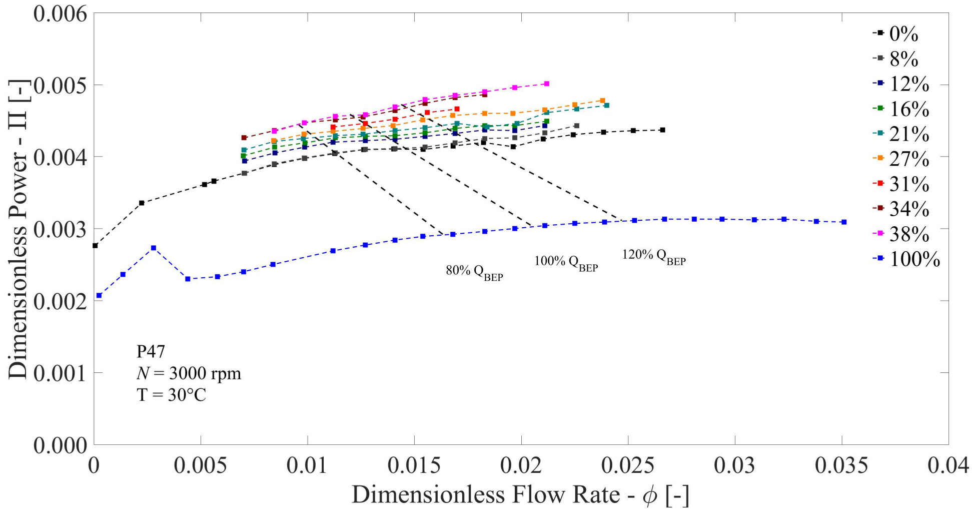

Figure A.62 – P47 Dimensionless Power at 3000 rpm, 30°C.

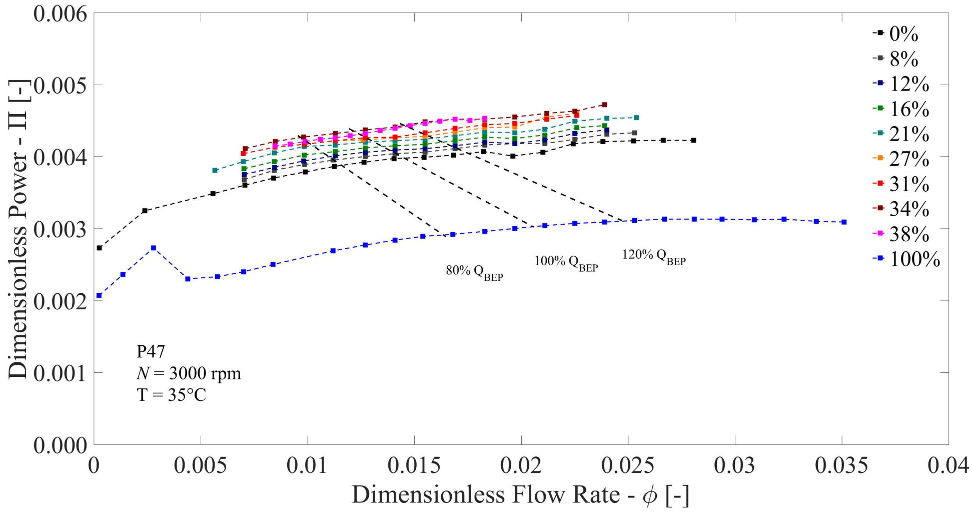

Figure A.63 – P47 Dimensionless Power at 3000 rpm, 35°C.

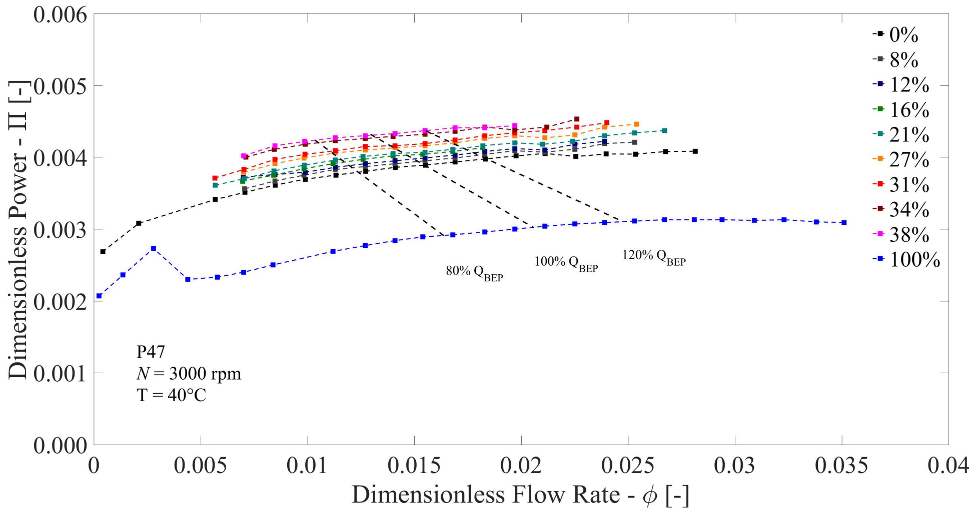

Figure A.64 – P47 Dimensionless Power at 3000 rpm, 40°C.

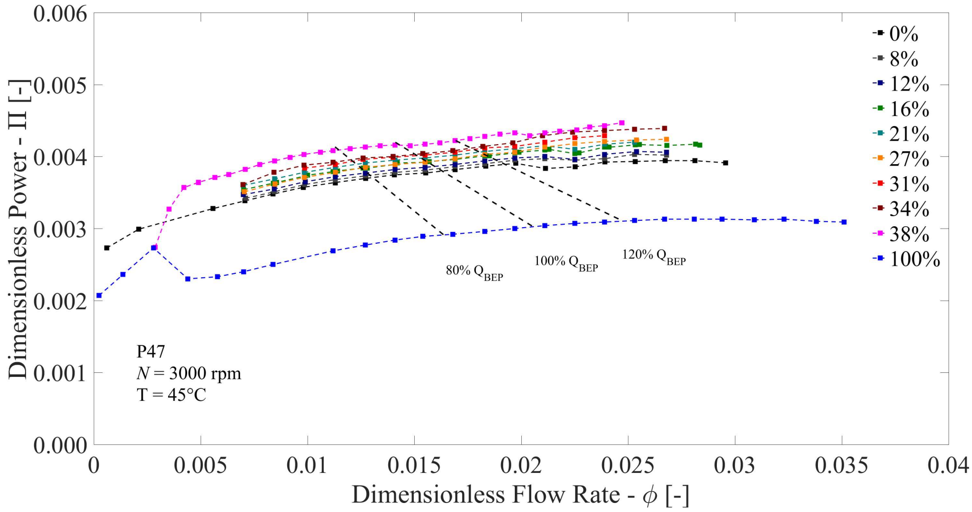

Figure A.65 – P47 Dimensionless Power at 3000 rpm, 45°C.

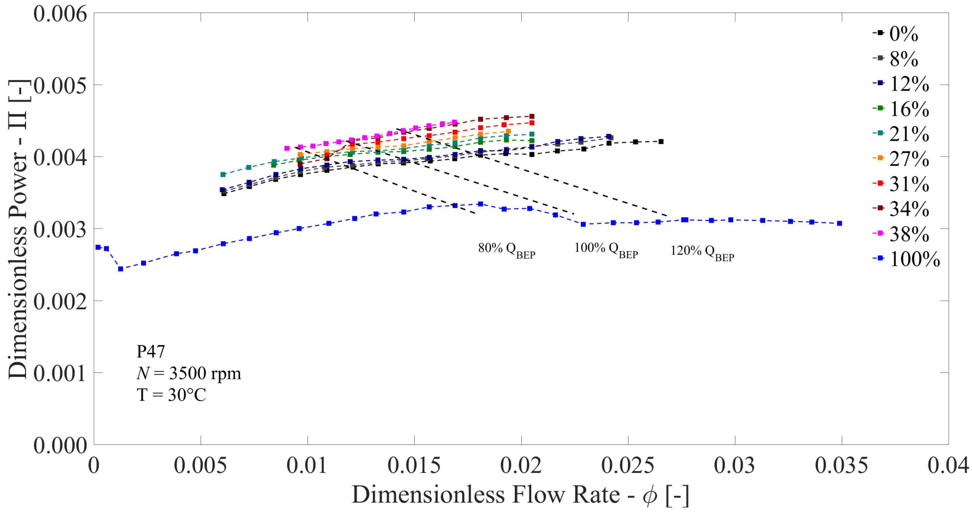

Figure A.66 – P47 Dimensionless Power at 3500 rpm, 30°C.

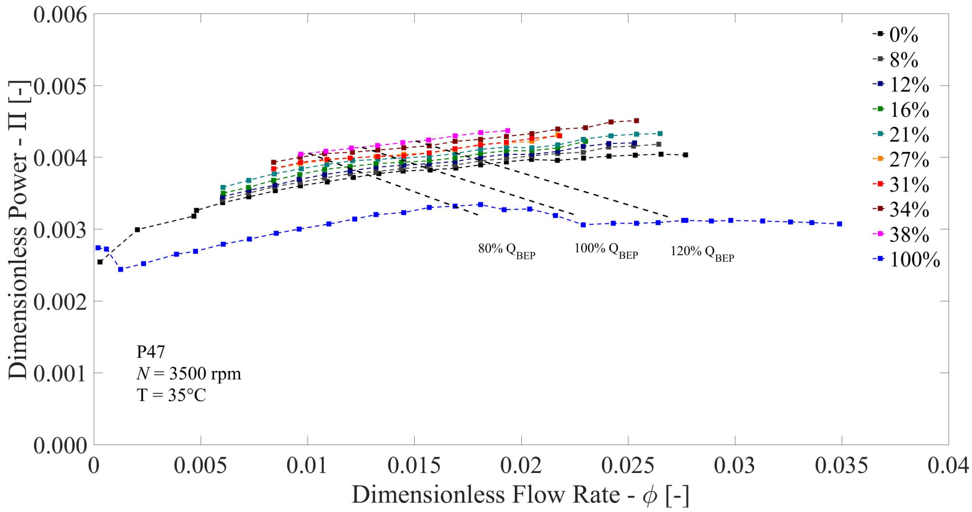

Figure A.67 – P47 Dimensionless Power at 3500 rpm, 35°C.

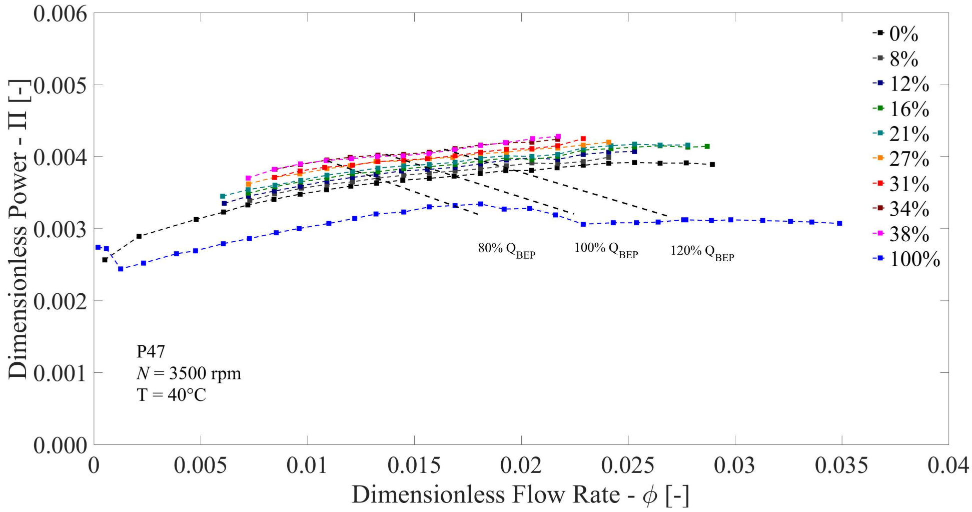

Figure A.68 – P47 Dimensionless Power at 3500 rpm, 40°C.

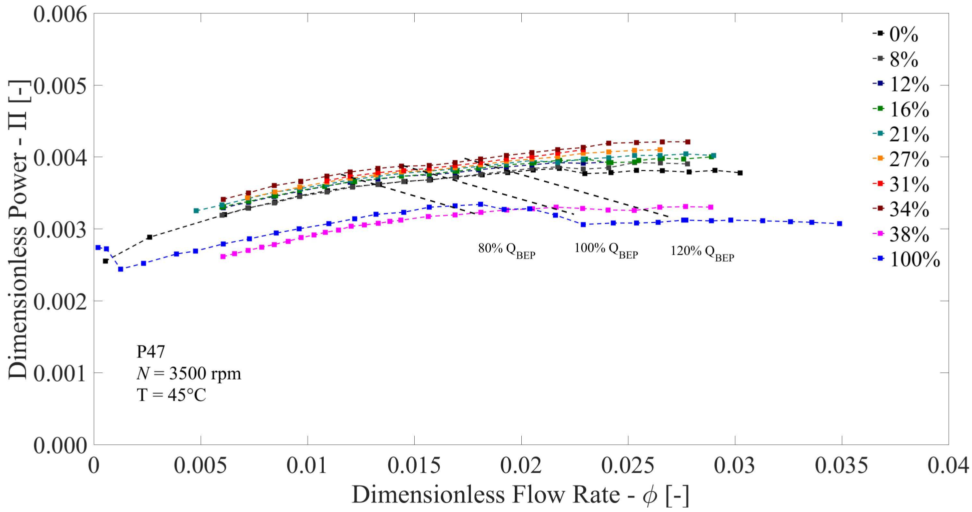

Figure A.69 – P47 Dimensionless Power at 3500 rpm, 45°C.

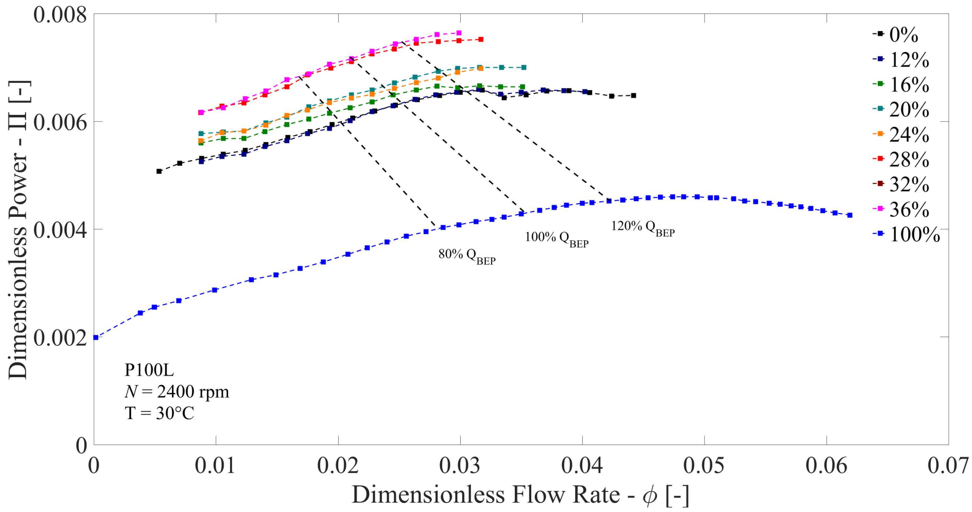

Figure A.70 – P100L Dimensionless Power at 2400 rpm, 30°C.

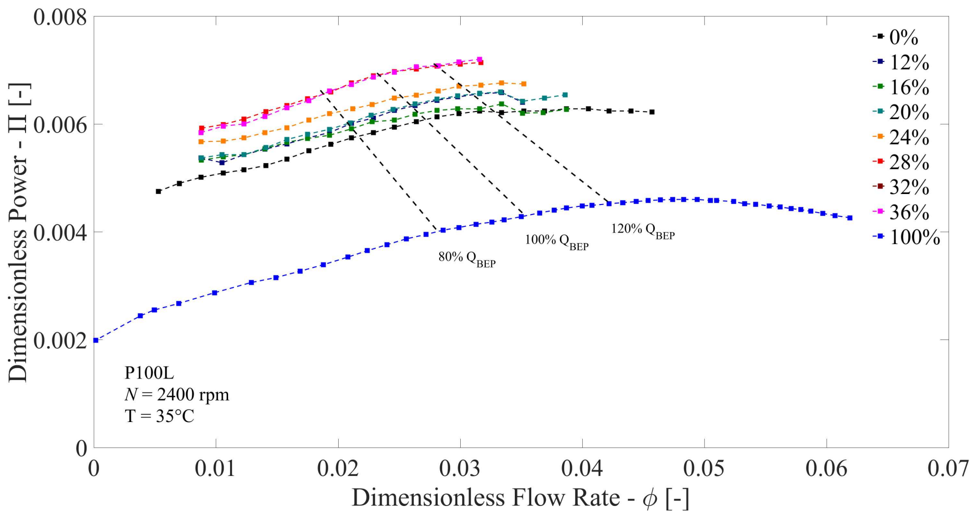

Figure A.71 – P100L Dimensionless Power at 2400 rpm, 35°C.

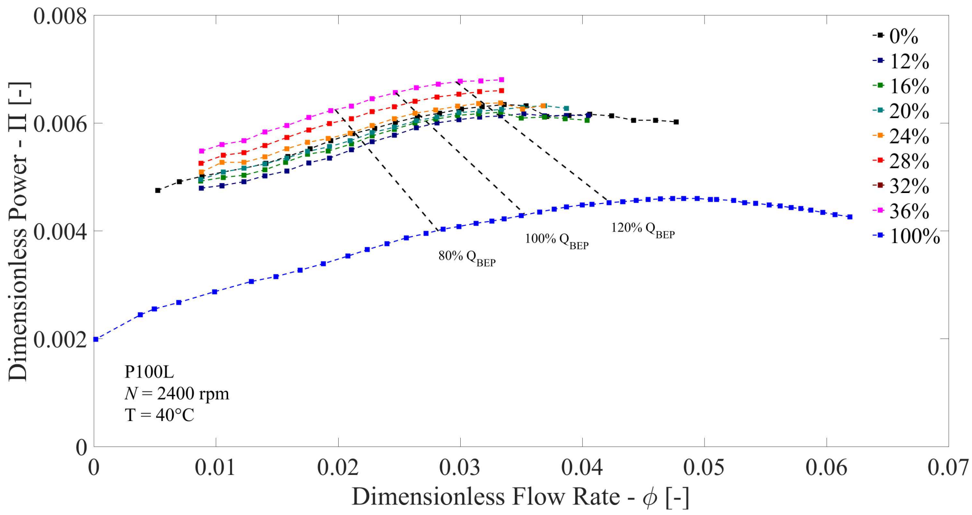

Figure A.72 – P100L Dimensionless Power at 2400 rpm, 40°C.

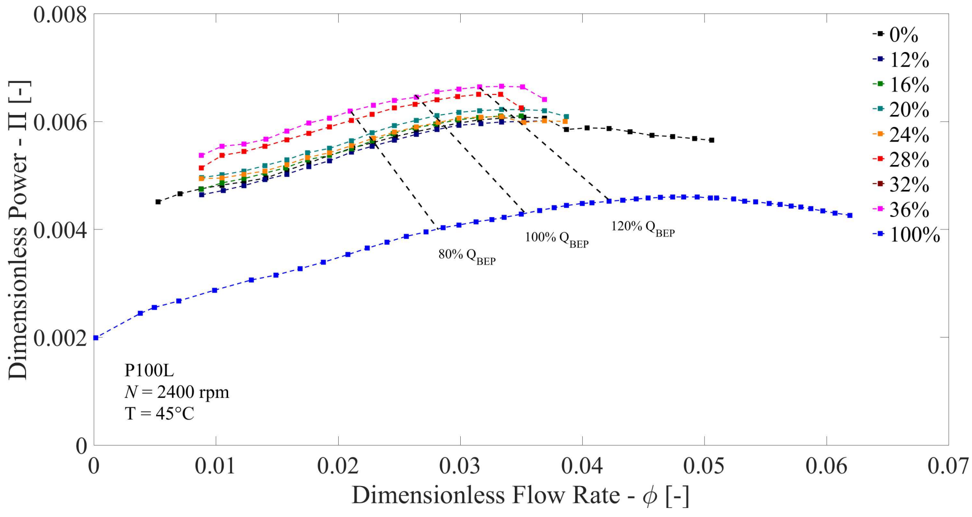

Figure A.73 – P100L Dimensionless Power at 2400 rpm, 45°C.

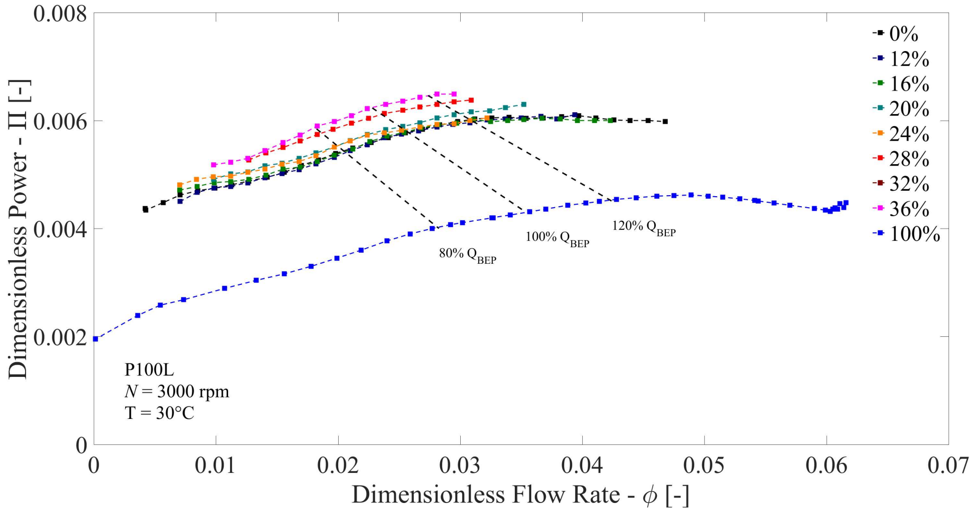

Figure A.74 – P100L Dimensionless Power at 3000 rpm, 30°C.

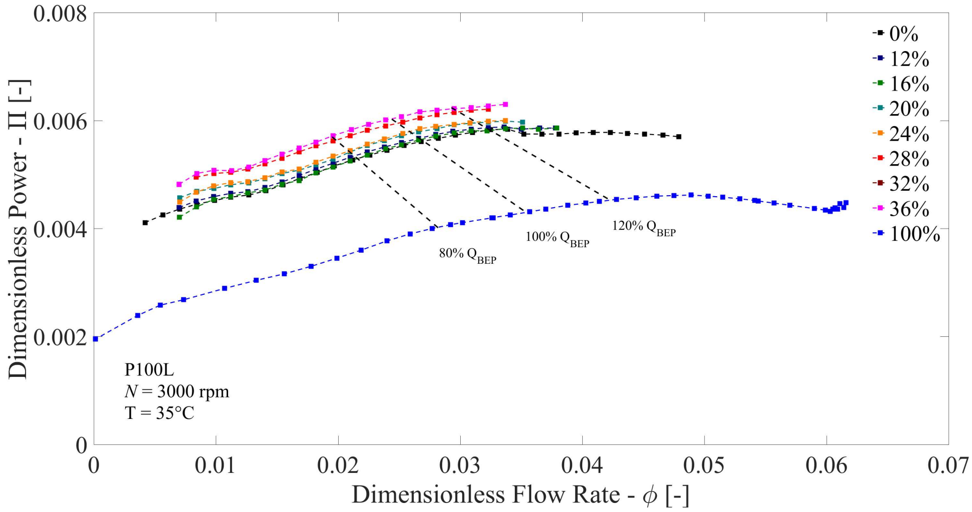

Figure A.75 – P100L Dimensionless Power at 3000 rpm, 35°C.

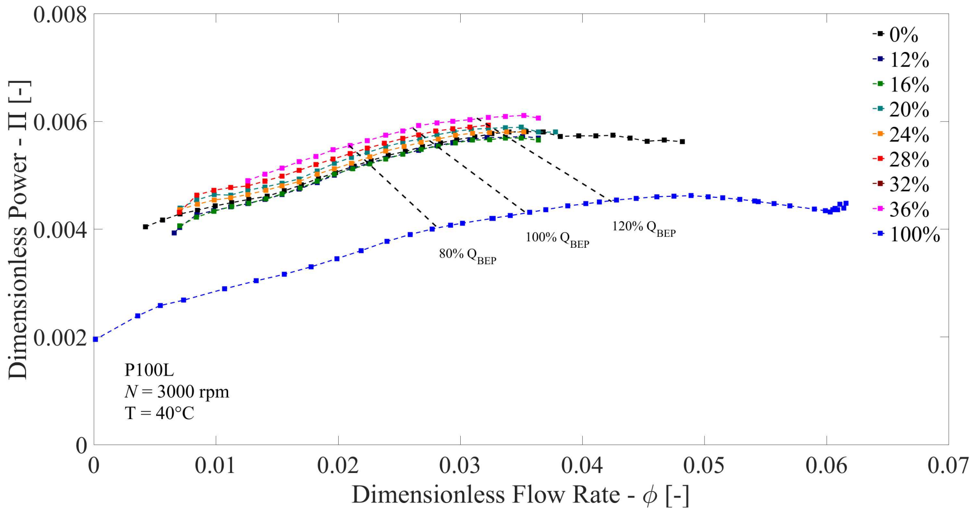

Figure A.76 – P100L Dimensionless Power at 3000 rpm, 40°C.

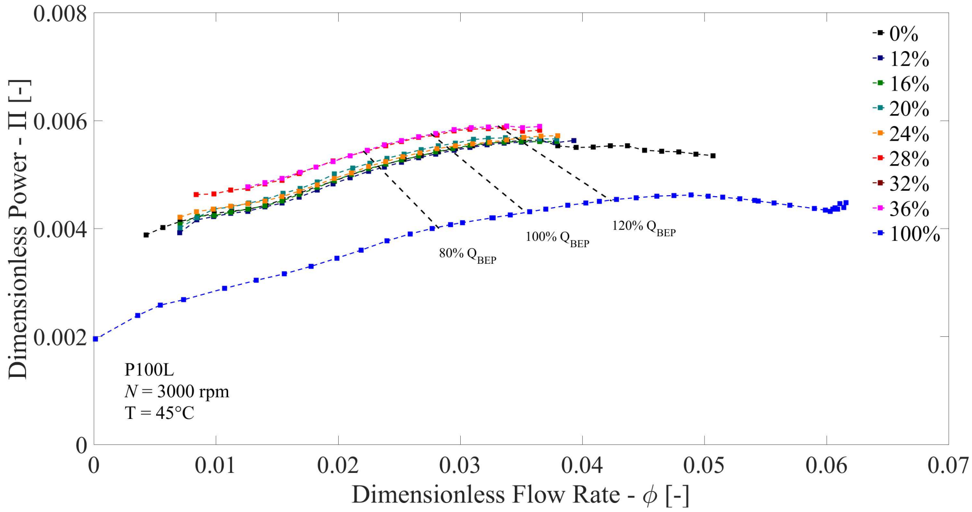

Figure A.77 – P100L Dimensionless Power at 3000 rpm, 45°C.

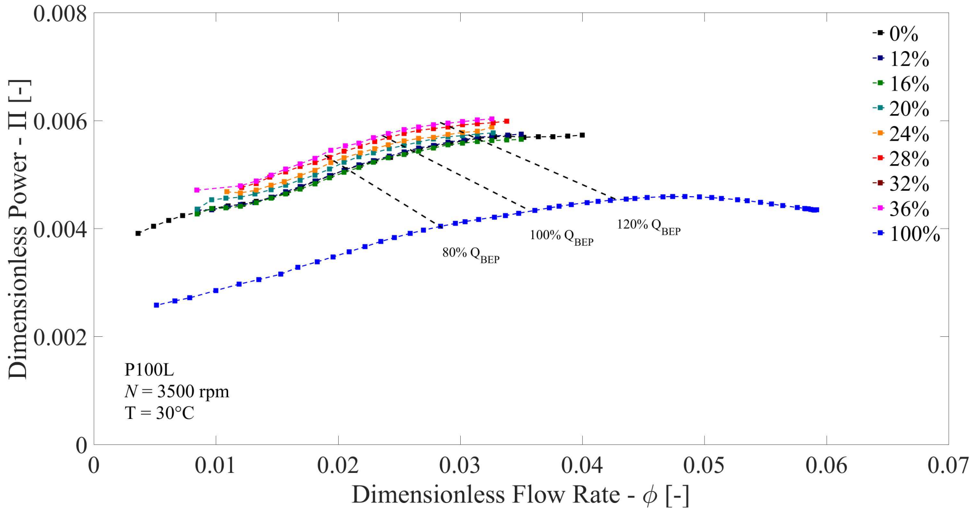

Figure A.78 – P100L Dimensionless Power at 3500 rpm, 30°C.

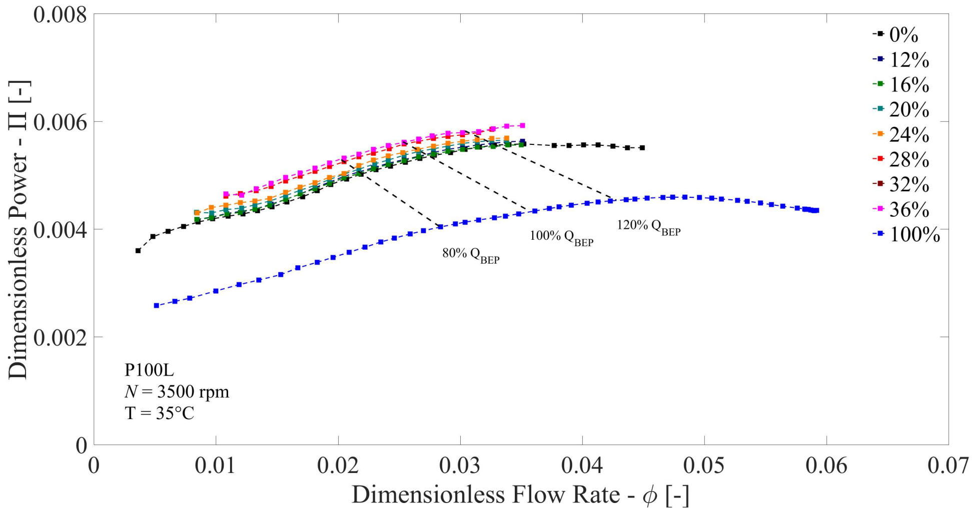

Figure A.79 – P100L Dimensionless Power at 3500 rpm, 35°C.

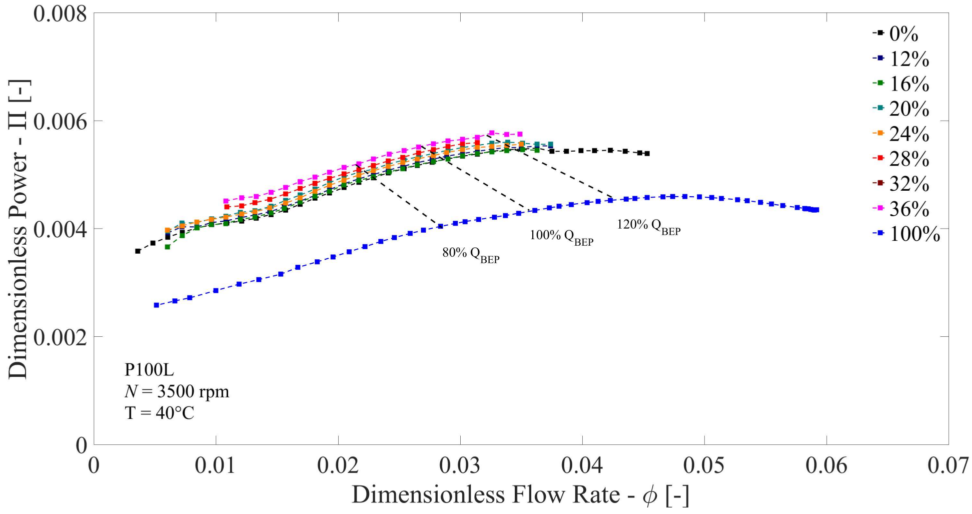

Figure A.80 – P100L Dimensionless Power at 3500 rpm, 40°C.

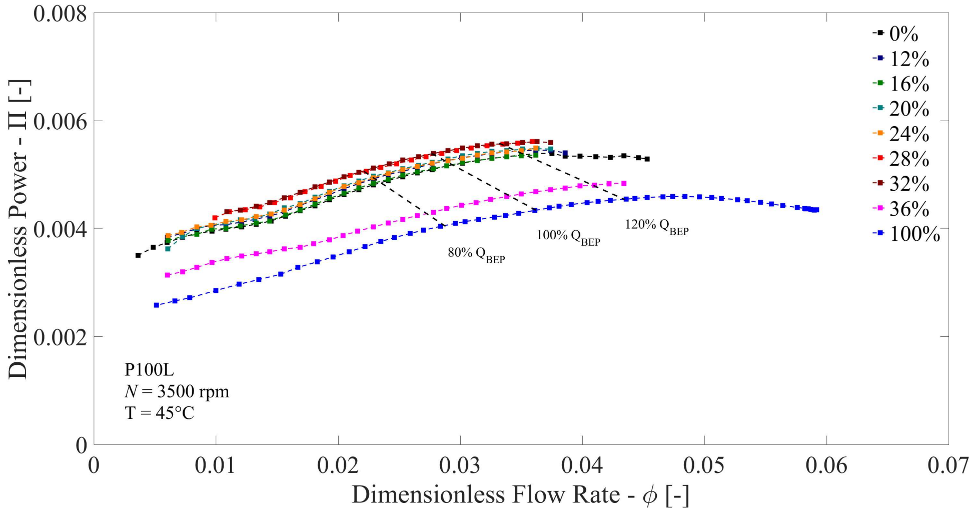

Figure A.81 – P100L Dimensionless Power at 3500 rpm, 45°C.

ANNEX B – RELATIVE VISCOSITY

B.1 ESP Relative Viscosity

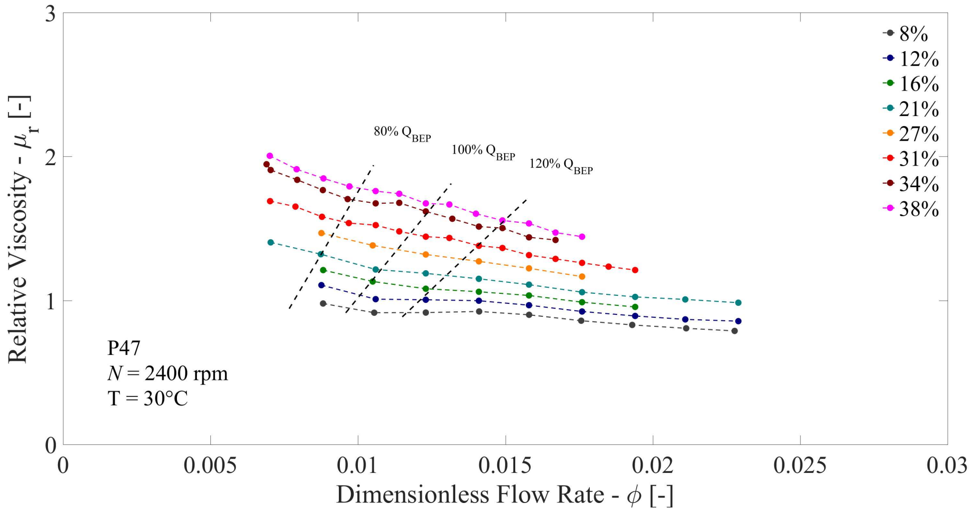

Figure B.1 – P47 Relative Viscosity at 2400 rpm, 30°C

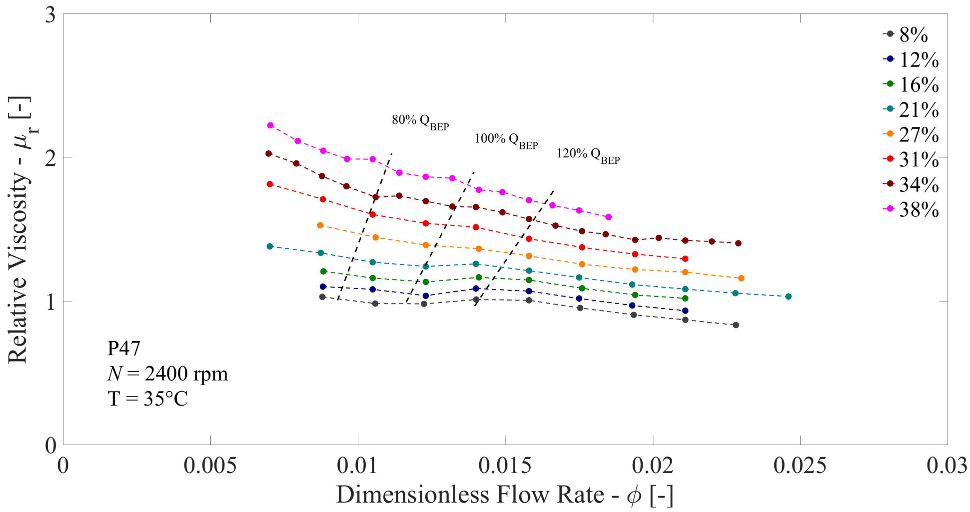

Figure B.2 – P47 Relative Viscosity at 2400 rpm, 35°C

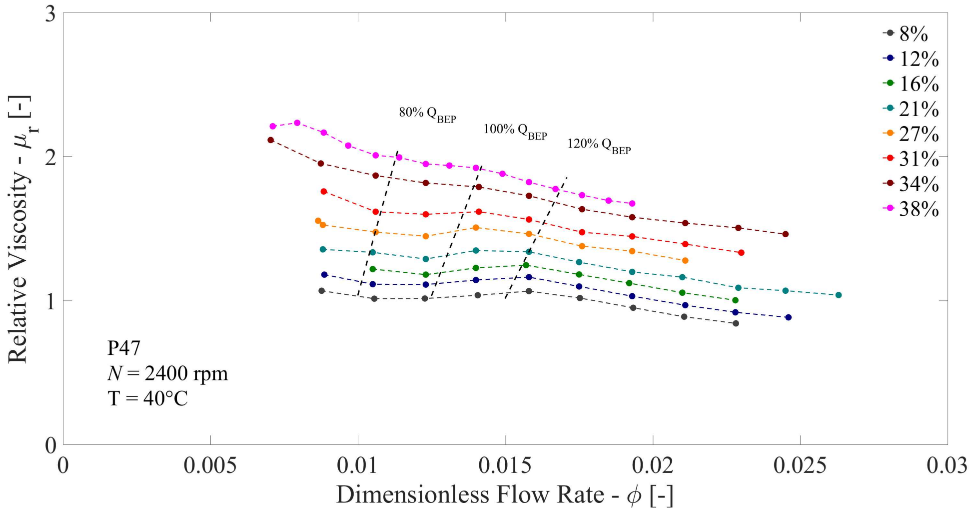

Figure B.3 – P47 Relative Viscosity at 2400 rpm, 40°C

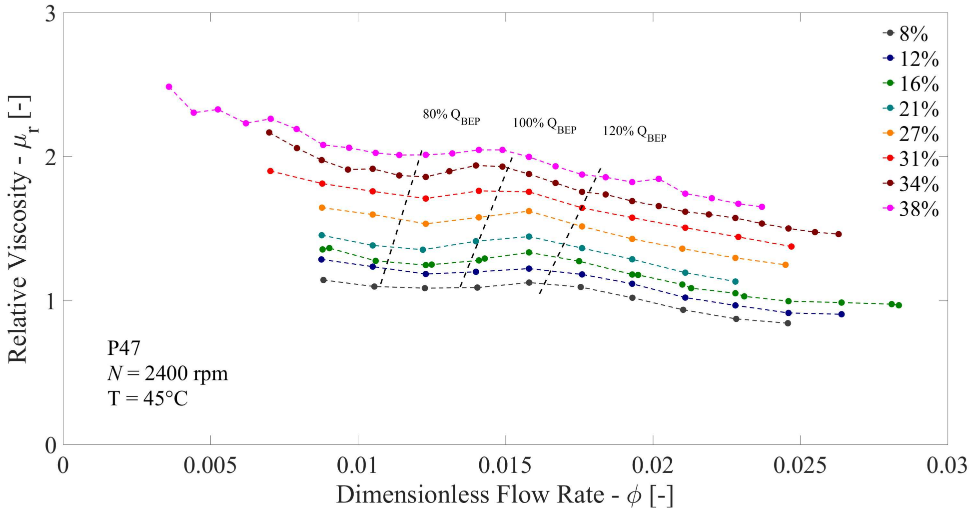

Figure B.4 – P47 Relative Viscosity at 2400 rpm, 45°C

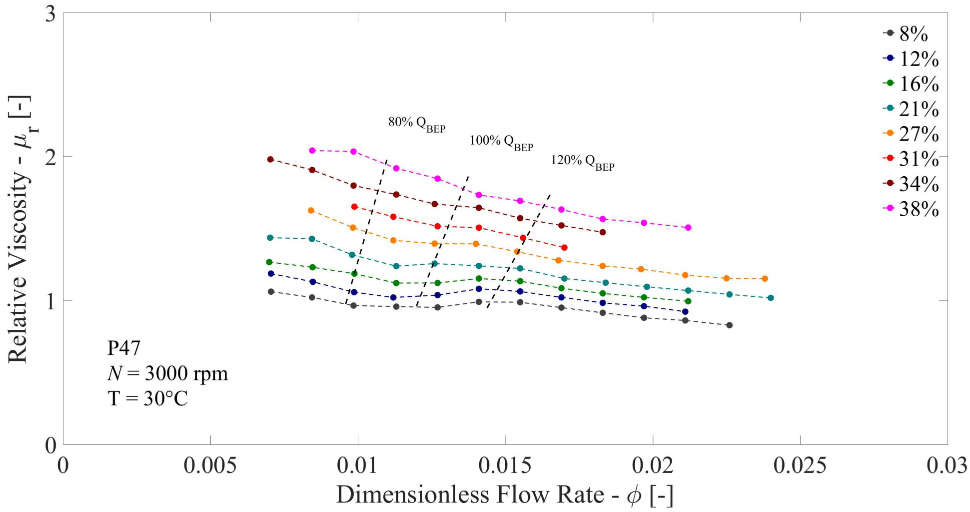

Figure B.5 – P47 Relative Viscosity at 3000 rpm, 30°C

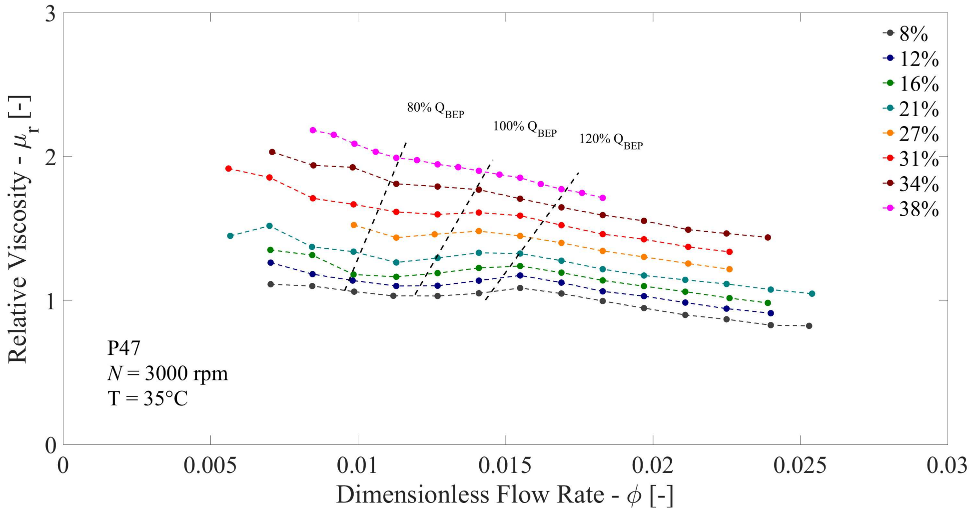

Figure B.6 – P47 Relative Viscosity at 3000 rpm, 35°C

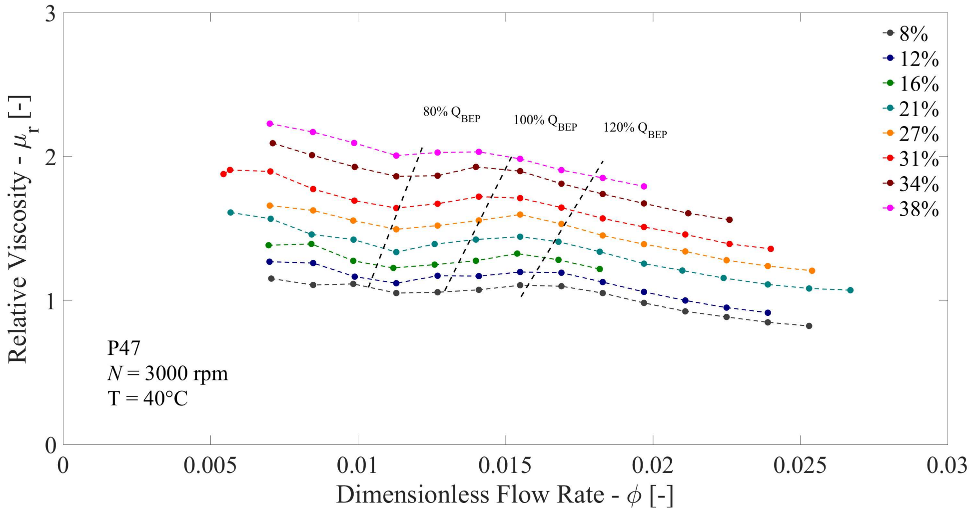

Figure B.7 – P47 Relative Viscosity at 3000 rpm, 40°C

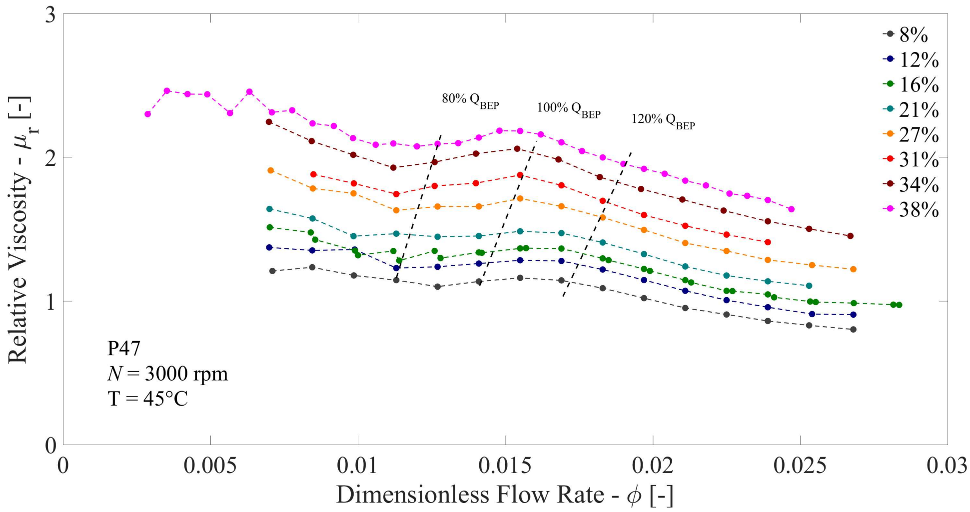

Figure B.8 – P47 Relative Viscosity at 3000 rpm, 45°C

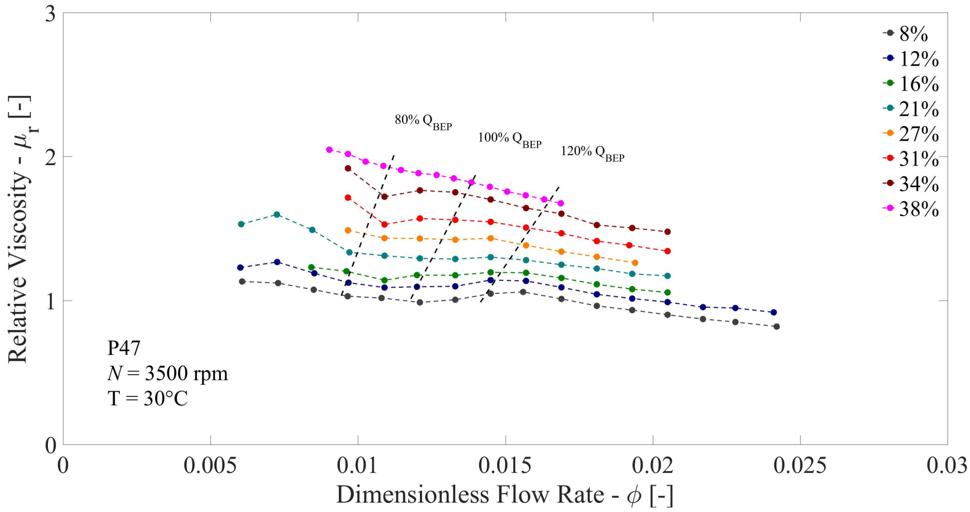

Figure B.9 – P47 Relative Viscosity at 3500 rpm, 30°C

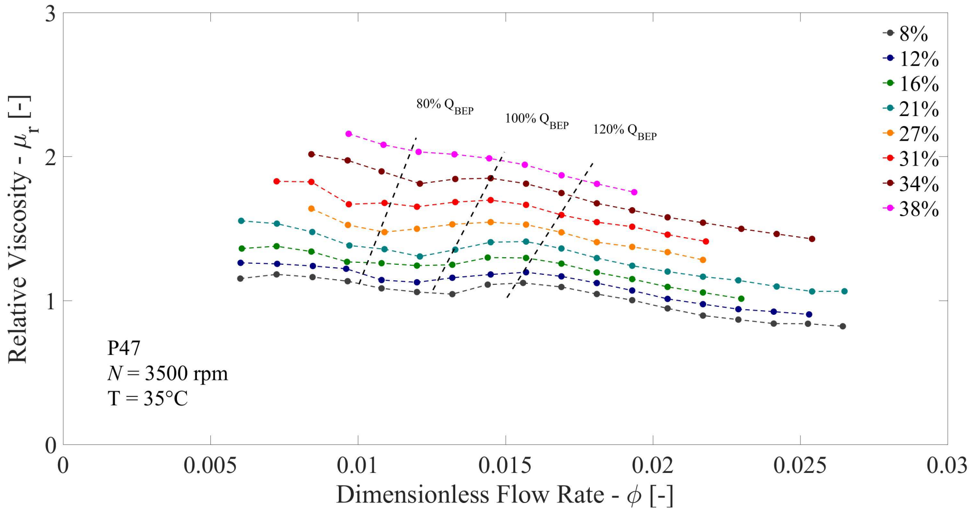

Figure B.10 – P47 Relative Viscosity at 3500 rpm, 35°C

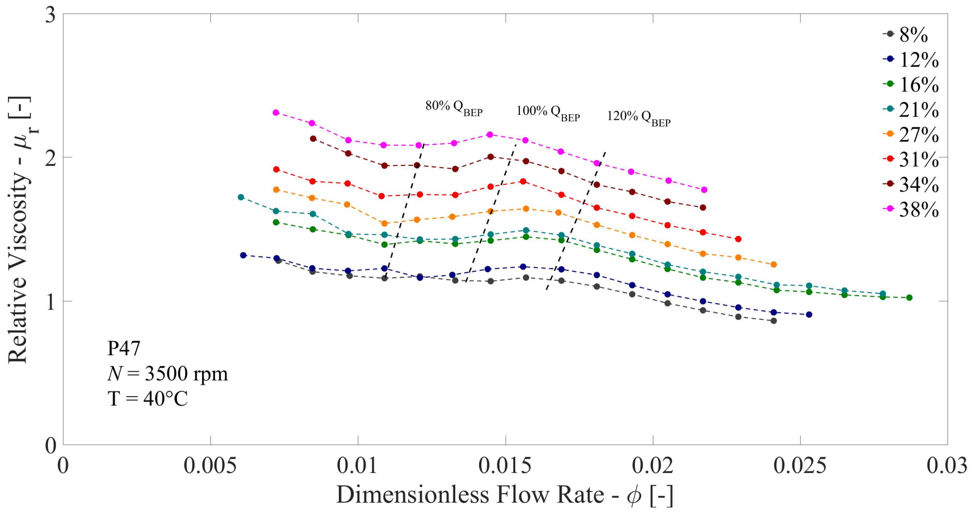

Figure B.11 – P47 Relative Viscosity at 3500 rpm, 40°C

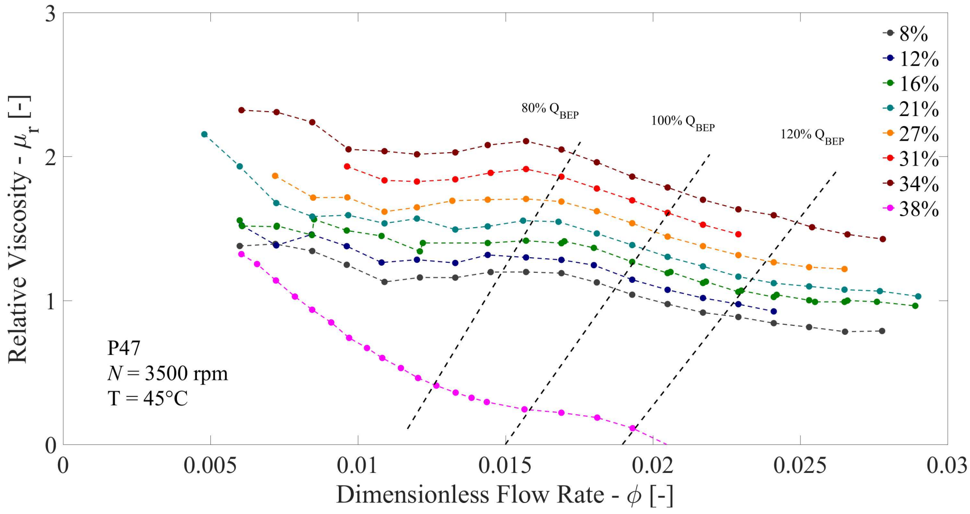

Figure B.12 – P47 Relative Viscosity at 3500 rpm, 45°C

B.1.1 P100L Relative Viscosity Graphs

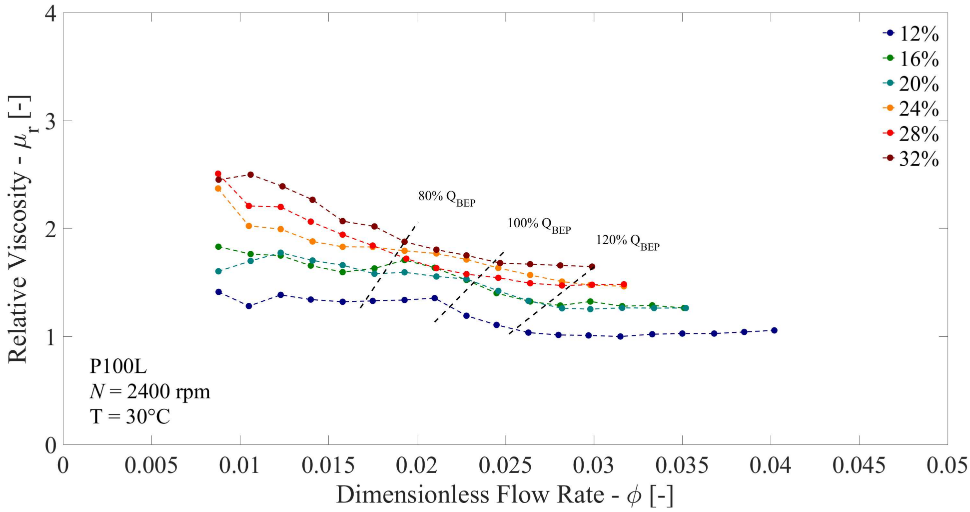

Figure B.13 – P100L Relative Viscosity at 2400 rpm, 30°C

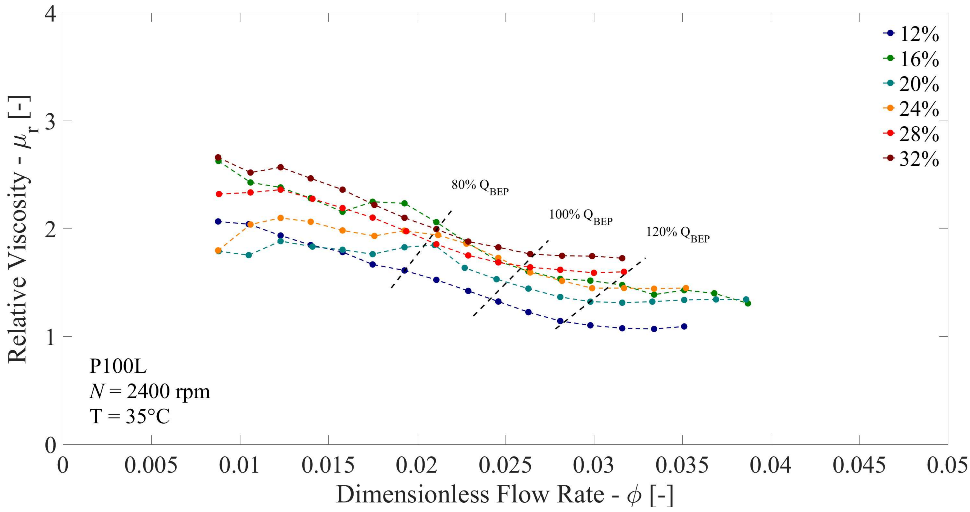

Figure B.14 – P100L Relative Viscosity at 2400 rpm, 35°C

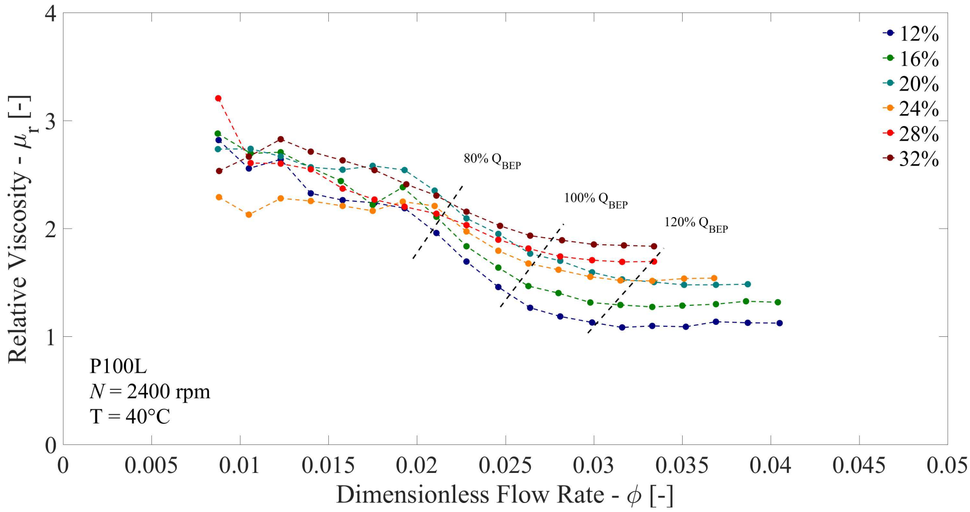

Figure B.15 – P100L Relative Viscosity at 2400 rpm, 40°C

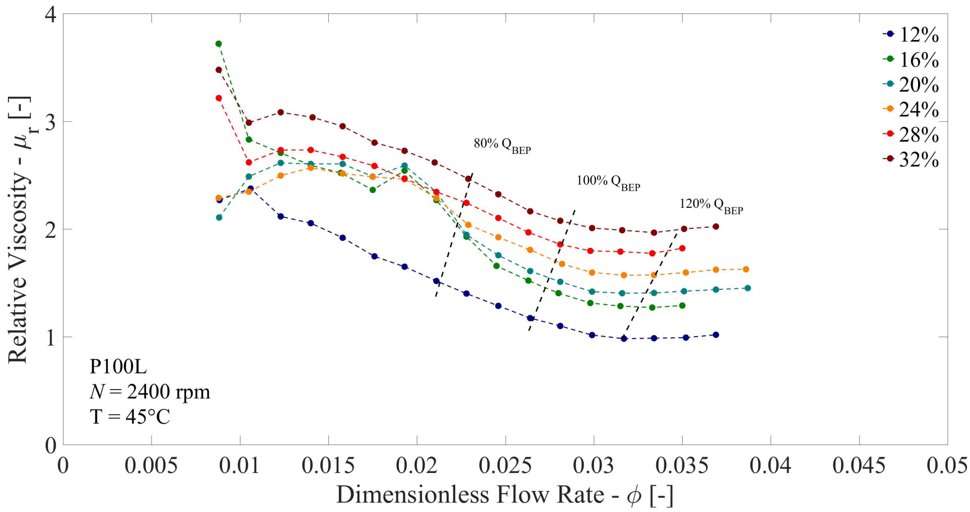

Figure B.16 – P100L Relative Viscosity at 2400 rpm, 45°C

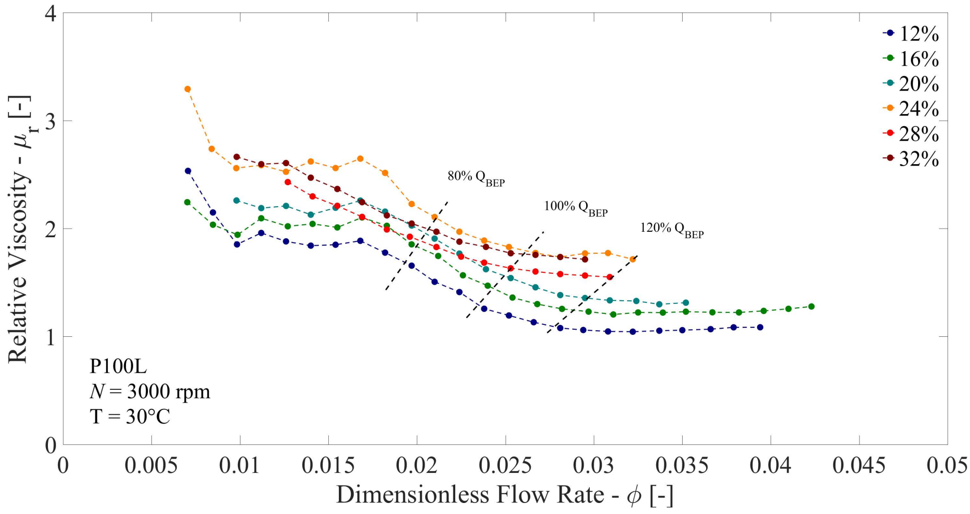

Figure B.17 – P100L Relative Viscosity at 3000 rpm, 30°C

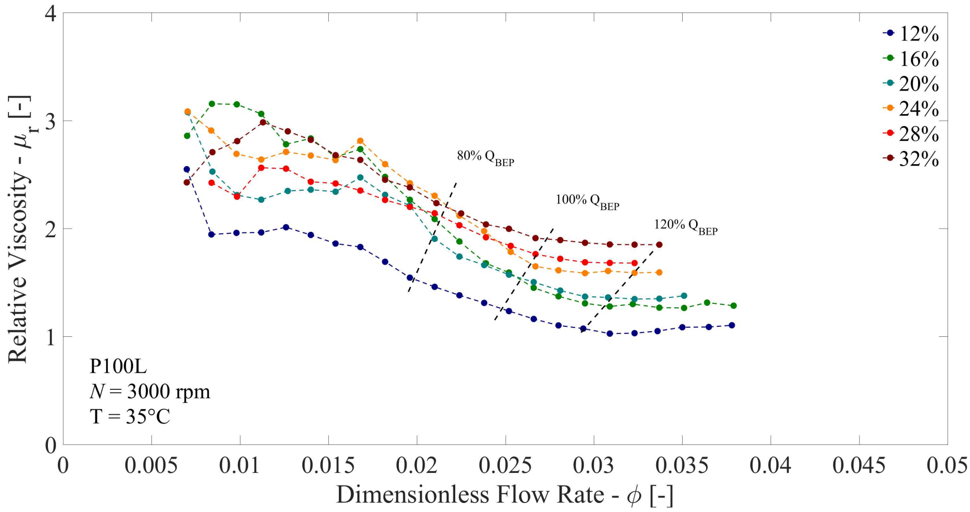

Figure B.18 – P100L Relative Viscosity at 3000 rpm, 35°C

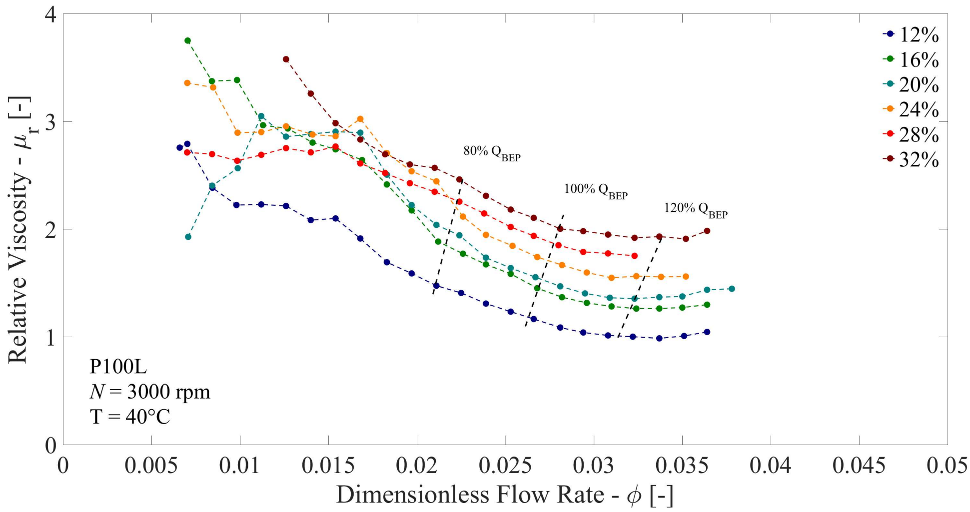

Figure B.19 – P100L Relative Viscosity at 3000 rpm, 40°C

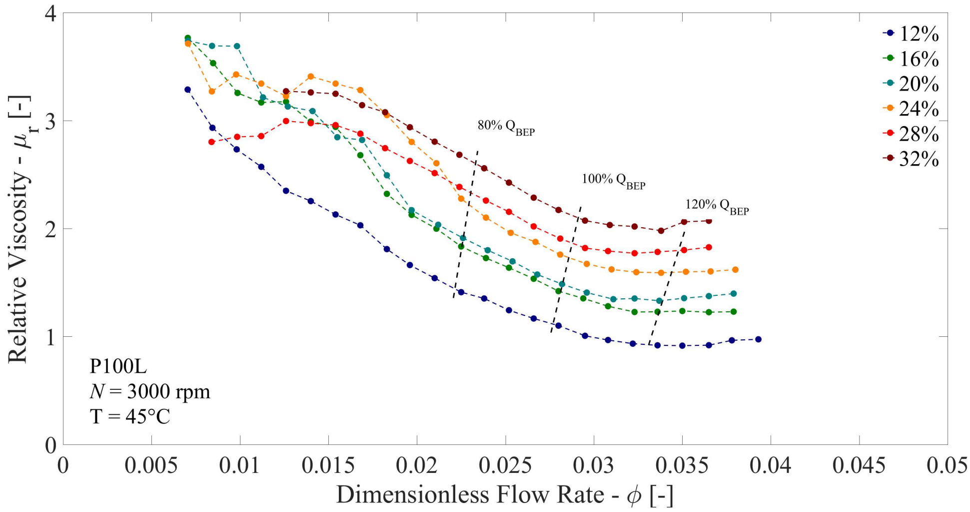

Figure B.20 – P100L Relative Viscosity at 3000 rpm, 45°C

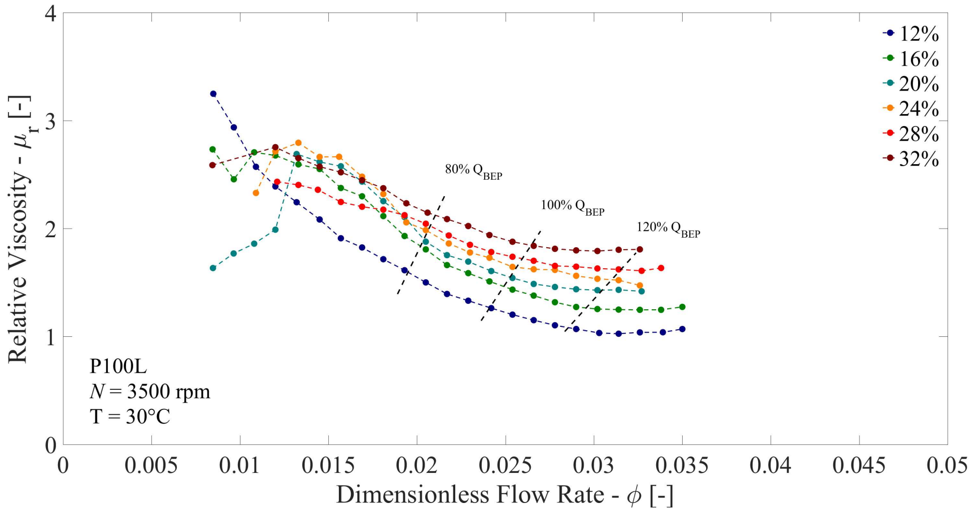

Figure B.21 – P100L Relative Viscosity at 3500 rpm, 30°C

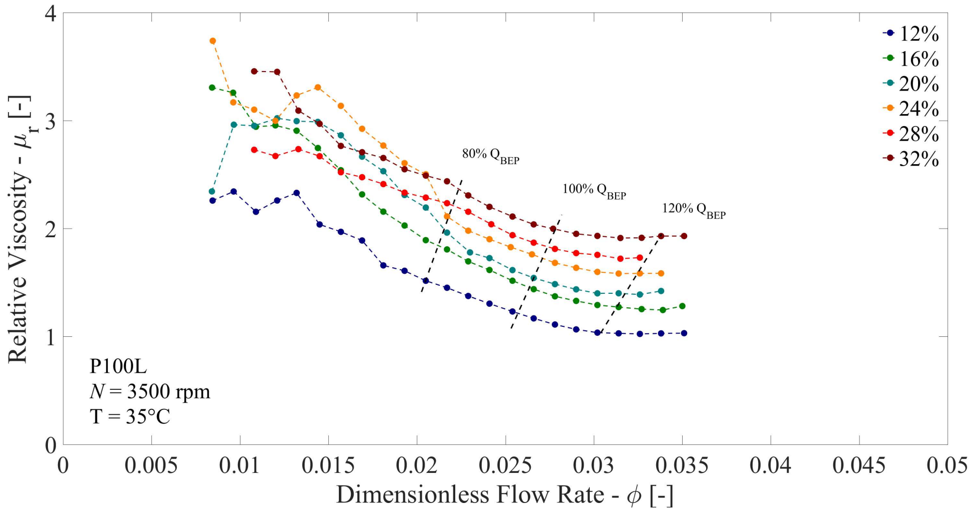

Figure B.22 – P100L Relative Viscosity at 3500 rpm, 35°C

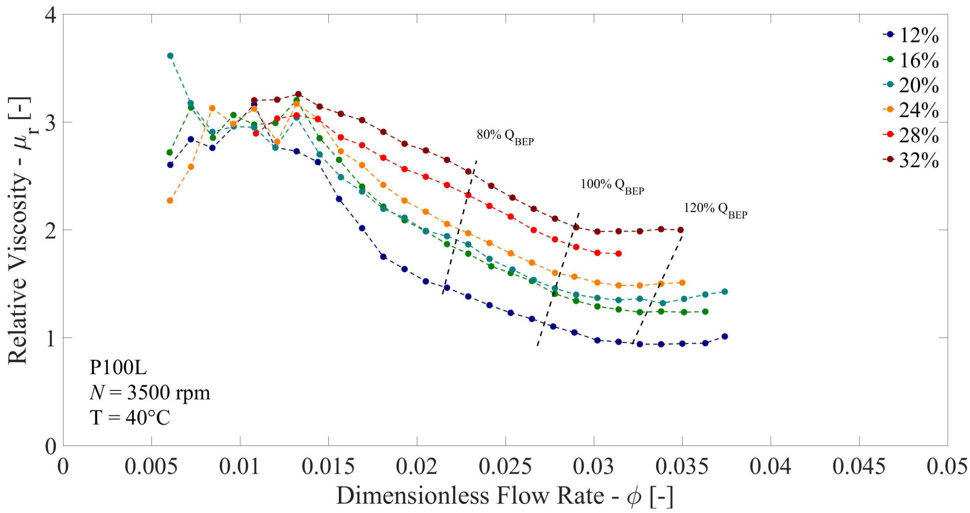

Figure B.23 – P100L Relative Viscosity at 3500 rpm, 40°C

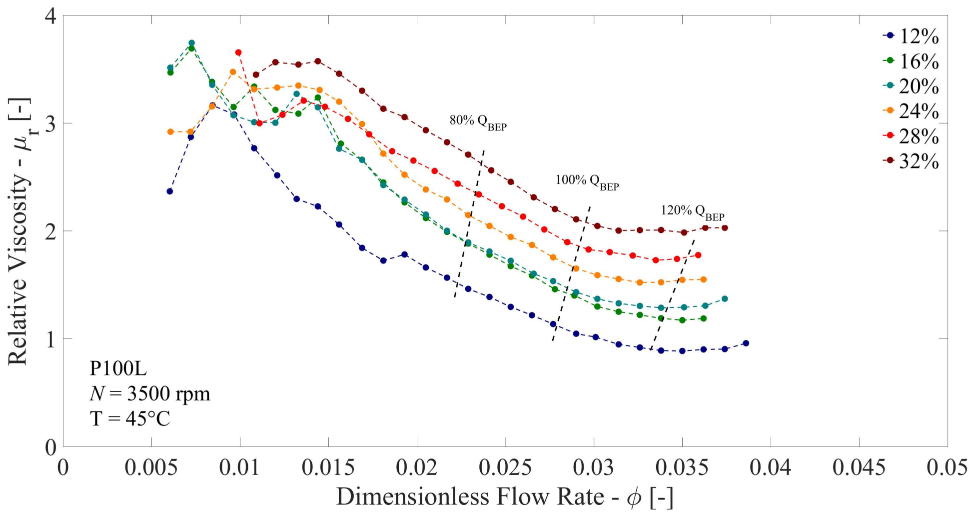

Figure B.24 – P100L Relative Viscosity at 3500 rpm, 45°C

B.2 Pipe Relative Viscosity

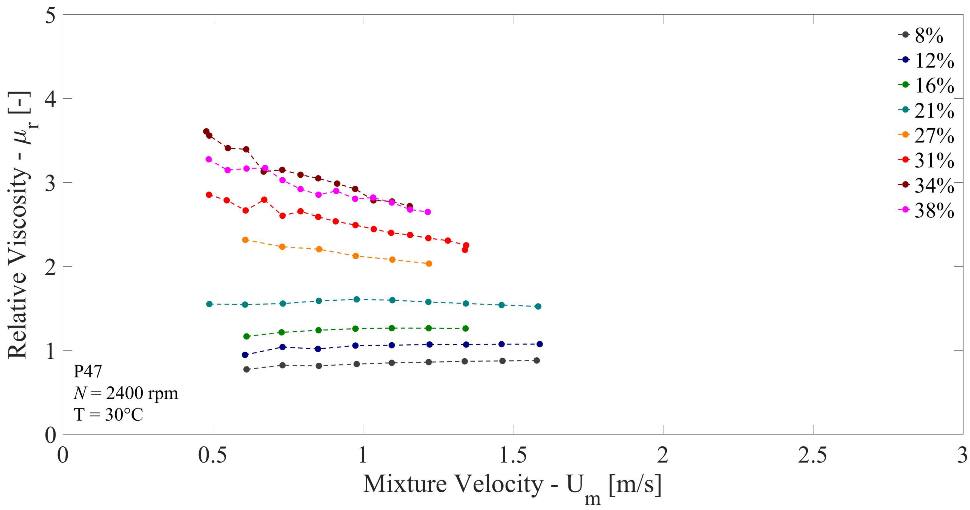

Figure B.25 – Pipe Relative Viscosity (P47) at 2400 rpm, 30°C

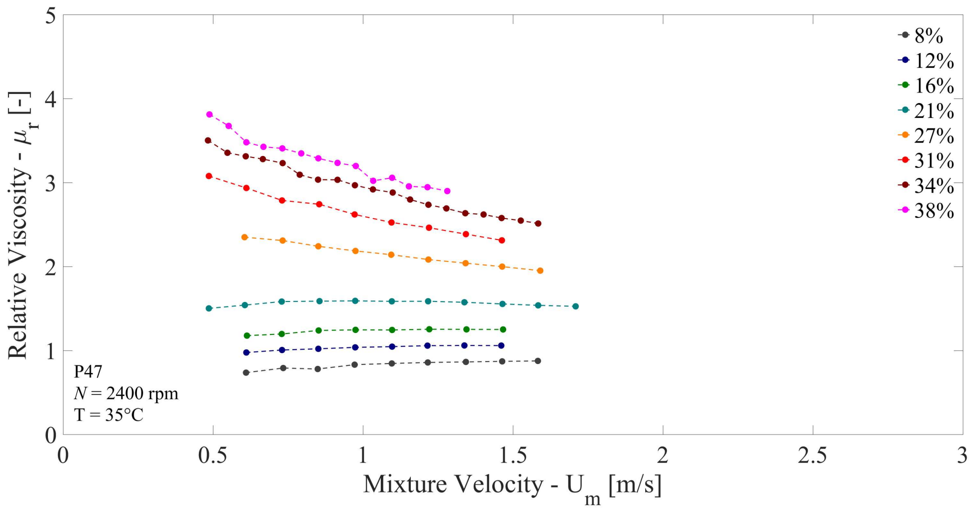

Figure B.26 – Pipe Relative Viscosity (P47) at 2400 rpm, 35°C

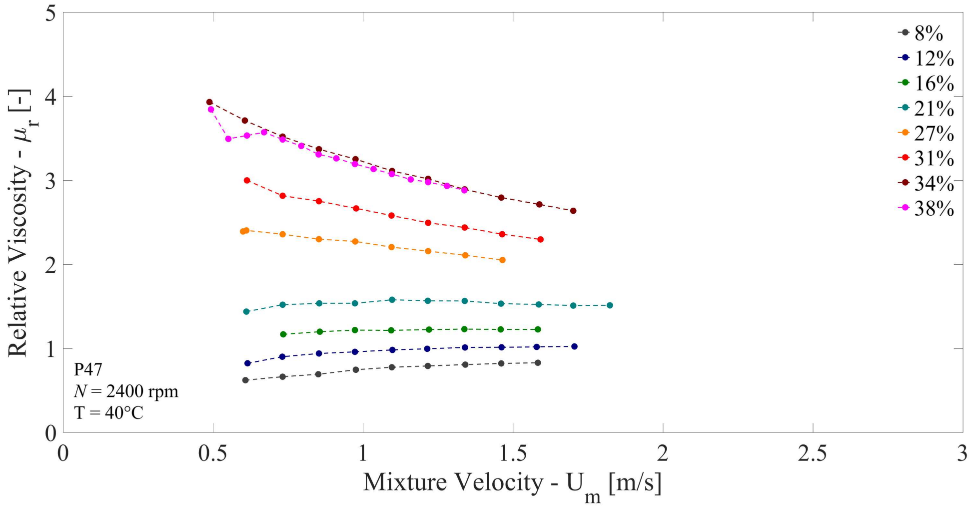

Figure B.27 – Pipe Relative Viscosity (P47) at 2400 rpm, 40°C

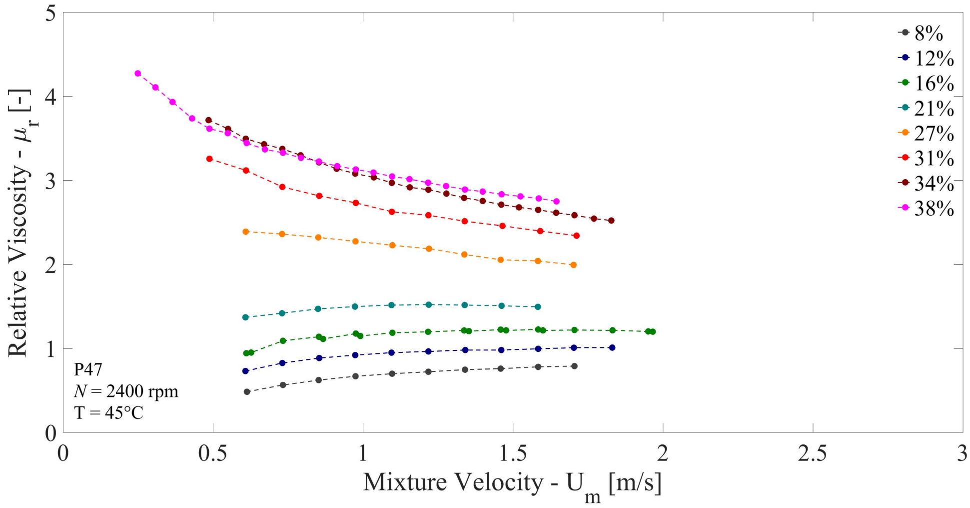

Figure B.28 – Pipe Relative Viscosity (P47) at 2400 rpm, 45°C

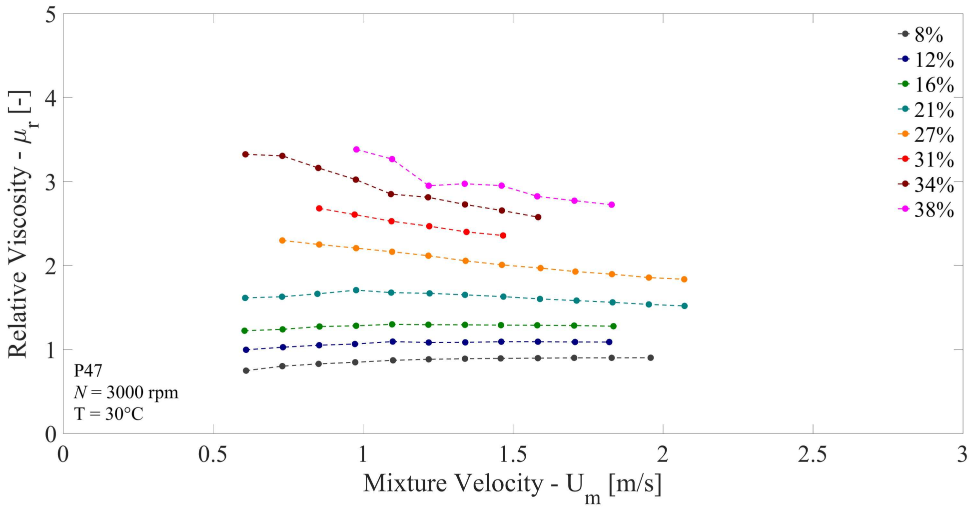

Figure B.29 – Pipe Relative Viscosity (P47) at 3000 rpm, 30°C

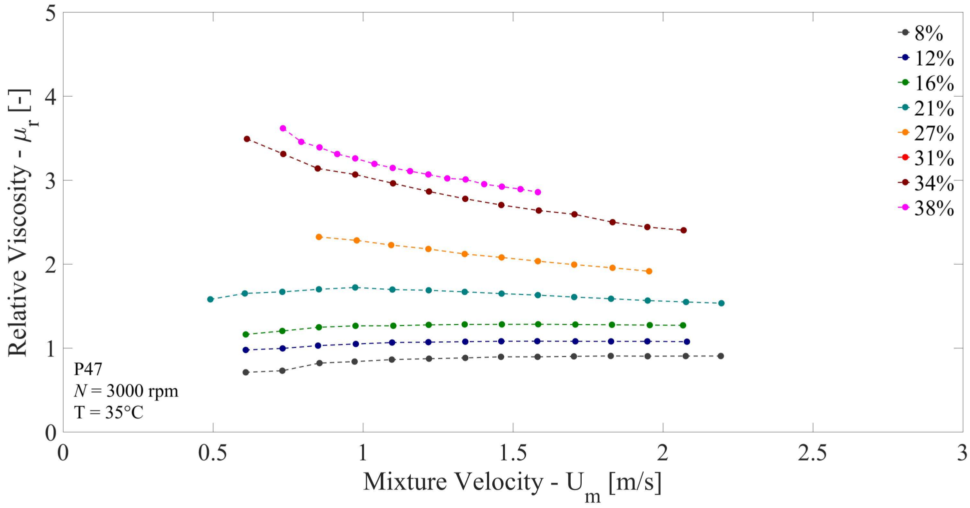

Figure B.30 – Pipe Relative Viscosity (P47) at 3000 rpm, 35°C

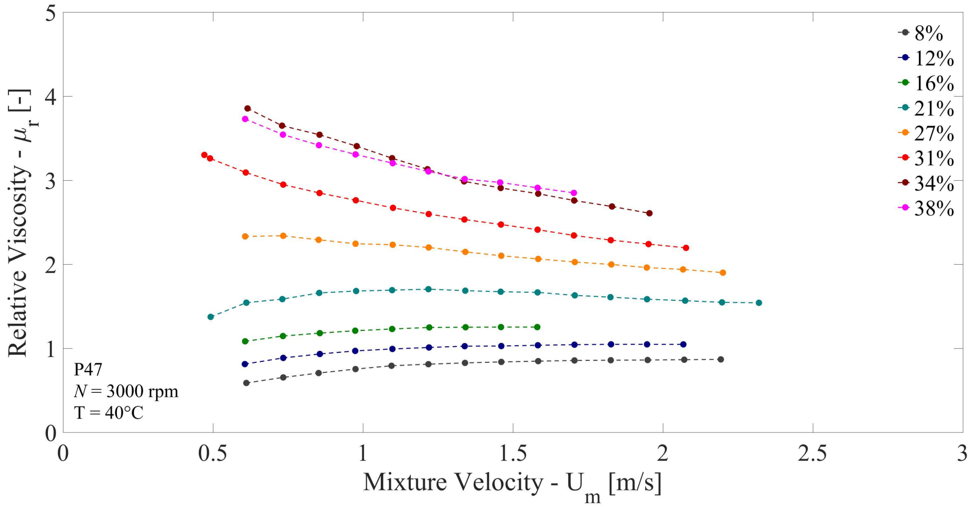

Figure B.31 – Pipe Relative Viscosity (P47) at 3000 rpm, 40°C

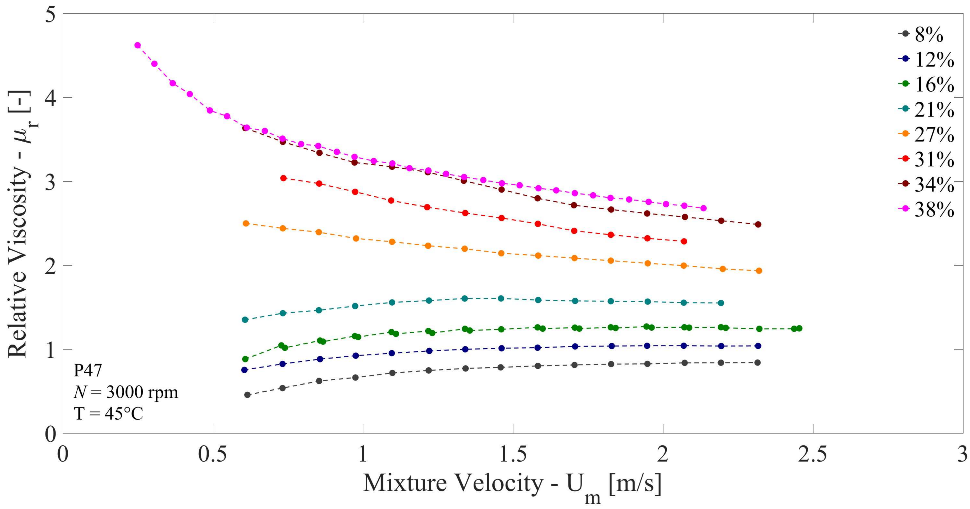

Figure B.32 – Pipe Relative Viscosity (P47) at 3000 rpm, 45°C

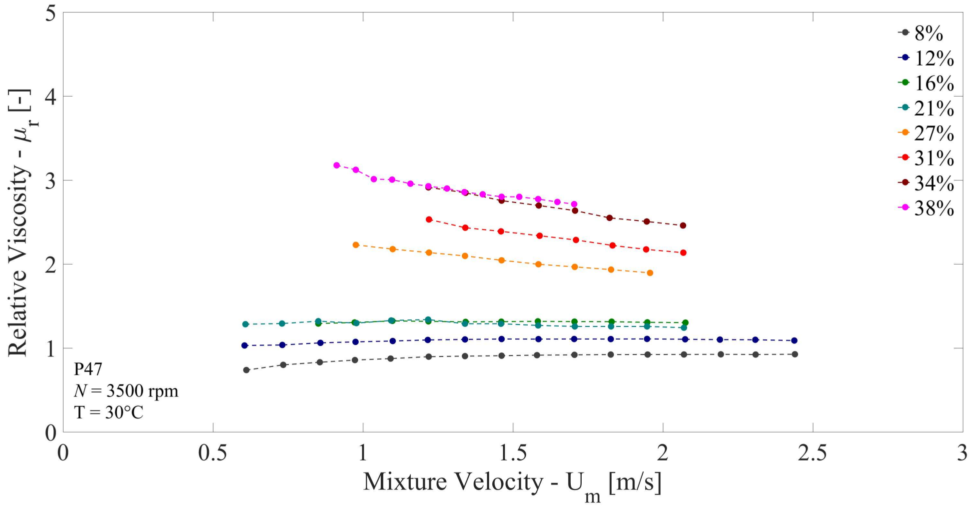

Figure B.33 – Pipe Relative Viscosity (P47) at 3500 rpm, 30°C

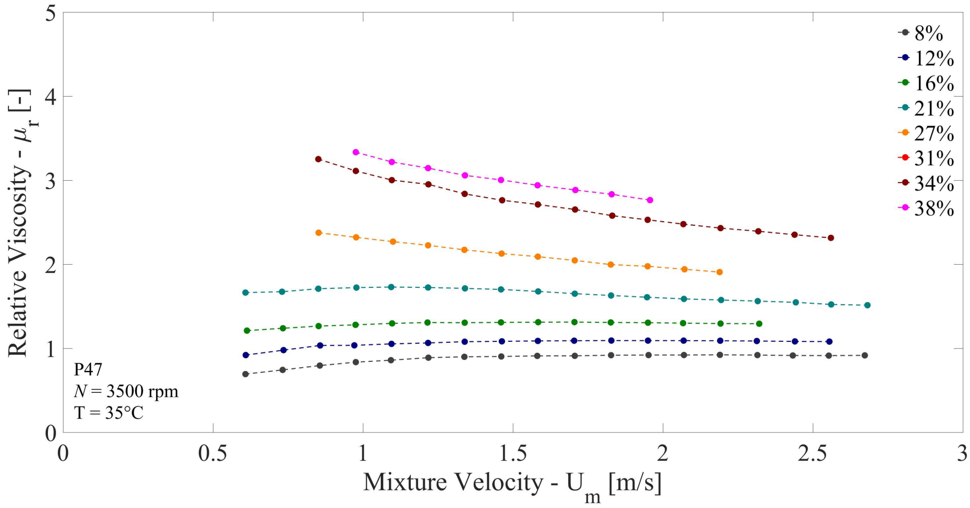

Figure B.34 – Pipe Relative Viscosity (P47) at 3500 rpm, 35°C

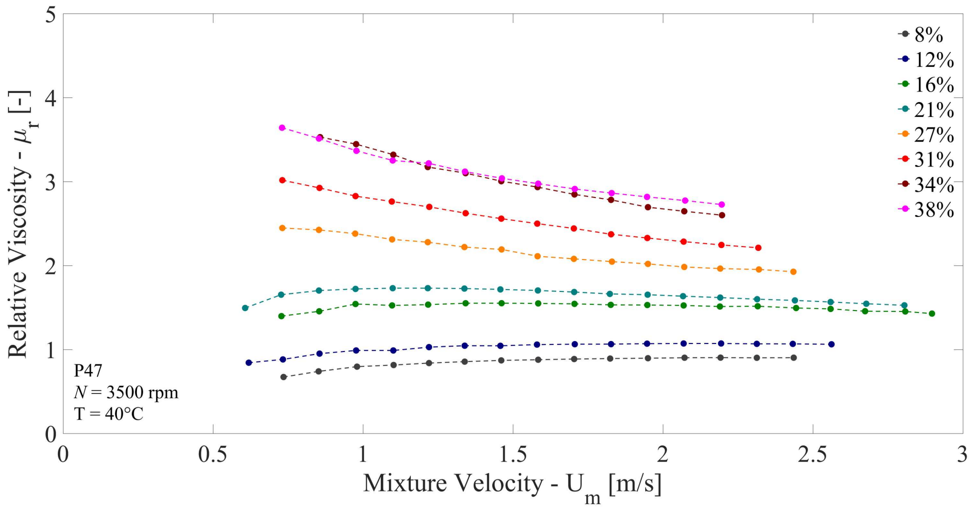

Figure B.35 – Pipe Relative Viscosity (P47) at 3500 rpm, 40°C

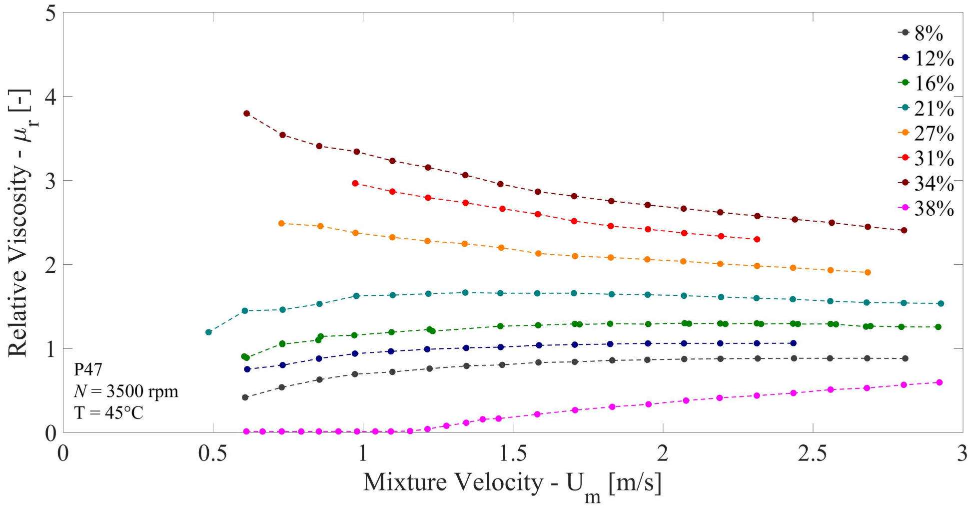

Figure B.36 – Pipe Relative Viscosity (P47) at 3500 rpm, 45°C

B.2.1 Pipe Relative Viscosity (P100L) Graphs

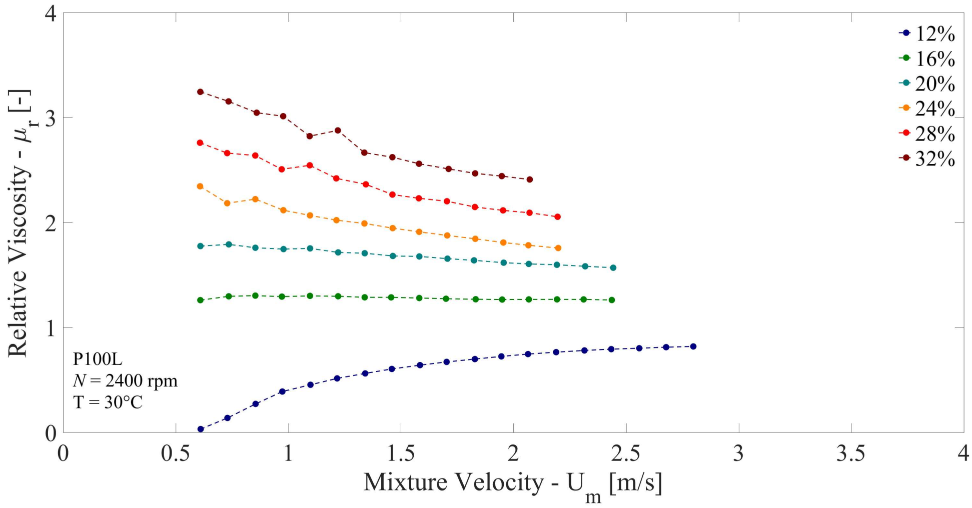

Figure B.37 – Pipe Relative Viscosity (P100L) at 2400 rpm, 30°C

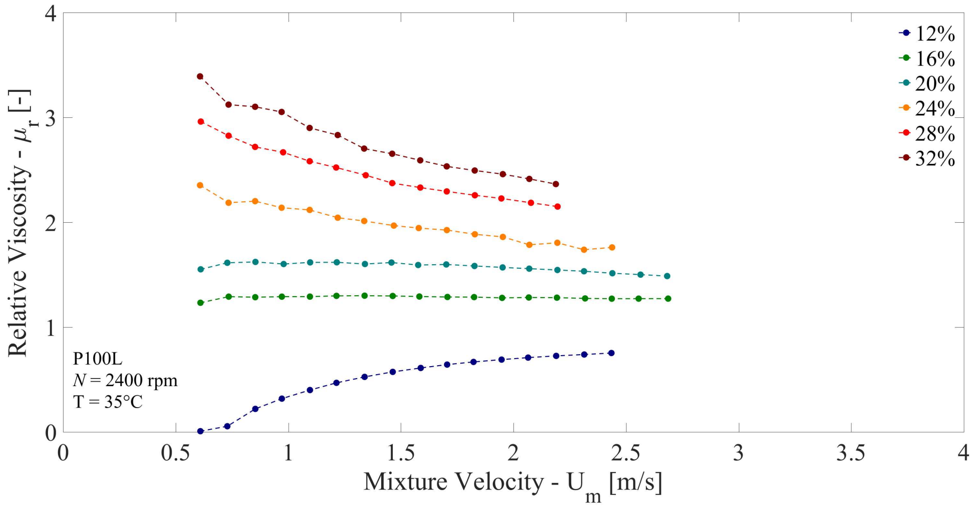

Figure B.38 – Pipe Relative Viscosity (P100L) at 2400 rpm, 35°C

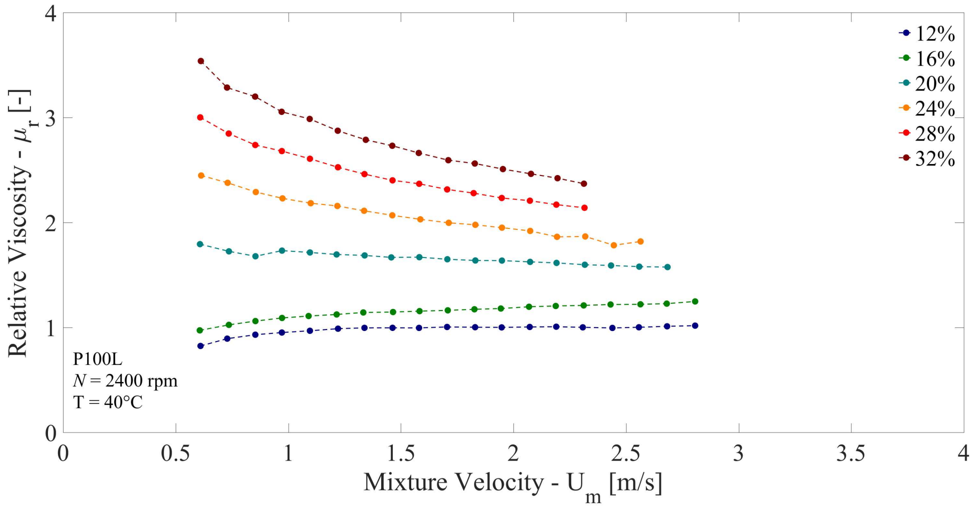

Figure B.39 – Pipe Relative Viscosity (P100L) at 2400 rpm, 40°C

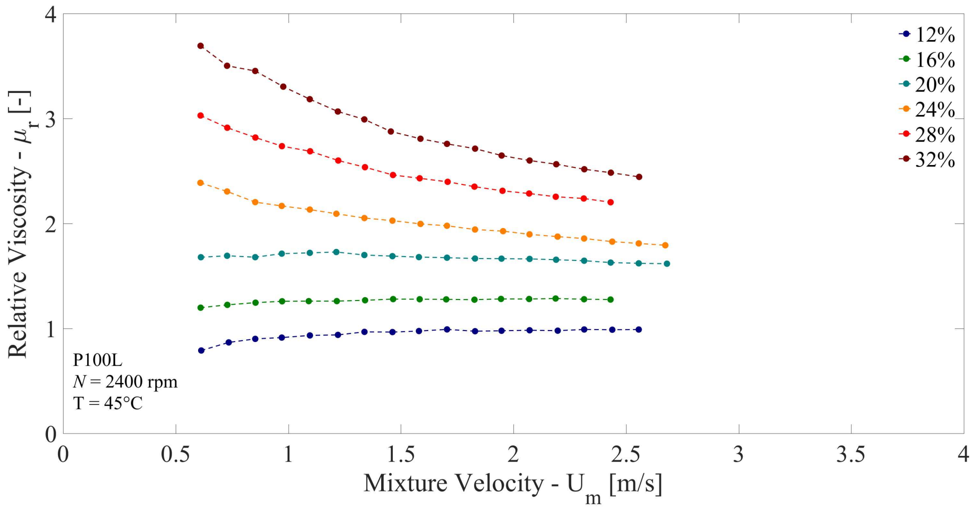

Figure B.40 – Pipe Relative Viscosity (P100L) at 2400 rpm, 45°C

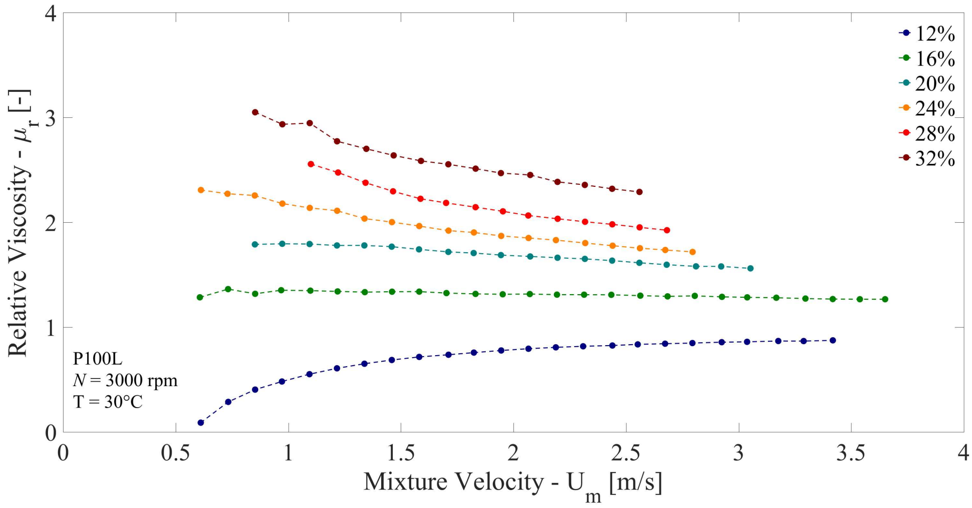

Figure B.41 – Pipe Relative Viscosity (P100L) at 3000 rpm, 30°C

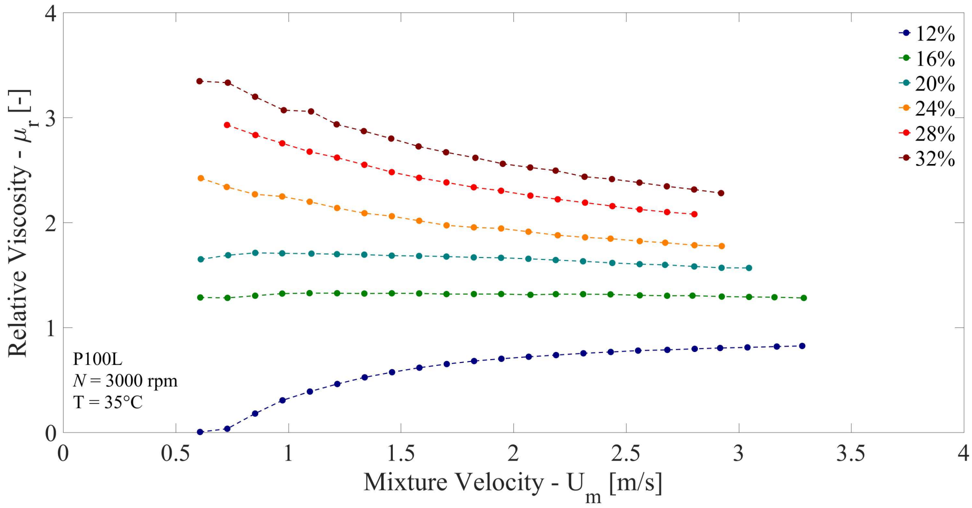

Figure B.42 – Pipe Relative Viscosity (P100L) at 3000 rpm, 35°C

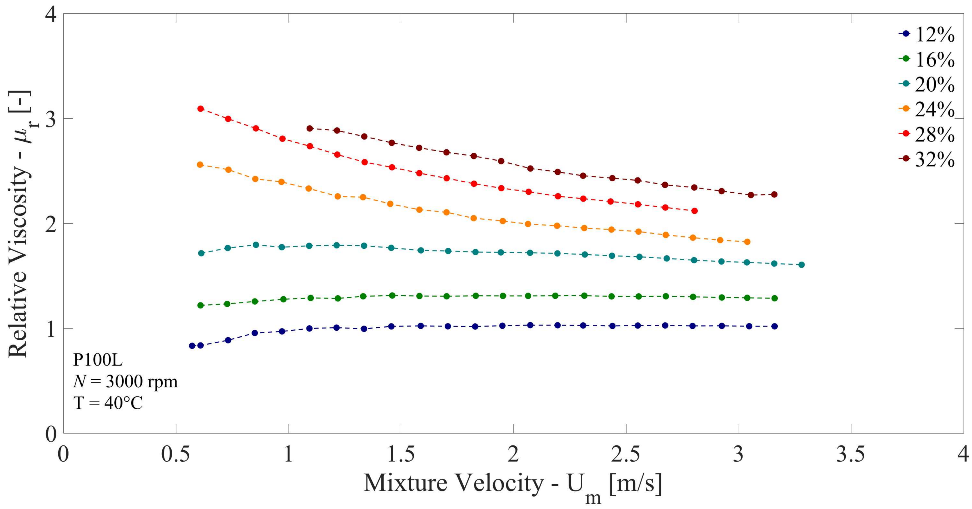

Figure B.43 – Pipe Relative Viscosity (P100L) at 3000 rpm, 40°C

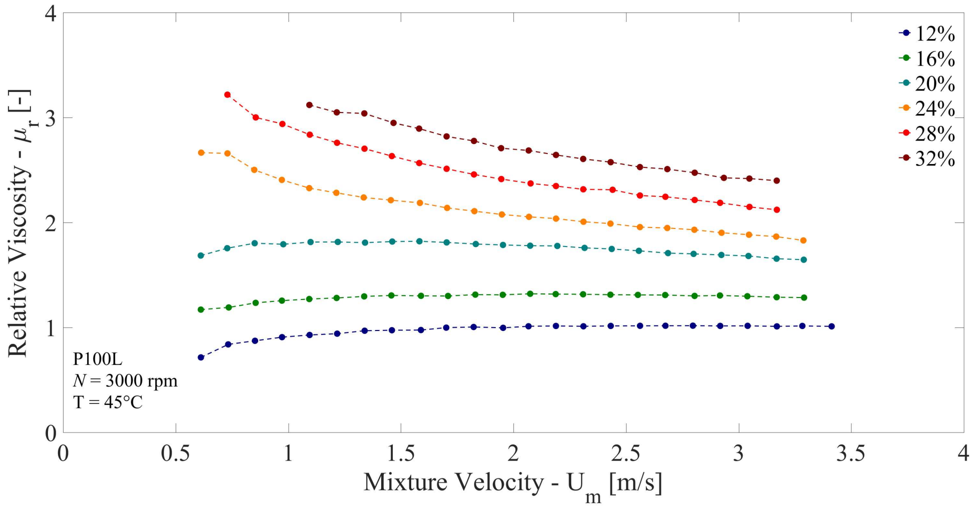

Figure B.44 – Pipe Relative Viscosity (P100L) at 3000 rpm, 45°C

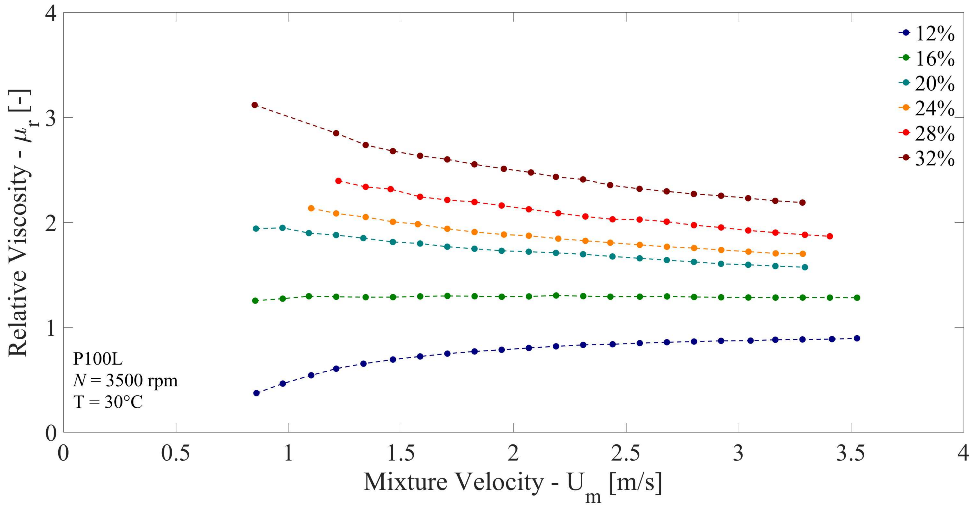

Figure B.45 – Pipe Relative Viscosity (P100L) at 3500 rpm, 30°C

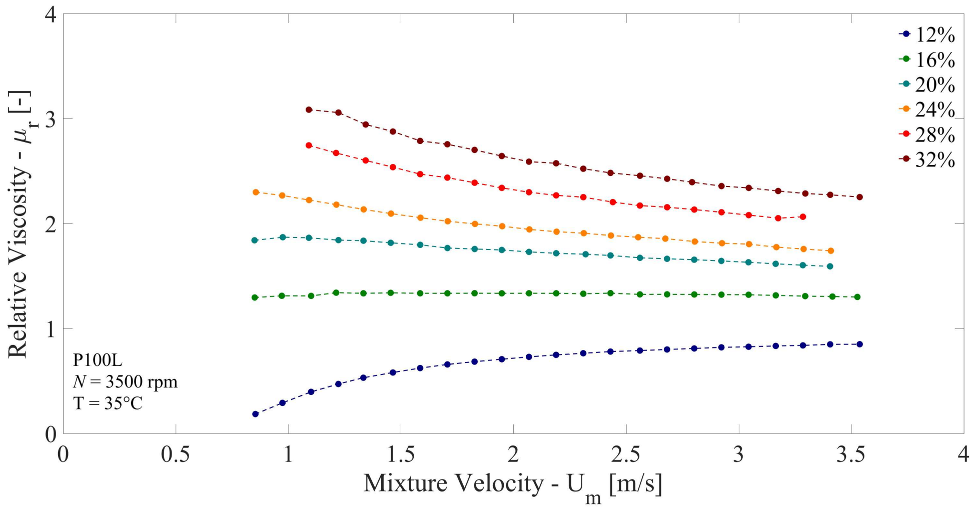

Figure B.46 – Pipe Relative Viscosity (P100L) at 3500 rpm, 35°C

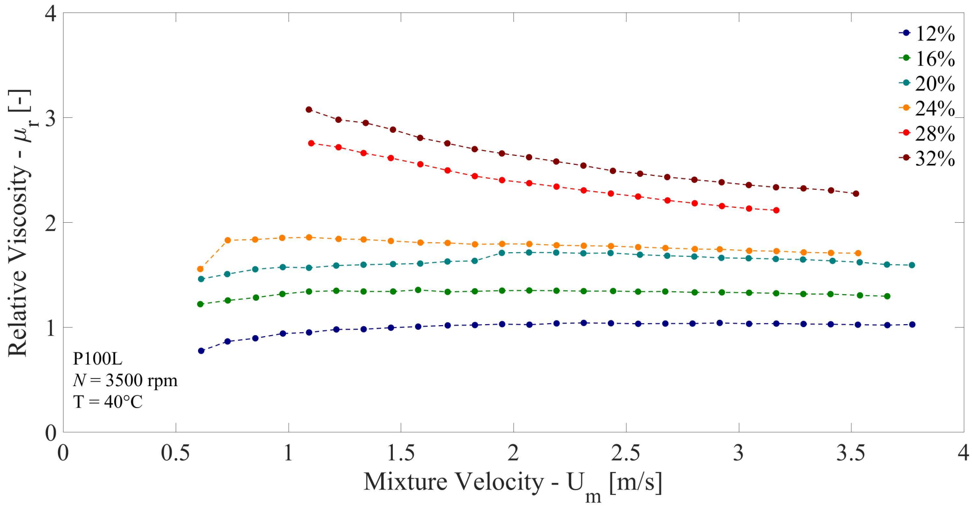

Figure B.47 – Pipe Relative Viscosity (P100L) at 3500 rpm, 40°C

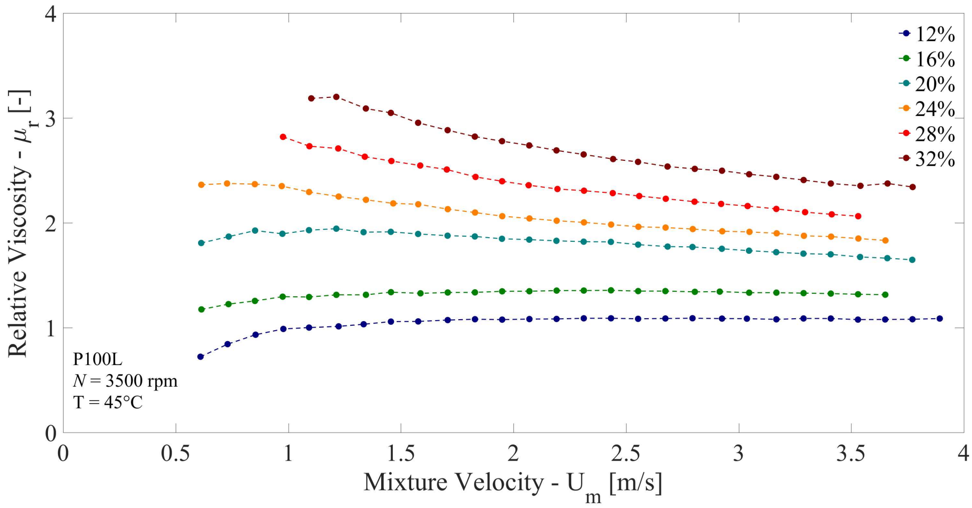

Figure B.48 – Pipe Relative Viscosity (P100L) at 3500 rpm, 45°C